DESIGN, DEVELOPMENT, AND VALIDATION OF A LOW-COST MEASUREMENT SYSTEM FOR RESIDENTIAL GROUND SOURCE HEAT PUMP SYSTEMS

By

ERIC M. BRINKMAN

Bachelor of Science in Mechanical Engineering.
Oklahoma State University
Stillwater, OK
2017

Submitted to the Faculty of the
Graduate College of
Oklahoma State University
in partial fulfillment of
the requirements for
the Degree of
MASTER OF SCIENCE
December, 2019

DESIGN, DEVELOPMENT, AND VALIDATION
OF A LOW-COST MEASUREMENT SYSTEM FOR
RESIDENTIAL GROUND SOURCE HEAT PUMP SYSTEMS

Thesis Approved:

Dr. He Bai

Thesis Advisor

Dr. Jeffrey Spitler

Dr. Christian Bach

ACKNOWLEDGMENTS

To my parents, Tim and Valerie Brinkman: thank you for your consistent love, support, and encouragement throughout the highs and lows of the past two years.

To my roommates, Ardalan Hayatifar and Matthew Staples: thank you for your encouragement, faithful-presence, and patience through all the long hours and late nights.

To my advisors, He Bai and Jeffrey Spitler: thank you for your guidance, expertise, and the consistent example of excellence you both set for me.

To the BETSRG and CoRAL research groups: thank you all for your cooperation and assistance throughout the design, fabrication, and calibration processes over the last two years. Going out to eat throughout the week and seeing you guys in classes was always a nice break from research. Special thanks to the undergraduate researchers who have specifically helped with the project along the way:

Bo Rogers - initial thermistor calibrations and circuit board work.

Luke Wang - initial flow meter calibration.

Collin Thornton - 3D printed energy meter cases.

Sheldon Hair - ultrasonic flow meter investigation.

Acknowledgments reflect the views of the author and are not endorsed by committee members or Oklahoma State University.

Name: ERIC M. BRINKMAN

Date of Degree: DECEMBER, 2019

Title of Study: DESIGN, DEVELOPMENT, AND VALIDATION OF A LOW-COST MEASUREMENT SYSTEM FOR RESIDENTIAL GROUND SOURCE HEAT PUMP SYSTEMS

Major Field: MECHANICAL AND AEROSPACE ENGINEERING

Abstract: There is still relatively little data available to properly analyze the performance of Ground Source Heat Pump (GSHP) systems in residential applications. While commercial-grade instrumentation is available, it is often expensive to deploy in residential systems. As a result, there continues to be a need for low-cost, properly installed sensor systems in residential GSHP systems.

To collect meaningful performance data from any heating and cooling system, accurate measurements of heat transfer and electrical power must be made. Specifically, high-accuracy temperature sensors, flow sensors, and power transducers must be properly calibrated and installed, with appropriate data acquisition software, in order to calculate the Coefficient of Performance ("COP") of any system. To support wider collection of meaningful performance data for residential applications, a low-cost energy meter & data acquisition system has been developed and its accuracy verified.

This paper describes the design, fabrication, and validation of the above mentioned clamp-on energy meter, and the associated validation test loop constructed to verify its accuracy. Preliminary field measurements, detailed parts list, associated Python programs, and suggestions for future modifications are included as well.

TABLE OF CONTENTS

LIST OF TABLES

LIST OF FIGURES

Figure Page

ABBREVIATIONS

ADC	Analog-to-Digital Conversion
CFM	Cubic Feet per Minute
COP	Coefficient of Performance
CT	Current Transducer
DOE	United States Department of Energy
EIA	United States Energy Information Administration
EPS	External Power Supply
EUI	Energy Use Intensity
FSV	Full-Scale Voltage
FT	Flow Transducer
GLS	Generalized Least Squares (Method)
GSHP	Ground Source Heat Pump
HVAC	Heating, Ventilation, and Air-Conditioning
LRA	Locked Rotor Amperage
MER	Monthly Energy Review
MWt	Mega-Watt-Thermal
NLR	No-Load Rating
NPT	National Pipe Thread
P&ID	Piping and Instrumentation Diagram
ppg	Pulses-per-U.S. Gallon
PWM	Pulse Width Modulation
RECS	Residential Energy Consumption Survey

R&D	Research and Development
RLA	Rated Load Amperage
RMS	Root Mean Square
RTC	Real Time Clock
SEPEMO	SEasonal PErformance factor and MOnitoring
SHH	Steinhart-Hart
SPF	Seasonal Performance Factor
SPS	Samples Per Second
TT	Temperature Transducer
U.S.	United States
VT	Voltage Transformer

NOMENCLATURE

VARIABLES	**UNITS**	**DESCRIPTION**
A	-	Steinhart-Hart Coefficient
B	-	Steinhart-Hart Coefficient
C	-	Steinhart-Hart Coefficient
c_p	J/(kg·K)	Specific heat
E	-	Absolute uncertainty
e	-	Fractional (relative) uncertainty
I	A	Current
$\widehat{I}$	A	Measured (Burden Resistor) Current
$\widetilde{I}$	A	Secondary (induced) Current
k	Pulses-per-gallon	Flow meter volumetric conversion constant
L	loops	Number of loops in a CT
m	quantization level or "bin count"	Output number from an ADC board
n	bits	Number of bits in an ADC board
p	pulses	Total pulses detected (sum of falling *and* rising edges)
P	W	Real Power
Q	Wh	Cumulative Calorimetric Heat Transfer
$\dot{Q}$	W	Instantaneous Heat Transfer Rate

$\widehat{\dot{Q}}$	W	Estimated Instantaneous Heat Transfer Rate
R	Ω	Resistance
S	VA	Apparent Power
SF	-	Safety Factor
T	°C [°F]	Temperature
$\widehat{T}$	°C [°F]	Estimated (on-pipe) Temperature
V	V	Voltage
$\widehat{V}$	V	Measured (Shunt Resistor) Voltage
$\widetilde{V}$	V	Secondary (induced) Voltage
$\dot{V}$	GPM	Volumetric flow rate
W	W	Cumulative Electrical Power Consumption
$\dot{W}$	W	Electrical Power Consumption

GREEK SYMBOLS	**UNITS**	**DESCRIPTION**
λ_1	$\frac{V}{\widetilde{V}}$	First conversion constant for VTs
λ_2	$\frac{V}{\widetilde{V}^2}$	Second Conversion constant for VTs

SUBSCRIPTS

AC	Alternating-current
AVG	Average
B	Burden (Resistance)
CNST	Constant
CP	Circulation Pump
D	(Voltage) Divider
EAT	Entering Air Temperature (relative to the HP)

EWT	Entering Water Temperature (relative to the HP)
F	Final
F-P	Fluid & Pipe (thermal resistance)
H1	Water Heater Element 1
H2	Water Heater Element 2
in	Input
INSL	Insulation
LAT	Leaving Air Temperature
LWT	Leaving Water Temperature
MAX	Maximum
OP	On-pipe
MIN	Minimum
P	Peak
ref	Reference
RMS	Root Mean Square
S	Shunt (Resistance)
SS	Steady-State
T	Thermistor
TOT	Total
0	Initial

CHAPTER I

Introduction

Ground Source Heat Pump (GSHP) systems are an energy efficient form of geothermal energy. At their most basic level, GSHP systems utilize the thermal mass in the shallow sub-surface of the ground as the heat source or heat sink for a heat pump. More specifically, the undisturbed ground temperatures at about 30 ft (9.1 m) below the surface are constant year round, and (depending on exact geographical location) typically range from 40°F to 70°F (5°C to 22°C) in most parts of the United States (U.S.) [Liu et al. (2019)]. The resulting small temperature difference between the ground temperature and the common indoor room temperature makes GSHP systems more efficient than conventional air source heat pump systems. The fundamental component used to characterize different types of GSHP systems, is the specific type of ground heat exchanger implemented (pictured in Figure 1.1). While the exact type of ground heat exchanger may vary (vertical loop, horizontal loop, etc.), the central design of using the ground as its main heat source and heat sink is what makes GSHP systems distinct from other heating and cooling systems.

Before discussing the development, fabrication, and validation of a GSHP energy monitor and test loop, it is important to examine the need and potential for studying the design and accuracy of residential GSHP monitoring equipment.

1.1 Current Geothermal Potential

The first known reference to a GSHP is in a Swiss patent issued in 1912 to Heinrich Zoelly [Ball et al. (1983)]. GSHP systems have been reported to have been installed

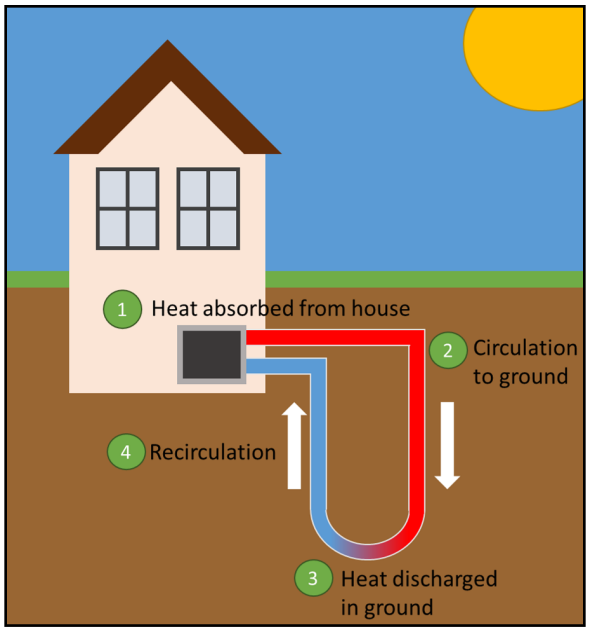

Figure 1.1: How a ground source heat pump works. (after `www.epa.gov`)

in the U.S. as early as World War II, and at the 2015 World Geothermal Congress, there were reported to be over 1.4 million units (12 kW size) in operation in the U.S. today [Boyd et al. (2015)].

According to the U.S. Department of Energy's Energy Information Administration (EIA), in 2018, residential and commercial buildings consumed approximately 40% of the total energy consumption in the U.S. [United States Energy Information Administration (2019a)]. In their most recent Residential Energy Consumption Survey (RECS), there were reported just over 80 million single-family homes that used approximately 7.5 quadrillion Btu of energy total (or approximately 2.2 trillion kWh total) [United States Energy Information Administration (2015)]. Of that, over 70% was reported to be used for heating and cooling applications. With such a large portion of the average U.S. household's energy going towards heating, ventilation, and air-conditioning (HVAC), the opportunity for advancements in renewable and more energy efficient technologies in the U.S. certainly remains today.

Furthermore, the residential sector has continued to show itself open to adopt such technologies, as the EIA's *Monthly Energy Reviews* historical data show a strictly

increasing trend in renewable energy consumption in the residential sector since 2006 [United States Energy Information Administration (2019b)]. Moreover, in the last update from the U.S. at the World Geothermal Congress in 2015, it was reported that GSHP units are found in all 50 states and are growing at about 8% per year [Boyd et al. (2015)].

The U.S. Department of Energy (DOE) considers four main types of renewable resources available in the U.S. today: solar, water, wind, and geothermal [United States Department of Energy's Office of Energy Efficiency & Renewable Energy]. GSHP systems fall under the "Geothermal" category, and when considering their implementation towards HVAC applications, they are in the sub-category "Non-Electric Sector." Just recently in 2019, the DOE's Geothermal Technologies Office just released their GeoVision report [United States Department of Energy (2019)] forecasting the potential for geothermal energy specifically within the U.S. This report was a multi-year research collaboration among national laboratories, industry, and academia to examine the potential for geothermal resources to play a key role in the nation's energy future, and lay out a specific plan and projection for getting there. Specifically they report that geothermal heat pump technologies have the potential to supply heating and cooling solutions for a capacity of up to 14 times greater than the current residential sector's installed capacity (16.8 gigawatts thermal). This potential represents about 23% of the total residential energy market share projected to exist by 2050. Certainly this indicates a potential area for readily applicable research and development (R&D).

Throughout the GeoVision report, key challenges are identified and discussed in order to define specific key objectives for growth in the GSHP market. The three key objectives identified specifically for growth in the U.S.' residential and commercial sectors are: better consumer awareness, improved financing options, and advances in technology that can lower the costs and improve efficiencies of heat pumps and

ground heat-exchanger loops. Specifically in *Key Action 1.5*, the report calls for an improvement in resource monitoring: "Improved monitoring would serve two primary purposes: 1) establishing the baseline status of the system and 2) creating a record of reservoir responses and performance over time that can be assessed to continually optimize the system." If advancements in GSHP technology are to occur, the GeoVision's *Task Force for Thermal Applications: Geothermal Heat Pumps* specifically calls for field performance data as well as ground thermal properties data [Liu et al. (2019)]. This report suggests that cost restrictions often limit the amount of monitoring data collected from GSHP systems, especially residential GSHP systems. Having access to quality field data would aid in the development and regulation of the suggested tax credits, rebates, and other incentive programs discussed in the report. Specifically in *Key Action 3.4* it is discussed how actual field performance of GSHP systems is important to enable third-party financing and other policies related to geothermal financial incentives.

From a global standpoint, geothermal energy has been steadily gaining attention as well. Lund and Boyd (2016) report that worldwide, a total of 82 countries have direct utilization of geothermal energy. Specifically their estimated total thermal energy capacity is 70,885 MWt and their estimated worldwide thermal energy use is approximately 164,635 GWh/year. Their data suggests that geothermal energy usage worldwide has been growing at a compounding rate of 6.9% annually. Of all direct geothermal applications worldwide, GSHPs have the largest energy use and installed capacity, accounting for about 70% of the installed capacity (or 50,258 MWt) and about 55% of the annual energy use (or 90,791 MWh/year).

Geothermal energy, most notably ground source heat pumps, undoubtedly have a bright and applicable future ahead in both the U.S. and abroad.

1.2 Literature Review

With such a ripe forecast for GSHPs worldwide, it is valuable to see what work has already been done to aid in the monitoring of the performance of GSHP systems. Additionally it is important to consider what suggestions have already been made regarding further R&D, within the GSHP community.

1.2.1 Current GSHP Monitoring

Monitoring the performance and energy consumption of building HVAC systems has been done extensively in research, with several topics and concerns in mind. However, whether to evaluate the accuracy of a simulation/modeling software used to design a building's HVAC system or to determine the energy "efficiency" of several "green-buildings" for qualifying tax rebate purposes, all research on the topic is unified on striving to help make HVAC systems more efficient and reliable. Research specifically dedicated towards monitoring the performance and energy consumption of GSHP systems has most recently been concerned about developing a methodology and terminology suitable for comparing the system at one site to another.

One common measurement used to compare GSHP systems to one another is comparing the site energy use intensity (EUI). EUIs are a measurement of building energy consumption over a unit of building floor area (often energy consumption per square foot or square meter). This is a common measurement used in rating how "green" a building is in theory, primarily because it only needs a minimum amount of data to compute it (only building utility bills and floor data). In fact, the U.S. DOE Buildings Performance Database contains over 740,000 buildings-worth of data, which allows for a variety of "big data" analyses to be performed [United States Department of Energy (2014)]. However, as seen in investigations using EUI, such as Scofield (2009) and Li et al. (2014), the relationship between the actual performance of GSHP systems and their EUIs may vary widely. For example, Li

et al. (2014) selected 51 "high-performance" office buildings in the U.S., Europe, China, and other parts of Asia, and found that their EUIs varied by a factor of 11. With limited amount of additional data on influencing factors, such as number of occupants and operation hours, no analysis was done to look at the impact of such factors across all the buildings (only two buildings had sufficient data for such analysis). Ultimately they concluded that no single factor alone determined the actual energy performance of these buildings. Additionally, they raised questions about the accuracy of "high-performance" certifications, and were unable to identify a set of "efficient" technologies that correlated directly to low EUIs in their study. As shown, EUI is not a sufficient stand alone metric for determining the efficiency of a building's GSHP system itself.

An alternative to using EUI is directly monitoring field performance of GSHP systems. This is often aimed at calculating the Coefficient of Performance (COP) for a system using Equation. (1.1).

$$COP = \frac{\text{heating/cooling output}}{\text{electrical power input}} = \frac{\dot{Q}}{\dot{W}} \tag{1.1}$$

This is inherently more difficult and expensive than calculating EUI, as it requires more sensors and data acquisition systems to calculate the calorimetric heat transfer achieved ($\dot{Q}$) by the system. It does however allow for better distinguishing between inefficiencies caused by the GSHP system and other factors such as occupant behavior or building envelope loads.

A need for clarification has arisen as heat pump manufacturer's often will list a 'COP' rating for their heat pump unit. This rating does not necessarily apply to the GSHP system the unit is installed in as a whole, nor to the system's transient operation. While the equation for COP above (Eq. 1.1) could generally apply to the whole system and transient operation, the heat pump manufacturer's rated 'COP' is just an equipment rating data point for a single operating condition at full capacity.

There is a need for distinction between a manufacturer's heat pump 'COP' performance metric and a separate COP performance metric that encompasses the GSHP system as a whole.

Furthermore, a significant topic of research and discussion among the GSHP community has been how to best measure and compare such performance metrics across systems with different sets of HVAC applications and system elements. An additional performance metric created to attempt to account for both system-wide and transient operation and loads across applications is the seasonal performance factor (SPF). The SPF is the average COP of a heat pump over a full heating or cooling season. By accounting for entire seasonal loads, the overall system performance can be better categorized and evaluated as a whole. However, measuring this does require measurement of entire system characteristics and not simply the submittal data of a heat pump unit.

This has led to a significant exploration of field performance boundary schemes for heat pumps. Recent discussion in the GSHP community has involved carefully defining SPF measurements, such that systems with varying loads and system elements can be better compared. Most notably, the SEasonal PErformance factor and MOnitoring (SEPEMO) boundary scheme [Nordman and Zottl (2011)] proposed the need for a performance metric that is more flexible to heat pump operating conditions. Nordman proposed the use of four different SPFs, each with unique system boundaries defined (depicted in Figure 1.2). Using the four SPFs allows for long-term performance of the heat pump unit to be calculated (capable of handling time-periods when operating at reduced capacities), as well as more clear and fair comparisons between systems in different field trails.

Specifically with regard to residential buildings, Gleeson and Lowe (2013) also tackled the issue of comparing different heat pump systems with differing components. Specifically they performed a meta-analysis of over 600 heat pump installations

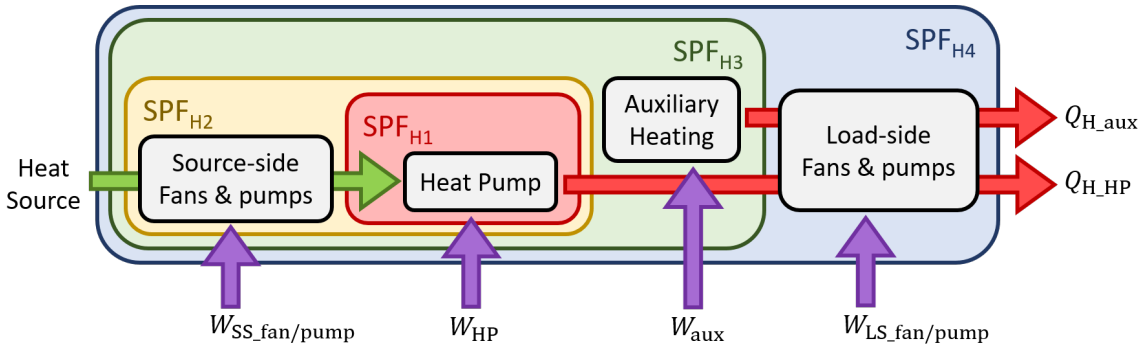

Figure 1.2: Diagram showing SEPEMO SPF boundary scheme for heating.

in Europe, reported in 8 field trials. The results of their paper specifically identify two boundary conditions, capable of calculating four different seasonal performance values. However, an interesting conclusion from their paper supposes that the inconsistencies they found across the performance data of the 8 trials examined could not be readily explained by the quality of the equipment or the building load profiles. Rather, the wide range, they supposed must be a result of the heat pump systems' sensitivity to their individual designs and installation practice. Gleeson and Lowe suggest that further development and re-analysis of system boundaries is necessary to better understand the found inconsistencies. Specifically, they point out that their study and analysis was limited by a lack of detailed monitoring data, namely specific monitoring intervals, completeness of data sets and treatment of errors.

Spitler and Gehlin (2019) have thoroughly reviewed this literature on the boundary schema applicable to both residential and commercial buildings. Most notably, they identify inconsistencies in the current SPF boundary schemes that make it difficult to simply compare long-term monitored GSHP systems (specifically 55 multifamily residential and commercial GSHP systems around the world with measurement data spanning longer than 1 year). Furthermore, they emphasize that only three of the 55 studies report any uncertainty analysis (and only one of those three provides any methodology in detail). Without data sources providing measurement/sensor accuracies, meaningful interpretations of the resulting SPFs is limited. Spitler and

Gehlin go on to accentuate how additional performance measurements, other than seasonal or annual performance factors, have been useful in identifying causes for poor performance in GSHP systems. Namely they demonstrate how daily performance factors and binned average values (aggregated by variables such as entering fluid temperature, and daily heating & cooling loads) are illuminating performance metrics.

Undoubtedly there has been progress in the GSHP community to identify and begin exploring meaningful performance metrics. However, regardless of what performance metrics are eventually decided on, there continues to be a need for more detailed data acquisition in residential GSHP applications.

1.2.2 Obstacles for Monitoring

While academic literature has begun addressing the issue of how to compare field data collection, there is a common, often indirect, call for better quality, longer-term GSHP field data. Specifically there are still relatively little data available to properly analyze the performance of GSHP systems in residential applications. While research-grade instrumentation is available, it is too expensive to deploy widely in residential systems. As a result, there continues to be a need for low-cost, properly installed sensor systems in residential GSHP systems. In articles or papers involving in-situ GSHP measurements, the authors almost always mention the potential limitations of their data, either as a result of the relatively short time-span of data recorded, unknown measurement uncertainties, or just plain missing data for a particular component in the system (completely or for a given time frame) [Gleeson and Lowe (2013)]. The following paragraphs present just a few specific examples of given reasons for why sufficient GSHP field data doesn't exist yet.

In the aforementioned *GeoVision* Report released by the DOE, cost is specifically given throughout the report as a common obstacle for sufficient monitoring data. Specifically in the rationale given for *Sub-Action 1.5.1 (Improve monitoring,*

modeling, and forecasting of reservoir performance), it is stated, "Cost restrictions often limit the amount of monitoring data collected at geothermal reservoirs, steam fields, power stations, and other infrastructure." Additionally, the specific *Task Force for Thermal Applications - Geothermal Heat Pumps*, specifically state multiple times throughout their report that "in situ measurements of these data are often too expensive for residential (GSHP) projects." They state in their conclusion that "substantial investment in R&D is needed to significantly reduce costs and improve the performance of (GSHPs)." They go on to list specific technological developments required: "the development of lower cost and performance neutral ground-loop heat exchangers, more cost effective equipment and system configurations, and automated processes for installation and performance evaluation." The DOE's projection ahead of GSHP use in the future, recognizes and includes the need for overcoming the cost barrier to monitor in residential applications.

While the DOE's overall monitoring of geothermal energy use in residential sector has paused in their annual RECS since 2011 [United States Energy Information Administration (2015)], there has been an increase home energy monitoring in general. This rise in home energy monitoring and "smart homes" primarily has its root in the development and adoption of the idea of a "smart grid" and "home energy management systems" [Zhou et al. (2016)]. Specifically it is described as the paradigm where communication occurs between smart home devices and power utilities, in order to provide an opportunity for economic incentives to shift residential electricity usage during peak-load periods in response to the changes in electricity prices. This integrated communication and optimization strategy gives incentives to "smart home" owners to monitor and adjust their HVAC systems, which has led to the development of third-party home energy monitors, such as *Open Energy Monitor*, *Sense Energy Monitor*, or *Neurio Home Energy Monitor*. However, as discussed previously, since most of these third party energy monitoring systems do not provide thermal energy

usage, but rather just electrical energy usage, the usefulness of the data to GSHP applications is limited similarly to how the calculation of EUI is limited.

Most installed GSHP monitoring systems in use in residential systems today (outside of those installed for research projects), are primarily provided indirectly through the heat pump manufacturer themselves. Typically the measurements made by the controls within the heat pump are similar to the measurements necessary to calculate the calorimetric heat transfer. These heat pump manufacturers are allowing control and monitoring capabilites for builders and homeowners, such as WaterFurnace's Symphony platform, by uploading the data to an online cloud for monitoring and analysis. Some heat pumps now provide data in 10 second increments and have been proven to help contractors diagnose and fix problems more efficiently [Horwitz-Bennet (2014)].

While relatively little residential GSHP monitoring has occurred via heat pump manufacturers, new third party developers (e.g., Ground Energy Support), and GSHP researchers, there is still a present need for thorough adoption and standardization of such heat pump monitoring systems. However, the acquisition of data does not necessarily imply the immediate quality and usefulness of said data.

1.2.3 Need for Quality over Quantity

While the need for more residential field data is apparent, there is also an important plea for *quality* data. The following paragraphs present just a few specific examples of (direct or indirect) calls from the aforementioned literature, for better quality, longer-term GSHP data and how that could be regulated/standardized.

The *GeoVision* report speaks specifically to the necessity of quality data for the advancement of geothermal technologies. In *Sub-Action 3.1.2 (Improve data and education to financial institutions for geothermal power, direct-use applications, and geothermal heat pumps)*, there is a clear plea for the standardization of data collec-

tion for the purposes of providing better quality data: "The need for large volumes of data can lead to miscommunication in project risk, which can ultimately drive higher financing rates. Standard data reporting and information can improve communication and education, thus helping to improve investor confidence and reduce the cost of financing." They later make this call for better quality data again as a bridge to help overcome the barrier of poor consumer and investor education on geothermal technologies: "Educational programs and case studies of installed (GSHPs) could provide investors with detailed and potentially quantified comparisons between (GSHPs) and conventional heating and cooling."

In the SEPEMO report, Nordman emphasizes the importance of the need for quality data as well. Specifically in the context of the value of having clearly defined system boundaries, he also says: "The quality of the measurements is directly influenced by the accuracy of the sensors and the sampling intervals for storing measured data." In the conclusion of that report, he states "In order to guarantee the quality of the recorded data to make a significant system evaluation it is highly important to set minimum requirements on the measurement equipment and in a second step, a proper equipment installation in the heat pump system is obligatory." In Zottl et al. (2011), the supplemental resource titled *Field Measurement Guideline*, referred to in the SEPEMO report, quality assurance recommendations are given [Zottl et al. (2011)]. Specifically it provides recommendations and justifications for accuracy and resolution of sensors, frequency of measurements, calibration verification, as well as how to calculate error margins based on the European heat meter and electrical standards (EN 1434-1 and EN62053-21).

As mentioned before, Spitler and Gehlin (2019) also emphasize the need for specific accuracy and uncertainty estimates to be stated when reporting SPF. Otherwise understanding the significance of the resulting SPF calculations is difficult to ascertain. They do provide a necessary framework for how to perform such uncertainty

analysis on a mixed-use GSHP system in Sweden. Additionally, they suggest that further study on the drift of temperature sensor pairs would be ideal, since the majority of the overall uncertainty is a result of the individual temperature errors. Nordman also proposes a need for sensor recalibration after use (before re-installation) in the *Field Measurement Guideline* [Zottl et al. (2011)].

Another repeated, notable comment made in several analyses of residential and commercial GSHP is the uncertainty associated specifically with temperature difference measurements. When calculating the amount of heating or cooling provided by the GSHP system, the difference between the inlet and outlet temperatures of the fluid plays a significant effect in the overall uncertainty, especially when the difference is very small (under 1°C). When calculating the uncertainty of the overall SPF or calorimetric heat transfer measurement, Spitler and Gehlin (2019), Nordman and Zottl (2011), and Tiljander et al. (2014) all comment on the significance of the small temperature difference measurements. This is a significant contributor to overall uncertainty and is argued to be precisely why uncertainty analysis is so critical to providing meaning to the final SPF measurement of the system.

In Gleeson and Lowe (2013), as mentioned previously, one of their primary issues came not with the issue of system boundaries or quality of the sensors themselves, but rather with other details on monitoring specifications. Specifically in their conclusion, they state (concerning the need for future in-depth individual system analysis) that the interpretation of measurements for heat pumps will depend on factors such as "monitoring intervals, completeness of datasets and treatment of errors. Unfortunately such detailed information on monitoring specifications is not available for several of the field trials referred to in this paper." This suggestion for standardization, or at least documentation, of the data acquisition system's measurement frequency and validation procedure is not uncommon. The SEPEMO report's *Field Measurement Guideline* provides a suggestion for the frequency of measurements, and

specifically recommends that the expected time frame for any system changes should be used to validate their suggestion.

Lastly, while home energy monitoring is increasing some with the gradual rise of "smart home" technologies allowing for monitoring energy use, and the previously mentioned heat pump manufacturers, there is still a limitation in the amount of public, quality data. Although, the data are being collected and saved for online viewing and may be used to help control the heat pump, the accuracy of the sensors and the measurements being made are often not confirmed by the GSHP installer, let alone even provided.

1.3 Contribution & Scope of Study

With such a gap calling for a major increase in quality, longer-term residential GSHP field data, this thesis aims to provide an initial investigation on the feasibility of producing a low-cost, sufficiently accurate GSHP energy monitoring sensor system for residential applications. With an understanding of the importance of recording not just electrical energy use, but also calculating the thermal energy achieved, this thesis will attempt to develop a device that gives data sufficient for calculating a GSHP system's SPFs, not just the building's EUI. Furthermore, with a clear lack of sensor uncertainty verification and error analysis in literature involving GSHP field measurements, this thesis will also provide an in depth verification and analysis of each sensor's calibration and measurement uncertainty.

In addition to providing the detailed theory, design, and fabrication of a residential GSHP energy meter, this thesis will also describe the design and fabrication of a validation test stand, capable of investigating the accuracy of a heat meter's measurements, with typical GSHP scenarios. While initial development of a measurement system took place first chronologically, this thesis will cover the developed test loop first. After both are designed and developed, a series of steady-state and

transient analyses will be performed to compare the accuracy and performance of the clamp-on versus in-line heat meters. The analysis of initial field data acquired using an earlier prototype of the clamp-on energy meter on a local residential GSHP will also be shown and discussed. And lastly, lessons learned and suggestions for future development and discussions on residential GSHP energy monitors will be provided.

CHAPTER II

Test Loop Development

In order to test and validate the accuracy of a GSHP energy meter, access to a completely controlled thermal system is necessary. More specifically, in order to perform a heat balance calculation and the accuracy of both the thermal and electrical energy measurements to be quantified, the exact amount of energy input into the system ($\dot{W}$) and the exact amount of energy dissipated from the system ($\dot{Q}$) must be fully controllable and measurable. While full, unrestricted, convenient access to a fully instrumented residential GSHP system, along with control over its heating/cooling load would be ideal, this was not feasible in the scope or timeline of this thesis. Instead, we decided to develop a small test loop, that has the ability to inject and remove heat pulses at a similar rate and thermodynamic response as a GSHP system would see in a residential application. Moreover, this test loop is designed to be compact and modular, such that future iterations and additions could be easily made, and components could be replaced without having to scrap the entire system. Lastly, a key design objective of this test loop was to allow for the measurement of both in-line and clamp-on energy meters, such that the accuracy of either measurement method could be calculated and compared. The following chapter describes the design and fabrication of such a test loop at Oklahoma State University as a key deliverable from this thesis.

2.1 Thermal System Design

In order to create a test loop of meaningful comparison to a residential GSHP, significant thought and several key engineering calculations were performed before purchasing parts and construction to achieve the desired similarity. This section describes the design and forethought that went into the energy meter validation test loop.

2.1.1 Overview

The test loop developed has four main processes: 1) injecting a heat pulse into water via electric resistance heaters, 2) circulating the heated water to a water-to-air heat exchanger, 3) exchanging the heat from the water to the cooler room air, and then 4) returning the cooled water through the loop to absorb more heat. A basic schematic of the test loop can be seen in Figure 2.1, including the location of temperature transducer (TT) and flow transducer (FT).

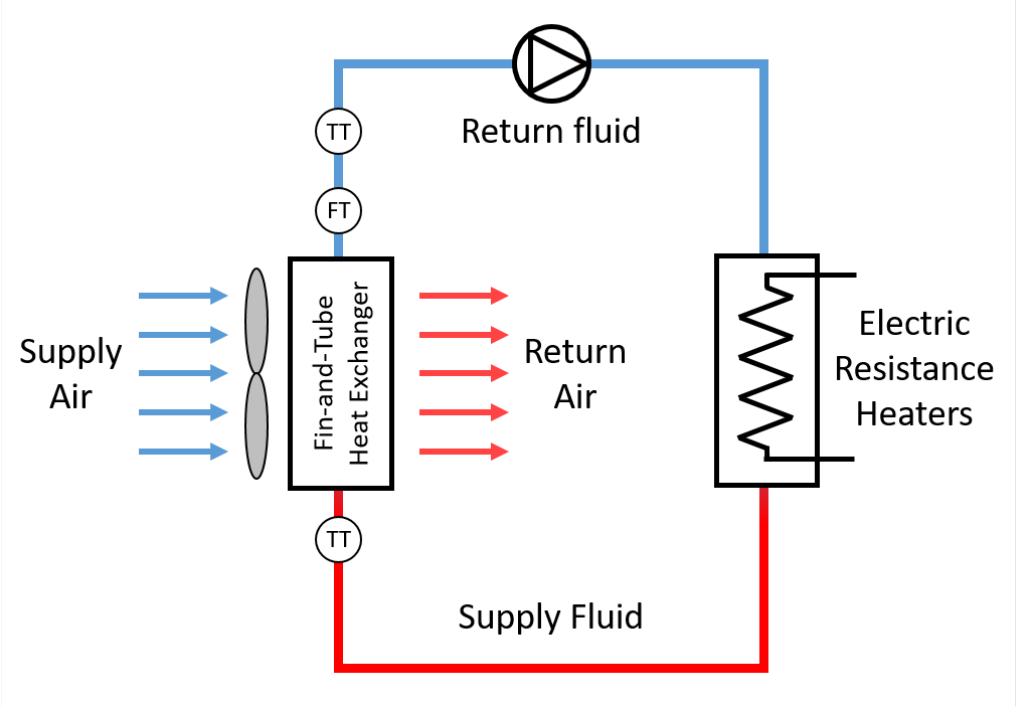

Figure 2.1: Basic schematic of instrumented test loop.

Three main pieces of equipment were initially sized to best allow for this test

loop to achieve similar thermodynamic characteristics to that of a residential GSHP system. Those three key components were the electric-resistance water heater elements, the fin-and-tube heat exchanger, and the circulation pump. The following sub-sections describe the sizing and selection of the main components in the test loop, with the aim of achieving a target flow rate, temperature difference, and heat pulse shape, similar to that of a small residential GSHP system.

2.1.2 Heat Injection

For the heat pulse injection part of the test loop, it was desired to be able to inject a heat pulse of a similar magnitude as those seen in small residential GSHP systems. Based on several residential GSHP studies examined, it was estimated that a sufficiently similar heating capacity of a small residential GSHP systems was in the range of 5-14 kW [Nordman (2016) and Tiljander et al. (2014)]. With a target magnitude of 1-10 kW selected, the exact method of injecting the heat is discussed next.

Sticking to the mobile, modular design objective, it was decided to use multiple electric-resistance water heater elements, rated for 120 V. That way the test loop could still be operated whenever it only had access to standard 120 V outlets (as is most common in the US). This method of injecting heat using a resistive-heating element is not uncommon in the GHSP community. Most thermal response test trailers involve directly injecting a heat pulse with similar resistive-heating elements in order to collect data for characterizing the thermal properties of borehole heat exchangers [Austin III (1998) and Spitler and Gehlin (2015)]. For this test loop, two 120 V water heater elements, capable of producing nominally 1500 W each, were purchased. These would allow the loop to provide a total capacity of nominally 3 kW (within the target 1-10 kW range for small residential GSHP systems). It was anticipated that future developments on the test loop could be made to control the power to each element with a high power potentiometer or pulse width modulation

(PWM). However, for the scope of this thesis, a variac transformer that could be put in series with the plugs for the water heater elements was made available whenever that need arose.

Furthermore, with safety in mind, a grounded housing was put together (Figure 2.2), so as to prevent any unintentional danger or harm caused from touching the wires of the 1500 W circuit when it is live. An "exploded" view of the water heater element housing can be seen in Figure 2.3 and a detailed parts list can be found in Appendix D.

Figure 2.2: Top view of assembled grounded housing.

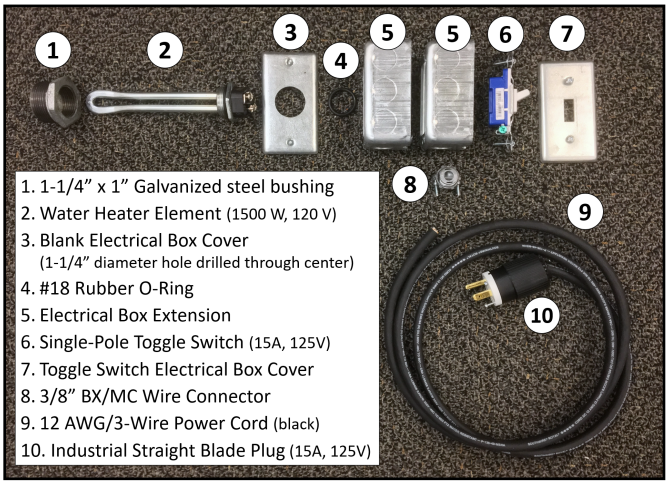

Figure 2.3: Exploded view of water heater element before assembling.

Most notably, each housing around the water heater elements is made up of two metal electrical box extensions, 2 rubber o-rings, 1 standard single-pole toggle switch, and 2 metal face plates (one with a 1-1/4 inch hole drilled through the center of it, and the other with a hole for the toggle switch). Coming out of the electrical box is 4 - 6 feet of 12 AWG/3-wire power cord, fitted on the end with an industrial straight-blade plug, rated for 15 Amps. This method of powering the water heater elements allows for them to be easily and safely powered by any 3-pronged, 120 V outlet (assuming the breaker it is connected to allows up to 15 Amps current).

The pipe size selected for this section of the test loop was based on the standard water heater element thread size in the US (1 inch NPT). Specifically a 1-1/4 inch

galvanized steel tee and a 1 inch to 1-1/4 inch bushing were selected to allow for the water-heater elements to be screwed into place, and still have appropriate clearance for the water to flow past the end "u-bend" of the element. Figure 2.4 shows a diagram of the water heater element from the perspective looking at the cross-section of the pipe.

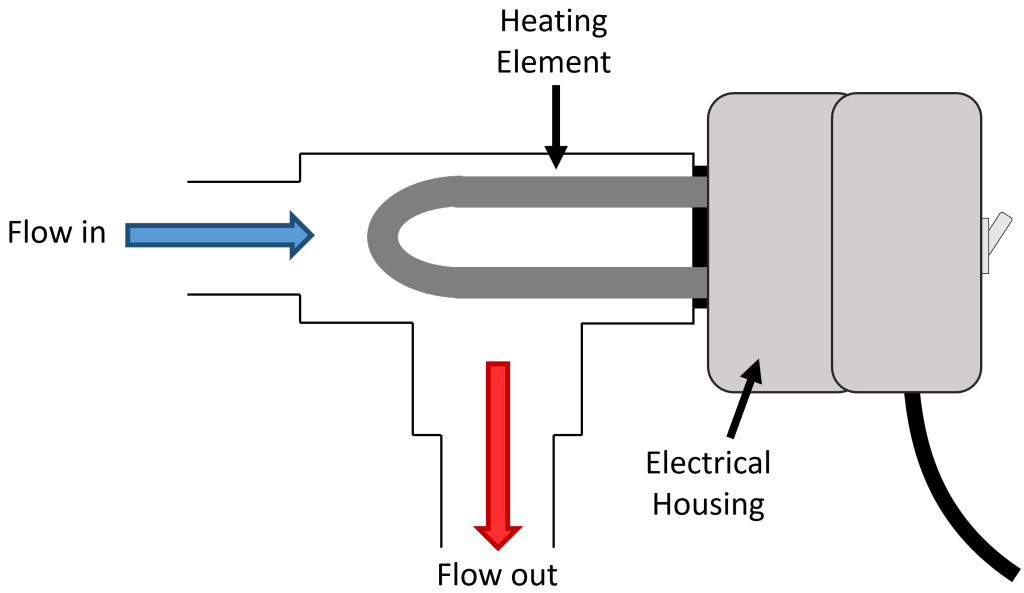

Figure 2.4: Cross-sectional diagram of water heater element in test loop.

It would later become clear that the pipe clamps on the frame need to be placed as close to the galvanized steel tees as possible, to support the weight of the entire water heater element assembly. Lastly, it is important to note that until power to the water heater elements is automated in the future, it was and is mandatory practice to unplug them from the wall after use, to ensure they do not accidentally get switched on, leading the water in the test loop to boil and likely pipe failure to occur.

2.1.3 Heat Exchanger & Fan

The primary design objective for the heat exchanger was to size it appropriately to achieve the desired temperature difference when dissipating the heat out of the loop. Due to the relatively small heating capacity of the lest loop (3 kW), a relatively small

and cheap water-to-air heat exchanger was selected. Specifically a copper, 12 inch by 12 inch, fin-and-tube heat exchanger from Outdoor Furnace Supply was purchased (Figure 2.5). Other than a nominal cooling capacity of approximately 16 kW, at a listed 10 GPM, 800 CFM, and 180 °F entering water temperature (EWT), very little actual performance data was given on the manufacturer's data sheet. It was determined that the capacity of the heat exchanger would be validated after initial assembling of the test loop. (See Section 2.1.7 for initial validation results).

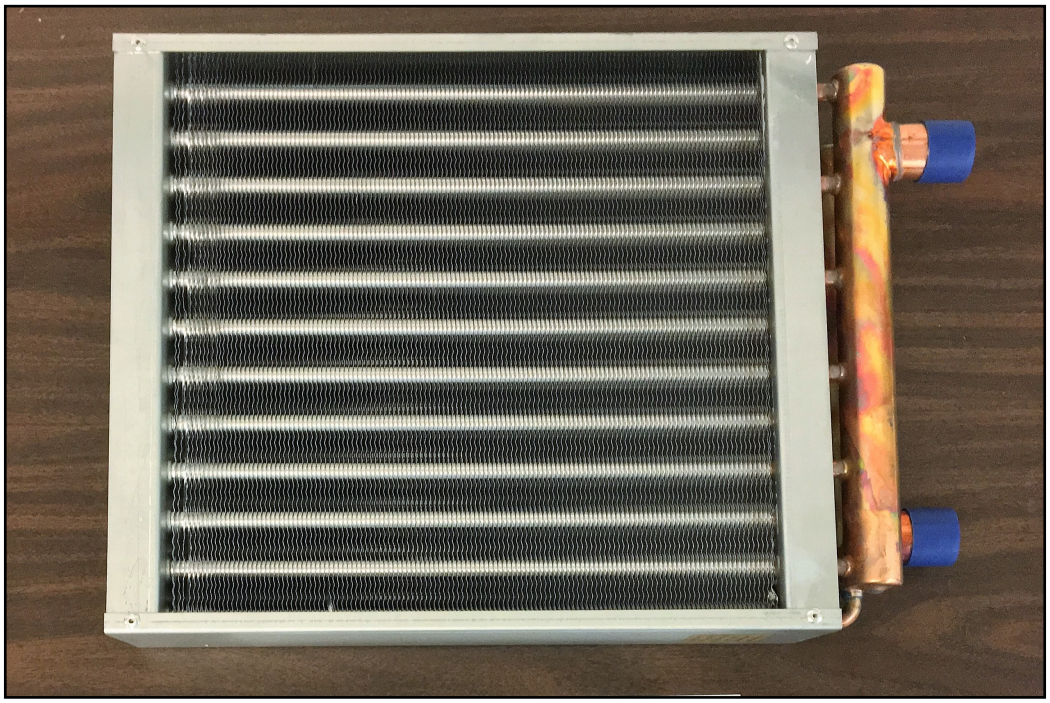

Figure 2.5: Picture of 12x12 fin-and-tube heat exchanger.

In addition to the heat exchanger, a fan was also needed that matched the rated air flow rate for the heat exchanger (at least 800 CFM). For initial capacity testing, a standard 3-speed box fan (1800 CFM) was used and later a high-velocity, 3-speed Lasko fan (2500+ CFM) was purchased and added to the test loop. The capacity and sizing of the heat exchanger and fan were later validated with initial capacity tests, since little performance data was provided.

2.1.4 Circulation Pump

Designing the test loop to flow at a rate of similar magnitude to actual systems found in the field allows for a more meaningful calibration/validation of the energy meters tested. Moreover, achieving a particular flow rate can also allow for the ability to achieve a similar temperature difference to actual systems. Thus, the sizing of the circulating pump began by gathering reports for several residential GSHP systems to determine the ideal flow range, comparable to a small residential GSHP system. Submittal data for several heat pump manufacturers were also used to verify the design flow rates similarity to actual GSHPs. The resulting fluid flow rate target range found was 0.85 GPM to 10 GPM [Uhlmann and Bertsch (2012) and Carmo et al. (2015)]. While GSHPs are designed for larger systems with flow rates as high as 18 GPM (for a 6 ton unit) [ClimateMaster (2009)], a slower (but still comparable) flow rate is preferred for the test loop in order to achieve a large enough temperature difference across the heat exchanger.

Next, the target temperature difference was determined. Again the design temperature difference across the test loop would ideally mimic the temperature difference found in a residential GSHP systems' fluid loops, allowing for more comparable measurements during calibration and validation of the energy meters. From the initial review of data available, a wide variety of steady-state temperature differences across residential GSHP systems were found. The finalized target steady-state temperature difference decided on for the test loop was set to be 0 °C to 10 °C. While a wide variety of steady-state temperature differences across residential GSHP systems exist, the majority examined fell within that range [Uhlmann and Bertsch (2012) and Szreder (2014)].

Subsequently, an initial calculation of the required flow rate was performed based on the maximum target temperature difference (10 °C) and estimated heat injection (3,000 W or 10,236 BTU/hr). Specifically, Equation (2.1) was used as the "back of

the envelope" calculation to estimate the target flow rate (in GPM) of water in the test loop [ClimateMaster (2009), p.190]. The resulting target flow rate (rounded to the nearest half gallon per minute) was 2.0 GPM.

$$\text{GPM} = \frac{\text{BTU/hr}}{500 \cdot \Delta T} \tag{2.1}$$

Lastly, an initial model of the anticipated system's pressure loss was developed, in order to determine which specific circulation pump to select. An estimation of the pressure drop for the heat exchanger, fittings, and straight pipe lengths, was performed using the method described in the ASHRAE *Handbook of Fundamentals Chapter 22—Pipe Sizing* [ASHRAE (2009)]. A picture of the loop's initially proposed piping and instrumentation diagram (P&ID) can be seen in Figure 2.6.

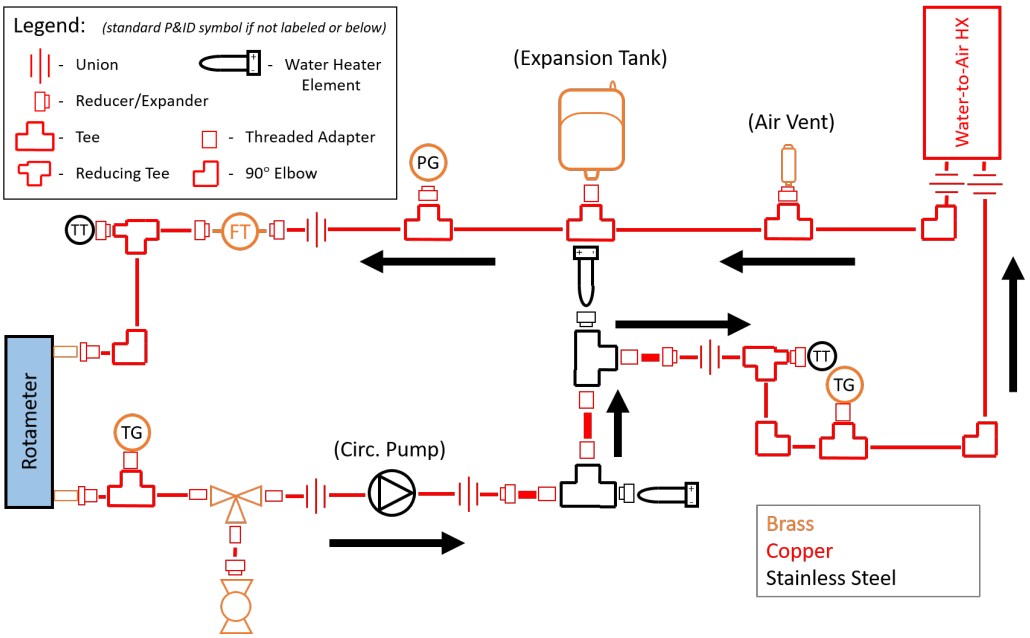

Figure 2.6: Initial P&ID of test loop used for estimating pressure drop along loop.

As a starting point, 1 inch copper pipe was used as the default nominal pipe size throughout the loop, since the selected heat exchanger already had 1 inch cooper pipe connections. Additionally, 1 inch copper unions were added into the calculation (for placement in between each major section of the loop to allow for easy replacement in

the future). The resulting calculations confirmed that 1 inch copper pipe would be sufficient.

Specifically, Equation 2.2 was used to estimate the pressure drop across the fittings, given their appropriate K-factor. The total pressure loss along the straight pipe in the loop was estimated using the Darcy-Weisbach equation (Eq. 2.3).

$$\Delta P = K\frac{\rho \bar{V}^2}{2} \cdot (\text{count}) \tag{2.2}$$

$$\Delta P = f\left(\frac{L}{D}\right)\left(\frac{\rho}{g_c}\right)\left(\frac{\bar{V}^2}{2}\right) \tag{2.3}$$

Table 2.1 shows each fitting's count, K-factor, and equivalent pressure drop (at 2.0 GPM) used in the initial calculation. The pressure drop across the heat exchanger was estimated based of the single pressure drop listed on the data sheet. The modeled water temperature was 120°F (temperature typical of residential water heaters).

Table 2.1: Initial list of test loop fittings & pressure drop (for 2.0 GPM and 120°F)

Component	Quantity	K-Factor	Pressure Drop (Pa)
90° 1 in. Copper Elbow	4	0.43	54
1 in. Copper Tee (straight flow)	6	0.26	49
1 in. Copper Tee (branch flow)	2	1.0	63
1-1/4 in. Galv. Steel Tee - Sch 40 (branch flow)	2	1.7	29
1 in. Copper Union	6	0.08	15
-	-	Sub-Total	210
Straight Pipe	10.5 ft	-	119
Heat Exchanger	1	-	9,606

As expected, due to the relatively small size of the test loop, the majority of the pressure drop across the loop occurs through the heat exchanger. The total pressure drop anticipated in the system was estimated to be roughly 9.95 kPa (3.4 ft of head). To develop a system curve, Equation 2.4 was utilized, emphasizing the square relationship fluid flow has to head loss. Note that because the system is a closed-loop system and the circulation pump will be installed horizontally, the head

loss due to elevation will be 0. Using the design flow rate determined earlier (2.0 GPM) the coefficient, C, was calculated to be approximately 0.840.

$$h_{L\_total} = h_{L\_friction} + h_{L\_elevation}$$
$$h_{L\_total} = (C \times GPM^2) + (0) \tag{2.4}$$

With a system curve now defined, pump curves for several small HVAC circulation pumps were evaluated to see which would result in the closest realized flow rate of 2.0 GPM. The selected pump for the system, was the *Taco 003B* circulating pump. It was purchased along with the appropriate reducer and expander to fit it into the test loop. Figure 2.7 shows the resulting pump curve and system curve used to calculate the anticipated operating flow rate in the system (assuming negligible pressure drop across the rotameter) [Taco (2018)]. While the *Taco 003B* is a single-speed pump, varying flows would later be attained through the use of a screw valve in the rotameter.

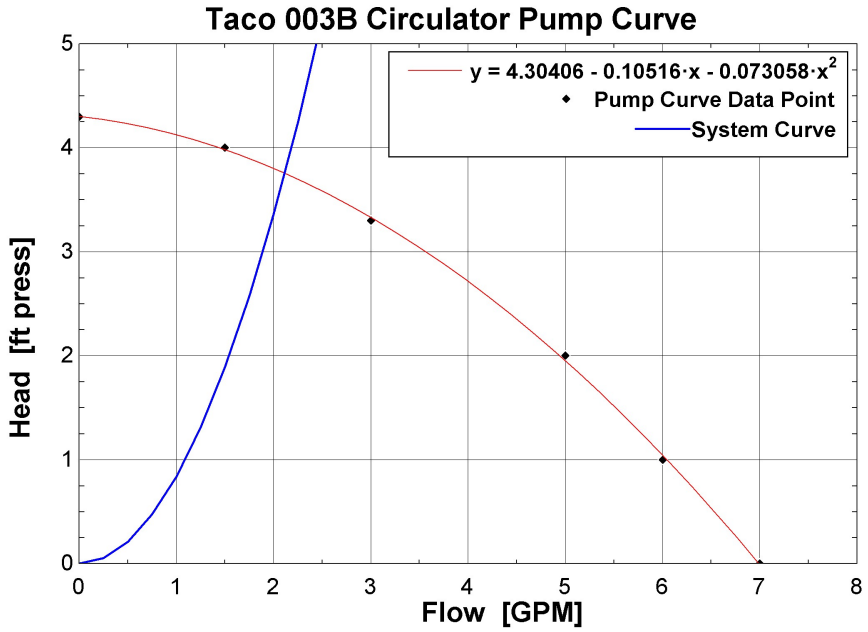

Figure 2.7: Estimated system curve and Taco 003B pump curve. [Taco (2018)]

2.1.5 Additional Components

The finalized piping and instrumentation diagram can be seen in Figure 2.8. This was used to purchase all of the final components and necessary fittings, now that the connection pipe sizes were known for all the key components.

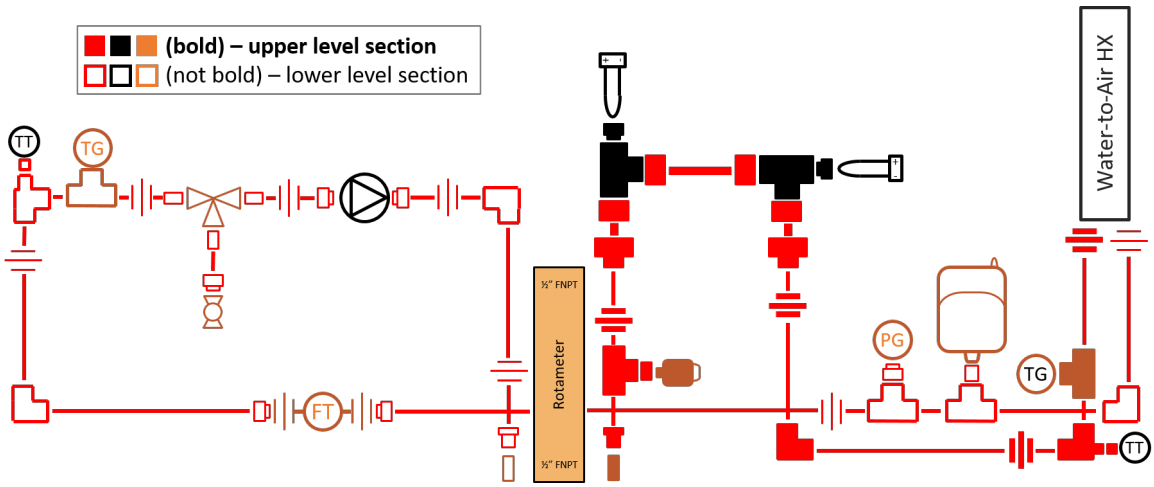

Figure 2.8: Final piping and instrumentation diagram for the validation test loop.

The test loop was designed to have a set of analog temperature gauges and a rotameter, so that an initial capacity test could be performed prior to any energy meter's monitor being set up. The analog temperature gauges (Figure 2.9) included thermowells that are screwed into 1/2-inch threaded tees. These were strategically placed before and after the branched copper tees that would later be used for the in-line temperature measurements of the in-line energy meter.

Figure 2.9: Winters analog thermometer with thermowell.

The rotatmeter selected was a *Dwyer* flow meter (Figure 2.10) rated for 0.8-7 GPM. The screw valve at its inlet (bottom), allows it to change the pressure drop across itself and effectively change the operating flow rate of the system.

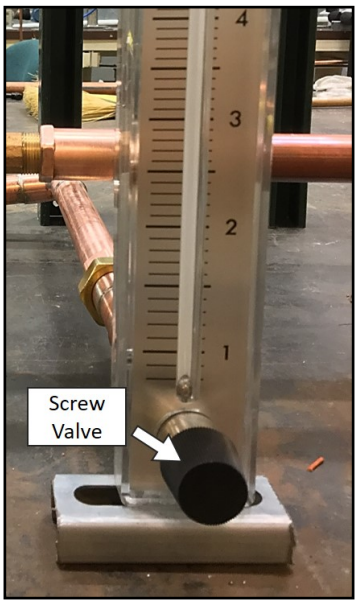

Figure 2.10: Dwyer RMC-144-SSV variable area flow meter.

Three other key components in the test loop are the three-way valve (Figure 2.11), leading to a ball valve with garden hose threads (Figure 2.12), and an air-vent (Figure 2.13). The three-way valve was placed on the lowest level of the loop, and the air-vent was placed at the highest level of the loop to allow for effective purging of the system when it was being filled.

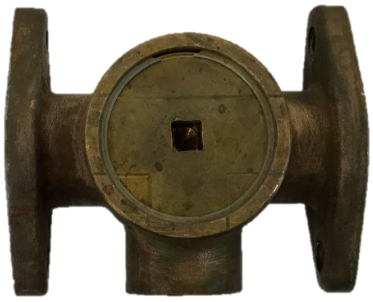

Figure 2.11: Three way valve.

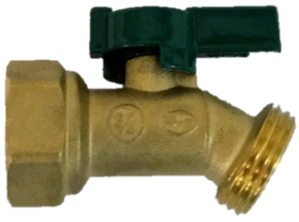

Figure 2.12: Ball valve converting NPT to GHT.

Figure 2.13: "Watts" air vent.

For operational and safety reasons, an expansion tank and pressure gauge were placed in the test loop. The two gallon expansion tank allows for the system to remain at a relatively constant operating pressure, and creates a space for the fluid in the loop to expand and contract as it changes temperature. The *Utilitech* expansion tank purchased has a Schrader valve for pressurizing and depressurizing its diaphragm. The pressure gauge is rated up to 200 psi and is plugged into a 1/4-inch tee. The other branch of the tee is plugged and should only be unplugged for pressure testing the system after soldering. It is important to note that future safety features should be implemented, including adding a thermostat switch that can break open the circuit going to the water-heater elements, whenever temperatures approaching boiling are detected. While the expansion tank would buy a little time if the water began to boil, it would not provide relief for long. Thus a quick release, high-pressure safety valve would be a valuable safety addition to this safety section of the test loop. For the purposes of this thesis, the operators (and those working in the same room) were informed of what to do in case of emergency and how to de-energize the heat-injection circuit if need be.

Additionally, a purposely straight section of pipe was placed in the middle level of the test loop. This was to provide a section of pipe, right after the in-line flow meter, that could be used to measure flow with an ultrasonic flow meter. This section of pipe was left straight for about 25 pipe diameters (roughly 25 inches), which should suffice to meet the straight-pipe requirements for most ultrasonic sensors.

In order to mount and secure the copper pipes to a rigid structure, a light-weight aluminum frame from *80/20 Inc.* was designed and purchased. Figures 2.14 and 2.15 show the anticipated test loop shape that was used to estimate the amount of aluminum needed. In addition to purchasing the necessary 90° elbow brackets and "T-nuts", 4 handles and 6 pivoting feet were purchased to allow for easier transportation and settling of the frame, wherever it should be placed in the future.

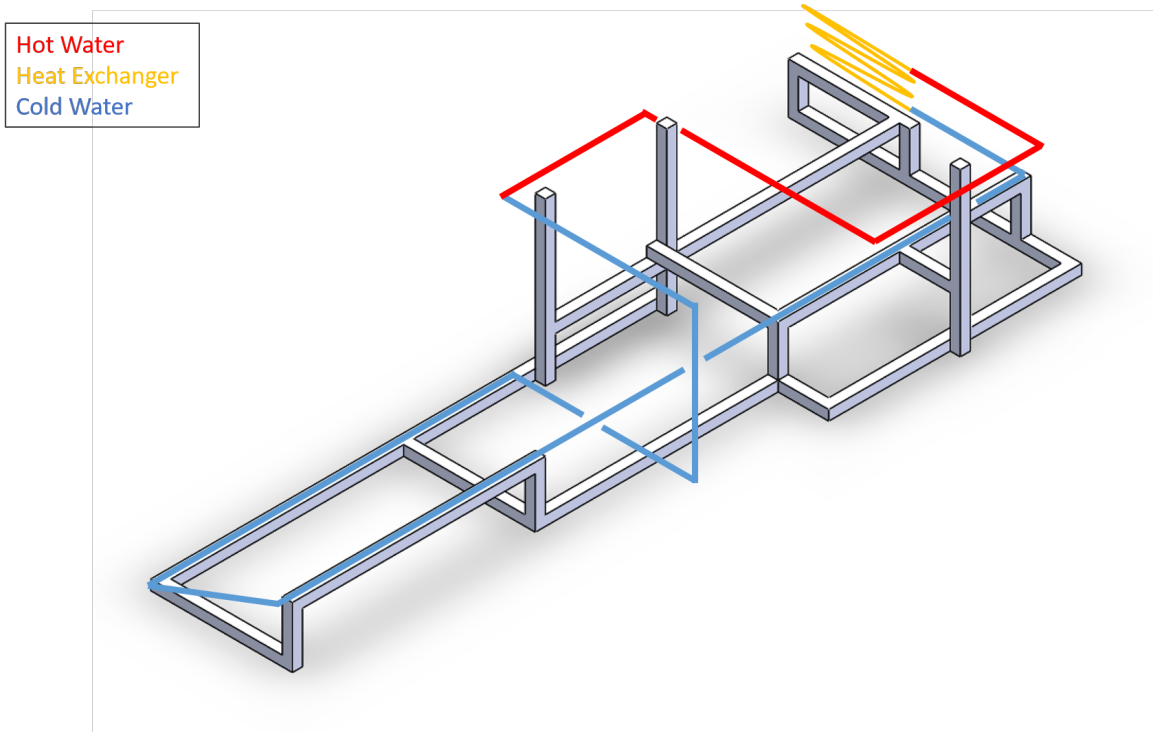

Figure 2.14: Initial test loop frame design with pipe colored by water temeprature.

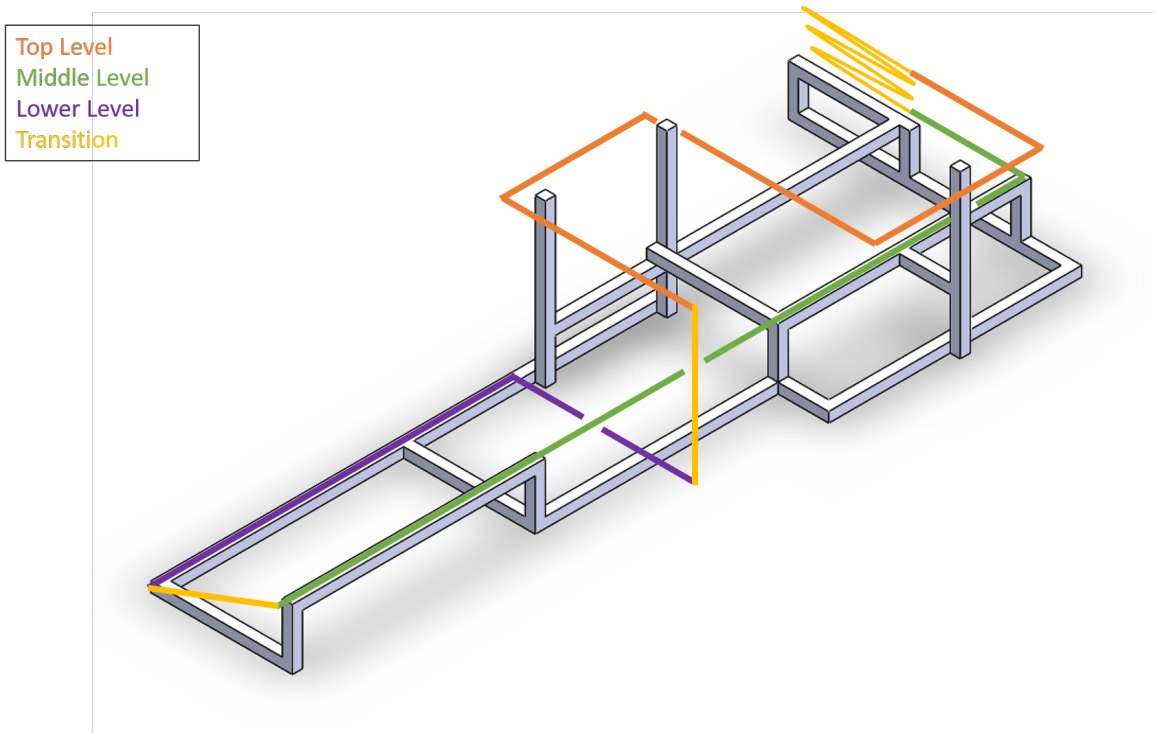

Figure 2.15: Initial test loop frame design with pipe colored by pipe height/level.

Lastly, the final component of the test loop that needed to be purchased was insulation. As alluded to previously, in order to properly perform a heat balance with an energy meter, all of the heat transferred in and out of the system must be controlled and measurable. In order to minimize the amount of heat lost through the section of the pipe between the two temperature ports, 1 inch foam pipe insulation (3/8-inch thickness) was purchased. It became apparent later, while running initial experimental scenarios, that approximately 15% of the heat injected was still being lost through the pipes and initial insulation. Therefore, a roll of R-13 insulation was purchased and was wrapped around the "leaky" parts of the system to thoroughly reduce any potential heat loss. The methodology of locating and applying the insulation will be discussed later in this chapter (see Section 2.1.8).

2.1.6 Assembly

The fabrication of the test loop took approximately 2 months to complete, as a result of the parts arriving at different times. All of the fittings and components were laid out initially, to measure the approximate length of each straight 1-inch copper pipe section. Figure 2.16 shows the initial parts laid out.

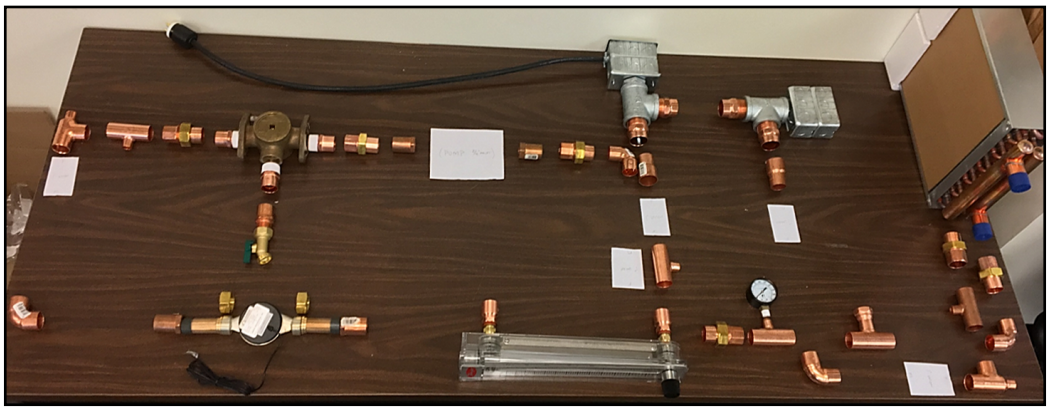

Figure 2.16: Parts laid out on table to measure lengths of straight pipe between fittings.

Next each section of straight pipe was cut and the ends deburred and cleaned.

Since the test loop was not going to be highly pressurized during normal operation, brazing the pipes together was substituted for soldering them together (Figure 2.17). Soldering took the majority of the assembling time, since there were 17 independent pipe sections that needed to be soldered together.

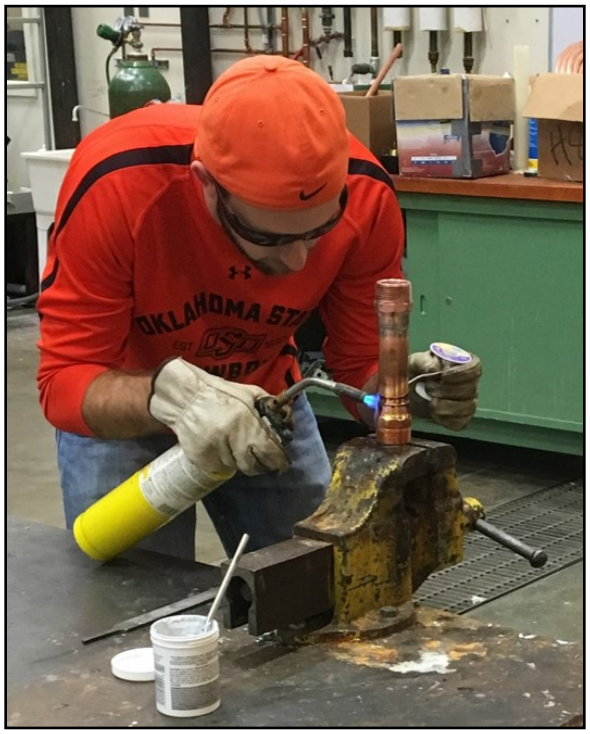

Figure 2.17: Soldering together threaded adapters to the end of a short pipe section.

After the majority of the piping sections were soldered together, they were laid out again and elevated to their approximate heights and orientations with the help of spare uni-strut (Figure 2.18). The exact lengths of the final remaining pipe sections were measured, cut, and soldered.

The aluminum frame arrived just in time, after all of the soldering was finished. The 6-foot aluminum extrusions were cut into the appropriate lengths and assembled (Figure 2.19). Next pipe clamps were slid onto the frame and spaced appropriately for each piping section. Due to the variety of component dimensions in a given pipe section, washers were used as spacers to elevate the clamp to the given height above the frame (Figure 2.20).

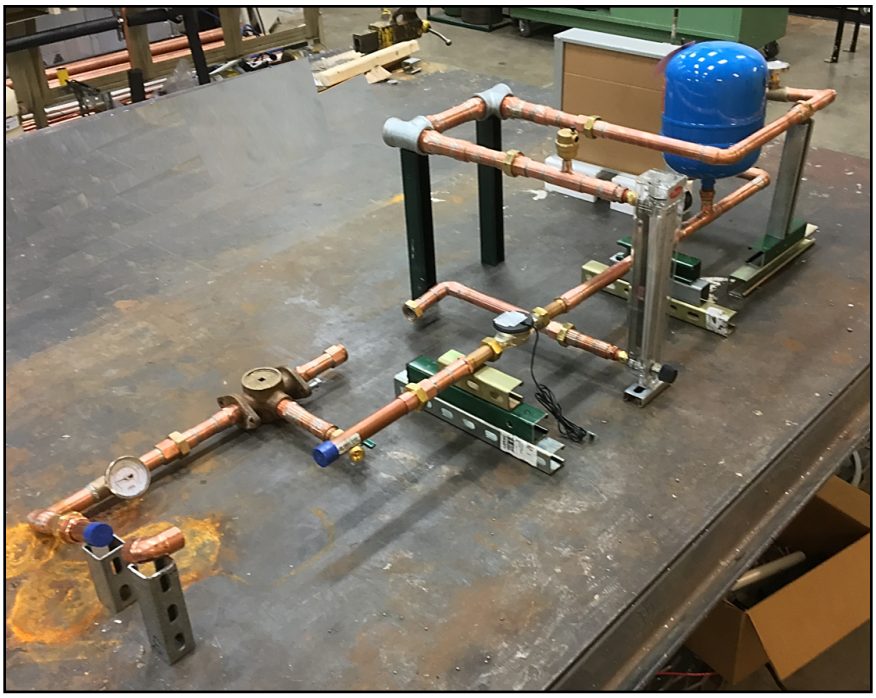

Figure 2.18: Soldered together pipe sections laid out in approximate orientation and height.

Figure 2.19: *80/20* aluminum extruded frame being assembled.

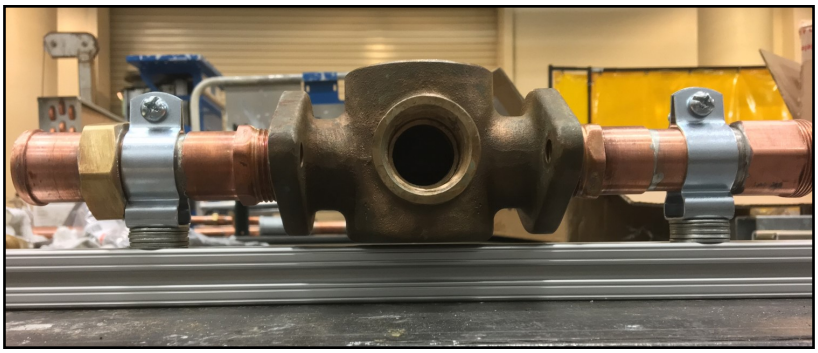

Figure 2.20: Pipe clamps positioned around 3-way valve piping section, with spacers adjusting height.

After all of the pipe clamps were properly spaced, the initial layer of 3/8-inch foam insulation was wrapped around the appropriate pipe sections (from one temperature sensor port to the other). The union fittings were then lined-up and blue, silicone gasket-maker paste (*Permatex Blue RTV Silicone Gasket Maker, #80022*) was applied to both male and female mating ends of the union (Figure 2.21). The unions were lined with thread tape and then screwed shut. After 24 hours, the paste cured into a custom gasket, and the unions were water-tight.

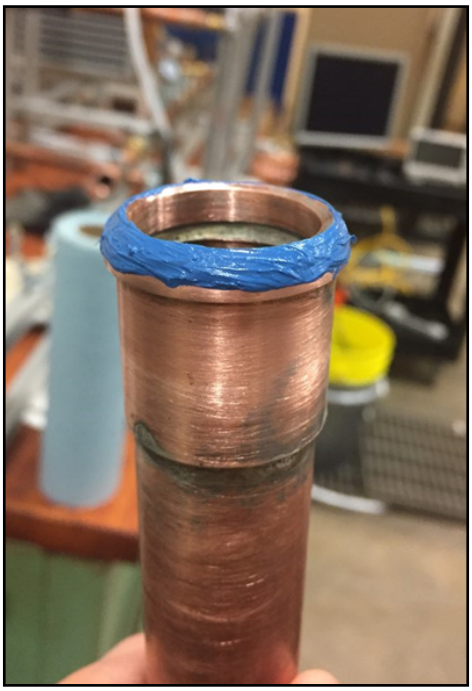

Figure 2.21: Blue silicone gasket maker paste applied to the male end of a 1-inch copper union.

Finally, all of the remaining auxiliary components (air vent, expansion tank, pressure gauge, etc.) were lined with thread tape and screwed into place. Figure 2.22 shows the assembled test loop, with major components labeled.

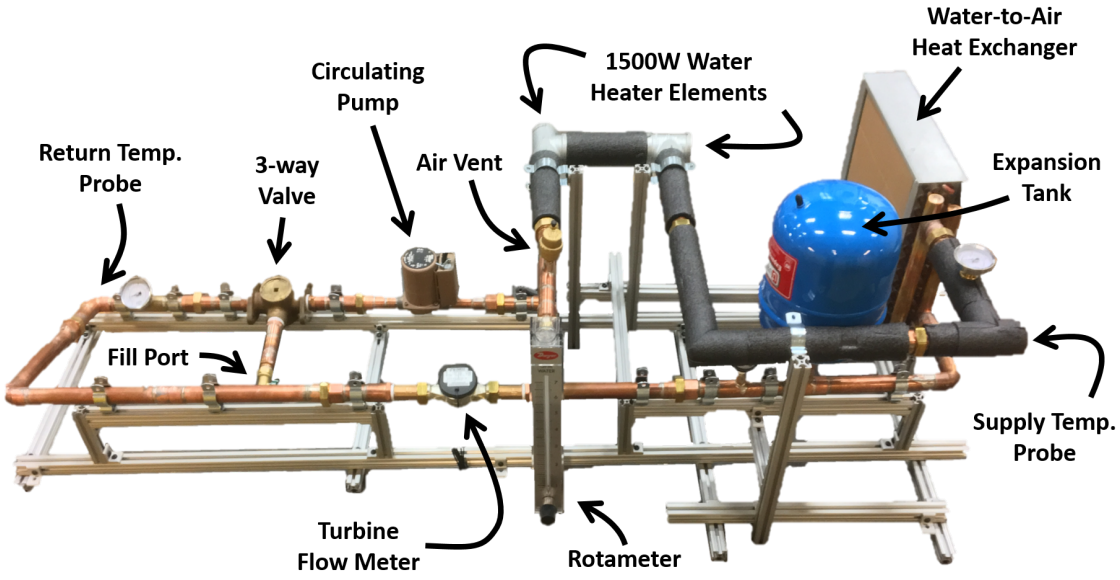

Figure 2.22: Test loop with key components labeled (without insulation).

The test loop was then closed, by plugging all of the temperature probe ports, closing the 3-way valve, and closing the air vent. A pressure test was then performed by connecting an air compressor into the tee with the pressure gauge (Figure 2.23). Specifically, the test loop was pressurized to approximately 60 psi and then the valve to the air compressor closed. The hose was disconnected and left for an hour, with negligible pressure loss occurring.

The system was then depressurized and the 3-way valve opened to prepare to be filled. Distilled water was then pumped into the loop using a submersible utility pump and a 5-gallon bucket. In order to purge the system, a second ball valve with a barb adapter was split off (using a tee) below the air vent at the top of the loop. This allowed for bubbles to be carried out of the system, back into the 5-gallon bucket, as water was filling up the loop at the bottom and flowing up through top. The system was purged for about 10 minutes, being careful to run at as fast a flow rate as possible

to ensure that any bubbles caught up inside the loop (namely in the heat exchanger circuit) would be moved around to the air vent. This is depicted well in Figure 2.24.

Figure 2.23: Close up of pressure gauge and air-compressor hose during initial pressurization of pressure test.

Figure 2.24: Close up of air bubbles being purged through the top valve of the loop.

2.1.7 Initial Heat Exchanger Capacity Verification

As mentioned previously, the initial capacity of the test loop's heat exchanger was immediately verified upon successful filling and purging of the test loop. The primary goal of this initial test was to determine if the heat exchanger and fan combination was sufficient to keep the mean water temperature at a reasonable temperature during steady-state operation in typical air-conditioned space (65°F-70°F). At the beginning of each test, the pump was turned on and allowed to run at 2.5 GPM, without either water heater element on, for about 5 minutes, to ensure even mixing across the loop. At the end of the experiment, all water heater elements were turned off, and the system was allowed to cool back down to room temperature.

As an initial "worst-case scenario"/"baseline" test, just a single water heater element was turned on (1500 W total), but the box fan was not. Temperatures were read from the analog temperature gauges and recorded to the nearest 1°F about every 2 minutes. As can be seen in the results plotted in Figure 2.25, the temperatures rose steadily at approximately 5°F per minute, without showing any signs of slowing. After about 8 minutes the test was aborted and the water heater element turned off. These rapidly rising temperatures, when the fan was not turned on, underscore the necessity of the test loop always being monitored, until further automatic safety features are implemented.

For the next test, the box fan was turned on, as well as one of the water heater elements (1500 W total). Temperatures were likewise recorded approximately every 2 minutes. After 30 minutes, the water in the system appeared to have sufficiently reached steady state at approximately 90°F on the return side and 86°F on the supply side (relative to the heat injection section of the loop).

The last initial capacity test was ran with the same flow rate and fan speed as the second, but with both water heater elements turned on (3000 W total). As expected the settling time of the system appeared to be the same as the previous.

The steady-state temperatures were approximately 114°F and 109°F for the supply side and return side respectively. Since, the overall mean water temperature remained well below boiling with the fan turned on, the heat exchanger proved adequate for keeping the mean water temperature well below boiling. A higher-speed Lasko fan was later purchased to ensure, when tests were ran at even lower flow rates, that the mean water temperature would not come close to approaching boiling.

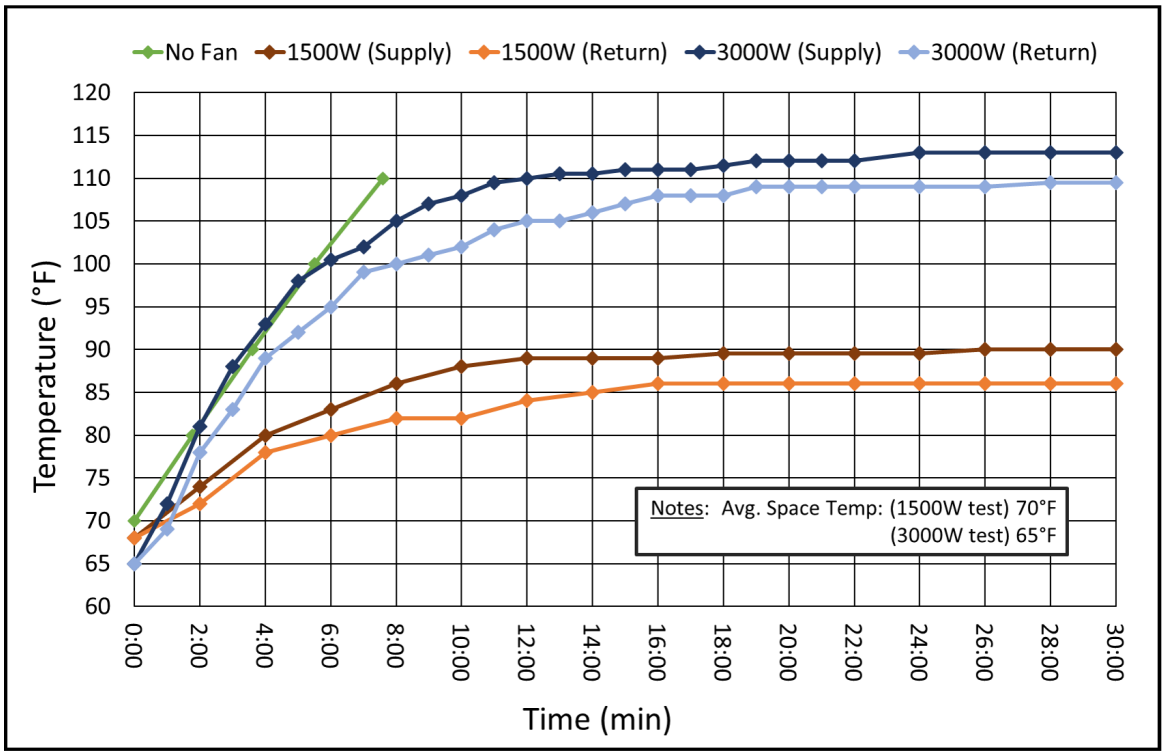

Figure 2.25: Data recorded during initial capacity tests performed to verify heat exchanger size.

2.1.8 Locating Heat Leaks Using an Infrared Camera

As was alluded to earlier, it was determined later during the experimental heat balances performed, that additional insulation needed to be added to the test loop. A roll of R-13 fiberglass insulation was purchased and cut into strips that could be effectively wrapped around both the pipe and the aluminum framing. Initially all of the test loop between the two temperature ports was wrapped in a single layer

of R-13 insulation. Then in order to identify what areas were still leaking heat, an infrared camera was later used to take pictures of the test loop while operating at a steady-state heat load, with large temperature differences across the heat exchanger. Figures 2.27 show an example of several images taken by the infrared camera to help identify "heat leaks". A picture of the test loop after being further insulated can be see in Figure 2.26.

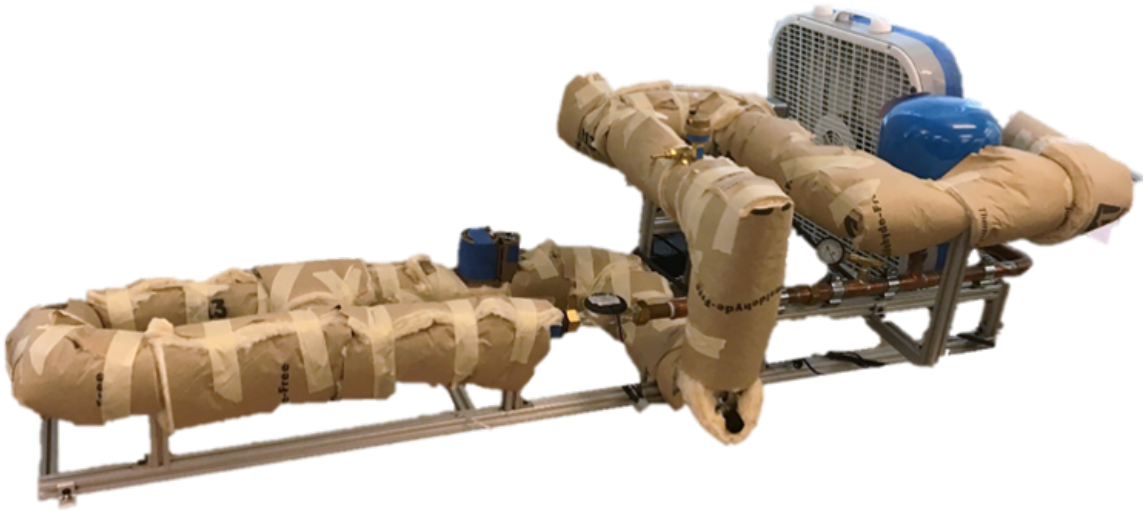

Figure 2.26: Test loop after being further insulated with R-13 fiberglass insulation.

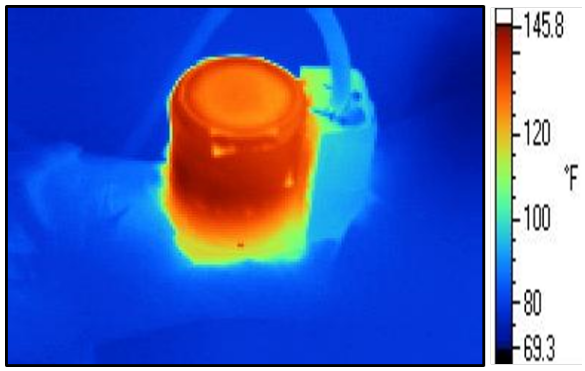

(a) Circulation pump

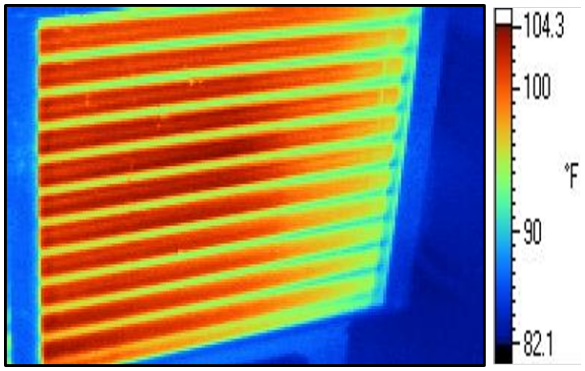

(b) Heat exchanger

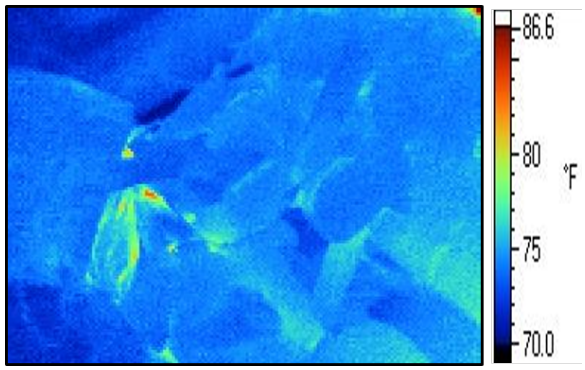

(c) Top of heater 1

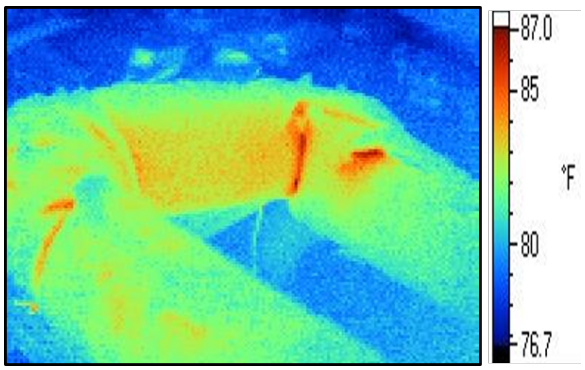

(d) Return temperature port

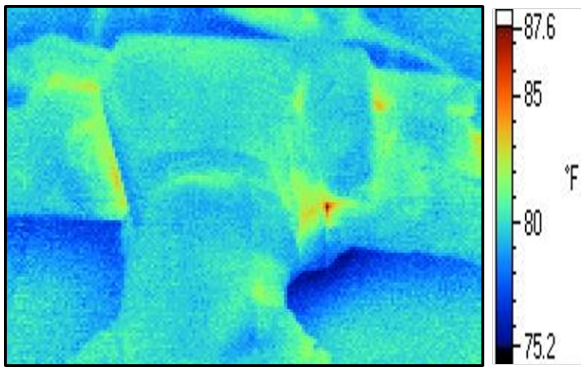

(e) Three-way valve

Figure 2.27: Several images captured by the infrared camera used to locate leaks through the insulation.

CHAPTER III

Energy Meter Development

As was presented in the Introduction (Chapter I), there continues to be a need for longer-term, quality field data for residential GSHP systems. This chapter describes the design, fabrication and calibration of an energy meter that was developed at Oklahoma State University for such a purpose. Specifically, the theory and engineering design calculations that went into the energy meter's key components, along with their affiliated calibration procedures and results are presented. While multiple iterations of the design were made, the following chapter's discussion will focus primarily on the final design and the primary design decisions that contribute to it. Key lessons learned that prompted the changes made throughout iterations can be found in Appendix H.

3.1 Overview

In order to collect meaningful performance data from any heating and cooling system, accurate measurements of calorimetric heat transfer ($\dot{Q}$) and electrical power consumption ($\dot{W}$) must be made. For residential GSHP systems, the calculation of calorimetric heat transfer (Equation 3.1) requires knowledge of the volumetric flow rate ($\dot{V}$), and the leaving and entering fluid temperatures (T_{LWT}, T_{EWT}). The density (ρ) and specific heat (c_p) can be calculated using the temperature measurements and assumed pressure (1 atm or 101.325 kPa).

$$\dot{Q} = \dot{V} \cdot \rho \cdot c_p \cdot (T_{\mathrm{LWT}} - T_{\mathrm{EWT}}) \tag{3.1}$$

Since we will be measuring the ground loop of a GSHP system, with knowledge of the power measurements, the cooling/heating provided can be estimated. The calculation of the electrical power consumption (Equation 3.2), requires knowledge of the voltage (V), current (I), and power-factors ($\cos(\phi)$).

$$\dot{W} = V(t)I(t)\cos(\phi) \tag{3.2}$$

Moreover, high-accuracy sensors must be properly calibrated and installed strategically within specific boundary schema in order to properly measure these characteristics and calculate meaningful SPFs for any system. The basic overview of such an energy monitoring system is depicted in Figure 3.1. The key components include: a flow sensor, temperature sensors, voltage transformers, current transducers, analog-to-digital conversion (ADC) boards, a micro-controller, and an online data storage system. The details about how each of these components function individually, and the necessary engineering design calculations associated, are discussed in further detail in the following sections.

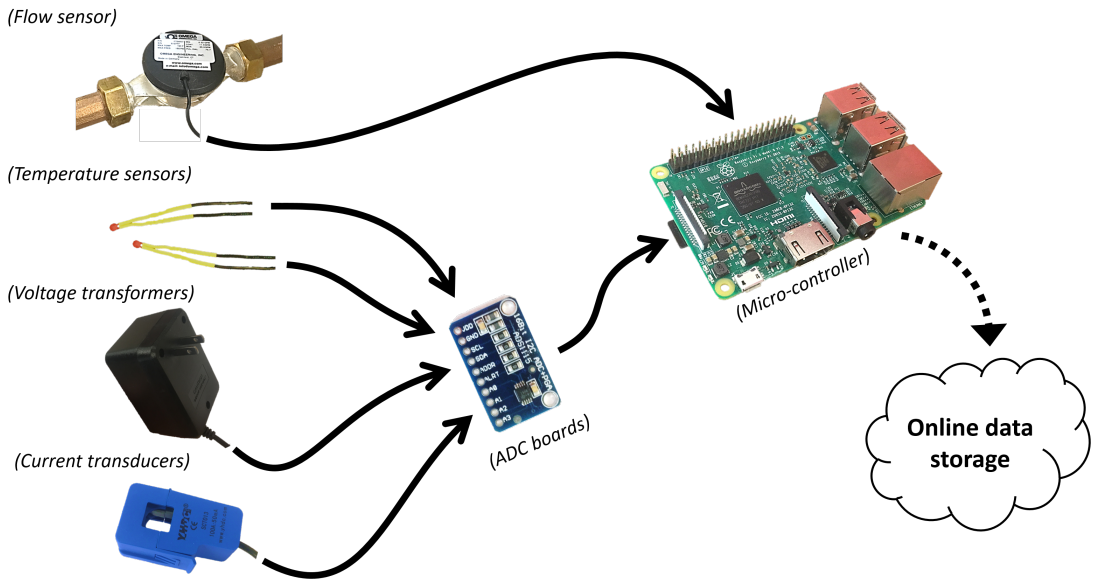

Figure 3.1: Basic schematic of an energy meter's key components.

Common "best-practice" for collecting fluid temperatures and flow rates is to install sensors in-line, such that the temperature and flow data are being recorded from sensors placed in the center of well-mixed, fully-developed flow. However, as mentioned in Liu et al. (2019), such in situ measurements are often considered too expensive for residential GHP projects. Moreover, unless such data is monitored within the equipment and made accessible by the heat pump manufacturer, most GSHP systems must have separate sensors installed post-facto. Thus, the ideal sensor system for a residential GSHP system owner would be non-invasive, cheap, and still accurate enough to perform meaningful performance analyses at any interval, over long histories of data.

To clarify, "non-invasive" sensors are considered those that would not require turning off the GSHP system and opening up the fluid loop somewhere to install the additional fittings and equipment necessary to monitor the system (e.g., thermowells, in-line flow meters, etc.). As a supplemental aspect of this thesis, in addition to developing a non-invasive ("clamp-on") energy meter, an in-line sensor system was also developed. The accuracy and effectiveness of the clamp-on energy meter will be compared to the performance of the standard in-line sensor system, later in Chapter VI. Their calibration procedures can be assumed to be identical, unless clearly distinguished.

As initially described in Nordman and Zottl (2011), the specific equipment and controls included in the measurement of electrical power consumption plays a large role in the corresponding system SPF calculated. As a result it would be ideal for a residential GSHP system to come equipped with multiple power loggers. Specifically, having multiple current transducers would allow for the GSHP installer/owner to monitor exactly the equipment necessary to calculate the SPF for the desired boundary scheme (e.g., determine SPF for the heat pump and for the system as a whole).

The following sections describe the individual component designs within the clamp-on energy meter in greater detail. Each section will go into sufficient detail to discuss the theory behind how that particular component works, any design calculations performed in the component selection process, its fabrication, and the corresponding calibration procedures and results.

3.2 Micro-Controller

In any monitoring system, something must act as the "brains" of the system by communicating with sensors, recording measurements, and storing and sending data to an online site for future access. Most commercial data acquisition systems, while arguably accurate and convenient if installed and organized properly, are often sold separately, require a separate computer for operation, and are often just as expensive as the sensors being measured. Moreover, commercial data acquisition systems are often operated with licensed programs that require the purchasing of a monthly or annual subscription to gain access and edit/customize the code. A micro-controller on the other hand is much cheaper and the programming languages used are often open-source. Thus we decided to implement a micro-controller as the "brains" of our low-cost energy meter. The key requirements and considerations used in deciding which particular micro-controller to purchase is summarized in the graphic on the next page (Figure 3.2).

The specific micro-controller selected for this project was the *Raspberry Pi 3 Model B+*. While it is only the foot-print of a credit-card, it effectively functions as a mini-computer and the standard, download-able "Rasbian" operating system allows for any user/GSHP installer to operate it with ease. The main characteristics that were considered when selecting the *Raspberry Pi* over other micro-controllers available were: cost, programming language, voltage measurement capabilities, time/clock accuracy, and internet accessibility.

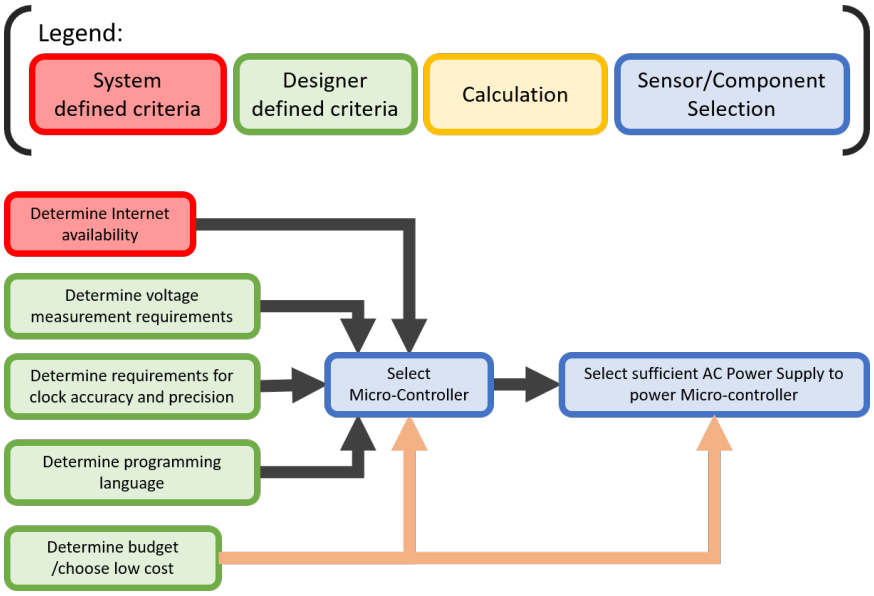

Figure 3.2: An overview of the design and selection process for the energy meter's micro-controller.

The cost of most micro-controllers researched were between \$20-\$50 in order to get them configured and operating. While on the expensive end of micro-controllers, a *Raspberry Pi* is easily an order of magnitude cheaper than then most other research-grade data acquisition systems. Assuming just the *Raspberry Pi* and 32 GB microSD card are needed (a mouse, keyboard, HDMI cable, and monitor are already on-hand), the cost is approximately \$50 (as of July 2019).

The *Raspberry Pi*, compared to other micro-controllers considered, also had the widest variety of open-source programming languages that could be used. In particular, the open-source programming language *Python* can be ran on it. Being able to program in *Python* was ideal because of its multitude of open-source resources and libraries available online. It also would allow for any subsequent OSU students to easily work on and upgrade the meter's code in the future (as the current undergraduate Mechanical Engineering curriculum requires an introductory *Python* programming course).

As will be seen in later sections of this chapter, measuring any sensor ultimately boils down to measuring voltages; specifically, either analog or digital voltages. As

depicted in Figure 3.3, a digital voltage signal can either be "high" or "low," while an analog voltage signal can vary continuously. While other micro-controllers considered are capable of measuring analog voltages independently, unfortunately the *Raspberry Pi* (by itself) is only capable of reading digital signals. This is not a problem for sensors that have digital outputs, but most temperature and current sensors used in HVAC applications output an analog voltage signal. This obstacle was compensated for by purchasing an Analog-to-Digital conversion (ADC) board (about $15) that was easily compatible with *Python* and *Raspberry Pi*s.

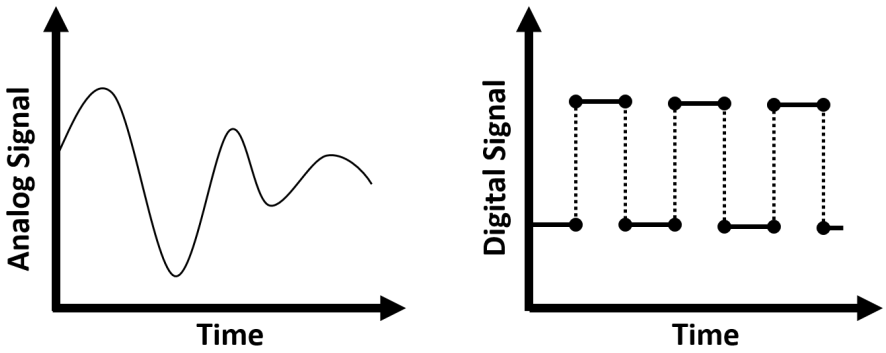

Figure 3.3: Example of analog and digital voltage signals.

A key criteria for any monitoring system is the ability to accurately time-stamp measurements. Without accurate knowledge of when a particular measurement was recorded, calculating and comparing performance over time would be extremely difficult, if not impossible. Unfortunately the *Raspberry Pi* does not have a "Real Time Clock" (RTC), so it is not capable of tracking time on the motherboard whenever it is shut down. Therefore, if the *Raspberry Pi* were to lose power suddenly (as is not unheard of in rural areas) and be forced to restart, the time-stamps would no longer be accurate. Fortunately, the *Raspberry Pi* automatically checks to synchronize its clock with the anytime it is connected to the internet, using standard "Network Time Protocol." While there are RTCs available as "hats" to be added on top of *Raspberry Pi*s, we decided not to spend money on them, since internet access was assumed to

be always accessible, as discussed below.

Lastly, in today's rising acceptance and implementation of smart-home devices that can be controlled and accessed remotely, we decided our energy meter should also be capable of sending and saving data remotely. The *Raspberry Pi 3 Model B+* comes with built-in bluetooth and WiFi connectivity, enabling the potential for continuous internet access (assuming it is available). Earlier models of the *Raspberry Pi* would have required the additional purchase of a USB dongle to gain internet access and be accessed remotely. Furthermore, there are several free softwares available that are specficially designed to allow remote access into a *Raspberry Pi*. For the purposes of this research, *VNC Viewer* was implemented to enable control of the *Raspberry Pi* remotely from a separate computer or smart phone. As will be discussed later, a free email account was set up to receive and store a backup of daily data logs on the internet.

3.3 Analog-to-Digital Conversion Boards

As mentioned previously, because the micro-controller selected can not read analog voltage measurements directly, additional ADC boards had to be purchased. An overview of the theory behind how ADC boards work, the design calculations and considerations leading to the final ADC board selection, and the ADC board's verification process is described in this section.

3.3.1 Theory

The fundamental processes of an ADC board are discretization and quantization (Figure 3.4). Discretization is effectively the process of changing a continuous-time signal into a discrete-time signal via sampling . The most common characteristic used to define an ADC's discretization process is sampling rate, often given in samples per seconds (sps or sometimes listed as S/s in some specification sheets).

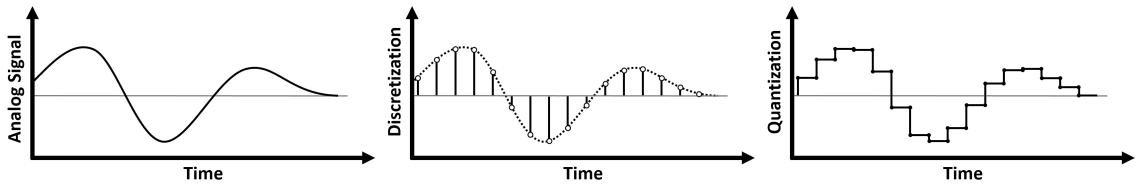

Figure 3.4: Example of an analog signal being discretized at specific sample points. (after `www.nutaq.com/blog/analog-digital---part-2-conversion-process`)

Quantization is effectively the process of replacing each real voltage value in the discretized signal with an approximation from a set of finite discrete values. The specific discrete value that is used to approximate the real-value is often referred to as the "quantization level" (or "raw count"). Appendix A contains more details as to how this physically takes place in typical comparator circuits.

Conveniently ADC boards are essentially complex comparator circuits, designed in advance with specific characteristics. The most common characteristics used to classify ADC boards are the number of bits they handle and the full-scale voltage (FSV) or "maximum readable voltage" the ADC board can read. Equation (3.3) shows how the number of bits (n) can be used to determine the number of quantization levels (m) that are possible outputs from an ADC. Equation (3.4) is then used to estimate the theoretical resolution (ΔV) of an ADC based on the FSV and quantization levels.

$$m = (2^n - 1) \tag{3.3}$$

$$\Delta V = \frac{\text{FSV}}{m} \tag{3.4}$$

As can be seen in Figure 3.5, the more bits in an ADC, the more precise the discretized signal becomes.

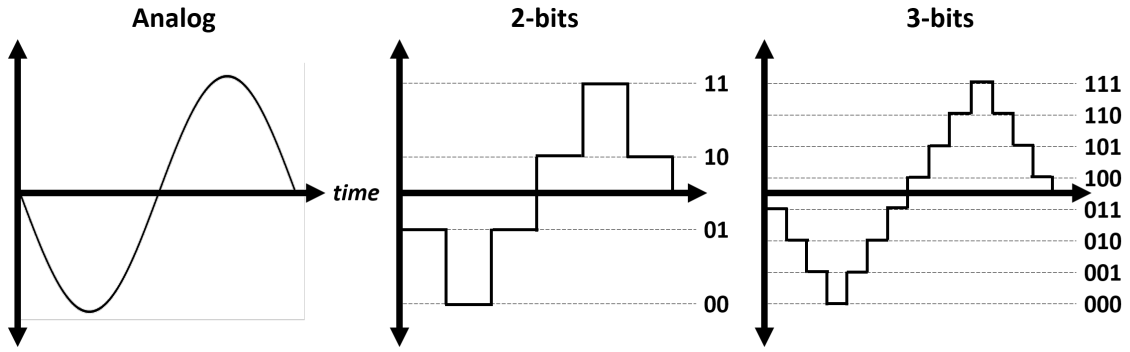

Figure 3.5: Comparison between infinite-bit (analog), 2-bit, and 3-bit resolutions. (after en.wikipedia.org/wiki/Quantization_(signal_processing))

3.3.2 Selection of ADC Board

The key requirements and considerations used in deciding which particular ADC board to purchase and implement is summarized in Figure 3.6.

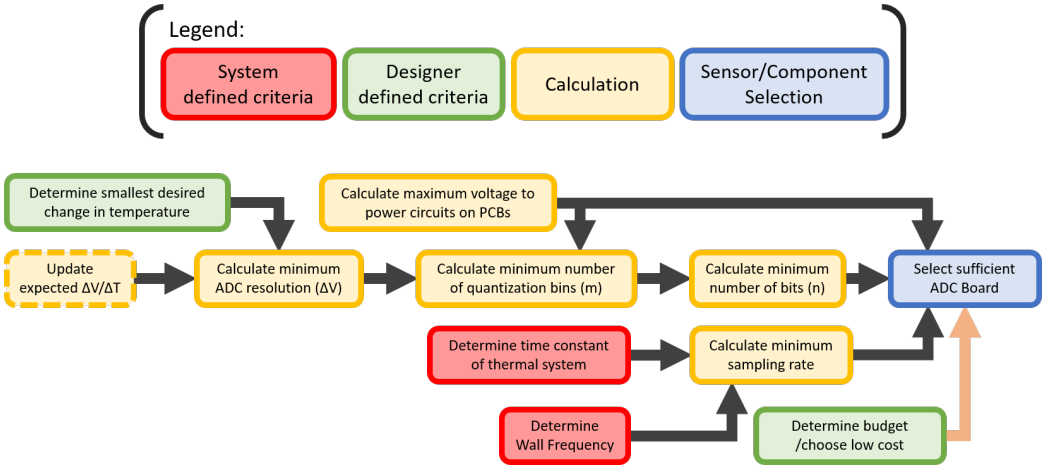

Figure 3.6: An overview of the design and selection process for the energy meter's ADC board.

The ideal ADC board would have the greatest number of bits possible, a FSV close to the maximum voltage output by the sensors, and a sampling rate fast enough to capture the entire signal. The rule of thumb for determining adequate sampling time to identify a continuous-time signal's characteristics is to select a sampling rate at least two times faster than the highest known frequency in its bandwidth [Shannon (1949)]. However, in practice, it is better to sample as much as 5 times faster than

the known signal frequency, if sufficient high resolution discretization of the signal is to occur. For the energy meter, the fastest changing sensor-output will be the power sensors. More specifically the voltage and current measurements will be sinusoidal signals, oscillating at a frequency equal to that which is coming out of the wall outlet (60 Hz in the U.S.). Thus, the ideal sampling rate acceptable for the energy meter's ADC board is at least 300 sps (or one sample every 3.333 μs). In a later sub-section, the combined sampling rate of all the individual measurements in sum will be confirmed to be fast enough to adequately track the transient responses in the GSHP system.

The ideal FSV of the ADC board is dependent on the maximum expected voltage reading from the analog sensors. While the specific design considerations of the temperature and power sensors circuits will be described in more detail later, choosing an ADC board with a maximum input voltage of 5.0 V was found to be suitable. This was determined by the initial temperature sensor's circuit design goal of being powered solely by one of the "5V-pins" on the *Raspberry Pi*. Thus, the ADC board's FSV would need to be equal to or greater than 5.0 V.

The ideal bit-count of the ADC board is dependent on the minimum expected change in voltage output from the analog sensors. As a result of the temperature circuit (sized in the following section), the anticipated minimum voltage change corresponding to a change in temperature of $\pm$ 0.018 $^{\circ}F$ ($\pm$ 0.01 $^{\circ}C$) was calculated to be approximately $\pm 350 \mu V$. Therefore, using that anticipated voltage change and a FSV of 5.0 V, Equations (3.3) and (3.4) were used to determine that at least 14-bit resolution will be sufficient.

The ADC board selected during the final iteration of the energy meter is an *Adafruit ADS1115* ADC board. (See Appendix H for significant lessons learned from selecting and operating another ADC board). The *Adafruit ADS1115* has 16-bit resolution and a maximum sampling rate of 860 sps. A single board can measure up to 4

individual single-ended channels (potential difference relative to ground) or 4 differential channels (potential difference relative to another channel). It uses an I2C interface and can specifically communicate with up to 4 different I2C addresses. Furthermore, *Adafruit* has conveniently made accessible their own *Python* library called `ADS1X15` (located on their repository `www.github.com/adafruit/Adafruit_Python_ADS1x15`), which made writing the code to measure the analog signals much easier. Table 3.1 shows the summarized design criteria compared with the *Adafruit ADS1115*'s specifications.

Table 3.1: ADC Board Design Criteria

Criteria	**Ideal**	**ADS1115**
Sampling Rate	$\geq$ 120 sps	860 sps
FSV	$\geq 5.0\ V$	$\pm\ 6.144\ V$
Resolution (Bits) at $\Delta T = \pm 0.01°C$	$\leq \pm\ 350\ \mu V$ (14-bits)	$\pm\ 70\ \mu V$ (16-bits)
Single-Ended Channels	≥ 4 (temp sensors)	4 (per board)
Differential Channels	≥ 6 (power sensors)	4 (per board)
Programming Languages	*Python*	*Python*, *Java*, *C*, *C++*, *HTML5*

3.3.3 Verification

The ADC boards used were put through a verification test to identify the accuracy in which they measure a steady analog voltage. Specifically they were tested at varying sampling rates, channel orders, and supply voltages. The basic setup of this calibration involved comparing the measurements recorded from the ADC boards to a state-of-the-art multimeter (*Fluke 8808A Digital Multimeter*), accurate up to ± 0.0002 VDC. The ADC board and multimeter were both hooked up to the same voltage-divider circuit being supplied with a constant voltage from a DC power supply (*MASTECH HY3005F-3*). The raw ADC counts (quantization levels) and reference multimeter voltage measurements were recorded.

Equation (3.5) was used to convert the raw ADC count (m) to the related voltage. Note that in the *Adafruit ADS1115*, the FSV was set to be 6.144 V and has 16-

bit resolution. However, in Equation (3.5) note that 15 is used as the bit-count in the exponent. This is because the first bit in the measured data is dropped during recording, since it just signifies if the value is positive or negative. Since all sensor measurements will be positive, this first bit is not needed.

$$V = m \cdot \frac{\text{FSV}}{(2^{(15)} - 1)} \tag{3.5}$$

During this validation process (and other preliminary sensor calibrations), several lessons were learned and can be found in Appendix H. The most notable result from these tests on the final ADC board implemented was the apparent effect varying supply voltage had on its accuracy. During the thermistors initial calibration tests, I found that the *Raspberry Pi*'s 5V-pin would spike randomly whenever the mouse was moved or it ran a task in the background. These events lined up perfectly with strange readings from the ADC board (depicted in Figure 3.7).

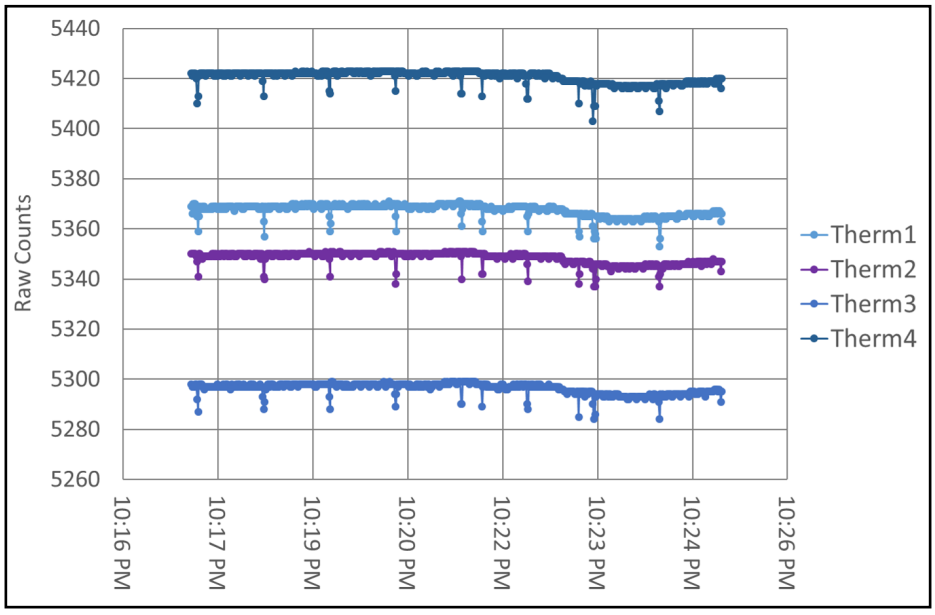

Figure 3.7: Plot showing the random spikes in voltage reading that correspond to mouse movement and and other *Raspberry Pi* processes.

Since it was originally being powered by the *Raspberry Pi*'s 5V-pin, the *Adafruit ADS1115* was experiencing significant fluctuations in its supply voltage during these

spikes. Through further investigation, I found that when the voltage that was powering the ADC board experienced significant spikes, its ability to consistently measure an unchanging analog voltage was poor. This investigation specifically involved measuring the ADC board's performance, while manually supplying the board itself with varying amounts of voltage from a DC power supply. More investigation could certainly be done to better understand the effects of varying supply voltages on ADC boards that function with internal reference voltages. However, for the sake of this thesis, a spare 5.0 V-4 A EPS was found and implemented that had much better stability than the *Raspberry Pi*'s 5V-pin. Furthermore, any significant errors in the measured voltage were assumed to be accounted for in the subsequent calibrations done on the overall sensor measurement (i.e., any error, unaccounted for in the ADC board, will be seen in the overall uncertainty of the end sensor measurement and accounted for in the overall sensor's uncertainty).

3.4 Temperature Measurements

As mentioned in Spitler and Gehlin (2019), the temperature difference measurements are most often the most influential in the overall uncertainty calculation for a particular GSHP system's calculated calorimetric heat transfer. Therefore, the most amount of time during this thesis was spent towards calibrating and attempting to tune temperature sensors. The theory, design methodology, fabrication, and calibration procedure for the final temperature sensor design are described in this section.

3.4.1 Theory

Multiple types of temperature sensors exist for measuring fluid temperatures and are well summarized in the ASHRAE *Standard 41.1 - Standard Method for Temperature Measurement* [ASHRAE (2013)]. The specific type of temperature sensor selected for this energy meter was a thermistor. A thermistor is a temperature-dependent

resistor. They are often made out of a ceramic material and are known for being able to achieve high-accuracy measurements (when calibrated well), while being cheaper than other high-accuracy types of temperature sensors. Specifically, compared to a Resistance Temperature Device (another common type of temperature sensor) that has a resistance which varies linearly with temperature, a thermistor's resistance varies non-linearly with temperature (Figure 3.8).

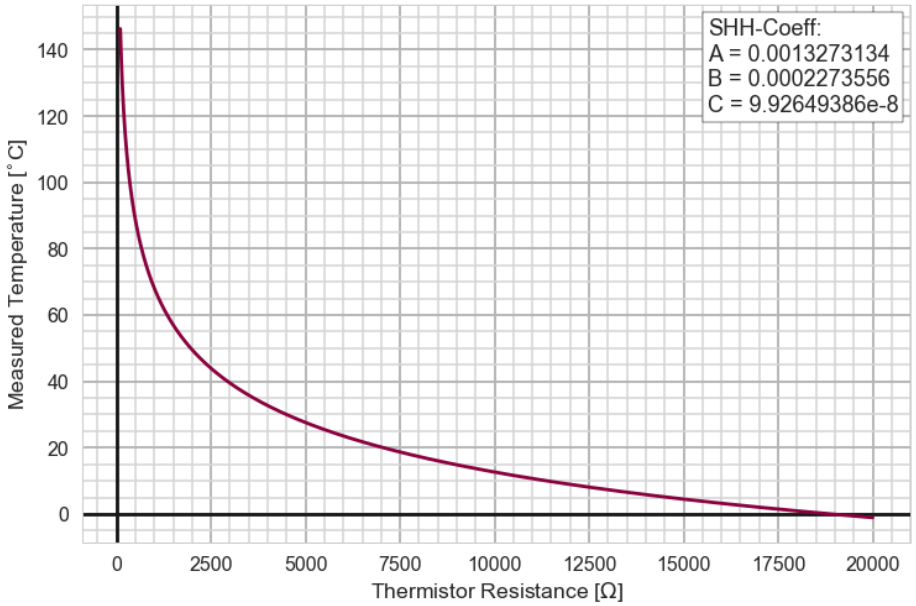

Figure 3.8: Temperature vs. Resistance curve for *Thermistor 1*.

Specifically, the most-commonly used equation for relating a thermistor's temperature (T - in Kelvin) with its resistance (R - in Ohms) is called the "Steinhart-Hart (SHH) Equation" (Equation 3.6).

$$\frac{1}{T} = A + B \cdot (\ln R) + C \cdot (\ln R)^3 \tag{3.6}$$

While Steinhart and Hart (1968) investigated equations with multiple coefficients, the 3-coefficient equation given above is reported to be sufficient for calculating temperatures with up to ± 0.000162 °C accuracy (depending on the quality of the thermistor itself and the accuracy of the reference thermometer used during calibration).

The most common methodology for calculating these SHH-coefficients, from a set of (at least three) known temperatures and resistances, is the Generalized Least Squares (GLS) Method (Equation 3.7). Other general curve-fitting methods can be used in the coefficient calculation process as well.

$$\text{Given} \qquad F = \begin{bmatrix} 1 & \ln(R_0) & \ln(R_0)^3 \\ 1 & \ln(R_1) & \ln(R_1)^3 \\ 1 & \ln(R_2) & \ln(R_2)^3 \\ \vdots & \vdots & \vdots \\ 1 & \ln(R_i) & \ln(R_i)^3 \end{bmatrix}$$

$$\text{and} \qquad Y = \begin{bmatrix} 1/T_0 \\ 1/T_1 \\ 1/T_2 \\ \vdots \\ 1/T_i \end{bmatrix}$$

$$[A, B, C]^T = (F^T F)^{-1} \cdot (F^T Y) \tag{3.7}$$

Since the resistance of the thermistor must be measured, typically voltage-divider circuits are implemented. Voltage-divider circuits are helpful because, fundamentally, resistances can not be measured directly. In a typical voltage-divider circuit (Figure 3.9), a second resistor of known resistance (often called a "shunt resistor") is placed in series with the resistor of interest (in this case a thermistor). Since the resistance of the shunt resistor is known, the current passing through the voltage-divider circuit can be calculated (Equation 3.8). Knowing the current, the other resistor's resistance can now be calculated, using its measured voltage (Equation 3.9).

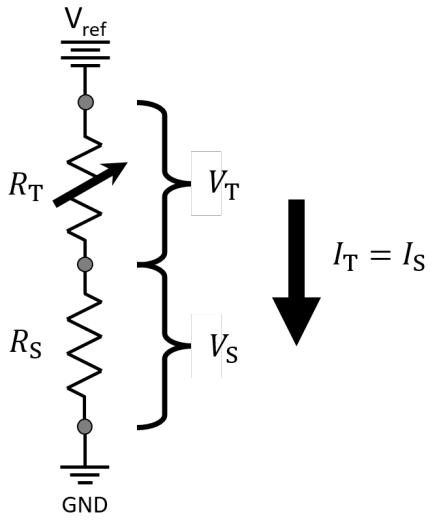

Figure 3.9: Example voltage-divider circuit with known shunt resistance (R_{S}) and unknown thermistor resistance (R_{T}).

$$I = \frac{V_{\mathrm{S}}}{R_{\mathrm{S}}} \tag{3.8}$$

$$R_{\mathrm{T}} = \frac{V_{\mathrm{T}}}{I} \tag{3.9}$$

(See Appendix H for lessons learned using other temperature circuit designs.) The exact thermistor and shunt resistor selected are sized and discussed in the following sub-section.

3.4.2 Selection

A summary of the key design requirements and calculations used to size the aforementioned components in the temperature sensor circuit are discussed in this section. Specifically the thermistor and shunt resistor sizes are calculated. Figure 3.10 shows an overview of the design and selection process followed.

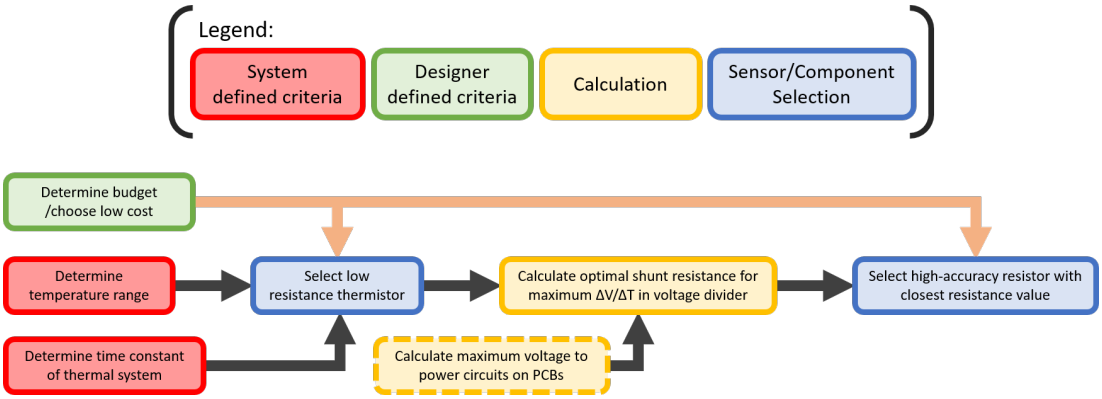

Figure 3.10: An overview of the design and selection process for the energy meter's temperature sensor.

3.4.2.1 Selection of Thermistor

When selecting thermistors for the residential GSHP energy meter's temperature circuit, there were four main design factors that guided the selection: expected temperature range, response time, nominal resistance, and cost.

The allowable temperature range was the main factor initially determining which thermistors were feasible. The normal undisturbed ground temperature range in residential GSHPs usually falls between 40°F - 70°F (5°C - 22°C). Furthermore, based on the initial capacity tests of the verification test loop, the operating temperatures the test loop's water would likely reach are between 68°F - 131°F (20°C to 55°C). Thus the design selection criteria for the expected temperature range of the thermistors considered had to be at least between 40°F - 131°F (5°C - 55°C).

Any heat-related measurement has the potential to lag in responses, due to the thermodynamics and heat transfer taking place. Thus, temperature devices should be selected to have considerably faster response times compared to that of the system being measured. Additionally, they should ideally have large surface area and small mass, so that they will reach equilibrium with their surroundings faster. Some manufacturers of thermistors will provide estimated thermal response times. The thermistors investigated that reported response times, were all faster than 30 seconds.

Another guiding design factor was the nominal resistance of the thermistor. On most specification sheets, the nominal resistance of the thermistor is usually given as its resistance at room temperature. Since thermistors are unfortunately known for self-heating, a larger resistance thermistor is preferred, so as to have the lowest amount of power consumed. The lower the amount of power consumed, the less heat would likely be dissipated to potentially cause self-heating.

The final guiding design factor was to choose the cheapest thermistor in order to keep the energy meter as affordable as possible. Regardless of price, every thermistor purchased was calibrated in our lab, in order to ensure that their quality/accuracy met the characteristics of our temperature requirements.

The thermistors selected for the clamp-on energy meter were nominally 5 kΩ thermistors sold from Jameco (*NTC-502K*). These were purchased in bulk in anticipation of multiple iterations and designs being made throughout the overall energy meter's development. The main modifications made to these thermistors included adding 6-foot long leads with male DC barrel jack adapters on the end, and heat shrink to hide the bare wire. Figures 3.11 and 3.12 show a thermistor as received and a thermistor after modifications were made respectively.

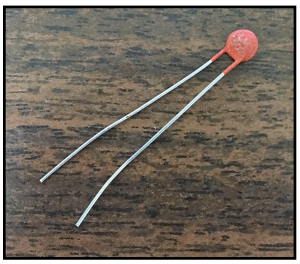

Figure 3.11: *NTC-502K* thermistor.

Figure 3.12: Finalized thermistor design (with leads and male DC barrel jack adapters).

The thermistors selected for the in-line energy meter were two tubular immersion thermistors from Omega (*ON-410-PP*). These were selected because they fit the temperature range and response time we required and we already had a pair available in the lab. While significantly more expensive than the clamp-on meter's thermistors,

this was justified in trying to keep the validation test loop's in-line energy meter as high a quality to compare to as possible. The Omega *ON-410-PP* thermistors came with 10 feet of jacketed cable and the thermistors themselves are inside of 4.5-inch long metal probes, with 1/8-inch NPT to allow for installation in the test loop's pipes. The only modification made to the *ON-410-PP* thermistors after they were received, was replacing the phone plugs with 2.1 x 5.1mm DC barrel jack adapters. Figure 3.13 shows a picture of the in-line, immersion *ON-410-PP* thermistor after it was modified.

Figure 3.13: In-line, immersion *ON-410-PP* thermistor modified with DC barrel jack adapters.

3.4.2.2 Selection of Shunt Resistors

In order to properly size the shunt resistors in the voltage-divider circuits, the expected thermistor resistances, namely across the expected range of temperatures, are needed. The data sheet for the *NTC-502K* thermistors selected for the clamp-on energy meter had 23 pairs of resistances and temperature data points listed (Jameco (2011)). The data sheet for the in-line *ON-410-PP* thermistors did not have any listed temperature-resistance data points beyond the nominal room-temperature resistance given, so four data points were quickly sampled using hot and cold water from a faucet, a *ThermoProbe Inc. TL1-A* thermometer, and a hand-held multimeter. From their thermistor data points, a rough approximation of their SHH-coefficients were

calculated using the GLS method.

With the approximate SHH-coefficients known, an Excel spreadsheet was made to model the expected voltage across a given shunt resistor, based on the design FSV and the modeled thermistor resistances. Using Excel's *Solver* tool, the ideal shunt resistor was sized by maximizing the sum of all the calculated changes in voltage per change in temperature ($\Delta V/\Delta^{\circ}C$), across the expected range of temperatures. Appendix C contains a link to the *Dropbox* folder that contains a copy of the file used for future reference.

Table 3.2 shows the results of optimizing the shunt resistor sizes generated by Excel's *Solver* tool. Note that the expected temperature range for the in-line meter was tightened to just the temperatures in the test loop, while the clamp-on thermistors were sized for both the undisturbed ground temperatures and the test loop's temperatures. The nearest high-tolerance ("blue") resistor we had in the lab was selected as the resistor to implement.

Table 3.2: Shunt Resistor Sizing Results

Sensor Type	**Expected Temperature Range**	**Optimal Shunt Resistor**	**Selected Resistor**
Clamp-on	$40^{\circ}F - 131^{\circ}F$ ($5^{\circ}C - 55^{\circ}C$)	4133 Ω	3000 Ω
In-line	$68^{\circ}F - 131^{\circ}F$ ($20^{\circ}C - 55^{\circ}C$)	1708 Ω	1500 Ω

Figures 3.14 and 3.15 show the resulting plots of the expected shunt and thermistor voltages and the expected rate of change in voltage as a function of temperature. Note how the maximum rate of change in voltage takes place in the center of the anticipated temperature range. This should be adjusted (by selecting a different shunt resistor) if the anticipated temperature range changes. Also, note that this was how the minimum rate of change in voltage per change in temperature was determined when sizing the ADC board (see Sub-Section 3.3.2).

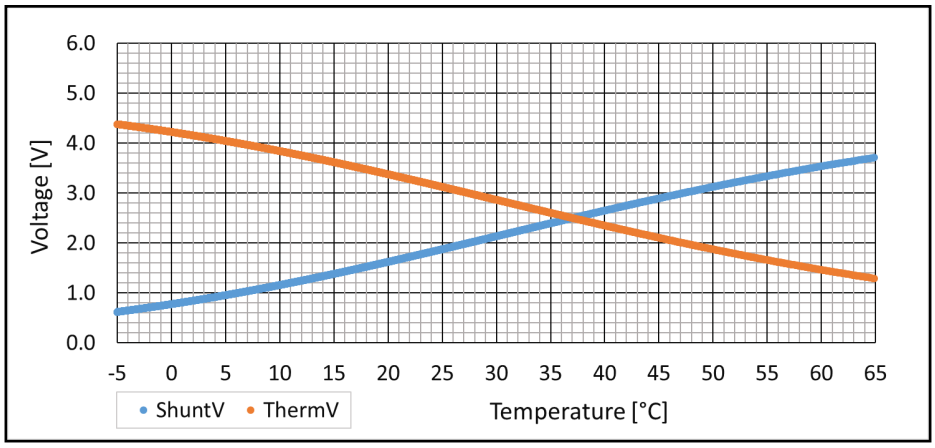

Figure 3.14: Estimated voltage across the voltage-divider of a 5k (clamp-on) thermistor and a 3000 Ω shunt resistor.

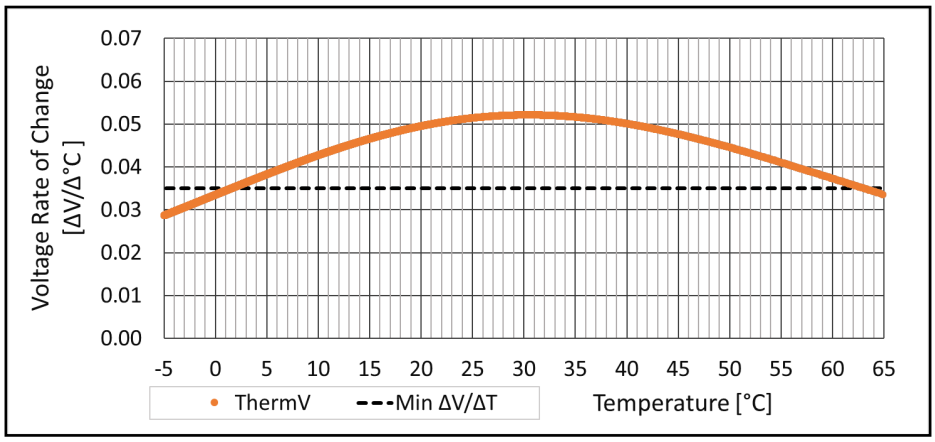

Figure 3.15: Estimated rate of change in voltage of a 5k (clamp-on) thermistor and a 3000 Ω shunt resistor about a given temperature.

3.4.3 Fabrication

With the shunt resistor and thermistor selected, a prototype circuit board (PCB) was designed. Specifically the PCB was designed with the ability to measure four different temperatures: Entering Water Temperature (EWT), Leaving Water Temperature (LWT), Entering Air Temperature (EAT) and Leaving Air Temperature (LAT). (Note that those are relative to the heating source). This was achieved by implementing four voltage-divider circuits in parallel.

Figure 3.16 shows the final temperature sensor's circuit design. Note that the flags in the figure denote a connection to a specific single-ended channel of a specific

ADC board (two boards were used for temperature measurements in the final design). Both ADC boards' grounds were connected to the common ground of the *Raspberry Pi* and the EPS. For the in-line energy meter, just two thermistors were needed (only water-side measurements), so only two voltage-divider circuits were put in parallel.

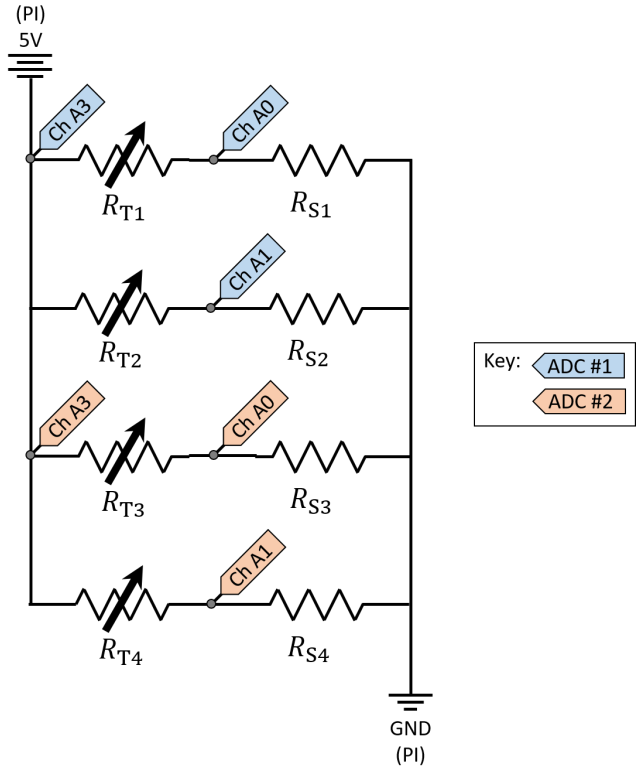

Figure 3.16: voltage-divider circuit developed for the clamp-on energy meter.

One of the key design features consummated in the fabrication stage was soldering in the thermistors' mating DC barrel jack adapters in the PCB. This allows the thermistors to be easily plugged and unplugged from the circuit. Ideally in the future, this would also allow for easy replacement of sensors that have drifted over time or been damaged. Additionally two 1x10 rows of male header pins were soldered into the PCB to allow for easy addressing and connecting of jumper wires for the signal clock line (SCL) and the signal data lines (SDA) of the I2C communication.

Figure 3.17 shows the first prototype temperature sensor PCB that was made (without the thermistors plugged in). Figure 3.18 shows the final PCB made (with the temperature sensor circuit specifically boxed).

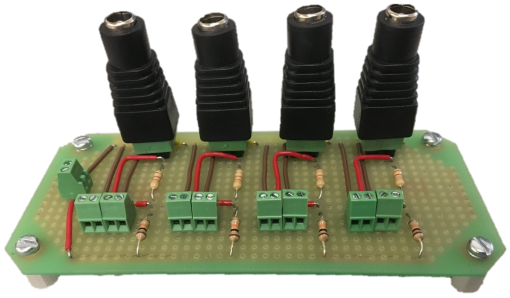

Figure 3.17: First functioning prototype of the temperature sensor circuit that was sent to the field for preliminary testing.

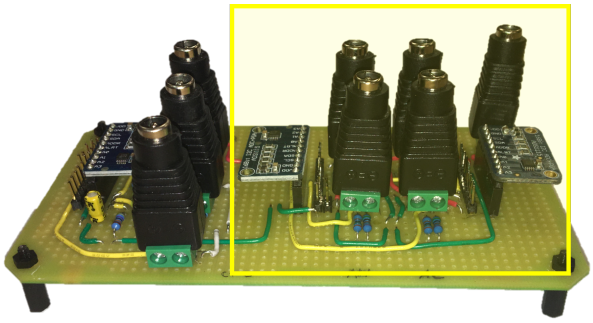

Figure 3.18: Finalized clamp-on energy meter PCB that was tested on the validation test loop (with the temperature sensor components highlighted).

3.4.4 Calibration & Validation

The six temperature sensors fabricated were given generic labels in order to keep them organized during calibration. The main purpose of calibrating is to verify the manufacturer's stated accuracy and to specifically identify the SHH-coefficients for each of the six thermistors.

The thermistors were calibrated against a high-accuracy reference thermometer in a constant temperature fluid bath. Specifically, an *Isotemp Bath Circulator* (Figures 3.19 and 3.20) was used to keep the calibration fluid at a relatively steady-state temperature during the calibration. Insulation was added to attempt to prevent heat from escaping and to reach steady-state faster during calibration (Figures 3.21 & 3.22 on the next page). The reference thermometer used was a *ThermoProbe TL2-A Laboratory Thermometer*. The calibration documentation for this specific thermometer (SN: *TL2-0043*) states that its "NIST traceable" calibration accuracy is within ±0.017°C (±0.030°F).

Figure 3.19: Picture of *Isotemp Bath Circulator* during in-line thermistor calibration.

Figure 3.20: Picture of *Isotemp Bath Circulator* during clamp-on thermistor calibration.

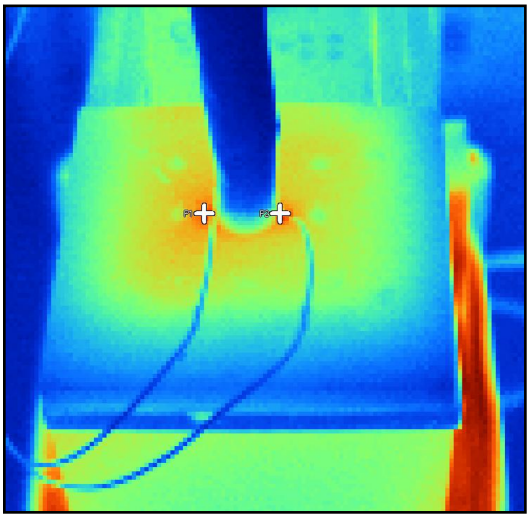

Figure 3.21: Infrared front view of the fluid bath circulator during the 35°C (95°F) sample.

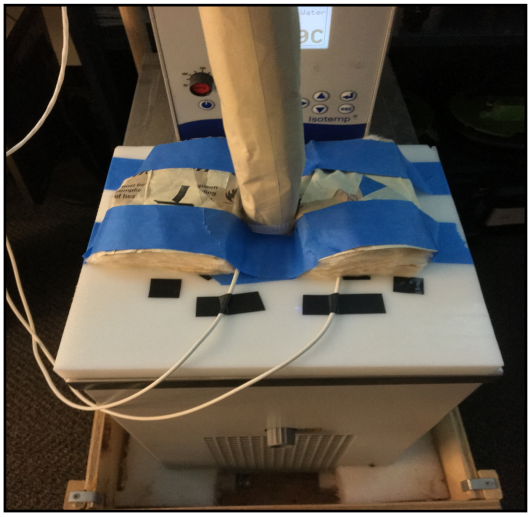

Figure 3.22: Front view of the fluid bath circulator after insulation was added.

The following process was followed for 8 different steady-state temperatures. The fluid bath circulator was set to desired temperature and the reference thermometer was used to monitor the fluids variance as the fluid bath heated and cooled the water. It was found that after approximately 45 minutes, the circulator was sufficiently able to maintain the fluid at a steady-state temperature, only varying with an average three standard deviations of $\pm 0.02^{\circ}F$ ($\pm 0.011^{\circ}C$). Meanwhile, each of the thermistors were fully submerged in the fluid and was assumed to have reached a similar steady-state resistance value.

The voltages of the shunt resistor and thermistors were then recorded and logged into a csv-file on the micro-controller, continuously for three separate 10 minute samples. Two of the sample sets would be used for calibration data, and the last sample set would be used as validation data. The reference thermometers values were also recorded and automatically written to a csv-file on a separate laptop. The sample time was set to 10 minutes because previous thermistor calibrations found that the oscillating period of the fluid bath was approximately 1 minute, so 10 minutes would adequately encompass multiple periods of temperature oscillation. Next the temperature set point was changed and the process repeated at the new temperature. Figure 3.23 shows the thermistor calibration setup.

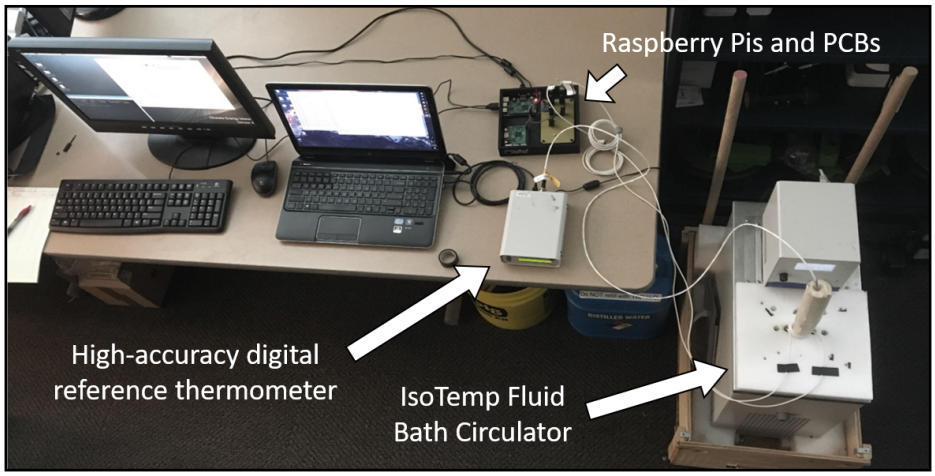

Figure 3.23: Bird's eye view of the thermistor calibration in the fluid bath circulator.

Figure 3.24 shows how the clamp-on 5k thermistors were placed inside a plastic bag and sealed to keep them from getting wet.

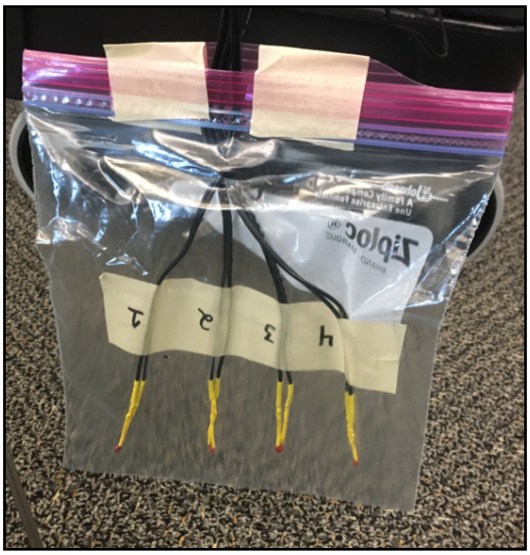

Figure 3.24: 5k thermistors inside of plastic bag to keep dry inside of the fluid bath circulator.

The python script `fluid_bath_calibration.py` was written to record the necessary data during the calibration process. The script starts by setting the sampling rate of the ADC board to its maximum speed (nominally 860 sps). When recording a voltage (using Equation 3.5), 200 samples are measured continuously and then averaged together before proceeding to the next channel. This is done in order to minimize any error due to noise or random spikes in the internal reference voltage during a single channel's recording. The *Raspberry Pi* first records the voltage across one entire voltage-divider branch, and then records the voltage across just one of the elements within it. The script later calculates the difference between the two to determine the voltage across the other element. Each voltage-divider branch's thermistor and shunt resistor were measured and recorded in a csv-file approximately every 2 seconds.

A post-analysis python script was developed using the *Jupyter Notebook* software. The script uploads each of the reference thermometer csv-files and the thermistor

voltage csv-files. If the time-stamps on the reference thermometer were noted to be offset (due to it not having a RTC), the time-stamps were corrected and synchronized with the time-stamps of *Raspberry Pi* thermistor voltages. Next the thermistors' resistances were then calculated using the methodology described previously (Equations 3.8 and 3.9).

The thermistors' resistances and reference thermometers temperatures were then grouped by nominal reference temperature and complete data sets were generated (3 samples sets at each temperature). Each thermistor's temperatures were then averaged and their standard deviations were calculated using the *Python* libraries `numpy` and `math`. Each thermistor's SHH-coefficients were then fit with the average resistance values and average temperature values from the first two data sets. Instead of using the GLS method, the *Python* function `scipy.optimize.curve_fit` was used to fit the dataset and solve for the coefficients. Table 3.3 shows the resulting SHH-coefficients for the six thermistors.

Table 3.3: Calibrated thermistor Steinhart-Hart Coefficients

Thermistor	**A**	**B**	**C**
Therm1 *(Clamp-on)*	0.001327313449	0.000227355566	$9.92649386 \times 10^{-8}$
Therm2 *(Clamp-on)*	0.001285879482	0.000232502734	$8.85692169 \times 10^{-8}$
Therm3 *(Clamp-on)*	0.001310288969	0.000229444096	$8.84628252 \times 10^{-8}$
Therm4 *(Clamp-on)*	0.001301712306	0.000230072896	$9.34578354 \times 10^{-8}$
Therm1 *(In-line)*	0.00145779807	0.000240555505	$8.86937580 \times 10^{-8}$
Therm2 *(In-line)*	0.00145048218	0.000242119326	$8.06398400 \times 10^{-8}$

The final sample at each temperature was then used as verification data. The error was calculated by finding the difference between the measured temperature and the reference thermometer. Figure 3.25 shows the calibration error plot for the in-line thermistors. Note that the final uncertainty was determined by adding the

reference thermometer's documented uncertainty with the error we measured relative to it during calibration.

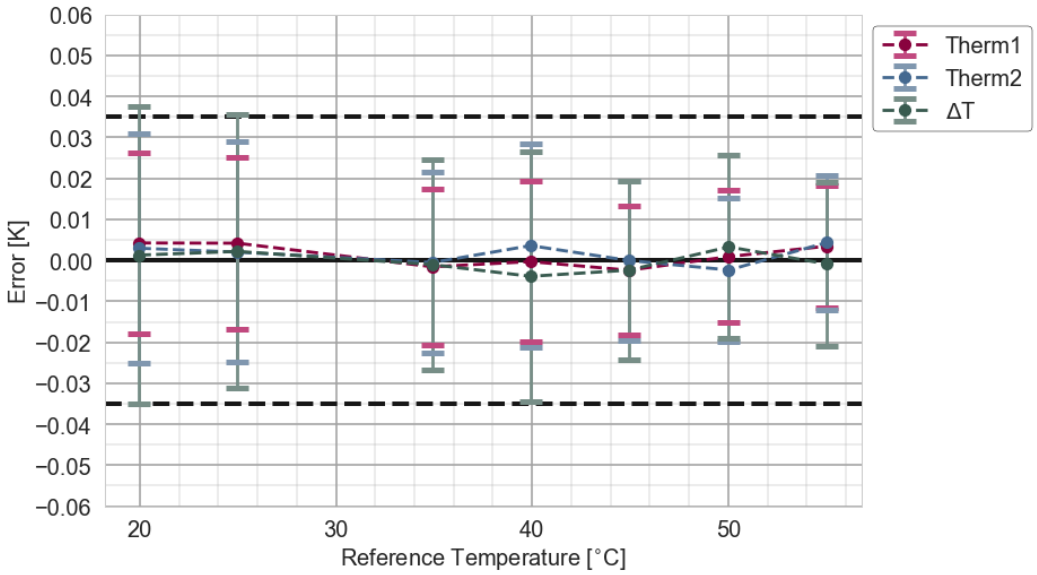

Figure 3.25: Error plot generated using the validation data from the in-line thermistor calibration.

Figure 3.26 shows the calibration error plot for the clamp-on thermistors. Note that the error (relative to the reference thermometer) for the water-side thermistors (Therm1 & Therm2) was ± 0.02 K (± 0.036 R) and the error for the air-side thermistors (Therm3 & Therm4) was ± 0.04 K (± 0.072 R).

Table 3.4 contains a summary of the final calibrated temperature sensors' uncertainties. Note that these include the calibrated uncertainties relative to the reference thermometer, plus the reference thermometer's documented uncertainty. The temperature measurements they would eventually measure on the validation test loop are also listed.

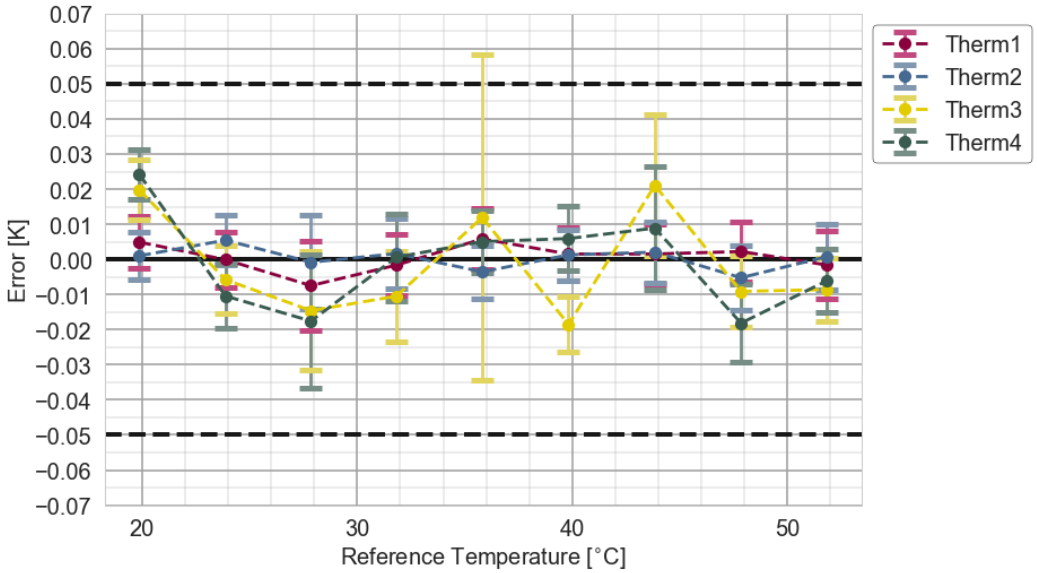

Figure 3.26: Error plot generated using the validation data from the clamp-on thermistor calibration.

Table 3.4: Finalized Thermistor Uncertainties and Test Loop Temperature Assignment

Thermistor Name	**Calibrated Uncertainty**	**Test Loop Temperature**
Therm1 *(Clamp-on)*	± 0.037 K (± 0.066 R)	EWT
Therm2 *(Clamp-on)*	± 0.037 K (± 0.066 R)	LWT
Therm3 *(Clamp-on)*	± 0.057 K (± 0.102 R)	EAT
Therm4 *(Clamp-on)*	± 0.057 K (± 0.102 R)	LAT
Therm1 *(In-line)*	± 0.047 K (± 0.084 R)	LWT
Therm2 *(In-line)*	± 0.047 K (± 0.084 R)	EWT

3.5 Flow Measurements

The flow rate of a fluid is a critical measurement when calculating the calormetric heat transfer achieved by a GSHP system. The following section describes the theory, design methodology, fabrication, and calibration procedure for the final flow sensor design.

3.5.1 Theory

There are several types of in-line flow meters, all aimed at calculating the flow of a given liquid. ASHRAE Standard 41.8 - *Standard Methods for Liquid Flow Measurement* [ASHRAE (2016)] provides a general summary of the various types currently used in the HVAC industry. In general, flow meters can be easily distinguished with two characteristics: 1) volumetric or mass flow measurement and 2) invasive or non-invasive.

Flow meters that measure the mass flow rate (e.g., thermal or Coriolis flow meters), make multiple independent sub-measurements in order to calculate the overall mass flow rate (e.g., density, volumetric flow, or temperature). However volumetric flow meters (e.g., turbine or differential pressure flow meters), only measure the volumetric flow rate and therefore require additional pressure, temperature, or density sensors in order to estimate the fluid's mass flow rate.

As discussed previously, invasive flow meters (e.g., turbine, differential pressure or vortex-shedding flow meters) must be installed in-line with the fluid in order to function properly. Invasive flow meters can be calibrated off-site and then installed, potentially without additional calibration required, since the instrumentation inside has not changed from its fixed orientation during calibration. However, while non-invasive flow meters (e.g. ultrasonic flow meters) can be installed externally on a pipe, they must be installed precisely and re-calibrated at each installation. As a result, non-invasive flow sensors are much more tedious to install and often more laborious to calibrate accurately.

Regardless of the flow meter type, it is common practice to install flow meters with a certain amount of straight pipe up-stream and downstream from the location they are measuring to the nearest fitting (e.g., elbow, reducer, expander, valve, etc.). This is done to ensure the fluid is well-mixed and the flow is fully developed. While the recommended amount of straight pipe may vary based on a manufacturer's internal

standards and the exact sensor type, most recommendations fall in the range between 20-50 pipe diameters up-stream and 5-10 pipe diameters down stream. The exact amount of straight pipe implemented should be verified with the manufacturer, as they do not always translate between sensor types.

Additionally, most flow meters come with a recommended flow range. This is often communicated by providing a *minimum*, *maximum*, and *continuous* flow rate on the specification sheet. Manufacturers will frequently provide measurement uncertainties based on what flow rate is being measured.

The two specific sensors investigated during this thesis were the in-line turbine flow meter and the ultrasonic flow meter. The turbine flow meter is an invasive, volumetric flow meter that functions through the interpretation of electronic pulses generated by a spinning paddle wheel. Basically, the fluid flow is directed into the meter's housing and forced to run into a paddle wheel inside. As the fluid flows through the meter, it causes the paddle wheel to rotate. As the paddle wheel is rotating, it causes an internal circuit to output a frequency of pulses on its signal wire (often by inducing a signal each time one of the paddle wheel's arms crosses over a magnetic pickup). As depicted in the plots of Figure 3.27, as the rate of volumetric flow increases, the paddle wheel spins faster and the frequency of the pulse output increases.

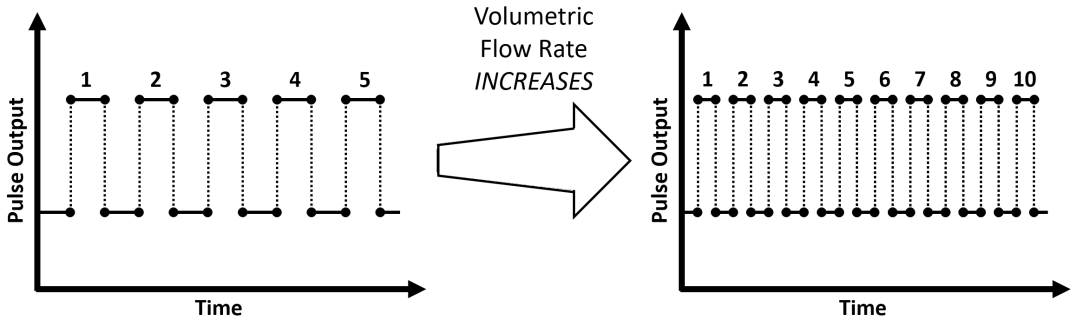

Figure 3.27: Typical pulse output of a turbine flow meter, depicting how pulse count increases proportional to flow rate.

These pulses are generally within measuring range of most micro-controllers' input pins (0 - 5 V). All that is required to measure them is a digital input pin and an

additional pull-up resistor (typically 1 - 10 kΩ). Figure 3.28 shows a simple circuit implementing a pull-up resistor to read a digital signal generated by a switch. Effectively the pull-up resistor functions to "pull" the voltage signal up to `HIGH` whenever the switch (or paddle wheel in this case) is open. If a pull up resistor was not implemented, the signal would just be "floating" when open. This could potentially cause false pulses to occur, should it float below the micro-controllers `LOW` threshold. Some micro-controllers also come with a programmable internal "pull-up" setting for their digital input pins. Implementing that feature would also be sufficient.

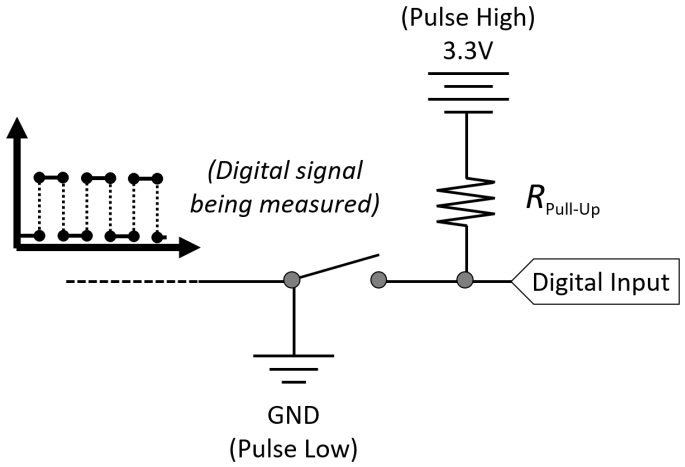

Figure 3.28: Typical pull-up resistor implementation for measuring a digital signal.

Most turbine flow meters come with a manufacturer's rated conversion constant to relate the number of pulses generated on the signal wire ("pulse" meaning both a *falling-edge* and a *rising-edge*), to a specific volumetric flow rate. Specifically Equation 3.10 is often utilized to convert the total pulse count (p) over a given time frame (t) to the volumetric flow rate ($\dot{V}$), using the conversion constant, k (often given in pulses-per-gallon or *ppg*). Manufacturers will often also give a measurement uncertainty for turbine flow meters based on the percentage of the measurement being read.

$$\dot{V} = \frac{p/t}{k} \tag{3.10}$$

Most turbine flow meters are also designed to have the fluid flow through them in a particular direction. It is important to verify that they are installed properly, otherwise significant error can occur. An arrow pointing in the direction of the intended flow is often indicated on the side profile of the meter itself (Figure 3.29).

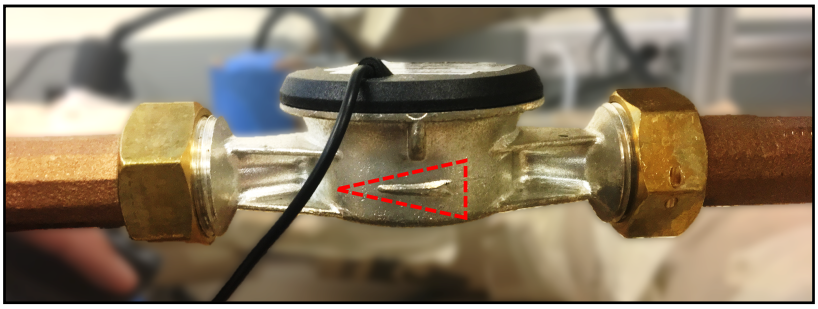

Figure 3.29: Picture of the profile of a turbine flow meter, emphasizing the indicated flow direction on the meter itself.

Ultrasonic flow meters come in both clamp-on and in-line forms. The non-invasive, clamp-on style was selected for investigation in this thesis at the start of the project, as they were considered the cheapest, non-invasive flow meter available at the time. Clamp-on ultrasonic flow meters function on the principle of acoustics. As pictured in Figure 3.30, the basic setup involves placing two ultrasonic transducers on a pipe of known dimensions and an acoustical signal is sent from one sensor to the other. When there is no flow, the time for the signal to go from one sensor to the other, in either direction is constant. However, when the liquid is flowing, the velocity of the liquid causes the ultrasonic signal to increase in speed in the direction of the flow and decrease in speed in the direction counter to the flow. This time difference is then correlated to flow, using the known fluid and pipe properties (e.g., density, inner diameter, outer diameter, etc.) and the transducer mounting orientation (V-method, Z-method, or W-method). As the cross-sectional diagram in Figure 3.30 illustrates, ultrasonic sensors should be mounted on the side of the pipe, so as to ensure the highest likelihood of avoiding signal interference, as a result of any air bubbles at the top of the fluid flow.

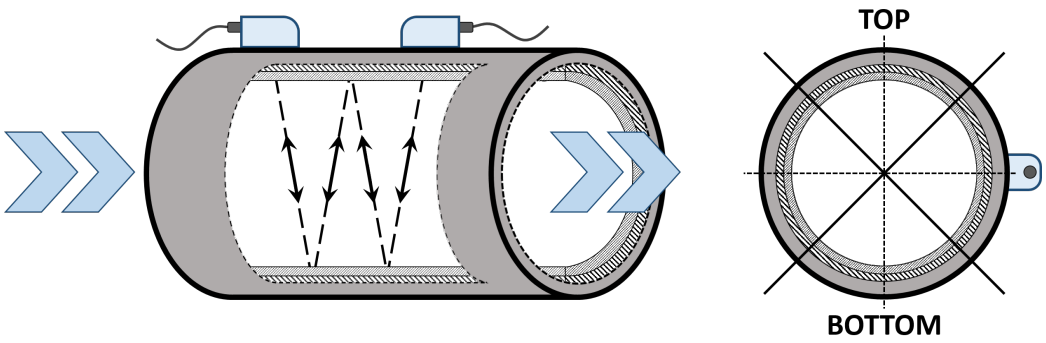

Figure 3.30: Diagram of ultrasonic flow sensors mounted on the side of a pipe using the W-method. (after *TUF-2000M-TS-2* manual)

Typically with ultrasonic sensors, there is no additional user-calculation required in order to calculate fluid flow rate. Most ultrasonic sensors either store the flow data internally, to be downloaded later, or output a 4-20 mA signal corresponding to the flow rate it is currently reading. A simple shunt resistor (typically 250 Ω) can be put across the 4-20 mA signal and its voltage recorded. The analog output settings on the meter will provide the conversion constant required to convert the 4-20 mA signal to volumetric flow rate.

3.5.2 Selection

A summary of the key design requirements and calculations used to select the aforementioned flow meters are discussed in this section. Figure 3.31 shows an overview of that design and selection process.

The three main criteria in selecting the in-line and clamp-on volumetric flow meters include flow range, pipe size, and cost. As previously discussed in Chapter II, the anticipated flow range for the validation test loop was originally between 0 - 10 GPM. Thus, flow meters capable of measuring that flow range, and namely those with a continuous flow at or near that flow range, were considered. Next, the ideal connection size for the flow meters was determined. Based on the need to match the pipe size of the validation test loop (1-inch NPT), meters that could clamp-on to 1-inch pipe

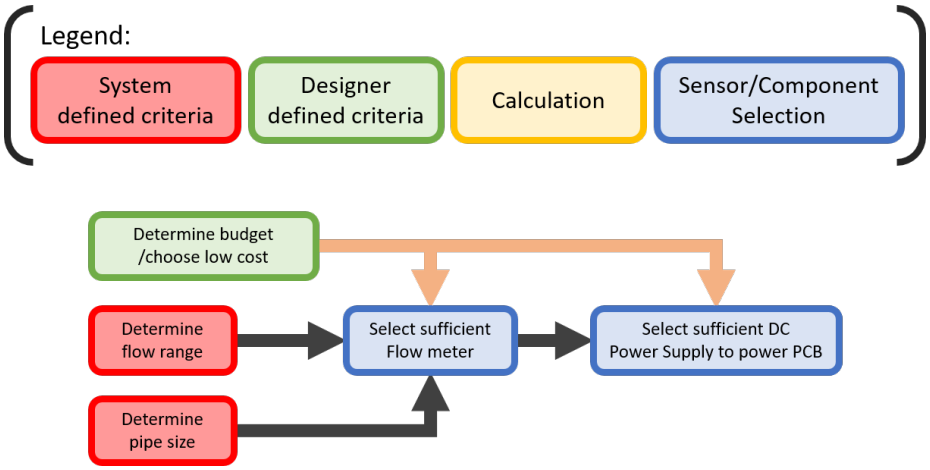

Figure 3.31: An overview of the design and selection process for the energy meter's flow meter.

or in-line meters that could easily be adapted to fit 1-inch adapters were considered. Lastly, the lowest costing sensor of those that remained was selected.

The turbine flow meter, selected for the in-line energy meter, was a *FTB-4607* turbine flow meter from *Omega*. It was a spare turbine flow meter, leftover from a previous project at OSU, and was within the desired accuracy for a "Grade 1" flow sensor (±3.5% of reading) (Zottl et al. (2011)). Specifically the *FTB-4607* is rated for flows between 0.22 GPM (minimum) and 20.0 GPM (maximum). At flow rates between 0.22 GPM and 1.1 GPM, the rated accuracy is ±2% of the reading. At flow rates above 1.1 GPM, the rated accuracy is ±1.5% of the reading. Its nominal conversion constant was 75.7 pulses-per-gallon.

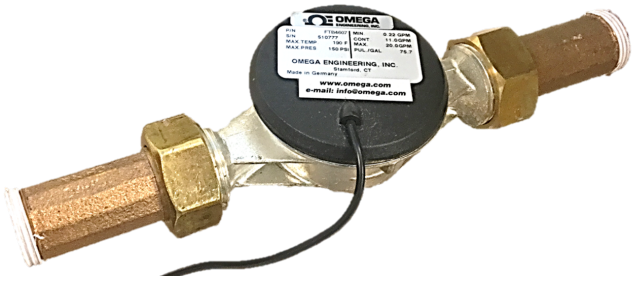

Figure 3.32: Picture of *FTB-4607* turbine flow meter.

As seen in Figure 3.32, the *FTB-4607* comes with the necessary union fittings for

easy replacement, and 3/4-inch ports with male NPT. It also comes with two O-rings (not pictured), to be used to help seal the union fittings. Two additional 1-inch to 3/4-inch pipe adapters were purchased to allow it to be threaded into the test loop 1-inch pipes. Furthermore, as seen in the wiring schematic in Figure 3.33 the *FTB-4607* requires an additional 9 - 16 VDC external power supply to power the output pulse signal. It also requires a pull-up resistor to positive DC voltage.

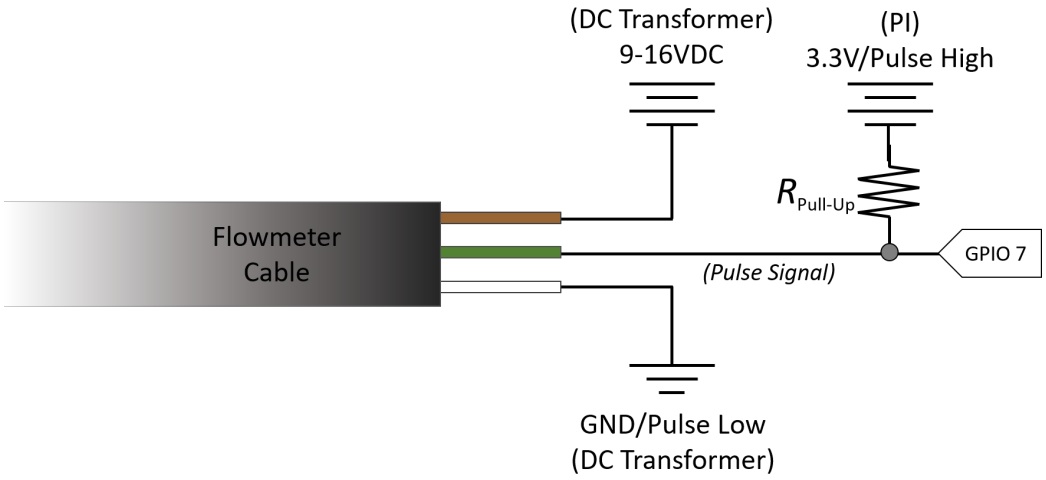

Figure 3.33: Wiring schematic for the *FTB-4607* turbine flow meter.

A spare 12 VDC charger was used to provide the external DC power supply and ground to the flow meter. One of the digital pins on the *Raspberry Pi* was allocated for the GPIO interrupt pin and a pull-up resistor of nominally 10 kΩ was used. A high resistance value was chosen, so that a low current would flow through the resistor and keep the power draw low.

At the start of the project, an ultrasonic flow meter was originally selected to be the specific type of flow sensor the clamp-on meter would utilize. This was because ultrasonic sensors were considered the current standard for non-invasive fluid flow metering. When the time came to purchase an ultrasonic flow meter, several sensors were investigated and it became apparent that most of the commercially available clamp-on style ultrasonic meters (rather than the in-line style) were quite expensive (between $1,000 - $6,000). In an effort to stick to the design goal of "cheap/affordable", we

decided to continue looking for cheaper ultrasonic meters. Eventually the *TUF-2000M-TS-2* ultrasonic meter kit was found for only $215 and purchased off of *Amazon*. According to the specifications given on *Amazon* (and the online manual), it was capable of measuring flow with an accuracy of better than 1% of the reading and was rated for pipes between 3/4-inch to 4-inches. As recommended, some additional acoustical couplant was purchased and would later be applied between the copper pipes and the transducers. Lastly, a 12 VDC power supply was stripped and adapted to power the display and electronics. A 250 Ω burden resistor was also found to allow for reading of the 4-20 mA output signal.

3.5.3 Fabrication

As mentioned in Chapter II, the *FTB-4607* turbine flow meter was installed in-line during the test loop fabrication process. The direction of the arrow on the flow meter was double checked after installation to confirm appropriate direction of flow through the meter. Additionally, the circulation pump was turned on and the flow meter output signal was monitored on an oscilloscope to verify it was working properly (Figure 3.34).

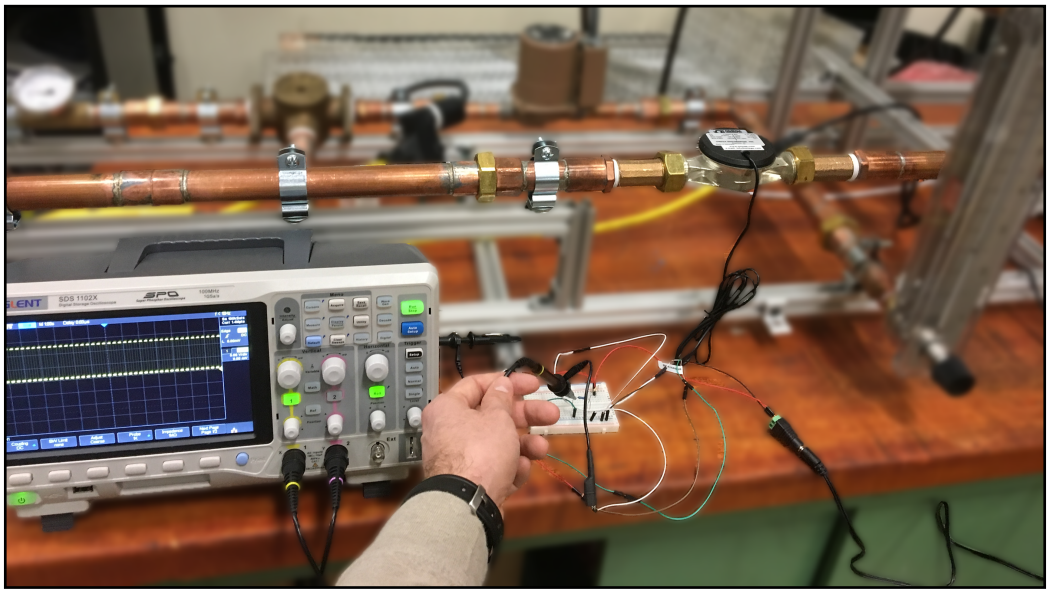

Figure 3.34: Initial flow meter test, verifying functionality of pulse output.

The pull-up resistor and necessary wires were then soldered into a PCB board. The flow meter signal and power wires were appropriately fit with male DC barrel jack adapters and their female mates were soldered into the PCB board to allow for easy plug-and-play capabilities. The final PCB for the in-line meter is seen below in Figure 3.35.

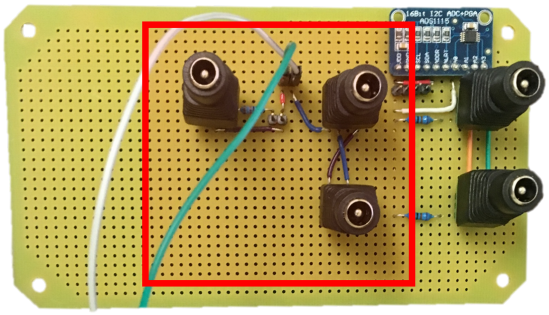

Figure 3.35: Finalized PCB for in-line energy meter (with flow meter components highlighted).

While chronologically, the ultrasonic flow meter was not installed or tested until after the turbine flow meter was completely installed and calibrated, the installation process for the *TUF-2000M-TS-2* ultrasonic flow meter is described here. The locations of the up-stream ultrasonic transducer was marked on the copper pipe with a pen. As the manufacturer recommended, it was 10 pipe diameters (approximately 10-inches) away from the in-line meter (the closest change in pipe up-stream). The pipe's outer diameter (1.122 inches) and its wall thickness (0.0512 inches) were measured and input as parameters to the meter. The ultrasonic meter then calculated and displayed the necessary amount of space between the two transducers using the W-method (1.161 inches). The second (down-stream) transducer location was marked and then verified to be more than 5 pipe diameters (approximately 5 inches) away from the next fitting down-stream. The respective locations on the pipe were prepared by cleaning the pipe surface with abrasive, open-mesh sand cloth (180 grit). As seen in Figure 3.36 the transducers were then clamped into place on the side of the pipe, using a custom, 3D-printed alignment tool, acoustic couplant, and zip-ties.

The meter was left untouched overnight, to allow the couplant to cure. The next day, we turned the circulation pump on and worked to verify that the ultrasonic meter's self-diagnostics were within their acceptable range.

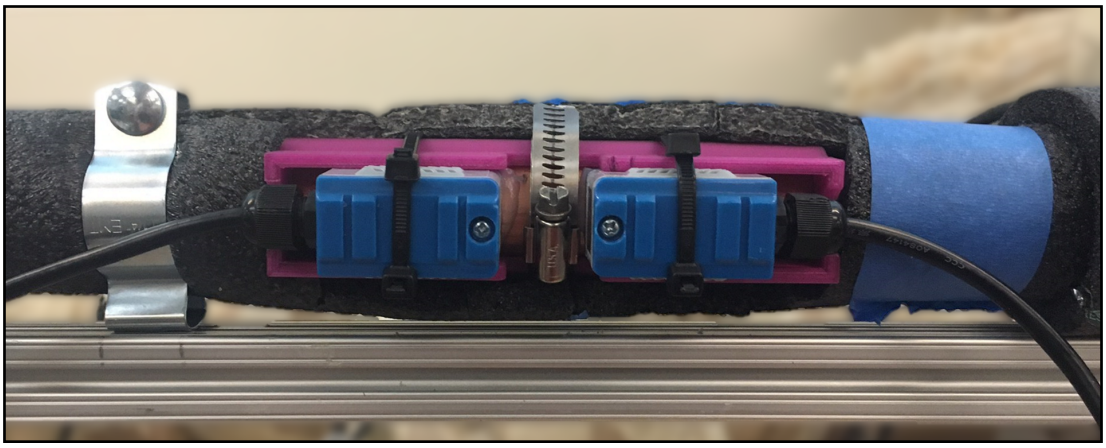

Figure 3.36: Picture of the ultrasonic transducers mounted on the test loop.

Unfortunately, even after fine-tuning the orientation of the transducers, a stable, accurate reading was never able to be attained. Specifically, the ultrasonic flow meter has a menu (*Menu 90*), in which its signal "Strength" and "Quality" parameters are displayed. After consulting the manual, as well as contacting its technical support team for assistance, it was confirmed that the required signal strength and quality measurements must be within 60.0 - 99.9 and 60.0 - 90.0 respectively. We were able to attain an up-stream and down-stream signal strength that stayed between 70.0 - 80.0, and a signal quality that stayed between 78 - 81 initially. However, after the couplant cured, the signal would fluctuate and then slowly decrease to 0 after about 15 minuets. During the time frames when the quality remained in the recommended range, flow readings continually fluctuated and were as much as 2.0 GPM away from the actual flow rate that the system was operating at (operating at 2.1 GPM). Appendix B describes the investigation undertaken to trouble shoot the low-cost ultrasonic flow meter, part of which involved recording the raw flow readings from the ultrasonic flow meter and averaging them overtime. However, this did not prove effective and the ability to maintain an unchanging "quality" reading that was within the required

range was never achieved.

Based on the inability to achieve accurate and stable readings from the most-affordable, clamp-on ultrasonic sensor we found, we decided that until advances in non-invasive flow technology made the price of more accurate sensors cheaper, or until problems with our low-cost ultrasonic flow transducer were resolved, we would need to measure flow via an alternative means. Other potential non-invasive flow measurement techniques include: accessing the flow measurements made by the heat pump controls, measuring and then correlating the circulation pump power to the system's corresponding flow rate (unlikely to be very effective), or simply assuming a constant flow rate in the system. However, for the sake of this thesis project, we decided that the data from the in-line flow meter would be shared by both the clamp-on and in-line energy meters.

3.5.4 Calibration & Validation

The *FTB-4607* turbine flow meter was calibrated using the "stopwatch and bucket" method. A few pictures showing the setup can be found on the next page in Figures 3.37 and 3.38.

Once the flow meter was installed and in place, the verification test loop was moved to an area that could get wet. In its new location, the closed loop was opened by turning the 3-way valve, such that it only allowed flow from the fill-port towards the circulating pump. The loop was opened on the opposite side of the 3-way valve by removing the cold-side thermistor port's plug. A 1/6 HP submersible pump was then used to pump distilled water through the loop out of a 5-gallon bucket. As water flowed from the 5-gallon bucket, up through the fill-valve and around the loop, it eventually came out the cold-side thermistor port and re-collected back into the 5-gallon bucket. Then, the rotameter's screw valve was adjusted to the nominal flow rate about to be measured. A second, empty 5-gallon bucket was then used to

Figure 3.37: Picture of "stopwatch and bucket" method.

Figure 3.38: Bird's eye view during 3rd flow meter calibration.

collect water flowing out of the thermistor-port. A timer was started simultaneously and then stopped, when the bucket was almost full. Occationally, additional water needed to be added to the first 5-gallon bucket, so multiple people were required. All the while filling up, the number of pulses from the flow meter were being counted by the micro-controller. The second bucket's weight before and after each flow rate's sample was measured and recorded using a *TI F9020a Electronic Scale* (accurate up to 0.5% of the reading ± 1 digit). The fluid's temperature was also measured with a *ThermoProbe Inc. TL1-A* thermometer (accurate up to ± 0.06 °C (± 0.1 °F)) in order to later calculate the density of the water in the bucket. Six different flow rates, ranging from 1 GPM - 3.5 GPM, were sampled three times each. Two of the data sets at each flow rate were used for calibration and the third was used as a validation data set.

The python script `flowmeter_calibration.py` was written to continuously count

edges (both *rising* and *falling*) detected on the specified GPIO pin (Pin 7). Specifically it utilizes an interrupt function and a global `edge_counts` variable to do so. The final script found in Appendix C, is the product of multiple iterations from lessons learned throughout the calibrations. The finalized python script records the cumulative sum of edges every 5 seconds, but does not zero the `edge_counts` variable each time it writes to the csv-file. Instead, it keeps track of the total running number of edges detected over the course of that particular flow rate's sample time, and then records the starting and ending time-stamps. The main reason for storing the total cumulative edge count is ultimately to achieve a higher resolution of pulses per gallon, by recording over the entire sample period. It was found that as many as 100 edges were lost in entire flow rate data sets when the counter was zeroed after logging the previous 5 seconds' data in the csv-file.

After all 18 data sets were collected, they were combined into one *Excel* workbook. As mentioned before, the first two samples at each of the 6 flow rates were used to calibrate the flow meters pulses-to-gallons ratio (k). The temperature of the water at the end of each test was entered into *Engineering Equation Solver* to generate the corresponding density of water at 1 atm (101.3 kPa). Equation (3.11) was used to generate the volume of water collected in the bucket. The pulses-per-gallon ratio was then calculated using Equation (3.12) (a re-arranged version of Equation (3.10) from before). Lastly the actual flow rate was calculated using Equation (3.13).

$$V = m \cdot \rho(T, P) \tag{3.11}$$

$$k = \frac{(\text{total edges})/2}{V} \tag{3.12}$$

$$\dot{V}_{\text{ref}} = \frac{V}{(t_f - t_0)} \tag{3.13}$$

The resulting pulses-per-gallon ratio (k) for the flow meter was 77.202 ppg. This is slightly greater than the manufacturer's stated ratio (75.7 ppg). Effectively that

means that we found the turbine wheel spins more easily than the manufacturer suggests in our flow range. The discrepancy could be a result of the flow meter being rated for continuous flow classified as 11 GPM, while our loop operates in the range between 1.0 - 3.0 GPM. The last sample at each of the flow rates was used as validation data to create the error plot (Figure 3.39).

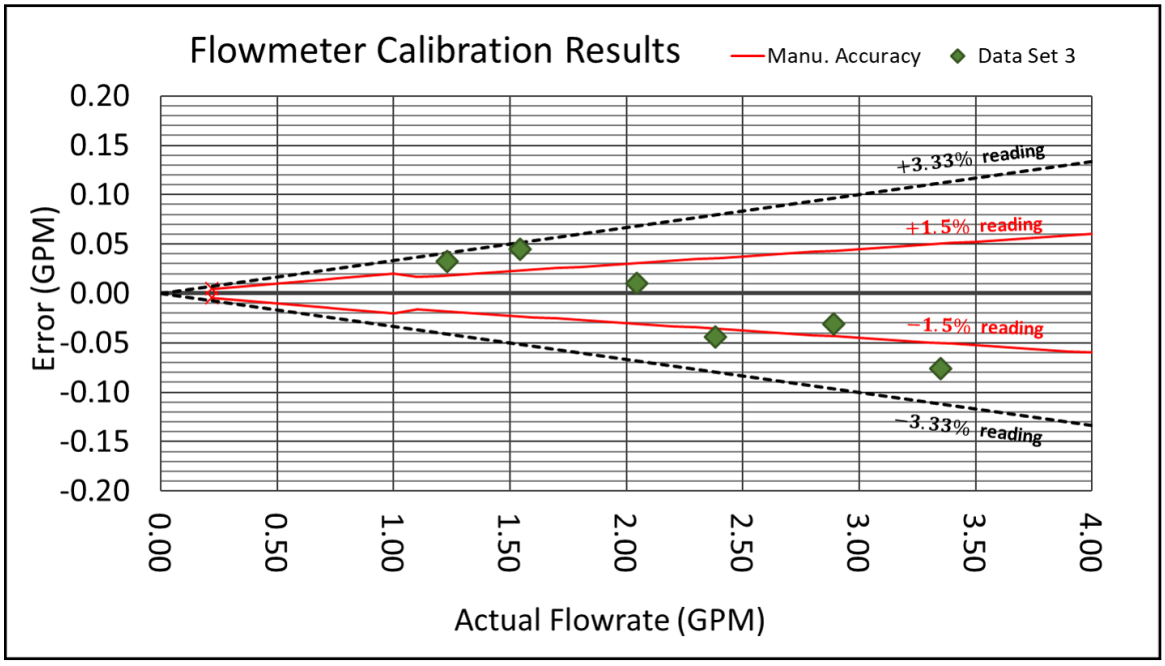

Figure 3.39: Error plot showing the results of the flow meter calibration.

Table 3.5 contains a summary of the calibrated flow meters' characteristics and uncertainty.

Table 3.5: Finalized Flow Meter Uncertainty

Flow Meter	**Type**	**Calibrated Uncertainty**
FTB-4607 *(In-line)*	Turbine / Paddle-wheel	± 3.33 % of reading
TUF-2000M-TS-2 *(Clamp-on)*	Ultrasonic (Clamp-on)	± 2 GPM

3.6 Power Measurements

Home electrical energy monitoring has increased in popularity and implementation significantly since the mid-2000s [Zhou et al. (2016)]. As a result there are a multitude of energy meter's available online. Additionally, there are a plethora of instructional websites for building your own power-meter. Specifically, `OpenEnergyMonitor.org` was found to be the most useful during the development of our energy meter [Open Energy Monitor (2018)]. Their electricity monitoring resources are based on standard electrical characteristics in the United Kingdom, but the fundamental design principles are applicable to electricity monitoring here in the U.S. too.

The main components of an electrical energy meter are a voltage transformer (VT) and a current transducer (CT). The following section describes the basic theory, design methodology, fabrication, and calibration procedures of the current and voltage sensors developed for the clamp-on energy meter.

3.6.1 Theory

For the purposes of measuring electrical power consumption in residential & commercial HVAC applications, the loads being measured come solely from equipment plugged directly into a wall outlet or otherwise connected to "domestic power" (also commonly referred to as "wall power", "household electricity", "Mains electricity", etc.). As a result, the specific type of electricity needing to be measured will be alternating-current (AC) electricity, rather than direct-current (DC) electricity.

3.6.1.1 Alternating Current Power

AC electricity can be characterized generally via its voltage and frequency. Specifically, most domestic power supplies around the world range between 100 - 240 V

and the most common frequencies are 50 Hz and 60 Hz. For the purposes of this thesis, the U.S.' domestic power characteristics are used as design parameters: 60 Hz frequency and 120 V/240 V. Since most heat pump units operate off of 240 V, our initial approach was to simply double the voltage measured at the nearest 120 V wall outlet. This effectively approximates the voltage across both legs of the utility power (which is what 240 V outlets are connected to). Eventually the final design should be sized to measure the 240 V directly. Household AC voltage and frequency are commonly regulated by the local utility or electricity provider.

The characterization of AC power drawn from a particular piece of equipment is often classified based on if it is purely resistive or if it has inductive or capacitive components in it as well. As seen in Figure 3.40, the voltage and current waveforms will be perfectly in sync if a load is purely "resistive" (e.g., water heater elements). Furthermore, the instantaneous power (voltage · current) of a purely resistive device will always be positive. However, "reactive" loads (e.g., circulation pumps, fans, compressors, etc.) on the other hand are composed of inductive and/or capacitive components, in addition to resistive components. The resulting voltage and current signals will consequently be shifted slightly out-of-phase from each other. This "phase shift" causes the instantaneous power to become both positive and negative (Figure 3.40).

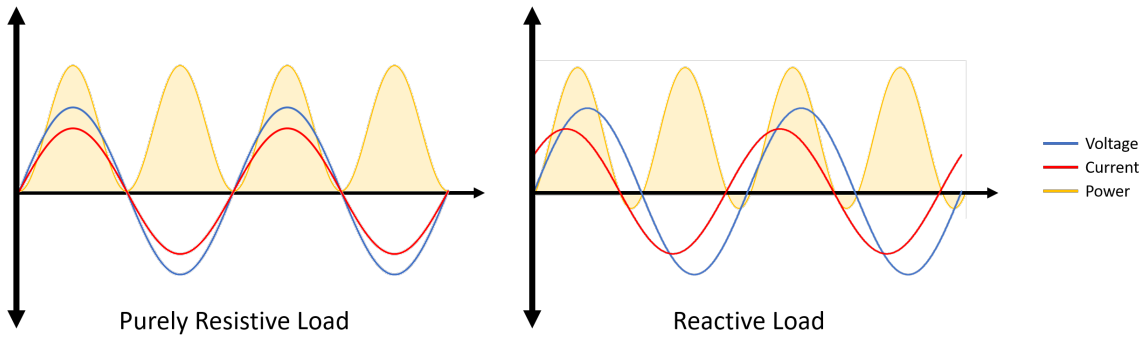

Figure 3.40: Plots showing the difference between equipment with resistive and reactive power loads. (after `www.learn.openenergymonitor.org/electricity-monitoring`)

Particularly when working with reactive loads, it is helpful to define the components that make up the overall power measurement. A common diagram used to show the components that make up AC power is the "Power Triangle" (Figure 3.41).

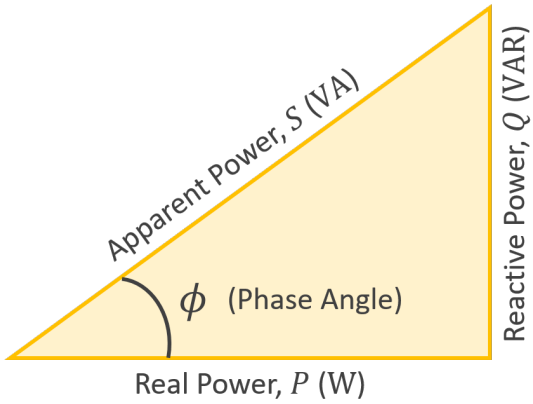

Figure 3.41: Diagram showing the relationship between Real, Reactive, and Apparent power measurements.

The "real" (or "active") power (P) is the measurement of the actual electrical power being consumed by a piece of equipment to do work. The "reactive" power (Q) corresponds to the power that is not actually consumed by the equipment, but oscillates back and forth between the load and the supply. Typically electricity suppliers will track reactive power and can potentially charge a "Reactive Power Charge" in their monthly utility bill, since that "extra"/"unused" electricity requires "bigger" electric lines and transformers to support the extra current. Finally, the "apparent power" (S) is a measure of both the "real" and "reactive" power. Essentially, this is power measured with the full effect of the phase shift taking place. Equations (3.14) through (3.16) show the mathematical relationship between the three forms of power measurement. As an alternative to directly calculating the phase shift (ϕ) of a reactive load, it is common to report the "Power Factor" ($\cos\phi$), as shown in Equation (3.17).

$$S = V_{\text{RMS}} \cdot I_{\text{RMS}} \tag{3.14}$$

$$P = (V_{\text{RMS}} \cdot I_{\text{RMS}}) \cdot \cos\phi \tag{3.15}$$

$$Q = (V_{\text{RMS}} \cdot I_{\text{RMS}}) \cdot \sin\phi \tag{3.16}$$

$$(\cos\phi) = \frac{P}{S} \tag{3.17}$$

Note that these measurements are calculated using the root-mean-square (RMS) voltage and RMS current. Equation (3.18) shows the numerical formula that should be used with n-discrete data from a current or voltage sensor to calculate the "true-RMS" of that value.

$$X_{\text{RMS}} = \sqrt{\frac{\sum_{j=0}^{n} (X_j)^2}{n}} \tag{3.18}$$

Another common way to measure an electric signal is to record its "peak" measurement. However, as Figure 3.42 illustrates, the peak value is not equivalent to the RMS value. While the peak value can be used to calculate an approximation of the RMS value (Equation 3.19), if the waveform is not perfectly sinusoidal, then error will be introduced. For this reason, if there is sufficient time between samples to measure the entire waveform, it is preferred to calculate the "true-RMS" voltage/current, rather than to approximate it with the "peak" measurement.

$$V_{\text{RMS}} = \frac{1}{\sqrt{2}} V_{\text{P}} \tag{3.19}$$

The simplest power measurement to attain is apparent power (S), because all that is required is the RMS-current and the RMS-voltage. This is sufficient for resistive loads, since their power factor is unity ($\phi = 0°$). However if a reactive load is being measured, then measuring just the apparent power will overestimate the true power consumption of the device. While apparent power is simplest to measure, real power (P) is the measurement most commonly used in HVAC applications, since it takes

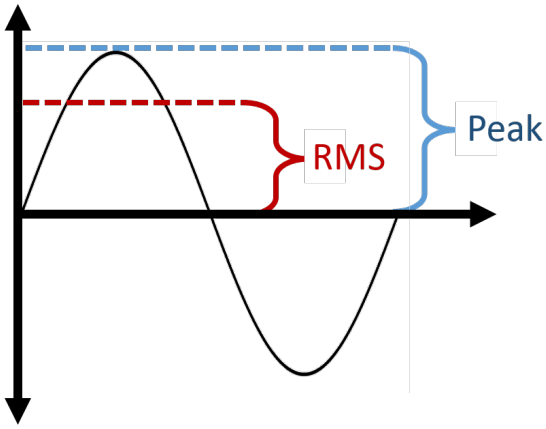

Figure 3.42: Plot showing the difference between a RMS measurement and a Peak measurement.

into account only the true amount of AC electrical power consumed by the device. In order to calculate real power, the phase shift (or power factor) must be known. There are several methods to calculating this, depending on what data is collected. If both the voltage and current signals are measured fast enough and with accurate time-stamps, then Equations (3.20) and (3.21) could be used to fit the data to recreate their waveforms and determine the phase-shift (ϕ).

$$V(t) = V_{\mathrm{P}} \cdot \sin(\omega t) \tag{3.20}$$

$$I(t) = I_{\mathrm{P}} \cdot \sin(\omega t + \phi) \tag{3.21}$$

The inherent obstacle in doing this with a single micro-controller is that only one measurement can be made at a time. Therefore, a key assumption that the wave forms do not significantly change in magnitude, phase, or frequency while you are recording the voltage signal and the current signal separately is essential. Additionally, depending on the processing speed of the micro-controller, performing these phase-shift calculations could take more than a few micro-seconds and thus increase your overall required sample time.

For the purposes of creating an initial prototype clamp-on energy meter that

could measure electrical power, simply measuring apparent power ($V \cdot I$) was pursued initially. As discussed in later chapters, this was sufficient for our set up, since the test loop's electrical water heater elements were purely resistive, and therefore their apparent power measurement was the same as their real power measurement.

3.6.1.2 Voltage Transformers

The fundamental goal through both VTs and CTs is to reproduce the signal of interest at a magnitude sufficient for a an ADC board to measure. This is done most often through the utilization of the physics principle of inductance. As a current flows through a wire that in placed inside a magnet, an equivalent current can be induced in a secondary wire that is wrapped around the same magnet. The induced current will be "stepped-down" proportionally to the number of turns in the secondary coil.

Specifically VTs are manufactured with multiple specifications. Most commonly, VTs are classified by their input (or "primary") voltage rating and their output (or "secondary") voltage rating at a given amp load. An additional specification that is helpful to know, but should always be verified before further designing the VT into a circuit, is its secondary "no-load" rating (NLR). This communicates what the expected output voltage should be when less than the rated amp load is being drawn. The ratio between this "stepped-down" voltage and the wall voltage will need to be characterized later through calibration, in order to be able to relate the two. Equation (3.22) shows the ideal relationship between the induced voltage ($\widetilde{V}$) and the actual wall voltage (V).

$$V = (\lambda) \cdot \widetilde{V} \tag{3.22}$$

In the case that the VT's "stepped-down" voltage is still too high for the ADC to measure, a voltage-divider circuit can be implement to further reduce the voltage to a measurable magnitude. However, since this signal is AC voltage, in order to record the entire waveform, a DC offset (or "bias") voltage must be applied, so that

the entire signal will be positive (relative to GND). Furthermore, in order for just the true transformed AC signal to be measured, instead of measuring the signal plus the DC-offset, the voltage recorded should be the difference between the transformed signal and the DC-offset voltage (depicted in Figure 3.43).

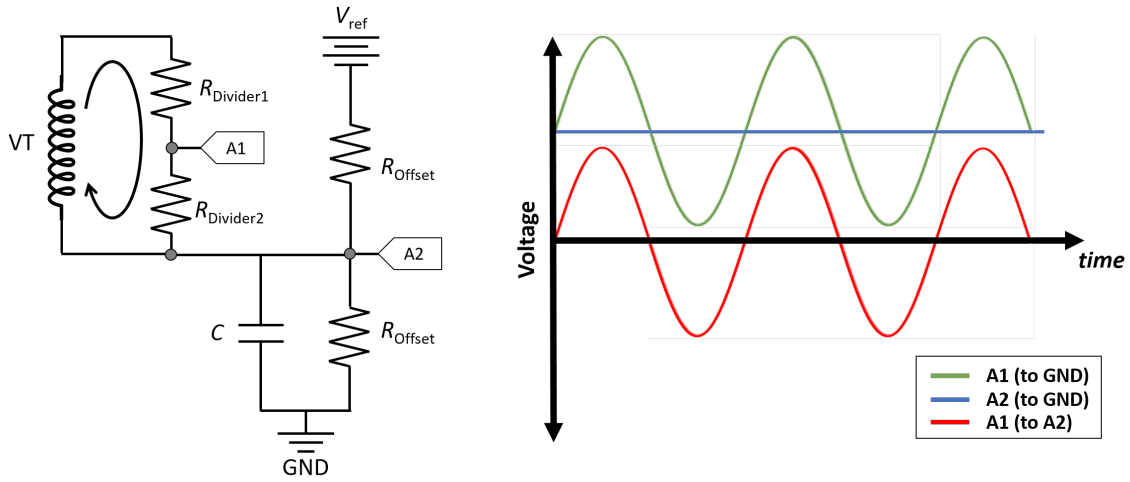

Figure 3.43: Typical circuit to measure the output voltage from the secondary coil of a voltage transformer. (after `www.learn.openenergymonitor.org/electricity-monitoring`)

Some ADC boards are capable of instantaneously measuring the voltage difference between two inputs, rather than requiring the difference between two independent measurements be calculated secondarily. Measuring the difference between two inputs is preferred, since two independent measurements would not be simultaneous. (If this is not possible, then a different method should be used to rectify the AC signal with a rectifier and RC-circuit. The rectified DC signal would need to be calibrated in order to map the DC measurement to its corresponding AC measurement). Figure 3.43 shows the typical circuit design implemented to accomplish this differential measurement.

When sizing the DC-offset voltage circuit it is common to choose high resistance values (R_{offset}) compared to the other resistors in the circuit. Additionally, selecting high resistance values for the DC-offset will minimize the quiescent energy consump-

tion when the circuit is powered up each time [Open Energy Monitor (2018)]. The capacitor is implemented to keep the DC-offset as steady as possible. It is typical to choose a capacitor that has a low reactance (often only a few hundred ohm), so that the current flow in the circuit is less impeded. Equation (3.23) below shows the equation to calculate the reactance of a capacitor (X_{C}), given a specific signal/supply frequency (f) and capacitance (C).

$$X_{\mathrm{C}} = \frac{1}{2\pi f C} \tag{3.23}$$

3.6.1.3 Current Transducers

Similarly CTs are manufactured with multiple specifications. Most commonly CTs are classified by their input current range, their "turns ratio", and whether or not they are "split-core" or "solid-core." The input current range is often physically set by the CT's two-way protection diode that prevents any current above a certain amount from passing through the circuit in either direction before breaking. The "turns ratio" is determined by the approximate number of loops (L) inside the CT. This relationship, expressed in Equation (3.24) is an approximation that should be verified through calibration.

$$I = (L) \cdot \widetilde{I} \tag{3.24}$$

As illustrated in Figure 3.44, CTs often are made in two different styles. A solid-core CT must have the wire it is measuring strung through its loop, which requires de-energizing the system for safety reasons, and often must be installed by a certified electrician. Split-core CTs on the other hand, separate and can open up like a "jaw", in order to clamp around the wires being measured. This is preferable for our application, since live wires are never tampered with and thus no electrician is required.

As a result of CTs inducing a current, a resistor with known resistance must be put

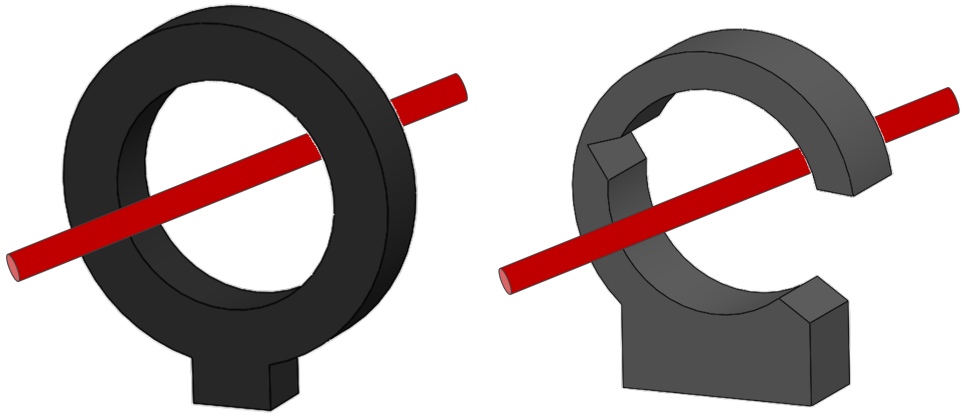

(a) (b)

Figure 3.44: Example showing the difference between solid-core (a) and split-core (b) current transducers.

across the CT's secondary wires, in order to produce a measurable voltage. While some CTs require this "burden" resistor be sized and implemented appropriately, some CT manufacturers size and install their own burden resistor (often specified as the "internal burden resistor"). Those with an already installed burden resistor often also provide the corresponding output voltage range. If a resistor (or other energy dissipating component) is placed across the output wires, but the circuit is not grounded, when the CT becomes clamped, any induced current will have no where to go and the CT will effectively become a charged capacitor. This creates a dangerous potential to charge the CT and cause an electric shock or arc when the circuit is eventually grounded. In an attempt to prevent this possibility of a floating capacitor, it is standard practice to never close a CT until it has been successfully grounded into its circuit.

Similarly to the common method of measuring a VT's analog output, Figure 3.45 shows a CT's typical circuit implementing a constant DC-offset voltage as well. Note that the offset resistors and capacitor are sized using similar conventions.

Lastly there are a few helpful tricks that help to achieve the highest quality signal when using a CT. Specifically with a split-core CT, in order to induce the best quality

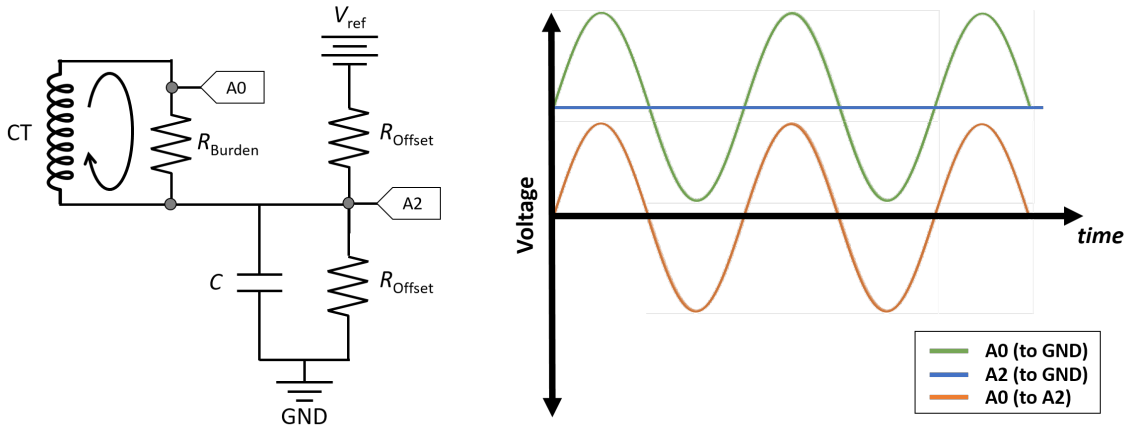

Figure 3.45: Typical circuit to measure a current transducer's output current. (after `www.learn.openenergymonitor.org/electricity-monitoring`)

signal, the split-core magnet must be properly clamped together. Occasionally the amount of wires put through a CT can become so thick that it can result in straining the magnet and can negatively influence the induced signal. Thus, the CT should be easily clamped shut and not under heavy strain. Additionally, it is important to note that the measured cable going through a CT must only contain either the live wire or the neutral wire, but not both. This is important since the fundamental electromagnetic principle at work involves the *net* sum of all the currents flowing through the magnet. Thus, if both the live and neutral wires are put through the CT, then current will be flowing through the CT in both directions, effectively canceling out each other's induced signal. Another helpful trick to magnify an induced current signal, is to loop the measured wire through the CT multiple times. Again, it is important that you loop the wire through the correct direction, so that the opposite facing wires do not end up canceling each other out.

3.6.2 Selection

A summary of the key design requirements and calculations used to size the aforementioned components in the voltage and current circuits are discussed in this section. Specifically the VT, CT and their shunt resistors and burden resistors respectively, are sized and calculated. Figure 3.46 shows an overview of the design and selection process followed.

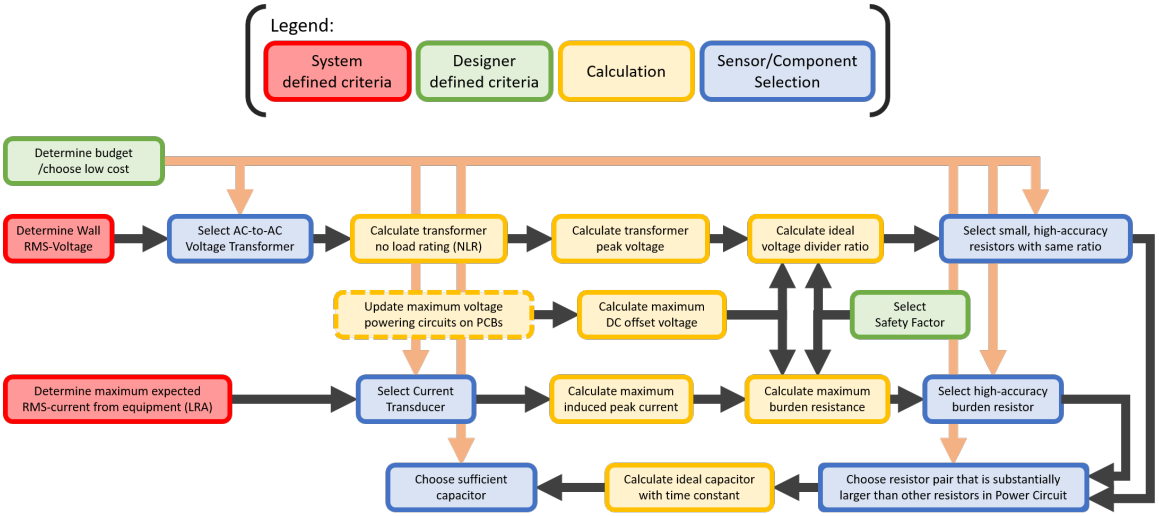

Figure 3.46: An overview of the design and selection process for the energy meter's power voltage and current sensors.

3.6.2.1 Voltage Transformer Selection

To start the sizing of the VT, the maximum expected RMS-voltage was determined. As mentioned previously, the U.S. standard wall outlet voltage was selected as the design voltage (120 V). Next, several VTs were researched and ultimately 120VAC-to-9VAC VTs were purchased. Note that 9 VAC was determined to be a low enough voltage to safely implement a voltage-divider on in the lab. Figure 3.47 shows the two specific brands of VTs purchased, *HQRP* and *Triad Magnetics*. These VTs selected have a rated amp draw of 1.2 - 1.3 A.

Figure 3.47: Picture of the two 120 VAC-to-9 VAC VTs implemented in the voltage sensors (Triad Magnetics and HQRP).

Upon arrival, the VTs were plugged in the wall and their NLR measured with a hand-held multimeter. They each had a NLR above their rated 9 V output voltage (approximately 12 V_{RMS}). The RMS-voltage was then converted to peak-voltage using the approximation mentioned previously (Equation 3.19). Next since 5 V was already the designed power supply for the PCB, the simplest DC-offset voltage by a voltage divider from two identical resistors would provide 2.5 V DC. This means that the peak of the induced voltage signal must remain less than 2.5 V, in order for the entire signal to remain positive. The exact resistors and capacitor implemented in the DC-offset will be discussed later. Equation (3.25) was then used to estimate the ideal voltage-divider ratio that achieves this maximum induced peak-voltage ($\widetilde{V}_P$), with a specified safety factor (SF).

$$\left(\frac{V_{\text{Divider2}}}{V_{\text{Divider1}}}\right) = \frac{V_{\text{Offset}}}{\widetilde{V} \cdot (SF)} \tag{3.25}$$

The resulting ideal voltage-divider ratio, with a 1.25 safety factor, was calculated to be approximately `0.124`. Then, the available high-tolerance burden resistors we had in the lab were examined. The closest set of resistors that could be combined to

achieve the desired ratio were a 1.4 kΩ resistor for R_{Divider2}, and a 1.5 kΩ in series with a 10 kΩ resistor to make up R_{Divider1}. The actual voltage-divider ratio with these resistors comes out to about `0.109`. Figures 3.48 and 3.49 show the plots generated to confirm that the induced current and measured voltage across R_{Divider2} and the 2.5 V DC-offset, would not exceed the ADC board limit.

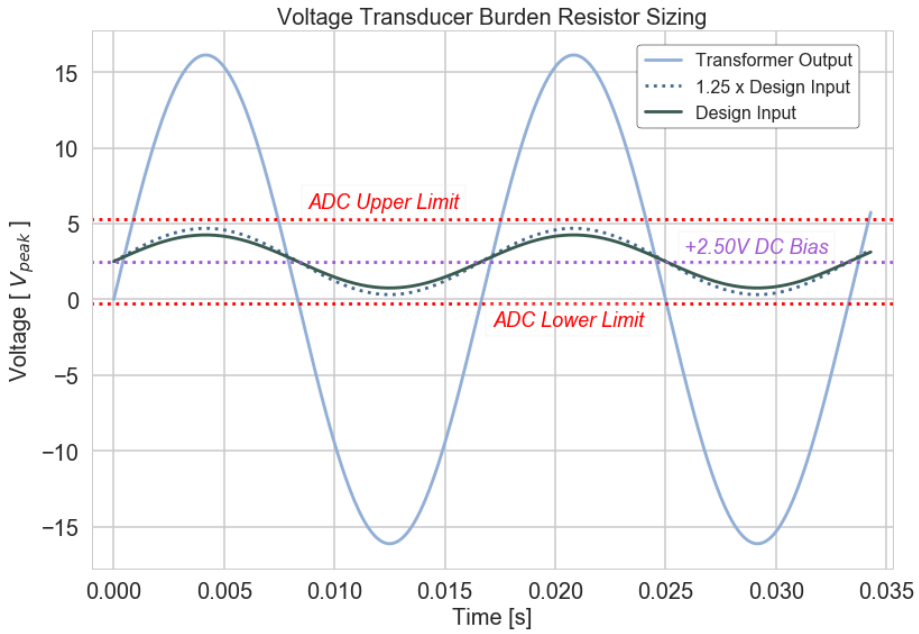

Figure 3.48: Plot of the expected induced voltage and the measured voltage in the voltage sensor.

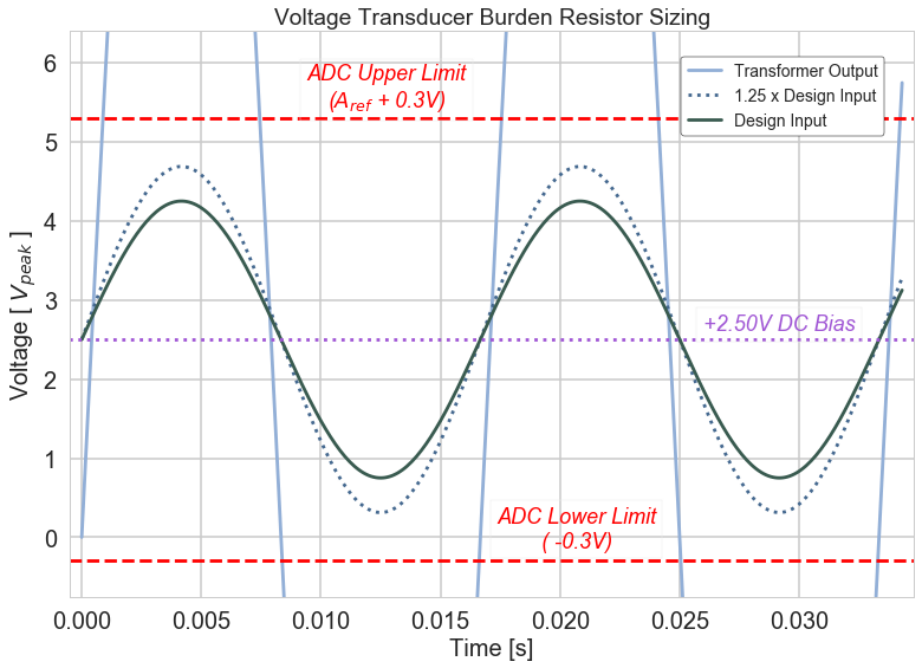

Figure 3.49: Zoomed in plot of the expected induced voltage and the measured voltage in the voltage sensor.

3.6.2.2 DC Offset Component Selection

As described previously, the DC offset resistors should be considerably larger than the other resistors used in the same circuit. Since the total resistance in the VT circuit was 12.9 kΩ, two 470 kΩ resistors were purchased to create the constant DC-offset voltage in the PCB board. Next, using the previous equation given (Equation 3.23), the ideal capacitor size to achieve a reactance of approximately 100 Ω, at 60 Hz frequency, was calculated to be 26.5 μF. A set of 10 μF capacitors were purchased, providing a realized inductance of approximately 265 Ω. The rise time of the corresponding RC-circuit was then checked by energizing and de-energizing the resistor and capacitor in parallel. The rise time (98% charged) was around 30 seconds, so an initial delay of at least 30 seconds was selected to be mandatory whenever power to the PCB was ever plugged in (or the *Raspberry Pi* was powered on), before collecting measurements.

3.6.2.3 Current Transducer Selection

To start the sizing of the CT, the maximum expected RMS-current was investigated. After looking through multiple sets of GSHP submittal data sheets, it was determined that the maximum current the sensor would potentially measure in the GSHP system we have access to is 56 A. Note this comes not from the GSHP's "rated load amperage" (RLA), but rather from its "locked rotor amperage" (LRA). While the RLA is the expected amount of current during regular operation, the LRA is the amount of current expected whenever starting the motor from rest (or if the motor shaft were to be held, fixed in place).

The resulting maximum expected current was then used to select a CT with a suitable range. The specific CT selected for the clamp-on energy meter was the *YHDC SCT-013-100* (Figure 3.50). It is rated for up to 100 A, so it can easily measure the expected LRA. The nominal turn-down ratio is 100A-to-10mA (or approximately 2000 loops), and it does not contain an internal burden resistor. It's rated accuracy is $\pm$ 1% of the reading.

Figure 3.50: Picture of the *YHDC SCT-013-100* CT selected for the clamp-on meter.

Next the specific burden resistor was sized. The magnitude of the anticipated induced signal, was calculated using a re-arranged form of Equation (3.24), which

shows the relationship between the number of loops (L) and the input current (I).

$$\widetilde{I} = \frac{I}{(L)}$$

Next, the maximum induced current ($\widetilde{I}$) was converted from RMS-current to peak-current. Then assuming that the same 2.5 V DC-offset voltage would be available on the PCB, that induced current signal could have a maximum amplitude of 2.5 V. Using Ohm's law, the calculated size for the ideal burden resistor was 58 Ω. Figure 3.51 shows the resulting plot of the nearest possible commonly manufactured resistors. A high-tolerance 56 Ω resistor was selected as the burden resistor for the current circuit. Note that with such a burden resistor, up to 70 A could be put through the CT, before it would exceed the maximum input voltage of the ADC board. That corresponds to a 1.25 safety factor.

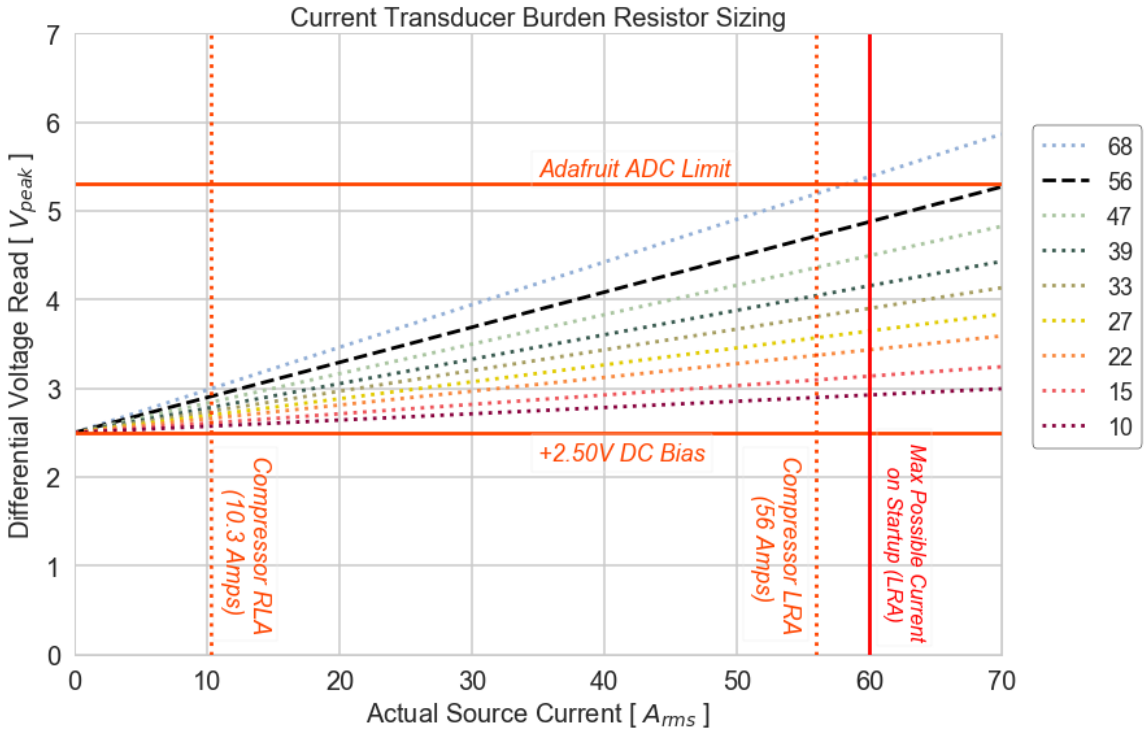

Figure 3.51: Plot of the closest possible actual resistors available for the CT circuit.

3.6.2.4 In-line Power Meter Selection

For the in-line meter, the *HOBO UX120-018 Plug-Load Data Logger* (Figure 3.52) was selected to provide the in-line meter's power measurements. Its maximum rated current is 15 A and is installed by simply plugging it in series with the 120V load that is to be measured. Three of these were implemented to record the electrical power to the two water-heater elements and the circulation pump (all of which were verified to pull under 15 A). Specifically the *HOBO UX120-018* simultaneously measures RMS-voltage, RMS-current, active power, apparent power, and the power factor with a reported accuracy of $\pm$ 1% of the reading. It has a programmable sampling rate that was set to record as fast as possible (1 sps).

Figure 3.52: Picture of the *HOBO UX120-018 Plug-Load Data Logger* used with the in-line energy meter.

3.6.3 Fabrication

As mentioned previously, in the Introduction, the ability to measure power via multiple boundary schema allows for a system to be more appropriately compared to others. In order for multiple boundary schemes to be measured, multiple electrical power monitors must be available and customizable. Thus the following CT and VT circuits fabricated in this sub-section were designed, such they could be easily replicated to produce 3 additional power sensors total.

In order to save space on the PCB, the voltage and current circuits were combined

into one circuit. Figure 3.53 shows the finalized schematic of the combined circuit that makes up one power sensor. Note that the flags represent three different analog channels that were used to measure the differential voltage across the burden and shunt resistors.

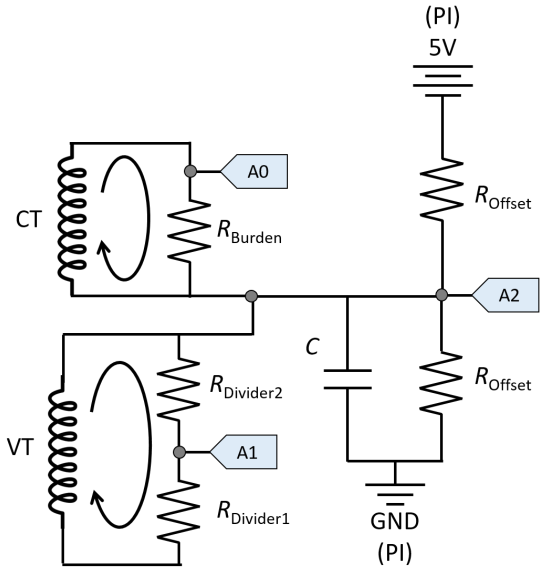

Figure 3.53: Combined current and voltage sensor circuit diagram.

The VTs purchased already came with DC barrel jack adapters, so no additional modifications were necessary. The only modifications made to the CTs were to replace their headphone jacks with DC barrel jack adapters.

After all of the previously sized resistors and capacitors arrived, they were soldered together on to two PCBs. Specifically circuits for three total sets of power sensors were soldered in place. The two ADC boards were connected with common voltage supply and grounds and their addresses were set using jumper wires. The necessary female DC barrel jack adapters were labeled to make referencing in the *Python* code more convenient later. The final PCBs for the clamp-on meter is seen in Figure 3.54.

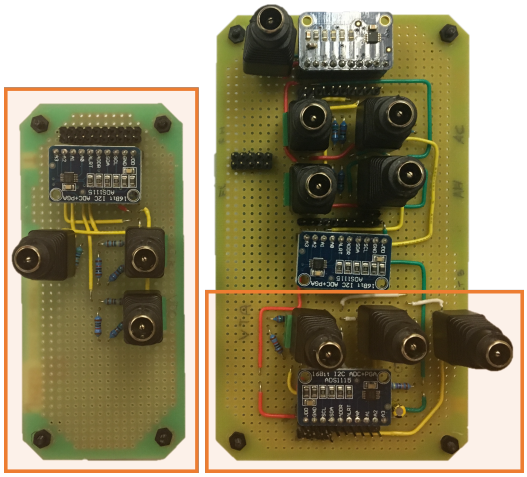

Figure 3.54: Finalized PCB for clamp-on energy meter (with current and voltage components highlighted).

3.6.4 Calibration & Validation

The voltage and current sensors were calibrated against the *HOBO Data Loggers*. A 120 V VARIAC transformer (Figure 3.55) was put in series with a *HOBO Data Logger* and one of the 1500 W water-heater elements. A modified extension cord, rated for 13 A, was used to connect the water-heater elements to the *HOBO Data Logger*. Figure 3.56 shows how the extension cord was carefully spliced and adapted to allow for the clamp-on CTs to easily be placed around just one of the wires. Before starting the calibration, the circulation pump and the fans were turned on, in order to ensure that the water would not get too hot while the water-heater element was turned on.

For calibrating the current and voltage sensors, the following process was repeated at 32 unique amp loads and 9 unique voltage loads. First, the water heater element was turned on and VARIAC was adjusted until the desired amperage/voltage was being read on the *HOBO Data Logger*. When higher amp loads were needing to be measured, the modified extension cord was looped around and fed through the CT multiple times to magnify the induced current signal. Next, the raw ADC counts were

Figure 3.55: Picture of the VARIAC 120/140 VAC power transformer used.

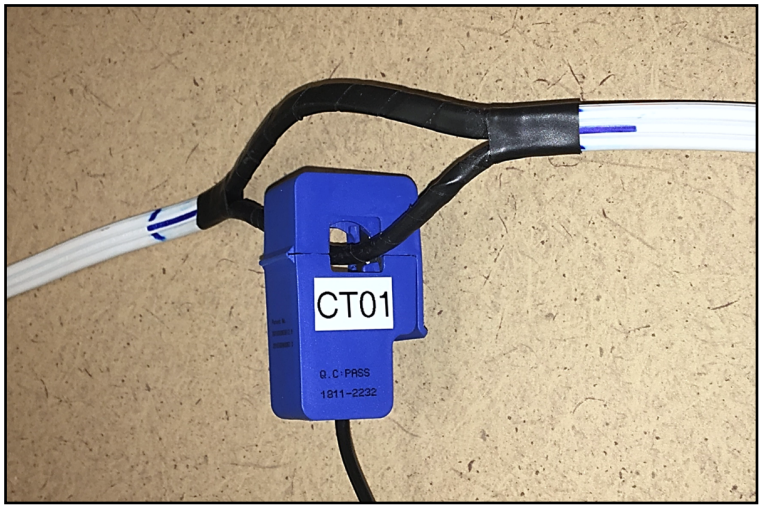

Figure 3.56: Picture of a spliced extension cord modified for a CT to measure current passing through one wire of the cable.

recorded from each of the three CTs and VTs for 5 seconds each. The *Python* scripts written (`ADS1115_CT_calibration.py` and `ADS1115_VT_calibration.py`) paused for 3 seconds between each subsequent sensor to allow the ADC board to fully discharge before recording on a different channel (Appendix H describes learning of this phenomenon). With the ADC board sampling at approximately 860 sps, each CT and VT collected sufficient data to reproduce the induced signal with great resolution (Figure 3.57).

After raw ADC-counts were collected at the desired amperage/voltage, the *Python* script would save the data to a csv-file and pause to wait for the VARIAC to be adjusted. When the next load was ready (and the extension cord looped if necessary), the *Python* script was prompted to proceed and the process repeated. Table 3.6 shows a list of all of the nominal loads measured at during the calibrations.

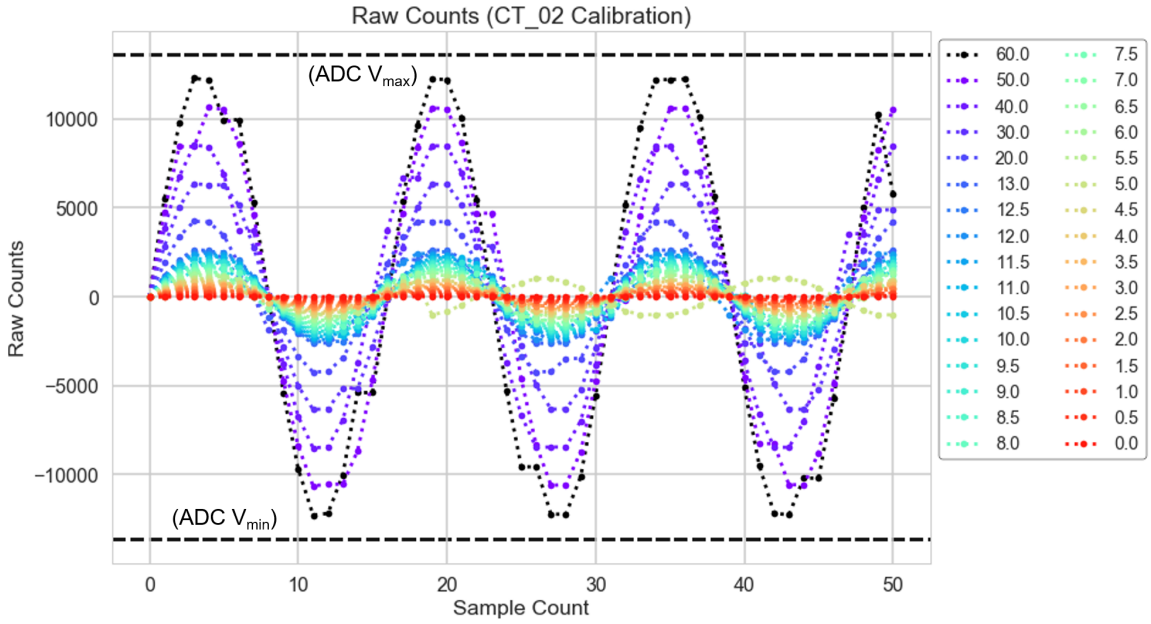

Figure 3.57: Plot of raw ADC counts recorded by CT_02 during the calibration procedure.

Table 3.6: Nominal loads measured during current and voltage calibrations.

Measured Voltage [$V_{\mathbf{RMS}}$]	**Nominal Current** [$A_{\mathbf{RMS}}$]	**Loops through CT**
140	60.0	5
135	50.0	5
130	40.0	4
125	30.0	3
120	20.0	2
115	13.0	1
110	12.5	1
105	12.0	1
100	11.5	1
	11.0	1
	10.5	1
	10.0	1
	⋮	⋮
	$\Delta V = -0.5$	⋮
	⋮	⋮
	1.0	1
	0.5	1
	0.0	1

This full calibration process was repeated multiple times (3 times for the CTs and 2 times for the VTs). The order in which the calibration loads were recorded at was reversed after each data set, in order to best eliminate any effect of hysteresis over the course of the entire calibration process. The raw *Raspberry Pi* data and raw *HOBO Data Logger* data were combined and analyzed in a Jupyter Notebook (see repository of all code referenced in Appendix C).

The Jupyter Notebooks made for post-calibration analysis starts by converting the raw ADC counts to voltages, using Equation (3.5). Then it calculates the true-RMS voltages (Equation 3.18) over every second in order to match the sampling rate with the *HOBO Data Loggers*. The measured resistances of the shunt resistors and the burden resistor were then used to back-calculate the sensors' induced signals' true-RMS values. Specifically, Equation (3.26) was used to calculate the VT's induced RMS-voltage ($\widetilde{V}_{\mathrm{RMS}}$) from its measured RMS-voltage ($\widehat{V}_{\mathrm{RMS}}$), and Equation (3.27) was used to back-calculate the induced RMS-current ($\widetilde{I}_{\mathrm{RMS}}$) from its measured RMS-voltage ($\widehat{V}_{\mathrm{RMS}}$) and the number of times the wire was looped through the transducer (n_{loops}).

$$\widetilde{V}_{\mathrm{RMS}} = \widehat{V}_{\mathrm{RMS}} \cdot \frac{R_{\mathrm{D1}}}{R_{\mathrm{D2}}} \tag{3.26}$$

$$\widetilde{I}_{\mathrm{RMS}} = \frac{\widehat{V}_{\mathrm{RMS}}}{R_{\mathrm{B}} \cdot n_{\mathrm{loops}}} \tag{3.27}$$

Next the induced signals' ideal scalar conversion factors were calculated to result in the corresponding reference RMS-values measured by the *HOBO Data Loggers*. Notice how Equations (3.28) and (3.29) are just rearranged versions of Equations (3.24) and (3.22) respectively.

$$(L) = \frac{I_{\text{ref}}}{\widetilde{I}} \tag{3.28}$$

$$(\lambda) = \frac{V_{\text{ref}}}{\widetilde{V}} \tag{3.29}$$

Specifically when calibrating the VTs, we found a noticeable difference between the two brands purchased. As can be seen in Figure 3.58, the *TRIAD Magnetics* VT's ideal conversion constant (λ) at each induced voltage measured ($\widetilde{V}$) was approximated best with a constant value. However, the *HQRP* VT's ideal conversion constant (λ) at each induced voltage measurement ($\widetilde{V}$) had a slightly increasing relationship, better approximated with a first-order linear equation.

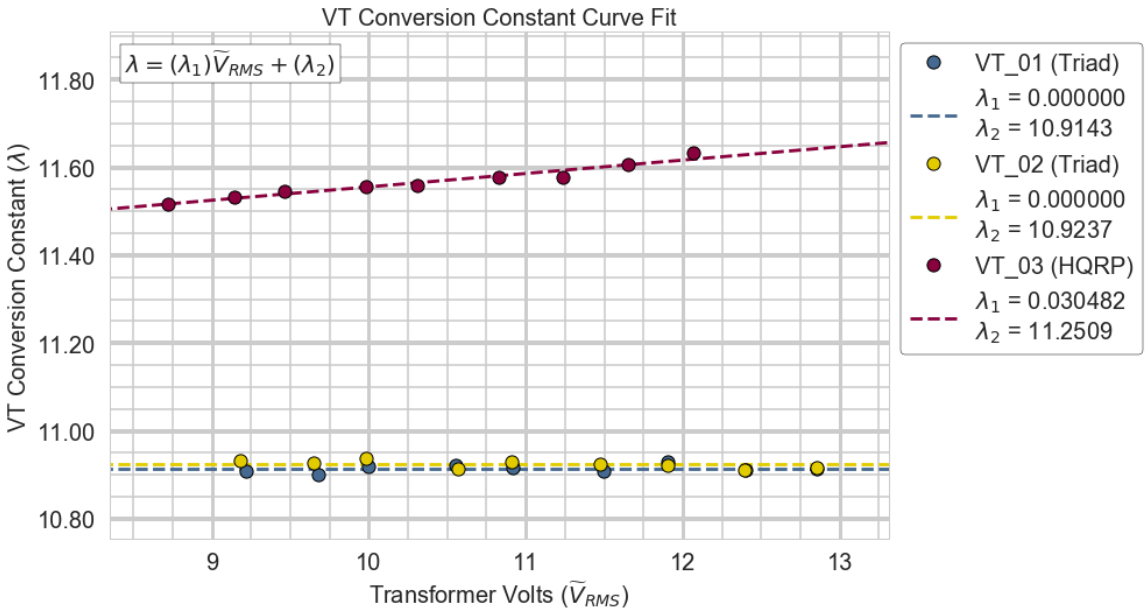

Figure 3.58: Plot of the ideal conversion constants calculated for the first VT calibration data set.

$$\lambda = (\lambda_1)\widetilde{V}_{RMS} + (\lambda_2) \tag{3.30}$$

Thus, Equation (3.30) was used to estimate each VT's conversion constant. Specifically the *Python* function `numpy.polyfit` was used to fit a first-order polynomial to the induced voltages and their corresponding conversion constants (λ). Note that the

TRIAD Magnetics VTs' λ_1 are 0, since they could be sufficiently approximated with a single scalar constant.

The first sets of data at each nominal current/voltage were used as calibration data and the final was used as validation data. Figures 3.59 through 3.61 show the error plots developed for the voltage sensors and current sensors respectively (specifically errors relative to the reference *HOBO* meters). Note that during the calibration process, the error found due to time of day (Figure 3.62) was still within the uncertainty bounds set ($\pm$ 0.5% of the reading).

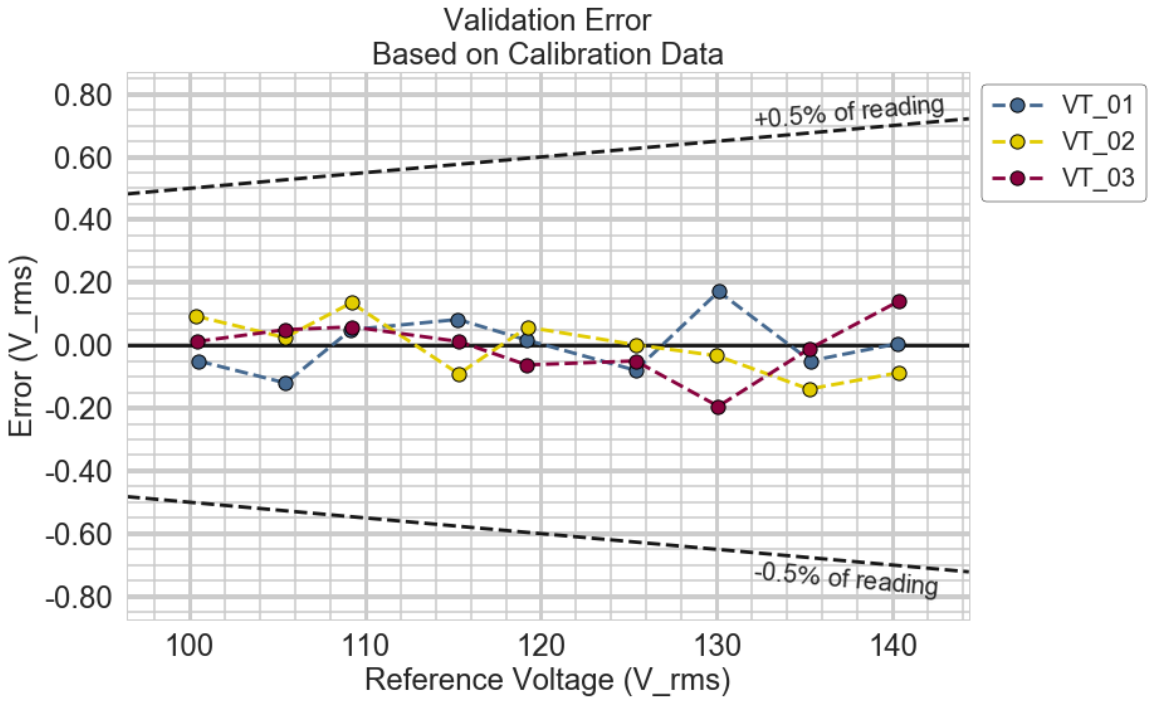

Figure 3.59: Error plot generated using the validation data from each VT.

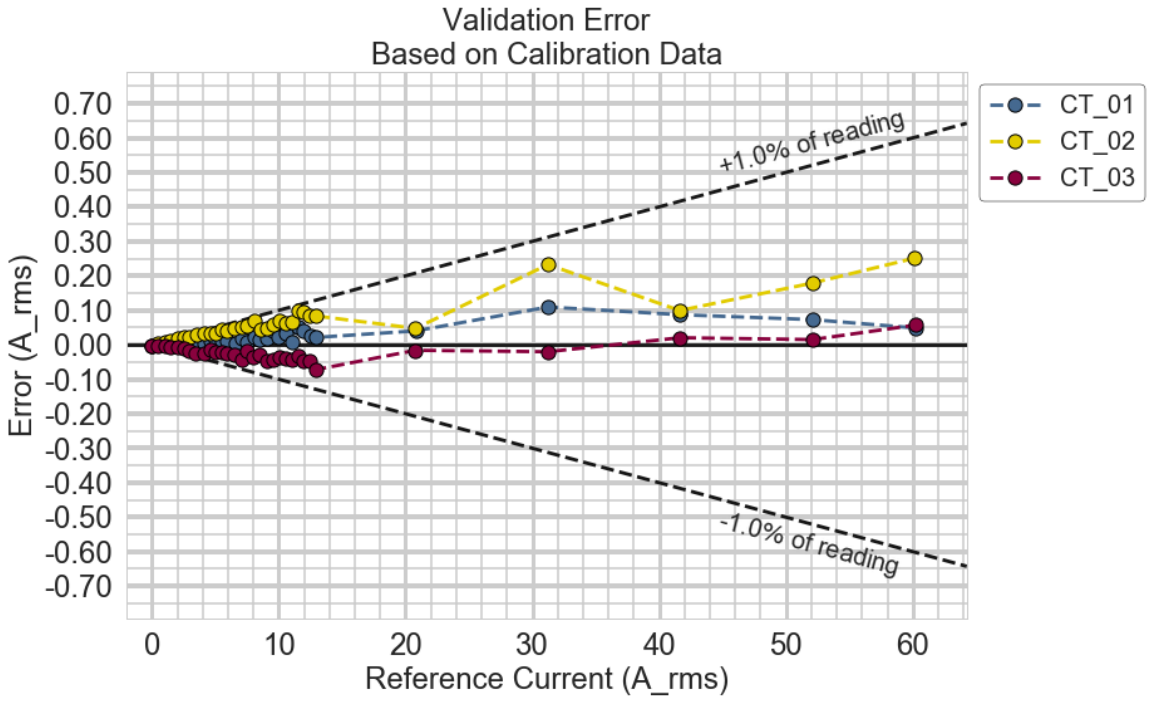

Figure 3.60: Error plot generated using the validation data from each CT.

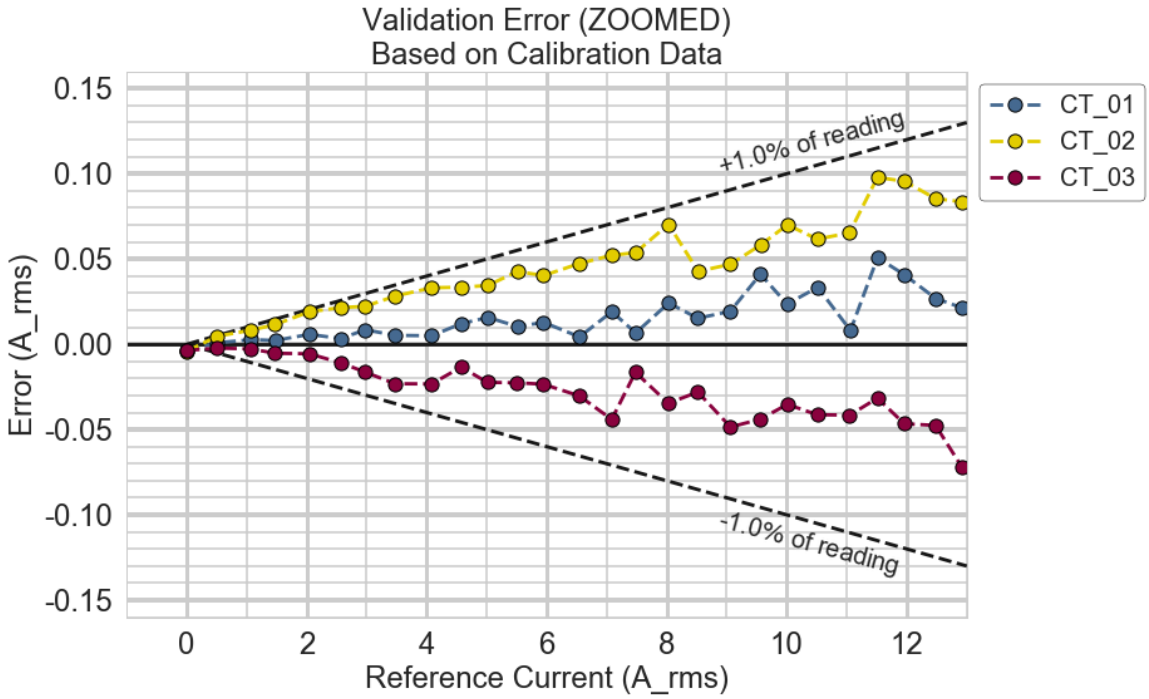

Figure 3.61: Zoomed in error plot generated using the validation data from each CT.

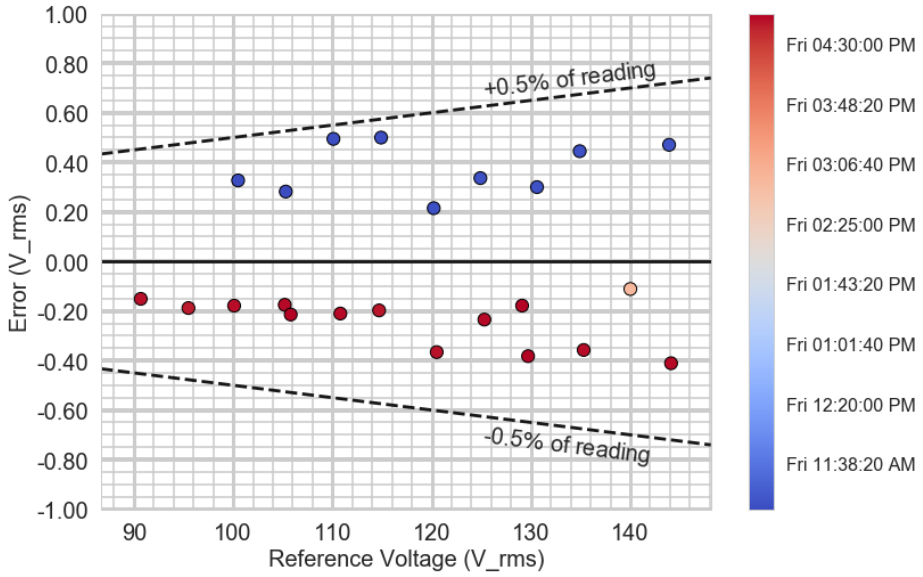

Figure 3.62: Error plot showing the results of tests performed at different times of the day with VT_01.

Table 3.7 contains a summary of the calibrated voltage and current sensors' characteristics and final uncertainties. Note that the listed final uncertainties were calculated by adding their calibration uncertainties (relative to the calibration reference) to the reference meter's reported uncertainty (1% of reading). Each of the sensor's assigned power measurement for the test loop are also given.

Table 3.7: Finalized Electrical Power Meter Uncertainty

Sensor Name	**Calibrated Uncertainty**	**Test Loop Measurement**	**Combined Apparent Power Uncertainty**
VT_01	± 1.5 % of reading	**Circulation Pump**	± 2.5 % of reading
CT_03	± 2.0 % of reading		
VT_03	± 1.5 % of reading	**Heater 1**	± 2.5 % of reading
CT_01	± 2.0 % of reading		
VT_02	± 1.5 % of reading	**Heater 2**	± 2.5 % of reading
CT_02	± 2.0 % of reading		

3.6.5 Summary

Figures 3.63 and 3.64 show the finalized PCB boards for the clamp-on and in-line energy meters respectively. Note that custom 3D-printed cases also have lids that were made to keep all of the jumper wires safe from getting caught on anything. Pictures and designs of the 3D-printed cases can be found in Appendix E.

The complete process and decision flow chart for the entire energy meter can be found in Figure 3.65 on page 111.

A summarized table of all the components sized and selected for the Clamp-On energy meter can be found below in Table 3.8 on page 112. A summarized table of all the components sized and selected for the In-Line energy meter can be found below in Table 3.9 on page 113.

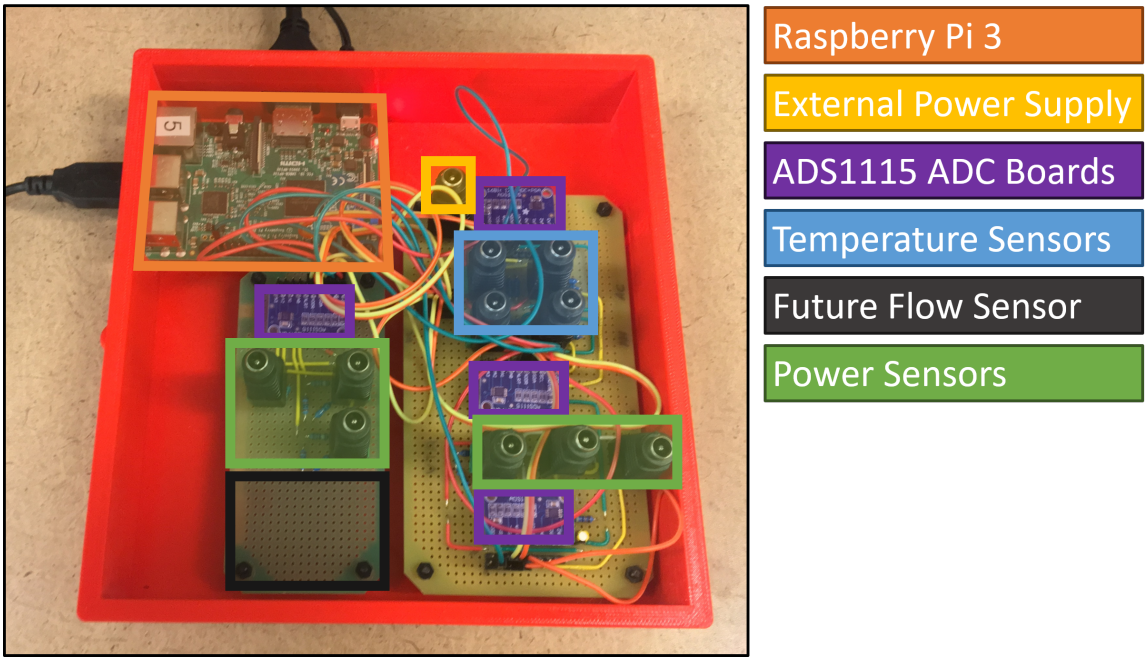

Figure 3.63: Labeled picture of the finalized clamp-on energy meter PCBs (without sensors plugged in).

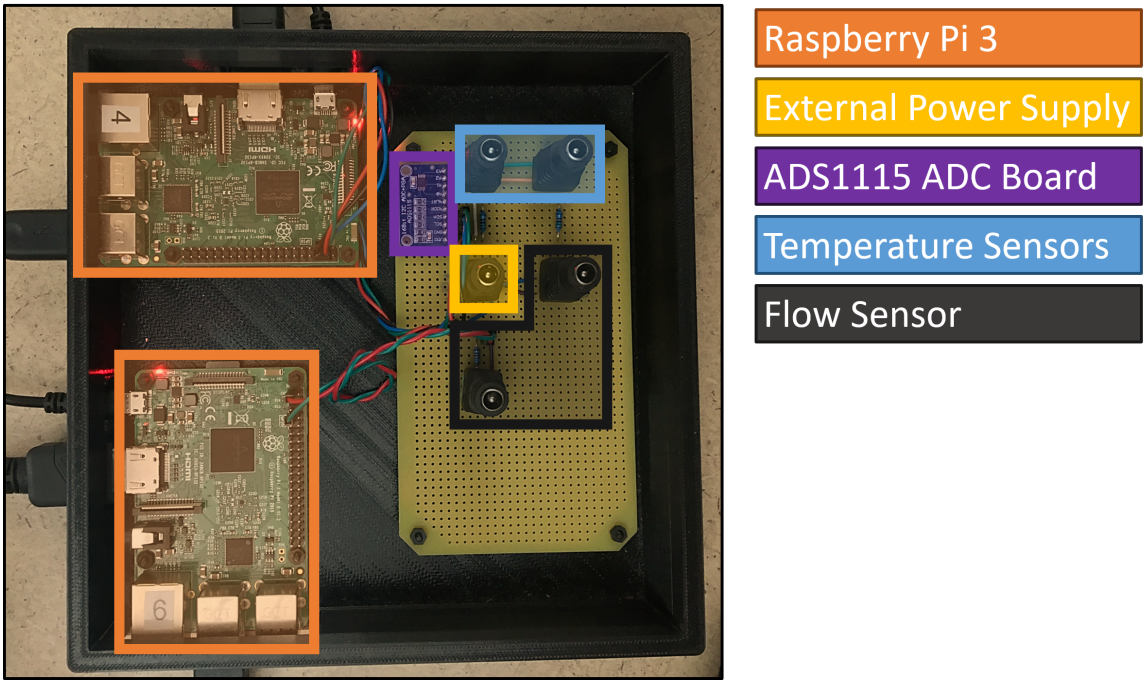

Figure 3.64: Labeled picture of the finalized in-line energy meter PCB (without sensors plugged in).

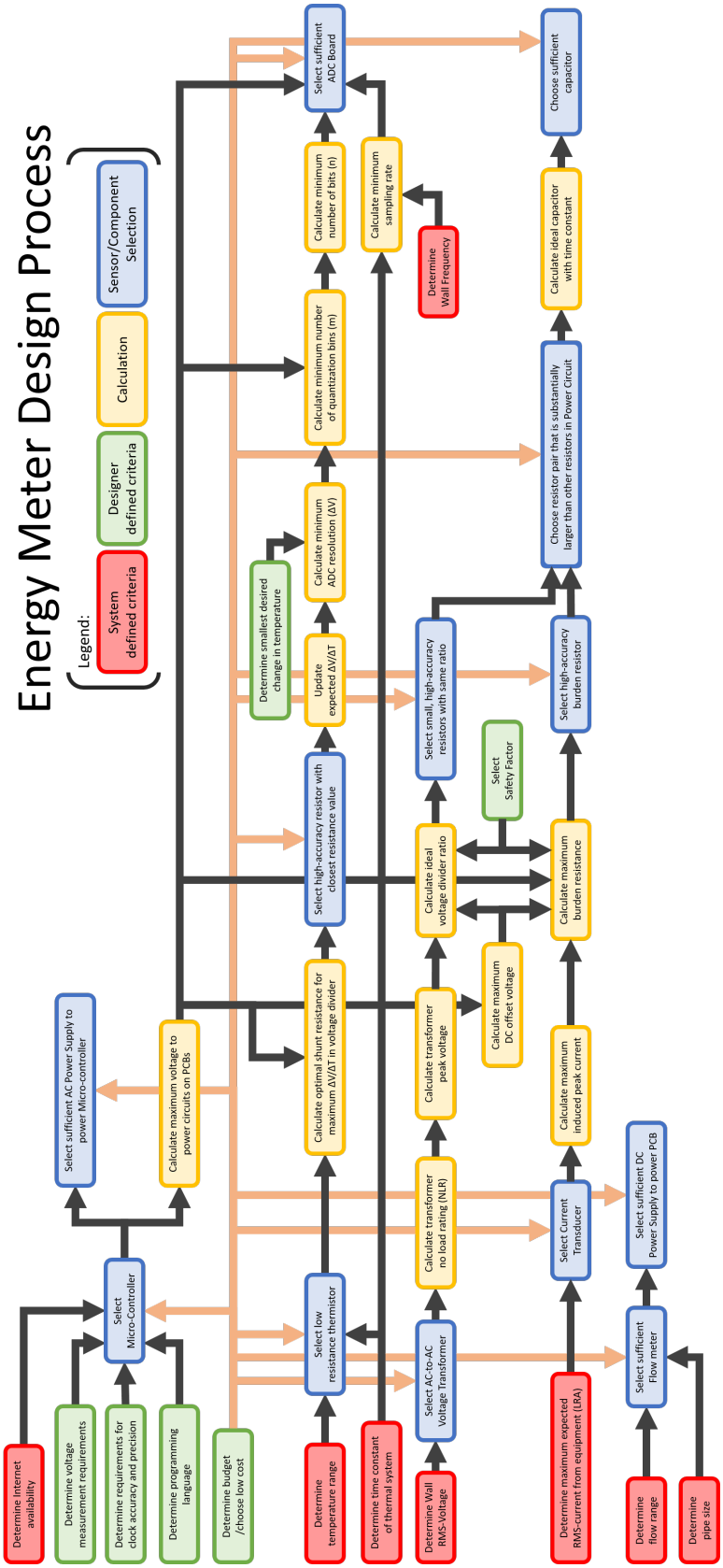

Figure 3.65: An overview of the design & selection process for the entire energy meter.

Table 3.8: Summary of Clamp-On Sensor System Key Components

Sensor Name	Component	Characteristic		Cost	Calibrated Uncertainty
		Notation	Value		
Therm1	5k Thermistor *NTC-502-R*	A	0.001327313449	\$0.50	± 0.037 K (± 0.066 R)
		B	0.000227355566		
		C	9.92649386×10^{-8}		
	Shunt Resistor	R_S	2998.6 Ω	\$0.07	
Therm2	5k Thermistor *NTC-502-R*	A	0.001285879482	\$0.50	± 0.037 K (± 0.066 R)
		B	0.000232502734		
		C	8.85692169×10^{-8}		
	Shunt Resistor	R_S	2998.9 Ω	\$0.07	
Therm3	5k Thermistor *NTC-502-R*	A	0.001310288969	\$0.50	± 0.057 K (± 0.102 R)
		B	0.000229444096		
		C	8.84628252×10^{-8}		
	Shunt Resistor	R_S	2998.4 Ω	\$0.07	
Therm4	5k Thermistor *NTC-502-R*	A	0.001301712306	\$0.50	± 0.057 K (± 0.102 R)
		B	0.000230072895		
		C	9.34578354×10^{-8}		
	Shunt Resistor	R_S	2998.6 Ω	\$0.07	
VT_01	120-to-9 VAC *Triad Magnetics*	λ_1	0.0000 V/V^2	\$16.36	± 1.5% of reading
		λ_2	10.9143 V/V		
	Voltage Divider Resistors	R_{D1}	1396 Ω	\$0.07	
		R_{D2}	11486 Ω	\$0.07	
VT_02	120-to-9 VAC *Triad Magnetics*	λ_1	0.0000 V/V^2	\$16.36	± 1.5% of reading
		λ_2	10.9237 V/V		
	Voltage Divider Resistors	R_{D1}	1393 Ω	\$0.07	
		R_{D2}	11473 Ω	\$0.07	
VT_03	120-to-9 VAC *HQRP*	λ_1	0.0305 V/V^2	\$16.95	± 1.5% of reading
		λ_2	11.2509 V/V		
	Voltage Divider Resistors	R_{D1}	1395 Ω	\$0.07	
		R_{D2}	11448 Ω	\$0.07	
CT_01	100A-to-50mA *SCT-013-000*	L	2023.72 loops	\$10.99	± 2.0%
	Burden Resistor	R_B	55.7 Ω	\$0.07	of reading
CT_02	100A-to-50mA *SCT-013-000*	L	2028.06 loops	\$10.99	± 2.0%
	Burden Resistor	R_B	56.2 Ω	\$0.07	of reading
CT_03	100A-to-50mA *SCT-013-000*	L	2022.94 loops	\$10.99	± 2.0%
	Burden Resistor	R_B	56.1 Ω	\$0.07	of reading

Table 3.9: Summary of In-Line Sensor System Key Components

Sensor Name	Component	Characteristic		Cost	Calibrated Uncertainty
		Notation	Value		
Therm1	2.25k Thermistor *ON-410-PP*	A	0.001457798071	\$82.11	± 0.047 K (± 0.084 R)
		B	0.000240555505		
		C	8.86937580×10^{-8}		
	Shunt Resistor	R_S	1499.0 Ω	\$0.07	
Therm2	2.25k Thermistor *ON-410-PP*	A	0.001450482176	\$82.11	± 0.047 K (± 0.084 R)
		B	0.000242119326		
		C	8.06398400×10^{-8}		
	Shunt Resistor	R_S	1499.5 Ω	\$0.07	
Turbine Flow Meter	Pulse Output *FTB-4607*	k	77.202 ppg	\$246.17	± 3.33% of reading
	Pull-Up Resistor	$R_{\text{Pull-Up}}$	10 kΩ	\$0.07	
B4 Power Meter	HOBO Plug Load Data Logger *UX120-018*	-	-	\$239.00	± 1% of reading
B9 Power Meter	HOBO Plug Load Data Logger *UX120-018*	-	-	\$239.00	± 1% of reading
B14 Power Meter	HOBO Plug Load Data Logger *UX120-018*	-	-	\$239.00	± 1% of reading

3.7 Data Acquisition

All of the *Python* scripts developed for the individual sensor calibrations were combined and put into a single script (`data_logger.py`) to be looped through by the clamp-on energy meter. Figure 3.66 shows an overview of the loops cycled through. Note that the clamp-on energy meter did not have any direct flow measurements made (the flow meter script was only implemented on the in-line energy meter), since the clamp-on meter's ultrasonic transducers were not accurate enough to be implemented at this time. The in-line meter also implemented the same temperature loop, but with only two thermistors (for the water-side measurements). All of the *Raspberry Pi*s active (in-line flow meter, in-line temperature meter, clamp-on energy meter) were connected to the internet, so that their clocks would become synchronized and their time-stamps accurate.

When the measurement loop is interrupted (via the keyboard interrupt: `CNTL+C`), it saves the sample summary (total samples, total sample time, etc.) to the bottom of the csv-file it was saving measurements in, zips the csv-file, and emails it to the free *GMail* account created: *okstateenergymeter@gmail.com*. Additionally, if the meter has been recording for 24-hours straight, or if it becomes 3:00 AM, then it will automatically save, zip, and email the csv-file and start a new one. This was implemented to be able to gain access to the previous day's data remotely.

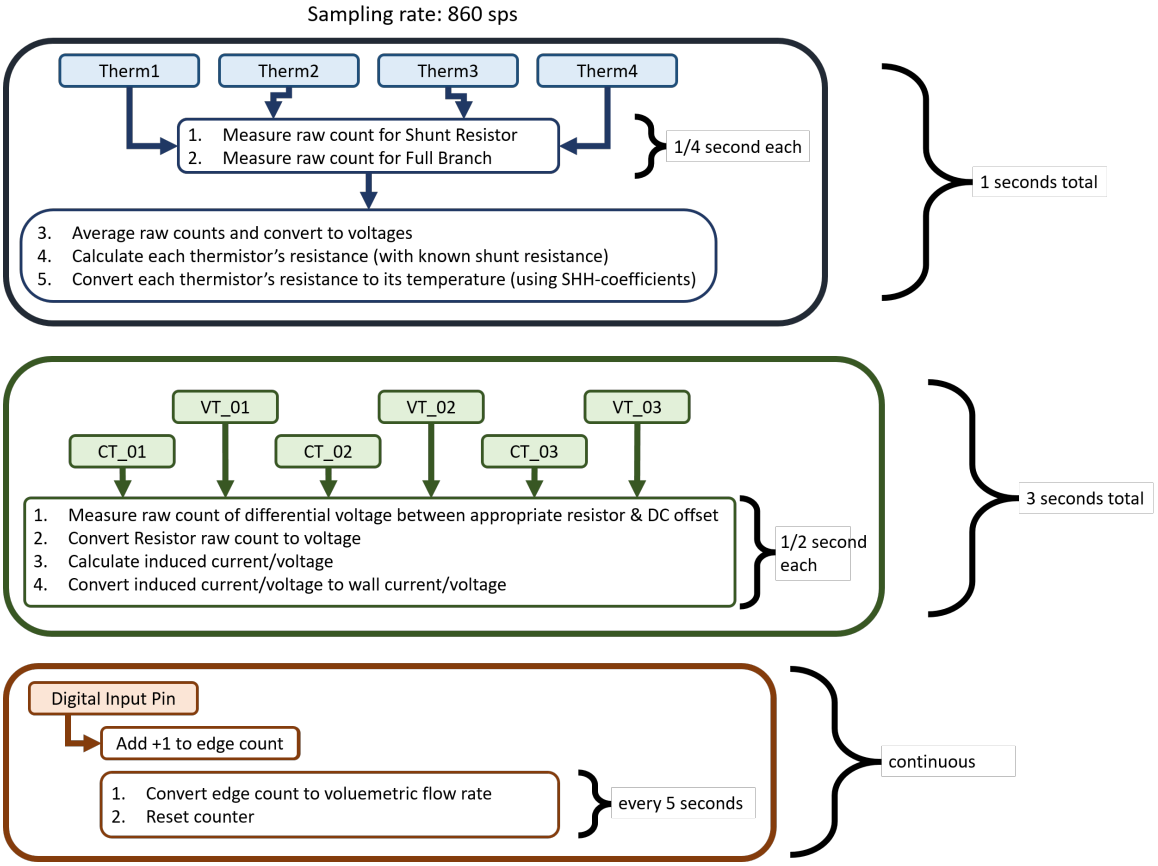

Figure 3.66: An overview of the three measurement loops the clamp-on meter cycles through consecutively.

3.8 Recommendations for Future Work

While the majority of this section will be repeated in the final chapter (Chapter VIII), it is important to note here some key conclusions and recommendations for future modifications to the developed energy meter design. While the developed clamp-on energy meter has four well-calibrated temperature sensors, and three well-calibrated pairs of current and voltage transducers, it is currently lacking a functioning ultrasonic flow meter. As described in Appendix B, the low-cost ultrasonic transducer purchased has issues that must be resolved before flow measurements can be properly implemented with the clamp-on energy meter. An additional recommendation for future work on the clamp-on energy meter includes designing and implementing a means of calculating phase shift/power factor. As mentioned previously, with only one micro-controller, the ability to measure both current and voltage at the same instance in time is not possible. However, if the assumption can be made that the voltage and current signals do not vary in magnitude between the two measurement periods, then time-stamped data could be collected and fit with sinusoidal curves to estimate their magnitudes and phase shift. Furthermore, the temperature sensors of the clamp-on energy meter that are designed to be mounted on the surface of the pipe, require further investigation as to how to properly estimate the center-of-pipe fluid temperature. Later chapters (Chapter VI) will attempt to apply a potential thermal resistance model to estimate true fluid temperature, based on the clamp-on meter's on-pipe temperatures and room air temperatures.

Our in-line energy meter functions properly with two in-line temperature measurements and volumetric flow measurements. The power measurements associated with the in-line meter come from *HOBO Data Loggers* that record voltage, current, and power factors. At the moment, all three of these measurements (temperature,

flow, and electrical power) are recorded independently by two separate *Raspberry Pi*s and three individual *HOBO Data Loggers*. Future work could include finding a way to control and measure these from a "master" micro-controller to make recording data from the test loop more convenient. Lastly, the in-line energy meter could have two additional temperature sensors installed in order to measure the entering and leaving air temperatures across the heat exchanger. If an anemometer was installed and implemented, an estimation of the air-side calorimetric heat transfer could also be calculated to verify the water-side heat transfer measured.

CHAPTER IV

Measurement Uncertainty

As mentioned previously in the Introduction, it is necessary for the uncertainty of overall performance calculations to be investigated in order for their significance to be properly understood. Uncertainty analysis can also provide insight on the effectiveness of the instrumentation selected for the measurements being made for a particular application as well. The uncertainty analysis in this chapter involves the calculation of the propagation of uncertainties from the individual, physical measurements to the final quantities of interest: calorimetric heat transfer ($\dot{Q}$) and electrical power consumption ($\dot{W}$). The procedure used is consistent with the description given in Taylor (1997) and ASME International (2013).

It is important to note that especially when working with electronic measurements, random error will certainly exist. However, through the collection of such measurements in large quantities, that random error is mitigated. More specifically in the situation of our energy meters, every raw-count read by the ADC board is either averaged with at least 100 others (1/4 second $\times$ 860 sps) or collectively used to calculate the RMS-value of the voltage that is eventually used to calculate the physical measurement. While the effect of random errors are of some interest, specifically the amount of random electrical noise in the wires and on the PCB, as well as the variance in the EPS supplying power to the ADC board, systematic errors are primarily of concern.

For the purposes of this thesis, the words "error" and "uncertainty" are used interchangeably. The naming convention that we use to express a measurement's

fractional uncertainty is a lower-case "e" and its absolute uncertainty is an upper-case "E". In general, if the measurement is "x", then its expected absolute error is $E_x = x \cdot e_x$, and its expected relative error is $e_x = E_x/x$.

Furthermore, if a particular quantity is calculated via sub-measurements that are independent to one another, then its uncertainty is the summation of those individual uncertainties in quadrature. The generic formula for such quantities is given below in Equation (4.1).

$$E_F = \sqrt{\sum_{i=1}^{n} \left(\frac{\partial F}{\partial x_i} E_{x_i} \right)^2}$$

$$E_F = \sqrt{\left(\frac{\partial F}{\partial x_1} E_{x_1} \right)^2 + \left(\frac{\partial F}{\partial x_2} E_{x_2} \right)^2 + \ldots + \left(\frac{\partial F}{\partial x_n} E_{x_n} \right)^2} \tag{4.1}$$

E_F is the absolute error associated with the measurement of interest, F, made up of n sub-measurements; $\partial F/\partial x_i$ is the partial derivative of F with respect to the independent sub-measurement x_i; and E_{x_i} is the absolute uncertainty of the sub-measurement x_i.

Subsequently, Equation (4.2) shows the general equation used to calculate the fractional uncertainty of a secondary measurement (arbitrarily named "F").

$$e_F = \frac{E_F}{F} \tag{4.2}$$

Furthermore, if that secondary measurement (F) is specifically calculated by taking the product of n independent sub-measurements ($F = x_1 \cdot x_2 \cdot \ldots \cdot x_n$), then the equation for its fractional uncertainty can be more specifically written using Equation (4.3).

$$e_F = \sqrt{\left(\frac{E_{x_1}}{x_1} \right)^2 + \left(\frac{E_{x_2}}{x_2} \right)^2 + \ldots + \left(\frac{E_{x_n}}{x_n} \right)^2} \tag{4.3}$$

The following sections discuss the uncertainties of the overall calorimetric heat transfer calculations ($\dot{Q}$) and the overall electrical power consumption calculations ($\dot{W}$) associated with the developed energy meter.

4.1 Overall Calorimetric Heat Transfer Uncertainty

Equation (3.1) was reproduced below to show the measurements that make up the overall calorimetric heat transfer calculation (from the water side).

$$\dot{Q} = \dot{V} \cdot \rho \cdot c_p \cdot (T_{\text{LWT}} - T_{\text{EWT}}) \tag{3.1}$$

$\dot{V}$ is the volumetric flow rate [converted to m^3/s]; ρ is the density of the water [in kg/m^3]; c_p is the specific heat of the water [in J/kg·K]; T_{LWT} is the leaving water temperature (relative to the test loop's heating elements) [in °C]; and T_{EWT} is the entering water temperature (relative to the test loop's heating elements) [in °C].

For our application on the validation test loop, the density (ρ) and specific heat (c_p) of the water were calculated using the temperature of the water passing through the flow meter (T_{LWT}). Additionally, the change in overall heat transfer, based on the error associated with the density and specific heat calculations were confirmed to be negligible compared to the volumetric flow rate and temperature difference. Thus, the only sub-measurement uncertainties considered in the overall calorimetric heat transfer uncertainty analysis were the volumetric flow rate uncertainty ($E_{\dot{V}}$) and temperature difference uncertainty ($E_{\Delta T}$). Equation (4.4) shows the absolute uncertainty associated with the overall heat transfer calculation (derived from the general equation, Equation 4.1).

$$E_{\dot{Q}} = \sqrt{\left(\frac{\partial \dot{Q}}{\partial \dot{V}} E_{\dot{V}}\right)^2 + \left(\frac{\partial \dot{Q}}{\partial \Delta T} E_{\Delta T}\right)^2}$$

$$E_{\dot{Q}} = \sqrt{\left(\rho c_p (T_{\mathrm{LWT}} - T_{\mathrm{EWT}}) \cdot E_{\dot{V}}\right)^2 + \left(\rho c_p \dot{V} \cdot E_{\Delta T}\right)^2} \tag{4.4}$$

Equation (4.5) shows the relative uncertainty associated with the overall heat transfer calculation (derived from the general equation, Equation 4.2).

$$e_{\dot{Q}} = \sqrt{e_{\dot{V}}^2 + e_{\Delta T}^2}$$

$$e_{\dot{Q}} = \sqrt{\left(\frac{E_{\dot{V}}}{\dot{V}}\right)^2 + \left(\frac{E_{\Delta T}}{\Delta T}\right)^2} \tag{4.5}$$

Note that the two absolute temperature measurements (T_{LWT}, T_{EWT}) are ultimately used to calculate a relative temperature difference in the water. Since the primary concern is the overall temperature difference across the heat exchanger, the errors in the individual absolute temperature measurements were combined together to form the overall temperature difference error (Equations 4.6). Adding them in quadrature assumes that they both have a normal distribution of error, so that the probability that the errors will be at opposite extremes is less than 5%. Equation (4.7) shows the corresponding fractional error associated with the overall temperature difference measurement.

$$E_{\Delta T} = \sqrt{\left(E_{LWT}\right)^2 + \left(E_{EWT}\right)^2} \tag{4.6}$$

$$e_{\Delta T} = \frac{\sqrt{\left(E_{LWT}\right)^2 + \left(E_{EWT}\right)^2}}{T_{\mathrm{LWT}} - T_{\mathrm{EWT}}} \tag{4.7}$$

Each sensor's individual calibrated uncertainty was recorded during their respective calibrations and summarized in tables throughout the previous chapter (Table 3.4, Table 3.5, and Table 3.7). In order to calculate the uncertainty in the energy meter's overall calculation of calorimetric heat transfer, data were collected at steady-state operating conditions on the test loop. Specifically, the circulation pump and fans were turned on (approx. 2 GPM), along with both of the water heater elements subsequently (approx. 3000 W total). After recording data with both the in-line and clamp-on energy meters for one hour, the raw measurements were saved and then the steady-state measurements were calculated, using a *Python* script in a *Jupyter Notebook* (Note that these steady-state measurements were collected during "Test Case B," described later in Chapter V: Experimental Design).

The overall calorimetric heat transfer measurement uncertainty was then calculated using the steady-state averages from the data set and the formulas just derived. The associated uncertainties for the calorimetric heat transfer measurements at steady-state conditions are summarized in Table 4.1.

It is important to emphasize that these uncertainties are given for a single operating condition. That operating condition was decided as the example, since its steady-state values were representative of other scenarios' steady-state operating conditions as well. At different operating conditions, the respective uncertainties of each measurement will likely vary from this specific scenario's.

Furthermore, it is important to note that the uncertainties associated with the

Table 4.1: Summary of Steady-State Calorimetric Heat Transfer Uncertainty

Measurement	Energy Meter	Specific Steady-State Value	Uncertainty	
			Absolute (E)	Fractional (e)
T_{LWT}	*Clamp-On*	41.86 °C (107.3 °F)	± 0.037 K† (± 0.066 R)†	-
	In-Line	43.28 °C (109.9 °F)	± 0.047 K (± 0.084 R)	-
T_{EWT}	*Clamp-On*	37.47 °C (99.5 °F)	± 0.037 K† (± 0.066 R)†	-
	In-Line	38.38 °C (101.1 °F)	± 0.047 K (± 0.084 R)	-
ΔT	*Clamp-On*	4.40 K (7.92 R)	± 0.052 K† (± 0.094 R)†	± 1.2 %† (± 1.2 %)†
	In-Line	4.89 K (8.81 R)	± 0.066 K (± 0.120 R)	± 1.4 % (± 1.4 %)
$\dot{V}$	(*BOTH*)	2.081 GPM (1.313×10^{-3} $\frac{\mathrm{m}^3}{\mathrm{s}}$)	± 0.069 GPM ($\pm$ 4.38×10^{-6} $\frac{\mathrm{m}^3}{\mathrm{s}}$)	± 3.33% ± 3.33%
ρ	*Clamp-On*	993.2 kg/m^3	*negligible*	*negligible*
	In-Line	992.8 kg/m^3	*negligible*	*negligible*
c_p	*Clamp-On*	4179.3 J/kg·K	*negligible*	*negligible*
	In-Line	4179.3 J/kg·K	*negligible*	*negligible*
$\dot{Q}$	*Clamp-On*	2397 W (8179 Btu/hr)	± 84 W† (± 287 Btu/hr)	± 3.5 % (± 3.5 %)
	In-Line	2667 W (9100 Btu/hr)	± 93 W (± 317 Btu/hr)	± 3.5 % (± 3.5 %)

† There is an additional amount of uncertainty due to the physical location of the thermistors on the outside of the pipe.

clamp-on energy meter's leaving water temperature (T_{LWT}) and entering water temperature (T_{EWT}) (and the subsequent uncertainty calculations that use them) are inherently under-estimates. As a result of the thermistors being "clamped-on" to the outside of the pipe, they are not truly measuring T_{LWT} or T_{EWT} in the center of the pipe. The resistance in the pipe and potential boundary layers in the water itself will cause the surface of the pipe to be a different temperature than the fluid at the true, center of the pipe. The effects of this unknown thermal resistance between the true-T_{LWT} and the measured clamp-on temperatures, will be discussed later in

Ch.VI. Additionally, an initial attempt at modeling the pipe and insulation's thermal resistance network in order to estimate the true fluid temperature will be discussed.

When designing and selecting the components of a metering system, knowing each measurement's contribution to the overall uncertainty can help determine what sensors are causing the most error at specific operating conditions. The contribution of each individual measurement's uncertainty to the overall uncertainty can be calculated to determine which sensor to improve to achieve the greatest improvement in overall uncertainty. Note that the equations to do such a calculation (Equation 4.8 and Equation 4.9), are derived from the overall absolute uncertainty equation (Equation 4.4) by simply finding the ratio of the individual component's squared contribution to the square of the total uncertainty.

$$\% \text{ uncertainty due to } \dot{V} = \frac{\left(\rho c_p (T_{\mathrm{LWT}} - T_{\mathrm{EWT}}) \cdot E_{\dot{V}}\right)^2}{\left(E_{\dot{Q}}\right)^2} \tag{4.8}$$

$$\% \text{ uncertainty due to } \Delta T = \frac{\left(\rho c_p \dot{V} \cdot E_{\Delta T}\right)^2}{\left(E_{\dot{Q}}\right)^2} \tag{4.9}$$

Characteristics from the aforementioned steady-state data were used to generate the following uncertainty contribution pie chart. Specifically, Figure 4.1 represents the in-line meter's overall calorimetric heat transfer uncertainty distribution at a flow rate of approximately 2.0 GPM and a temperature difference of approximately 8.8 °C. At these specific operating conditions, the in-line energy meter's overall calorimetric heat transfer measurement was calculated as having about 85% of its overall uncertainty contributed by the flow meter measurement's uncertainty. Again, note that the clamp-on energy meter's overall calorimetric heat transfer uncertainty distribution was not calculated, as its true temperature uncertainties, due to the uncertainty from its physical placement, were still unknown.

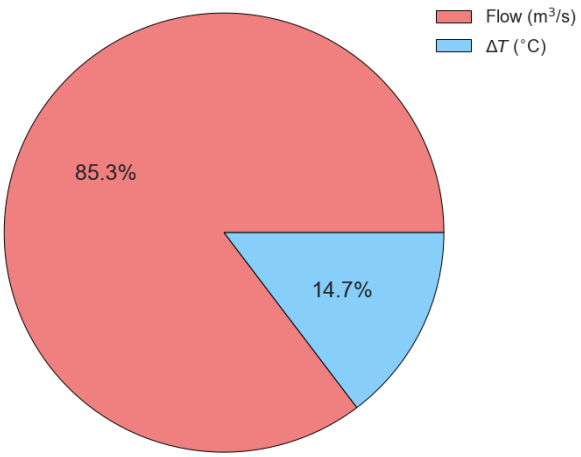

Figure 4.1: Uncertainty contribution for the In-line energy meter's calorimetric heat transfer measurement at a flow rate of 2.081 GPM and a temperature difference of 8.81 °C.

Additionally, the same calculation was performed during the period in the data with no heat injection. The flow was still approximately 2.0 GPM, but the resulting temperature difference was much smaller: approximately 0.08 °C. Figure 4.2 shows the in-line meter's overall calorimetric heat transfer uncertainty allotment during this specific operating condition (just circulation pump on, with all water heater elements off). As was mentioned in the Introduction, the significantly larger effect of a small temperature difference, can be clearly seen.

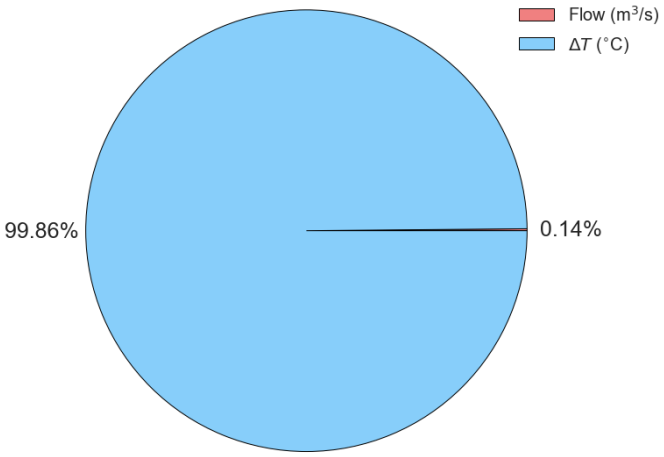

Figure 4.2: Uncertainty contribution for the In-line energy meter's calorimetric heat transfer measurement during small temperature differences.

4.2 Electrical Power Consumption Uncertainty

Equation (3.2) was reproduced below to show the measurements that make up an individual device's power consumption.

$$\dot{W} = \Big(V \cdot I \cdot \big(\cos(\phi) \big) \Big) \tag{3.2}$$

Where $\dot{W}$ is the electrical power consumption [in W]; V is the voltage [in V_{RMS}]; I is the current [in A_{RMS}]; and ϕ is the phase shift [in radians or degrees].

In our setup on the validation test loop, three sets of power measurements were made: power drawn by the circulation pump ($\dot{W}_{CP}$), power drawn by the first water heater element ($\dot{W}_{H1}$), and power drawn by the second water heater element ($\dot{W}_{H2}$). Assuming these measurements are independent of one another, the total power consumption uncertainty is calculated by summing each of their uncertainties in quadrature (Equation 4.10).

$$E_{\dot{W}_{TOT}} = \sqrt{\sum_{i=1}^{n} \left(E_{\dot{W}_i}\right)^2}$$

$$E_{\dot{W}_{TOT}} = \sqrt{\left(E_{\dot{W}_{CP}}\right)^2 + \left(E_{\dot{W}_{H1}}\right)^2 + \left(E_{\dot{W}_{H2}}\right)^2} \tag{4.10}$$

As a result of the total power consumption measurement being a simple sum of its individual power measurements, the corresponding relative uncertainty for the total power consumption is simply the quotient of its absolute uncertainty and the its calculated value. Equation (4.11) shows the corresponding formula for the total

power consumption measurement's relative uncertainty.

$$e_{\dot{W}_{\mathrm{TOT}}} = \frac{E_{\dot{W}_{\mathrm{TOT}}}}{\dot{W}_{\mathrm{TOT}}} = \frac{E_{\dot{W}_{\mathrm{TOT}}}}{\left(\dot{W}_{\mathrm{CP}} + \dot{W}_{\mathrm{H1}} + \dot{W}_{\mathrm{H2}}\right)} \tag{4.11}$$

As mentioned previously, for the clamp-on meter's power measurements, the uncertainty of the overall power measurement is the individual VT's and CT's uncertainties added in quadrature. The specific equation used to calculate this is found below (Equation 4.12). Note that the uncertainty in the power factor ($\cos(\phi)$)/phase shift (ϕ) was not included, because it was not measured in this initial design of the clamp-on energy meter.

$$E_{\dot{W}} = \sqrt{\left(\frac{\partial \dot{W}}{\partial V} E_V\right)^2 + \left(\frac{\partial \dot{W}}{\partial I} E_I\right)^2}$$

$$E_{\dot{W}} = \sqrt{\Big(\big(I\cos(\phi)\big)E_V\Big)^2 + \Big(\big(V\cos(\phi)\big)E_I\Big)^2} \tag{4.12}$$

During the same experiment conducted to record steady-state data for the calorimetric heat transfer overall uncertainty at a common operating condition, power measurements were also collected. Table 4.2 summarizes the associated uncertainties for the electrical power measurements during this specific operating condition of steady-state heat-injection. As was previously discussed in Chapter III, the clamp-on energy meter's power calculation is just the "apparent power", measured in VA. Apparent power is calculated by taking the product of the respective VT and CT measurements, without considering the power factor or phase shift. The in-line energy meter's power measurements are recorded by the HOBO data loggers, which do calculate power factor, so their reported power measurement in Table 4.2 is "active power", measured in W.

The same method described in the previous section was used to calculate the

Table 4.2: Summary of Steady-State Electrical Power Consumption Uncertainty

Device	Measurement	Steady-State Value	Uncertainty	
			Absolute (E)	Fractional (e)
CircPump	I_{RMS}	0.48 A	± 0.01 A	± 2.0 %
	V_{RMS}	121.6 V	± 1.8 V	± 1.5 %
	($\dot{W}_{\text{Clamp-on}}$)	(58.2 VA)	(± 1.5 VA)	(± 2.5 %)
	$\dot{W}_{\text{In-line}}$	56.5 W	± 0.6 W	± 1.0 %
Heater 1	I_{RMS}	11.92 A	± 0.24 A	± 2.0 %
	V_{RMS}	115.4 V	± 1.7 V	± 1.5 %
	($\dot{W}_{\text{Clamp-on}}$)	(1376 VA)	(± 34 VA)	(± 2.5 %)
	$\dot{W}_{\text{In-line}}$	1372 W	± 14 W	± 1.0 %
Heater 2	I_{RMS}	11.96 A	± 0.24 A	± 2.0 %
	V_{RMS}	116.3 V	± 1.7 V	± 1.5 %
	($\dot{W}_{\text{Clamp-on}}$)	(1391 VA)	(± 35 VA)	(± 2.5 %)
	$\dot{W}_{\text{In-line}}$	1370 W	± 14 W	± 1.0 %
TOTAL	$\dot{W}_{\text{TOT\_Clamp-on}}$)	2824 VA	± 70 VA	± 2.5 %
	$\dot{W}_{\text{TOT\_In-line}}$	2798 W	± 28 W	± 1.0 %

contribution to overall power consumption uncertainty from each of the clamp-on energy meter's VTs and CTs. Equations (4.13) and (4.14) show the generalized equations used to calculate the contribution from each VT and CT respectively.

$$\%\text{ uncertainty due to CT}_X = \frac{\left(V \cdot E_{(\text{CT}_X)}\right)^2}{\left(E_{\dot{W}_{\text{TOT}}}\right)^2} \tag{4.13}$$

$$\%\text{ uncertainty due to VT}_X = \frac{\left(I \cdot E_{(\text{VT}_X)}\right)^2}{\left(E_{\dot{W}_{\text{TOT}}}\right)^2} \tag{4.14}$$

The resulting pie plot (Figure 4.3) shows that 99.9% of the overall uncertainty in the electrical power consumption measurement (at this specific operating condition) comes from the voltage and current transducers associated with measuring the water heater elements. Since the significant majority of the uncertainty in the overall power consumption measurement came from the two purely-resistive measurements

("Heater1" and "Heater2"), not calculating the small phase shift in the circulation pump power, proved insignificant to the overall power uncertainty for this scenario. In operating conditions where the clamp-on energy meter's overall power consumption is made up of primarily the circulation pump (or other inductive or capacitive devices), then the uncertainty resulting from not calculating the power factor/phase shift will become more prevalent.

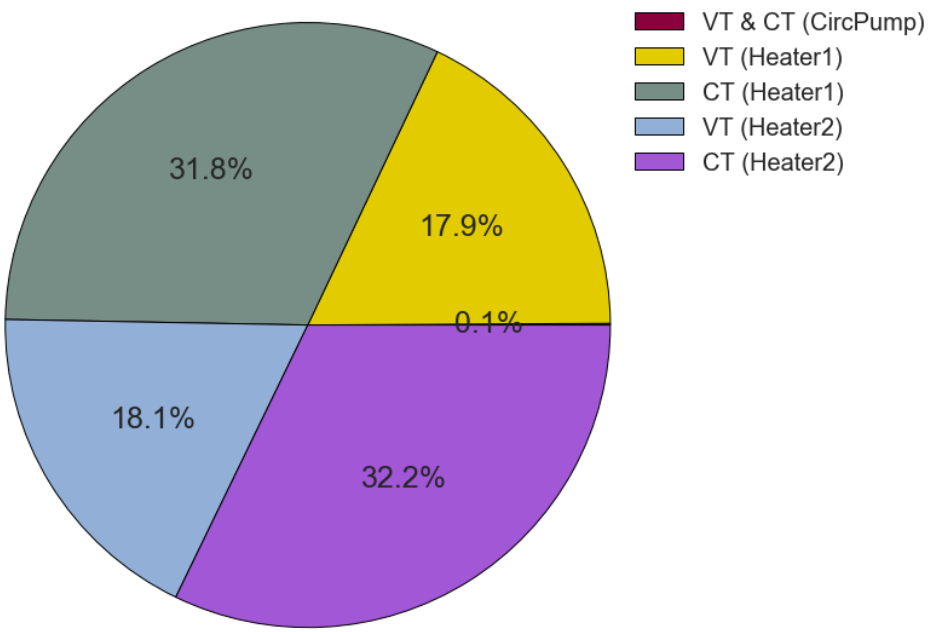

Figure 4.3: Uncertainty contribution for the Clamp-on energy meter's power consumption measurements.

CHAPTER V

Experimental Design

As mentioned previously, the purpose of the test loop was to evaluate and quantify the accuracy of the residential GSHP energy meters developed, and specifically compare the clamp-on and in-line measurement techniques. To do so, a series of tests were designed and conducted in order to collect data from each energy meter, under various system conditions. This chapter describes the motivation and procedures for these tests. The following chapter (Chapter VI), will present and discuss the results.

5.1 Test Loop Capacity

The first series of tests ran on the validation test loop were a series of capacity tests to determine the range of fluid temperature differences that could be achieved at various flow rates. With knowledge of the achievable flow rates, maximum fluid temperatures, and maximum temperature differences, the future uses for the test loop could be determined. The most important goal of these tests were to effectively acquire more accurate limits of the temperature differences attainable from the validation test loop. They are effectively more accurate attempts of the initial capacity test performed immediately after building the test loop, originally done to validate if the heat exchanger was large enough (see Chapter II).

The basic procedure followed during the "Test Loop Capacity Tests" was to turn on the fans and the circulation pump at the beginning. Next, the energy meter's were confirmed to be connected to the internet (to synchronize their clocks), and recording begun. The rotameter's screw valve was then adjusted to achieve the approximate

flow rate being tested at. Both water heater elements were then turned on for 45 minutes to 1 hour, in order to allow for the fluid to reach steady-state. After the timer finished, the water heater elements were turned off and the pump was allowed to run until the water inside reached steady-state conditions at room temperature (approx. 70 °F or 21 °C). Lastly, the energy meters were stopped and their data emailed and saved. Then the process was repeated for the remaining flow rates.

Table 5.1 shows the flow rates tested at during these "Test Loop Capacity Tests". The flow rates were selected to range from the lowest flow the flow meter was calibrated at, increasing by 0.5 GPM up to the highest flow rate the circulation pump could achieve. Note that the term "heat pulse" (in Table 5.1) is used to describe a period of continuous heat injection into the fluid from the water heater elements.

Table 5.1: Test Loop Capacity Tests Key Characteristics

Nominal Flow Rate (GPM)	Heat Pulse Duration (min)	Heat Pulse Count (pulses)	Nominal Heat Pulse Magnitude (kWh)
1.0	45-60	1	3.00
1.5	45-60	1	3.00
2.0	45-60	1	3.00
2.5	45-60	1	3.00

Note that the "Test Loop Capacity Tests" were performed before the final clamp-on energy meter was finished being calibrated. As a result the data collected will only contain measurements from the in-line energy meter and HOBO data loggers. Additionally, it is important to note that during the capacity tests with the maximum amount of temperature difference, the infrared camera was used to again take pictures and evaluate where any potential heat leaks were occurring. Appropriately R-13 insulation was added to the locations, as described in Chapter II.

5.2 Instantaneous Heat Balance

The remaining series of tests were conducted with the purpose of performing a heat balance on both the in-line and clamp-on energy meters with the validation test loop. A heat balance is effectively an account of all the heat supplied to a system, along with all of the heat extracted from that same system. In the case of our validation test loop, the heat supplied, is considered the total electrical power measured ($\dot{W}$) and the heat extracted is considered the total calorimetric heat transfer measured ($\dot{Q}$).

It is important to note here that that some portion of the electrical energy from the water heater elements and circulation pump will not be fully converted into heat energy and absorbed up by the water. Instead this energy is expected to be dissipated as heat through other means, such as the heating of the circulation pump housing or the electrical wires themselves. As a result, there is an inherent uncertainty associated with amount of heat injected into the system, when we measure that solely based off of the electrical power consumption of each device. While a portion of this uncertainty in heat loss could be estimated using the surface temperature of the circulating pump and an estimation of its unknown convection and radiation coefficients, it can also be estimated by comparing it to the measured calorimetric heat transfer in the heat balance test. In other words, for our test loop, the amount of heat extracted from the system ($\dot{Q}$) should theoretically match the total power measured and any difference will represent the aforementioned heat lost elsewhere. Specifically any difference or "in-balance" in the heat injected ($\dot{W}$) and heat extracted ($\dot{Q}$) will shed light on the energy lost via the inefficiencies in the system components, or the dissipation of heat directly from the fluid to the surrounding room space.

The first series of heat balance test data collected were focused on evaluating the steady-state conditions of the test loop. While data would be collected continuously, only data recorded while the system was at steady state would be considered in the

heat balance. The reason for evaluating at steady-state conditions is so that at any instance in time, it would be proper to assume that all of the heat being injected into the loop (via the water heater elements and circulation pump), is simultaneously being extracted from the loop across the heat exchanger. Effectively the goal is to reach a controlled operating state, such that $\dot{Q}_{\mathrm{IN}} = \dot{Q}_{\mathrm{OUT}}$. The results of each energy meter's heat balance will be compared to give insight to the accuracy of measuring via clamp-on versus in-line ("invasive") means.

The procedure used to collect data for these steady-state conditions was performed by first running the circulation pump at approximately 2.0 GPM. After the flow rate was set, the fans were turned on, along with both of the energy meters. A few minutes of data were collected, to allow the previously-stagnant water to reach equilibrium with the room air. Then, both water heater elements were turned on for approximately 1 hour to heat up the water and reach steady-state. After 1 hour of being on, the heaters were turned off for about 40 minutes to allow the water to cool back down to room temperature. Table 5.2, shows the key details of this "Instantaneous Heat Balance Test".

Table 5.2: Instantaneous Heat Balance Test Key Characteristics

Nominal Flow Rate (GPM)	Heat Pulse Duration (min)		Heat Pulse Count (pulses)	Nominal Heat Pulse Magnitude (kWh)
	ON	OFF		
2.0	60	40	1	3.00

5.3 Cumulative Heat Balance

The other type of heat balance performed will be a cumulative heat balance. Rather than making an account for all the energy in and out of the system at a single instance in time or at an instantaneous, steady-state operating condition, an account of the heat in and out of the system will be evaluated over a period of time. This is a

useful heat balance to perform, as it allows for the accumulation of measurement error at varying operation conditions to take effect over time, as they would in real GSHP systems. In transient operation of thermal systems, the magnitude of the injection of heat is not immediately detectable from a typical calorimetric stand point. Often times the heating or cooling provided by a heat pump has a delayed response, as a result of some of the initial energy going towards heating up the fluid within the system. Additionally the initial heat injection could go towards heating up the immediate space around the compressor itself, before it initially reaches the room air. Furthermore, entire thermal systems as a whole (on a scale larger than just the heat pump itself) can have a transient response to a heat injection too. In general this delayed/transient response to a heat injection/extraction occurs in systems that are described as having a "thermal capacitance."

The "thermal capacitance" of a system is seen calorimetrically through the delayed, gradual change in temperature, whenever a heat pulse is first injected to or extracted from that system. Similar to the response of an electrical RC-circuit, a discrete-change or "step" input to a capacitive thermal system will also have a delay before it reaches its final steady-state condition. One general specification used to characterize this delay in capacitive systems is its "time constant" (τ). As illustrated in Figure 5.1, the time constant of a capacitive system is empirically defined as the amount of time it takes for the system to reach approximately 63% of the overall change. That specific percentage comes from the general formula used to model a capacitive system as exponential (Equation 5.1), with respect to time, in terms of its initial state (T_0), final state (T_F), and its time constant (τ). Specifically, when the time is equal to one time constant the value of the exponential term (e^{-1}) is approximately 0.368.

$$T(t) = T_0 + \left(1 - e^{(-t/\tau)}\right) \cdot \left(T_F - T_0\right) \tag{5.1}$$

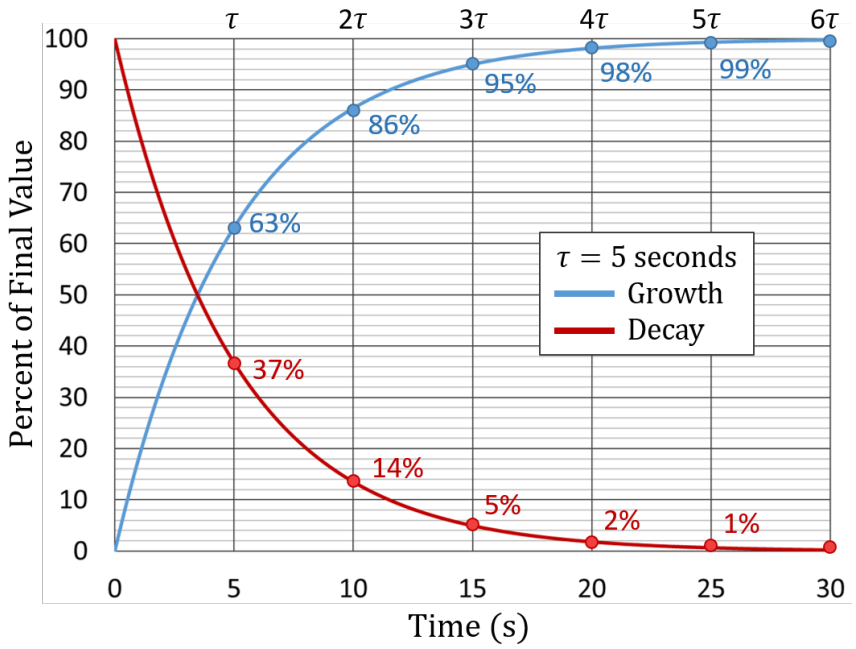

Figure 5.1: Plot showing the relative percentage of the overall change taking place during an exponentially decaying and exponentially growing function.

The plots in the following chapter (Ch.VI - Experimental Results) confirm this expected exponential response from the measured calorimetric heat transfer in our test loop. Further discussion and utilization of this transient relationship will be discussed in later sections.

This delay in the measurement of the calorimetric heat transfer at the beginning of a heat pulse injection and right after the pulse is turned off, can cause interesting limitations to the usefulness of an instantaneous heat balance. In general, the purpose of performing a controlled cumulative heat balance with different heat pulses of varying magnitude, frequency, and duration, will allow for better understanding of the accuracy of our energy meters relative to multiple transient/dynamic loads over time.

5.3.1 Continuous Circulation

The first type of cumulative heat balance data that were collected involved the circulation pump running continuously after the heating stopped. As mentioned previously,

the delayed response in calorimetrically detecting the true magnitude of the heat injected into the water, poses potential error in its cumulative measurement. Thus, in order to fully capture all of the heat injected into the water inside of our test loop, the circulation pump will continue to pump and dissipate the injected heat stored in the thermal capacitance of the test loop, for an extended amount of time after heating has turned off. With water flowing throughout the entirety of the test, up until all of the heat has been extracted out of the water and the system has effectively reached steady state with the room, any error due to the limitations of the calorimetric heat transfer measurement will be minimized.

The procedure used in these "Continuous Circulation, Cumulative Heat Balance Tests" started by turning the circulation pump on (approx. 2.0 GPM), along with the fans. Before any tests were recorded, in order to allow the previously-stagnant water to reach equilibrium with its surroundings, the pump was let run for 30 minutes. Then, for each test, the energy meters were started, and initial conditions were recorded for 5 minutes. Then, both of the water heater elements were turned on and left on for their specified amount of time. After the corresponding heat pulse was injected into the water in the test loop, the heaters were simultaneously turned off and the water left circulating for 30-40 minutes, or until the water had effectively reached equilibrium with the surrounding room air. Then, the heat injection process was repeated, for the remaining number of heat pulses that test entailed.

Table 5.3 shows a summary of all of the tests conducted with continuous water flow (approximately 2.0 GPM). Note that Test A was the same test used to collect data for the uncertainty analysis and the instantaneous heat balance test. The data set is the same (only recorded once), but the purpose of the analysis and calculations performed in each differs.

Table 5.3: Cumulative Heat Balance Test (Continuous Circulation) Key Characteristics

Test Name	Total Amount of Heat Injected (kWh)	Heat Pulse Count (pulses)	Duration of Each Heat Pulse (min)	
			ON	OFF
A	6.00	2	30	40
B	3.00	1	60	
C		2	30	
D		3	20	
E	2.50	1	50	
F		2	25	
G	2.00	1	40	
H		2	20	
I	1.50	1	30	
J		3	10	
K	1.00	1	20	
L		2	10	
M	0.50	1	10	
N		2	5	
O	0.25	1	5	

5.3.2 Cyclical Circulation

The final set of tests conducted in order to perform a cumulative heat balance, were tests wherein the circulating pump was shut off at a specified time after the heat pulse was injected. This series of scenarios were designed and developed, such that the cyclical nature of real residential GSHP systems could be simulated. More specifically, in most GSHP systems, the circulation pump will turn on and turn off at prescribed times before and after the compressor of the heat pump turns on and off respectively. The offset "power-up" and "shut-down" times between the circulation pump and compressor pump is implemented by the controls of the GSHP based on its pre-set parameters for operation. While this saves energy by not running the circulation pump as long before or after the compressor shuts off, this creates the potential for error in measurements of the heating and cooling provided, via calorimetric heat transfer measurements. Essentially, once the compressor shuts off, there is still the

potential for additional heating and cooling to be measured calorimetrically, but this is cut short once the circulation pump stops (i.e. the flow becomes 0, and effectively the measured calorimetric heat transfer as well). Thus, with such system operation limiting the effectiveness in measuring the true amount of heating and cooling provided to a space via continuous calorimetric heat transfer calculations, an improved means of estimating the total heating and cooling provided to the system would be advantageous.

In an attempt to replicate such a cyclical cycle, and investigate the energy meter's ability to estimate the total amount of heat injected into the loop, without calorimetrically measuring the heat after the circulation pump stops, the following "Cyclical Circulation Cumulative Heat Balance Tests" were performed. While the true dynamics and causes of a GSHP system's transient response is much more complex, the procedure followed is an attempt to provide a similar operation to that of a real GSHP in heating mode. The overall goal using our test loop will be to simply inject a known amount of heat into the test loop via the water heater elements (analogous to the "heating provided") and measure the initial cumulative calorimetric heat transfer up until the point when the circulation pump turns off. Then, using the system characteristics calculated during that initial time period, model parameters will be fit and used to further estimate the total amount of heat injected, despite the circulation pump turning off.

The same procedure as the Continuous Circulation tests described previously will be used, except that the amount of time between when the heaters turn off and the pump turns off is specified. Additionally, the amount of time the circulation pump will remain off between the two heat pulses injected is specified for each of these tests. To further clarify, just before the second heat pulse is injected (heaters switched back on), the circulation pump and fans are turned back on to make sure the 3.00 kWh of heat does not get injected into stagnant water. At the end of the second heat

pulse, the same amount of time is waited before turning the pump off. Then after the specified amount of time, the circulation pump is turned back on and let run until it reaches equilibrium with the room temperature and fully dissipates and remaining injected heat. The purpose of this final dissipation of heat is to compare the estimated total heat injection, with the realized calorimetric heat transfer measured, including that at the end.

Table 5.4 shows the key characteristics defining these additional non-continuous pump tests.

Table 5.4: Cumulative Heat Balance Test (Cyclical Circulation) Key Characteristics

Test Name	Total Amount of Heat Injected (kWh)	Duration of Individual Heat Pulses (min)	Circulation Pump OFF after... (min)	Next Heat Pulse ON after... (min)
P	3.00	30	40	5
Q	3.00	30	30	5
R	3.00	30	20	5
S	3.00	30	10	5
T	3.00	30	5	5
U	3.00	30	2	5
V	3.00	30	1	5

Along with these additional tests where the circulation pump will physically turn on and off while data is being measured, the previous Continuous Circulation test data will also be used to artificially simulate the circulation pump stopping prior to all of the heat injected being fully measured calorimetrically. Specifically this will be done by only considering the data up to a certain point after the heaters are turned off and then using the developed system model to estimate the response that "would have followed." That estimation will be compared against the true cumulative calorimetric heat transfer measured, along with the total electrical power measured (serving as an approximation of the total amount of heat injected into the loop).

After all of the heat balance-related tests were conducted, the corresponding sets of data were emailed, downloaded, combined, and saved for later analysis. The following

chapter will discuss the related analysis methods and results for the tests described in this chapter.

CHAPTER VI

Experimental Results

The following analyses described in this chapter were performed using the *Python* programming language coded within a *Jupyter Notebook*. Each of the individual scripts have been thoroughly commented and are available in the shared *Dropbox* folder referenced in Appendix C. As mentioned previously, the Test Loop Capacity data were collected prior to finishing the clamp-on energy meter's calibration, so its analysis is performed in a separate *Jupyter Notebook* written (`flow_rate_investigation.ipynb`). All of the other tests' analyses can be found in the other *Jupyter Notebook* (`test_loop_data_analysis.ipynb`). In order to run the respective analyses, the `Raw_Data` folders must be in the same directory as the *Jupyter Notebook*.

A few of the key *Python* libraries used throughout the analyses include: `Pandas` (for easy time-series analysis and data visualization); `Numpy` (for easy mathematical & scientific calculations); various `scipy.optimize` functions for curve fitting; `CoolProp`, specifically for the `CoolProp.PropsSI` function (for estimating fluid properties); and `matplotlib` (for plotting). *Python 3* was the version of Python utilized.

Each of the *Jupyter Notebooks* developed begin by importing the necessary libraries and uploading all of the respective raw data files. Next, any post-facto corrections to the data (merited from updated calibration constants since the raw data was originally recorded) were performed on the appropriate data sets. Next, all of the data from the clamp-on meter, in-line meter, and *HOBO Data Loggers* were combined in to one large *Pandas* data frame (similar to the format of a Microsoft Excel spreadsheet). The combined data frames were then re-sampled on 5 second intervals

and saved to individual `csv` files for quicker uploading in the future. Note that the 5 second re-sampling rate was determined by the 5 second sampling rate used to record the in-line turbine flow meter measurements. Next, the thermodynamic properties of the cold water (T_{EWT}) at each point in time were calculated, namely its specific heat (c_p) and density (ρ). These properties were calculated using the `CoolProp.PropsSI` function with the fluid type as 'Water' and the pressure assumed to be atmospheric (101.3 kPa).

In the following sections, the remaining data analysis processes for each series of tests are described individually and their respective results presented and discussed.

6.1 Test Loop Capacity

As a reminder, the purpose of the "Test Loop Capacity" tests was to more accurately determine the range of operating conditions that the validation test loop could achieve after it was officially assembled. The results will serve to characterize and put limits to the amount of heat transfer achievable with the current design. Since this data was collected a few months before the clamp-on energy meter was finished being calibrated, it uses just the in-line energy meter's data.

After the combined data collected at the four different flow rates were uploaded (as described previously), the system's "steady-state" conditions achieved during heat injection were calculated. This specific operating condition will be referred to as "steady-state-on." The data were parsed to only consider data recorded while the water heaters were constantly injecting heat, and the water temperatures reached their steady maximum temperature (effectively $\dot{Q}_{IN} = \dot{Q}_{OUT}$). Numerically this steady-state-on condition was determined through the use of two filters (or "masks") applied to *Pandas* data frames: the total power measured must be greater than 2000 W (i.e., heaters were on), and the hot-side water temperature must not be varying by more than ± 0.05 K (± 0.09 R) from its sample 1 minute prior (i.e., the

temperature was steady for at least 1 minute). Figures 6.1 through 6.4 show the resulting plots of the raw data. Note that the data considered as "steady-state-on" is clearly marked between the vertical dashed lines. The current measured by the *HOBO Data Loggers* were plotted, as well, so that a common y-axis scale could be used to display meaningful power-related data.

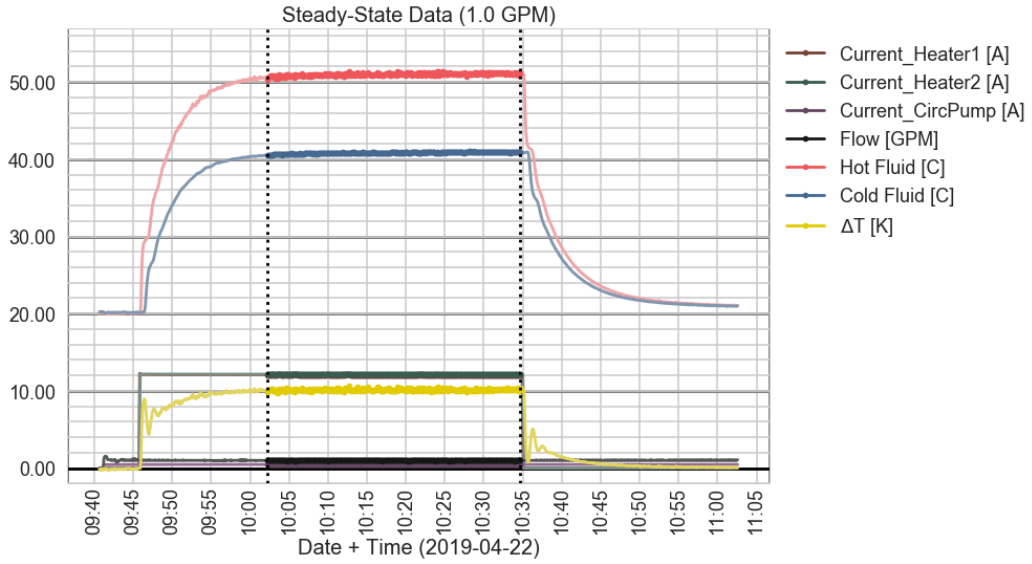

Figure 6.1: Plot showing the raw data considered as "steady-state" during the 1.0 GPM capacity test.

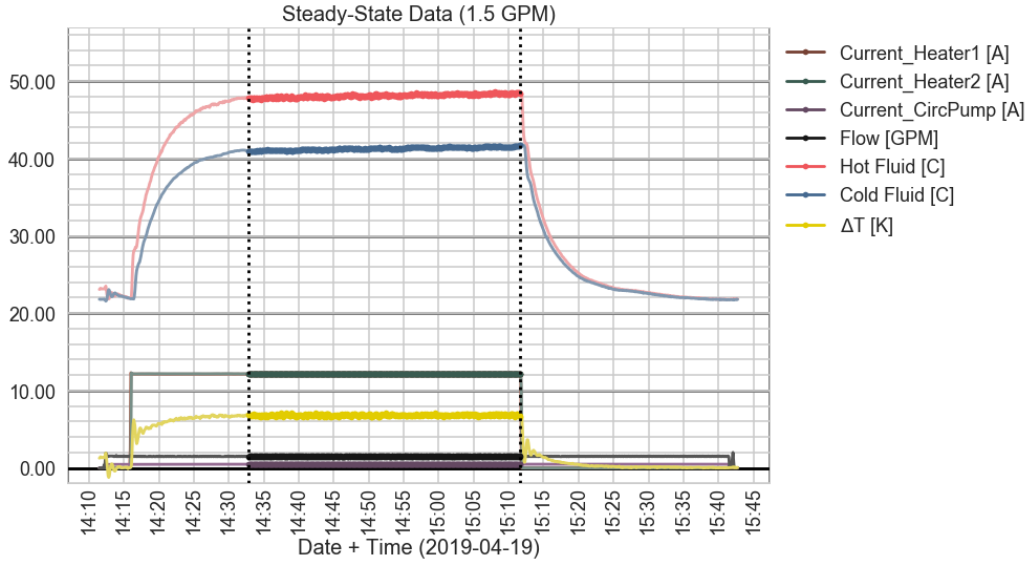

Figure 6.2: Plot showing the raw data considered as "steady-state" during the 1.5 GPM capacity test.

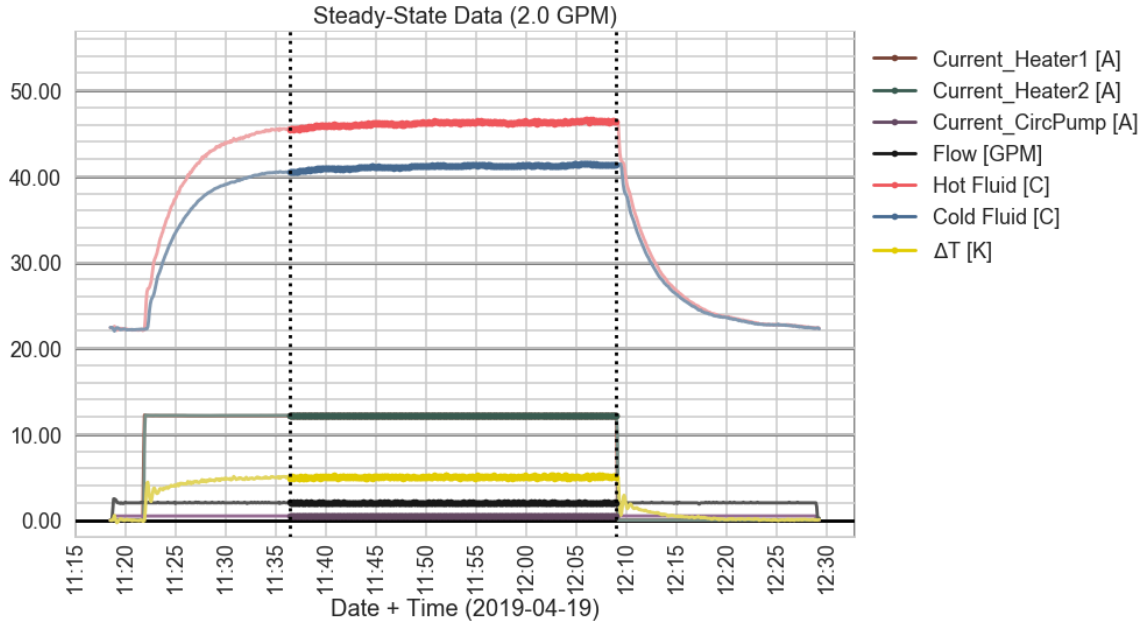

Figure 6.3: Plot showing the raw data considered as "steady-state" during the 2.0 GPM capacity test.

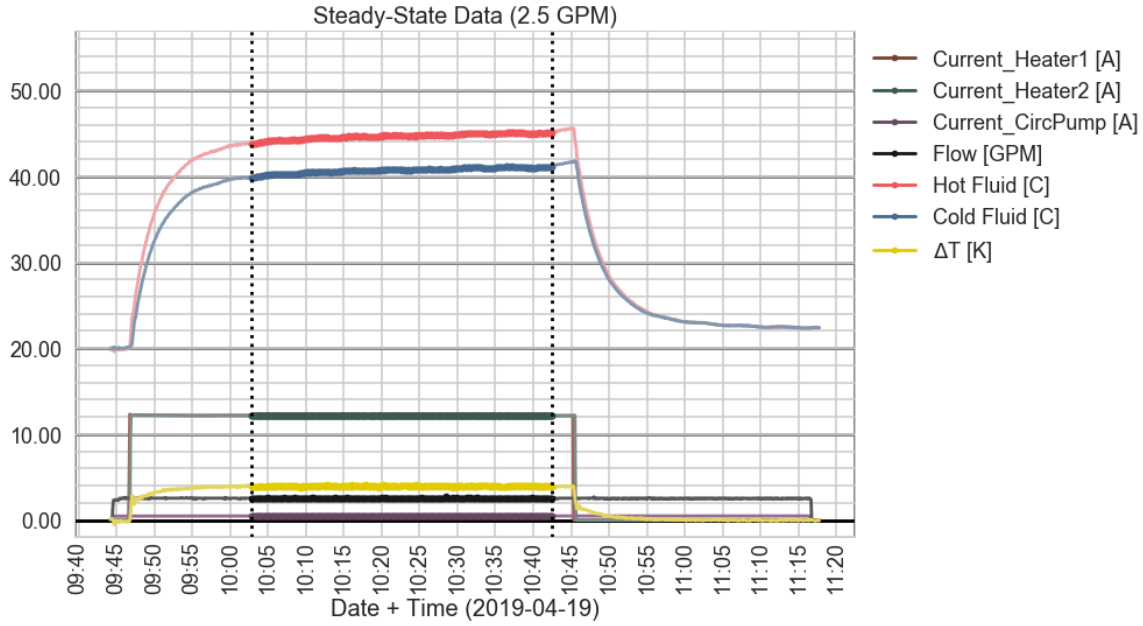

Figure 6.4: Plot showing the raw data considered as "steady-state" during the 2.5 GPM capacity test.

Next, each of the data that were marked as "steady-state-on" had their measurements averaged together. Table 6.1 summarizes the corresponding capacity tests' steady-state temperature conditions. These serve to show the range of various tem-

perature measurements attainable in our validation test loop, during operation at room temperatures of approximately 20.6 ± 0.5 °C (69 ± 0.9 °F). Most notably the achievable range of temperature differences (ΔT) across the heating section of the loop was determined to range from approximately 4.0 K to about 10.1 K (7.13 R to 18.2 R).

Table 6.1: Test Loop Capacity Tests - Temperature Results

Nominal Flow	ΔT ($T_{\mathrm{LWT}} - T_{\mathrm{EWT}}$)	T_{LWT} ("Hot-fluid")	T_{EWT} ("Cold-fluid")	T_{AVG} $\left(\frac{T_{\mathrm{LWT}}-T_{\mathrm{EWT}}}{2}\right)$
1.0 GPM	10.11 K *(18.2 R)*	50.94 °C *(123.7 °F)*	40.82 °C *(105.5 °F)*	45.88 °C *(114.6 °F)*
1.5 GPM	6.83 K *(12.3 R)*	48.13 °C *(118.6 °F)*	41.30 °C *(106.3 °F)*	44.72 °C *(112.5°F)*
2.0 GPM	5.01 K *(9.02 R)*	46.18 °C *(115.1 °F)*	41.18 °C *(106.1 °F)*	43.68 °C *(110.6°F)*
2.5 GPM	3.96 K *(7.13 R)*	44.68 °C *(112.4 °F)*	40.72 °C *(105.3 °F)*	42.70 °C *(108.9°F)*

This test also served as a means to locate spots where significant amounts of heat was leaking out from the pipe to the surrounding room space. Pictures were taken with an infrared camera during the hottest portions of these tests to identify such areas and then additional R-13 insulation was added where necessary. In addition to the infrared pictures given during the "Test Loop Development" chapter (arrayed in Figure 2.27), a few more are provided below. Figure 6.5 shows the heat leaks around the inside corner and bottom of the cold-side temperature port (T_{EWT}). Notice how the *8020* aluminum frame (just below the tee) was getting hot, so it was also wrapped in additional insulation. (Future modifications to the test loop could include putting thermal barriers such as heat resistant washers between the pipe clamps and framing.) Figure 6.6 shows the heat gradient at the bottom of the rotameter (where the water enters). After the flow rates were adjusted with the screw valve, insulation was put over the bottom face of the rotatmeter in order to prevent unwanted heat loss.

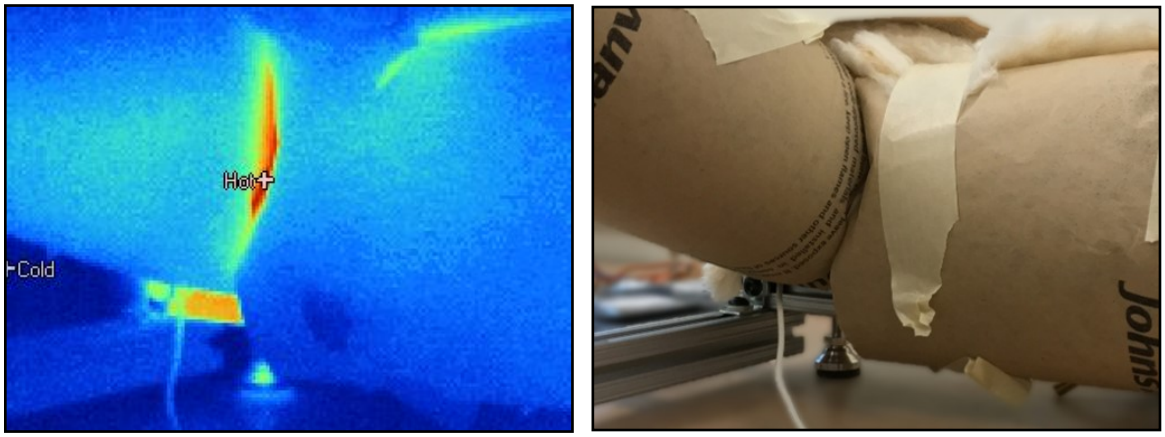

Figure 6.5: Pictures of the inside corner of the cold-side temperature port tee, taken during the capacity test runs (before additional insulation was added).

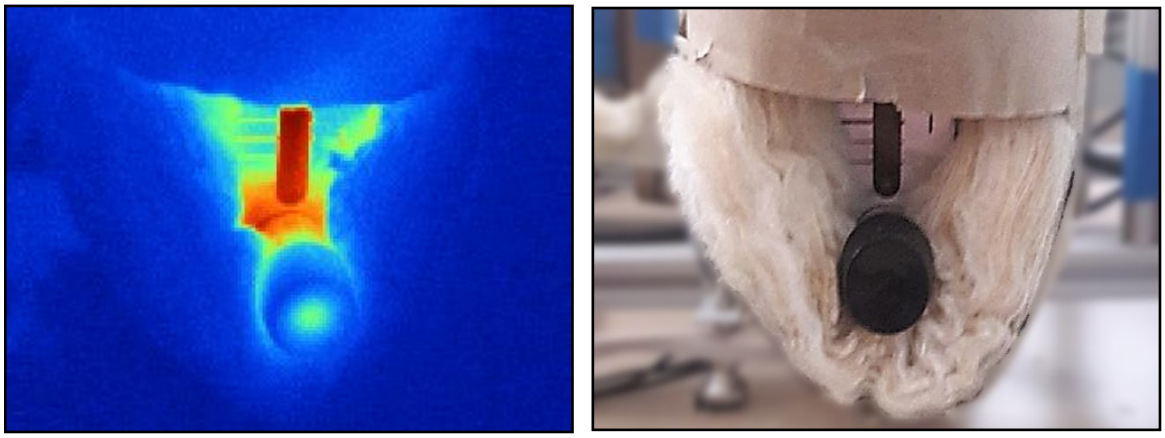

Figure 6.6: Pictures of the bottom of the rotameter, taken during the capacity test runs (before additional insulation was added).

As a result of insulation being added, the range of achievable temperature differences with the validation test loop was expected to have slightly increased from what was originally measured.

6.2 Instantaneous Heat Balance

The purpose of the "Instantaneous Heat Balance" test was to evaluate the accuracy of our energy meters by quantifying the amount of heat being injected to and extracted from the test loop at a single, "steady-state-on" operating condition. It is important to recall (as was discussed in the previous chapter) that there is an unknown uncertainty in our measurement of the heat injected into the system. Specifically, as a result of inefficiencies in the electrical devices, a portion of the measured total electrical power will not truly be transferred as heat into the fluid. This unknown uncertainty will be better approximated based on the results of this heat balance test.

Furthermore, there is an additional unknown uncertainty in the clamp-on thermistors temperature measurement, as a result of its position on the outside of the pipe and not truly in the center for the fluid flow. This will affect the clamp-on energy meter's temperature difference measurement and will add additional uncertainty to its overall calorimetric heat transfer measurement. Dealing with this unknown uncertainty associated with the thermistor's physical location will be addressed and discussed based on the initial results of this particular instantaneous heat balance.

In this instantaneous heat balance test, data were collected from both the in-line and clamp-on energy meters and combined using the procedure described previously. The raw data (excluding the voltage measurements) can be seen in Figure 6.7. Note that as anticipated, the clamp-on energy meter's temperature measurements were each varying from the in-line meter's temperatures, in the direction towards the room temperature. Also, note that the current transducers of the clamp-on energy meter are very closely following the professional *HOBO Data Loggers* measured current. This supports the high-accuracy with which we are able to measure the apparent power with the clamp-on energy meter.

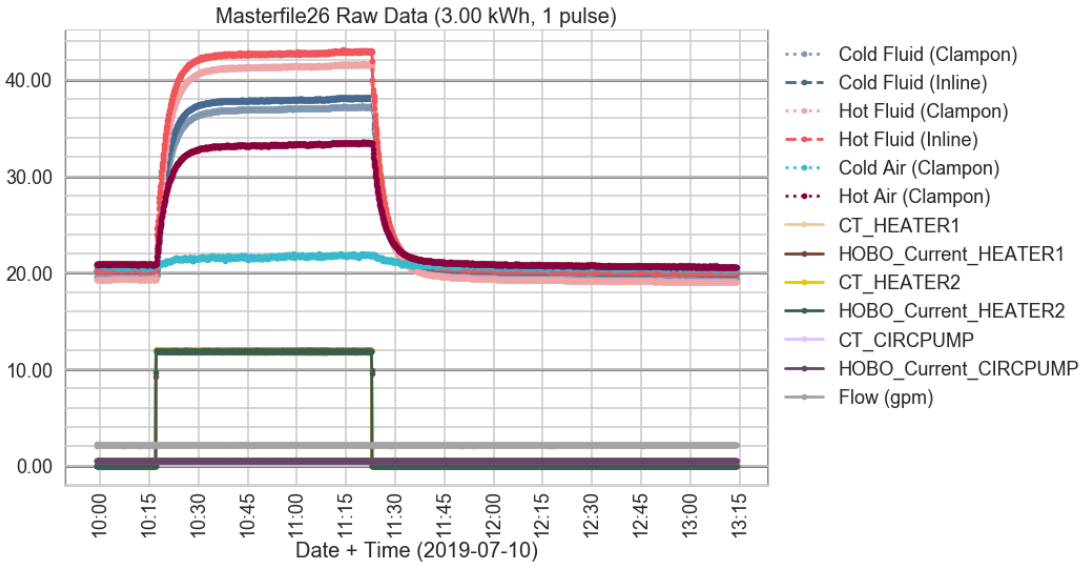

Figure 6.7: Plot showing the raw data considered during the instantaneous heat balance test (a single heat pulse injected of approximately 3.00 kWh).

Next, the instantaneous heat injection was estimated by summing all of the electrical devices' measured powers together. The instantaneous heat extracted was then estimated by calculating the overall calorimetric heat transfer, using the temperature measurements of each of the energy meters and the flow data from the in-line turbine flow meter. Figure 6.8 shows the initial measurements of instantaneous total electrical power and instantaneous calorimetric heat transfer over time.

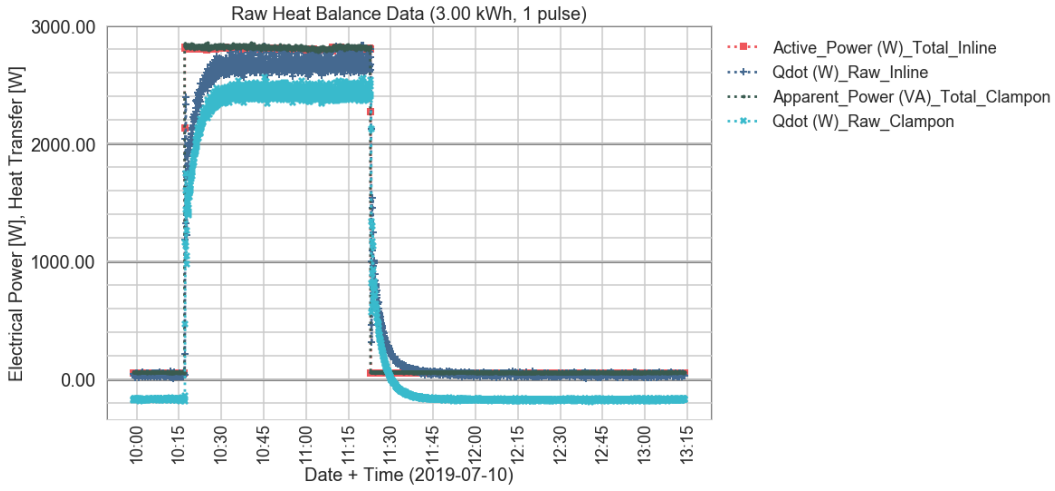

Figure 6.8: Plot showing the raw instantaneous electrical power and calorimetric heat transfer calculations during the instantaneous heat balance test (a single heat pulse injected of approximately 3.00 kWh).

As expected, the error in the clamp-on energy meter's temperature measurements (as a result of their physical location) can be clearly seen by its relatively lower instantaneous heat transfer measurements compared to the in-line meter's heat transfer calculation. At steady-state-on conditions, the clamp-on energy meter's raw calculation of instantaneous heat transfer measured 9% less of the total instantaneous power measured, compared to the in-line energy meter. The in-line energy meter's difference from the total instantaneous power measured is assumed to be the result of heat loss through the pipes to the surrounding space, as well as a result of the inefficiencies of the electrical devices causing less than 100% of their electrical energy to transfer as thermal energy into the fluid.

It was noted that the clamp-on temperature sensors behaved unexpectedly after the heaters turned off. More specifically once cooled back down to room temperature, the clamp-on meter measured negative values of instantaneous heat transfer, since its temperature difference was negative. This implies that the surface of the pipe is being continuously cooled by the surrounding room temperature whenever water is just being circulated around the loop. The expected behavior of the true water measurement was closer to that of the in-line energy meter's measurement, where a small amount of heat was being injected (as a result of the energy from the circulation pump). A side-investigation was then performed in the analysis, to attempt to better understand and correct the clamp-on energy meter's on-pipe temperature measurements.

6.2.1 On-Pipe Temperature Error Investigation

The expected temperature difference across the entering and leaving water temperatures can be estimated using a known heat injection at a known flow rate. Equation (6.1) shows the specific formula used to back calculate this expected temperature difference (ΔT) using a known electrical power measurement ($\dot{W}$) as the heat injection value, along with a known flow rate ($\dot{V}$), density (ρ), and specific heat (c_p).

$$\Delta T = \frac{\dot{W}}{\rho \cdot c_p \cdot (\dot{V})} \tag{6.1}$$

In hind sight, the amount of heat injected would have been easily assumed to be 0 W, had the only elements that could possibly inject heat between the two temperature ports been just the two water heater elements. Unfortunately, since the circulation pump was also placed between the two temperature ports as well, an estimation of the total amount of heat injected at a constant flow rate must be approximated by including the total power measurement from the circulation pump with the power from the water heater elements. Assuming the majority of the circulation pump's measured power is transferred as heat energy into the water, the estimated heat injection by the circulation pump (at 2 GPM) is about 56 W. Therefore, the corresponding expected temperature difference across the water (at room temperature) should be about 0.1 K (0.18 R).

In order to confirm that the true "center of pipe" temperature measurements (recorded by the in-line energy meter) are consistent with that expected value, temperature data was collected over the course of 8 hours while just the circulation pump was running. The fans were also turned on to allow the system to reach steady-state and not just dangerously heat the fluid continuously. Figure 6.9, shows the plot of that data's measured temperature difference, for both the in-line temperature sensors

and the clamp-on temperature sensors.

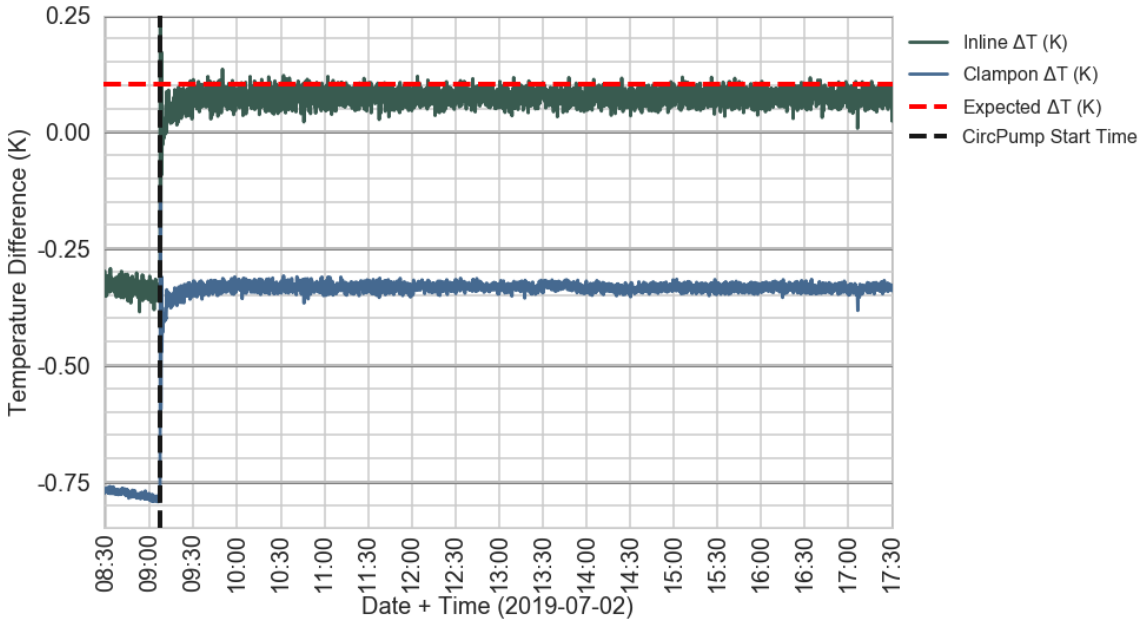

Figure 6.9: Plot showing the raw instantaneous electrical power and calorimetric heat transfer calculations during the instantaneous heat balance test (a single heat pulse injected of approximately 3.00 kWh).

As seen in Figure 6.9 once the test loop reached steady-state heat transfer with the surrounding room air, the average error in the temperature difference measurements for the in-line meter and clamp-on meter were approximately -0.026 K (-0.05 R) and -0.434 K (-0.78 R) respectively. Since, the in-line energy meter's temperature difference error was within the magnitude of it's absolute uncertainty ($\pm$ 0.066 K or $\pm$ 0.12 R), the previously estimated temperature difference based on the circulation pump power was confirmed. However the clamp-on energy meter's temperature difference average error was magnitudes larger than its calibrated uncertainty ($\pm$ 0.052 K or $\pm$ 0.09 R). This confirms that the clamp-on temperature sensor does have a significant error due to its physical location on the outside of the pipe.

Figure 6.10 shows the thermal resistance network we developed in order to estimate the intermediate temperature at the location of the clamp-on thermistors, between the center of the pipe and the outside room air. If the thermal resistances of the fluid & pipe section ($R_{\text{F-P}}$) and the insulation section (R_{INSL}) were both known, Equation

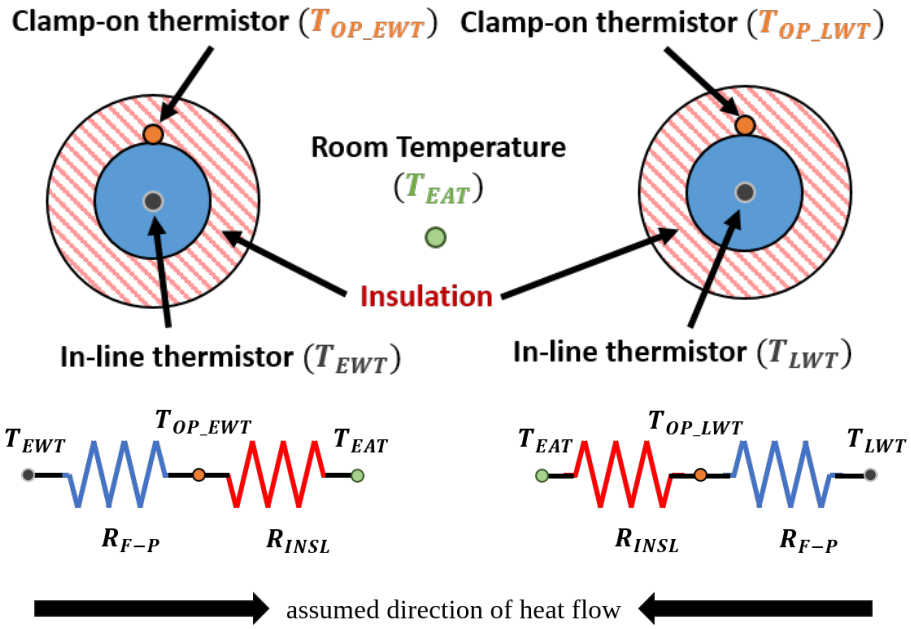

Figure 6.10: Diagram showing the cross-section of the pipe where the clamp-on energy meter's thermistors measure and a proposed thermal resistance network.

(6.2) could be used to estimate the true fluid temperature (T_{LWT} or T_{EWT}), given the entering room air temperature (T_{EAT}) and the clamp-on energy meter's respective "on-pipe" temperature (T_{OP}). Appendix G contains the complete derivation of Equation (6.2) from a basic heat transfer energy balance. Note that the "U-value" (or "overall heat transfer coefficient") of a material is the inverse of its thermal resistance (U = 1/R). A is the surface area of heat transfer.

$$T_{\text{EWT}} \text{ (or } T_{\text{LWT}}) = T_{\text{OP}} - \frac{(UA)_{\text{INSL}}}{(UA)_{\text{F-P}}} \cdot (T_{\text{EAT}} - T_{OP}) \tag{6.2}$$

Next we proceeded to use the original data we collected to try to estimate these two "UA-values". Specifically, since we had a set of known fluid temperatures, air temperatures, and on-pipe temperatures, an estimation of the ratio between the two UA-values was performed.

$$\widehat{T}_{\text{OP}} = \frac{T_{\text{F}}(UA)_{\text{F-P}} + T_{\text{EAT}}(UA)_{\text{INSL}}}{(UA)_{\text{F-P}} + (UA)_{\text{INSL}}} \tag{6.3}$$

Equation (6.3) represents an estimation of the on-pipe temperatures ($\widehat{T}_{\mathrm{OP}}$), given known fluid temperatures (T_{F}), entering air temperatures (T_{EAT}), and UA-values. By adjusting the UA-values to minimize the square of the error between this estimated on-pipe temperature ($\widehat{T}_{\mathrm{OP}}$) and the actual measured on-pipe temperature (T_{OP}), the ideal ratio between the UA-values can be found. For clarification, the objective function we used in our optimization is written out below (Equation 6.4).

$$\text{minimize}\Big((\widehat{T}_{\mathrm{ON\_EWT}} - T_{\mathrm{ON\_EWT}})^2 + (\widehat{T}_{\mathrm{ON\_LWT}} - T_{\mathrm{ON\_LWT}})^2\Big) \tag{6.4}$$

Using `scipy.minimize` to minimize the objective function, a set of "optimal" UA-values were generated for every measured data point. The initial guesses for the UA-values were selected to be 100 and 10 (with the insulation section having the latter initial guess, since it is much more resistive to heat flow than water & copper pipe). These initial values were arbitrary as it is the ratio between the two that is ultimately needed. The resulting plot of the estimated UA-values using the original instantaneous heat balance data is given in Figure 6.11.

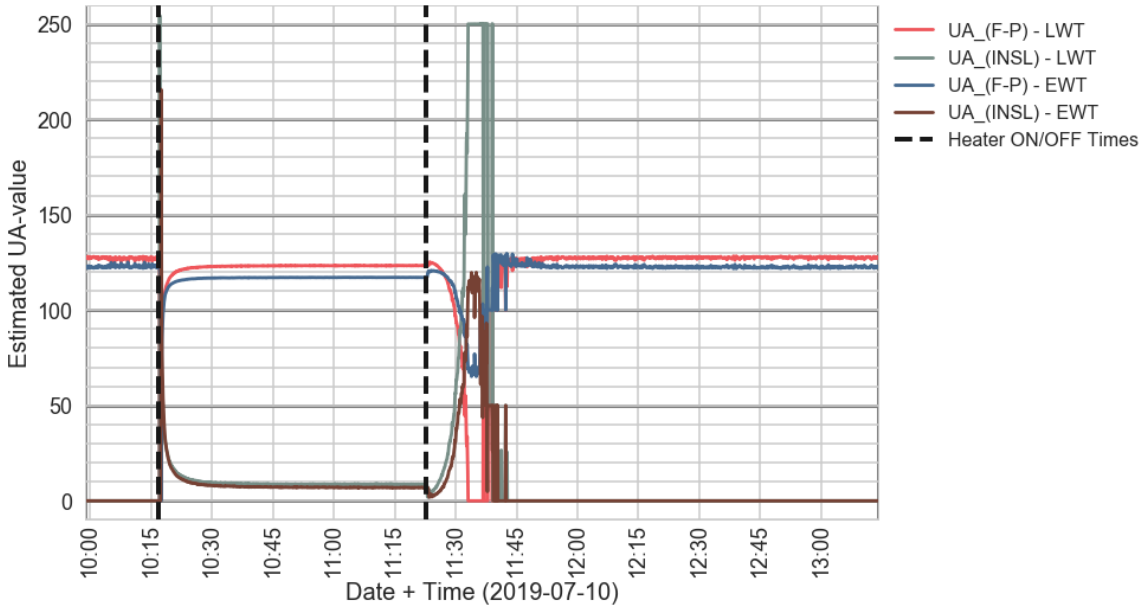

Figure 6.11: Plot of the estimated UA-values at every given data point in the original instantaneous heat balance data data set.

Note that for the time after the heaters were turned off, the optimization tool was unable to generate a meaningful solution. Specifically, the estimated UA-values for the insulation became effectively `0`. This is likely due to the assumed direction of heat transfer between the three temperature nodes in our thermal resistance network model changing when the heaters turned off. Thus, the formulated equation used to estimate the predicted on-pipe temperatures became no longer valid (Equation 6.3).

Further investigation should be done in the future to better estimate the UA-values when the direction of heat changes in our thermal resistance network model at various operating conditions. Specifically, an external heat source (connected to the node representing the surface of the pipe) should likely be included in the model, in order to account for the heat conducted from the over-heating circulation pump through the copper pipe and aluminum frame.

Due to time and man-power the UA-values that did converge were used and implemented to test their application across other recorded operating conditions. The implemented ratios between the two UA-values are given below. These were derived by calculating the average of all the converging solutions generated by the optimization tool).

$$\left(\frac{(UA)_{\text{INSL}}}{(UA)_{\text{F-P}}}\right)_{\text{EWT}} \approx \frac{1}{16.51} \approx 0.0606$$

$$\left(\frac{(UA)_{\text{INSL}}}{(UA)_{\text{F-P}}}\right)_{\text{LWT}} \approx \frac{1}{14.35} \approx 0.0697$$

Using these ratios above and Equation (6.2), the clamp-on meter's on-pipe temperatures were used with the measured air temperatures to estimate the true fluid's temperature in the center of the pipe. These new temperatures were then plotted against the original temperature difference measurements. Figure 6.12 shows the resulting temperature difference correction plot for Test Case F (which was data not used in the calibration of the UA-values).

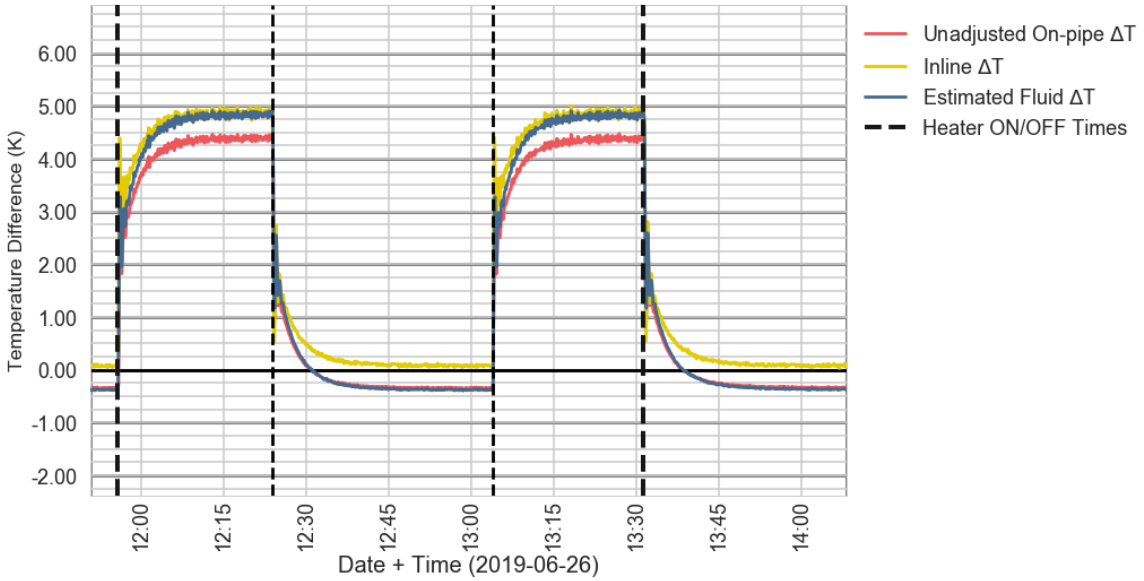

Figure 6.12: Plot of the adjusted and raw temperature differences measured during Test Case F (including the updated UA-adjusted clamp-on temperature estimates).

As expected, the estimated fluid temperatures had significantly improved accuracy (relative to the in-line temperature measurement), while the heaters were on for the "steady-state-on" operating condition. This confirms the path of heat transfer was modeled correctly and the associated UA-values ratio were accurate for that operating condition. However, there is still significant error in the estimated fluid temperatures whenever the fluid in the test loop is not as hot and therefore the predicted path of heat transfer changes. Further investigation on approximating the in-line fluid temperature, based on clamp-on "on-pipe" temperatures and room air temperatures is recommend as future work.

A heat balance was performed on the portion of data that had accurate clamp-on fluid temperature estimations. Specifically the instantaneous measurements of the heat injection ($\dot{W}$) and heat extraction ($\dot{Q}$) were averaged during "steady-state-on" operating conditions. "Steady-state-on" was again considered to be when all the heaters were turned on and the EWT ceased to vary by more than $\pm$ 0.05 K ($\pm$ 0.09 R) from its sample 1 minute prior. The instantaneous heat balance results are presented in the bar graph below (Figure 6.13).

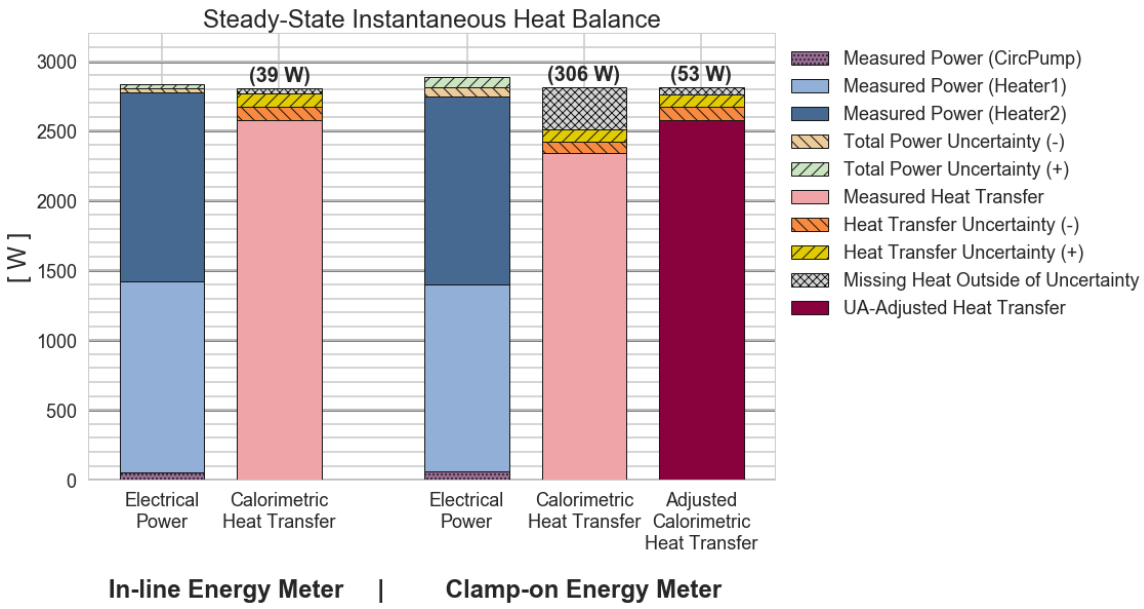

Figure 6.13: Bar plot of the measured heat injected and extracted during the steady-state instantaneous heat balance test.

Note that the top of the calorimetric heat transfer bars have a black and white, hatched section that represents the difference in heat measured calorimetrically and the total electrical power measured. The amount of heat listed above the calorimetric bars represents the "missing heat" beyond the instantaneous uncertainty associated with this operating condition.

The aforementioned "additional unknown uncertainty" related to the clamp-on thermistor's location can now be approximated as that specific amount of "missing heat" (for this specific operating condition). Table 6.2 summarizes the key results of this instantaneous heat balance at steady-state-on operating conditions. The absolute uncertainty of the "missing heat" measurement was calculated by adding the respective electrical power and calorimetric heat transfer absolute uncertainties in quadrature.

At this particular operating condition, the in-line energy meter was able to account for approximately 95% of the injected heat, and the clamp-on energy meter (after correctly modeling the thermal resistance network) was able to account for approximately 95% also. The remaining 5% of heat missing during this steady-state-on

Table 6.2: Instantaneous Heat Balance Results During "Steady-State-On" Conditions

	In-Line Energy Meter	Clamp-On Energy Meter	
		(On-Pipe)	(Adjusted)
Heat Injected ($\dot{W}$)	2805 ± 28 W	2815 ± 70 VA	
Heat Measured ($\dot{Q}$)	2670 ± 96 W	2423 ± 86 W	2670 ± 94 W
Abs. Missing Heat ($\dot{W} - \dot{Q}$)	135 ± 100 W	392 ± 111 W	146 ± 117 W
Rel. Missing Heat $\frac{(\dot{W} - \dot{Q})}{\dot{W}}$	4.8%	13.9%	5.2%

operating condition is likely either being lost as heat from the pipes to the surrounding room air, or from heat lost through inefficiencies in the electrical power injection. Further work could be done to experimentally measure the amount of heat lost through the circulation pump housing and prototype water heater element housings. Specifically one could potentially estimate the amount of heat lost (i.e. not injected into the fluid), if they measured the housings' surface temperatures and estimated the respective radiation and convection coefficients.

As a result of this clamp-on energy meter's need for further development in order to accurately estimate the true in-line fluid temperature, only the in-line energy meter's measurements will be considered in future tests' analyses.

6.3 Cumulative Heat Balance

As a reminder, the intended purpose of the "Cumulative Heat Balance Tests" was to provide better understanding of the accuracy of the developed energy meter's ability to measure total cumulative heat transfer over time, through various transient/dynamic loads. As introduced in the previous chapter, the apparent lag in the calorimetric response, due to the "thermal capacitance" of most HVAC systems, poses the potential for instantaneous errors in measured heat transfer to accumulate

as time goes on.

The general formulas used in the following analyses to accumulate uncertainty over time from instantaneous measurements are found below. Equation (6.5) was used to calculate the accumulation of instantaneous absolute uncertainties associated with the general measurement (F), accumulated over the time period (τ), made up of n samples with Δt_i time between samples. Equation (6.6) was used in the following analyses to calculate F's corresponding relative accumulated uncertainty over the same time period.

$$E_{F,\tau} = \sum_{i=1}^{n} E_{F,i} \cdot \Delta t_{\mathrm{i}} \tag{6.5}$$

$$e_{F,\tau} = \frac{E_{F,\tau}}{\sum_{i=1}^{n} F_i} \tag{6.6}$$

In the case of our energy meter, the sampling frequency was 5 seconds. The instantaneous calorimetric heat transfer rate ($\dot{Q}$) and instantaneous electrical power consumption ($\dot{W}$) were multiplied by the time difference between samples to calculate the cumulative electrical power (W) and cumulative heat transfer (Q) respectively during that sample.

6.3.1 Continuous Circulation

The 15 different heat injection scenarios proposed for the "Continuous Circulation, Cumulative Heat Balance Tests" varied in total heat injected, duration, and the number of heat pulses injected during the entire test. While varying in those characteristics, the main consistency between each scenario was that the circulation pump ran continuously. Calorimetric heat transfer data continued to be collected for a sufficient time after the water heater elements were turned off, so that the system cooled

off to a steady-state condition such that no remaining heat transfer was continuing to take place (other than the small amount provided via the circulation pump). Essentially the goal was to extract as close to 100% of the heat injected, without stopping the pump before it had all been measured calorimetrically. In total, measuring these 15 different heat injection scenarios took about 4 days. Future work should certainly include automating this recording process (with appropriate safety features implemented).

The 15 sets of combined data all had their instantaneous calorimetric heat transfer calculated, along with the corresponding instantaneous total power consumption measurements. Next, their instantaneous uncertainties were calculated at every data point. The total power consumption and the calorimetric heat transfer measured were plotted versus time (with their associated error bars shown every 10^{th} measurement). The 15 time-series plots are provided on the following pages (Figures 6.14 to 6.28).

Note how the exponential-like response of the system alluded to in the previous chapter can clearly be seen in each of these sets of data. This delayed response in calorimetric measurement is due to the "thermal capacitance" of the system. Specifically the heating provided is stored as internal energy and raises the overall temperature of the water, until the rate of heat transfer to the room air (across the heat exchanger) is equal to the rate of heat injection to the water (i.e., "steady-state-on" condition). Characterization of this delayed response will be performed in the following section.

It is also interesting to note that the aforementioned uncertainty as a result of inefficiencies in the transfer of electrical power completely to heat injected into the water can be visually seen as the electrical power measurement is continually about 100 watts greater than the measured heat transfer at "steady-state-on" conditions.

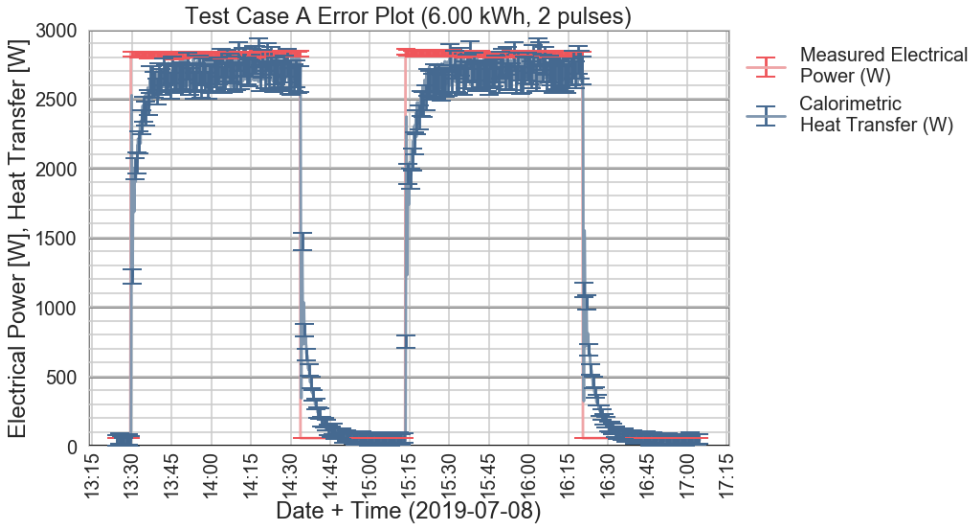

Figure 6.14: Measured power consumption and calorimetric heat transfer over time, during continuous pump Test Case A (6.00 kWh total over two 60-minute injections). Error bars indicate overall measurement uncertainty.

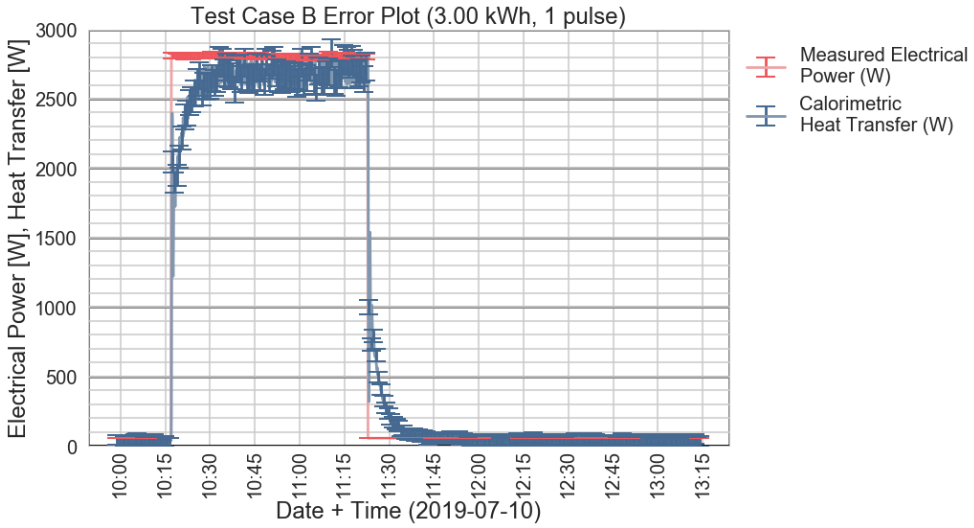

Figure 6.15: Measured power consumption and calorimetric heat transfer over time, during continuous pump Test Case B (3.00 kWh total over one 60-minute injection). Error bars indicate overall measurement uncertainty.

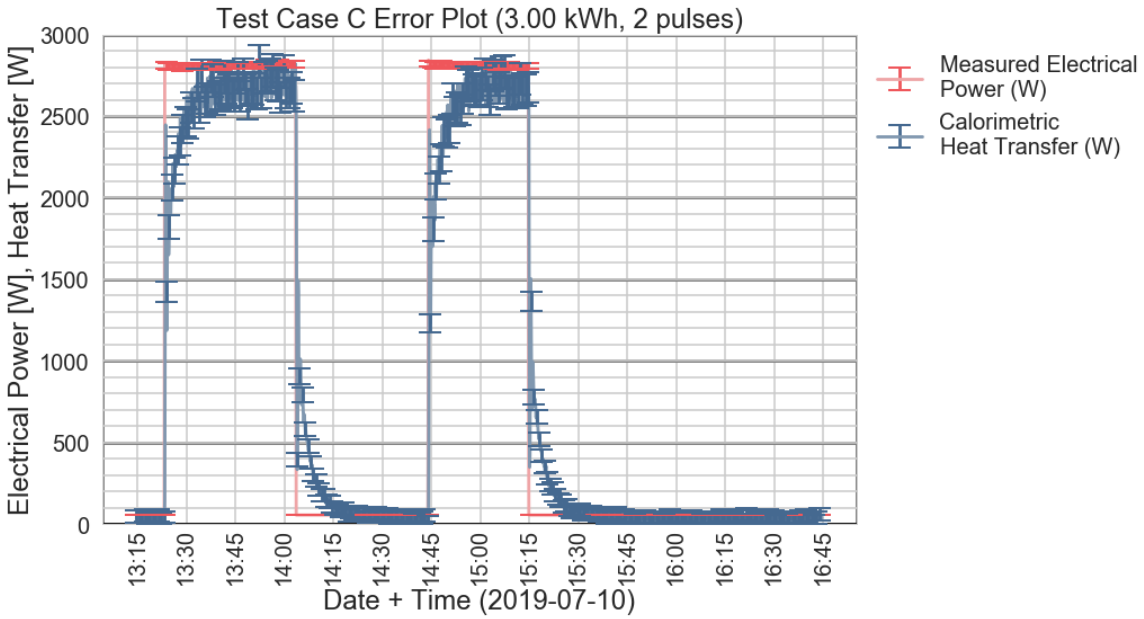

Figure 6.16: Measured power consumption and calorimetric heat transfer over time, during continuous pump Test Case C (3.00 kWh total over two 30-minute injection). Error bars indicate overall measurement uncertainty.

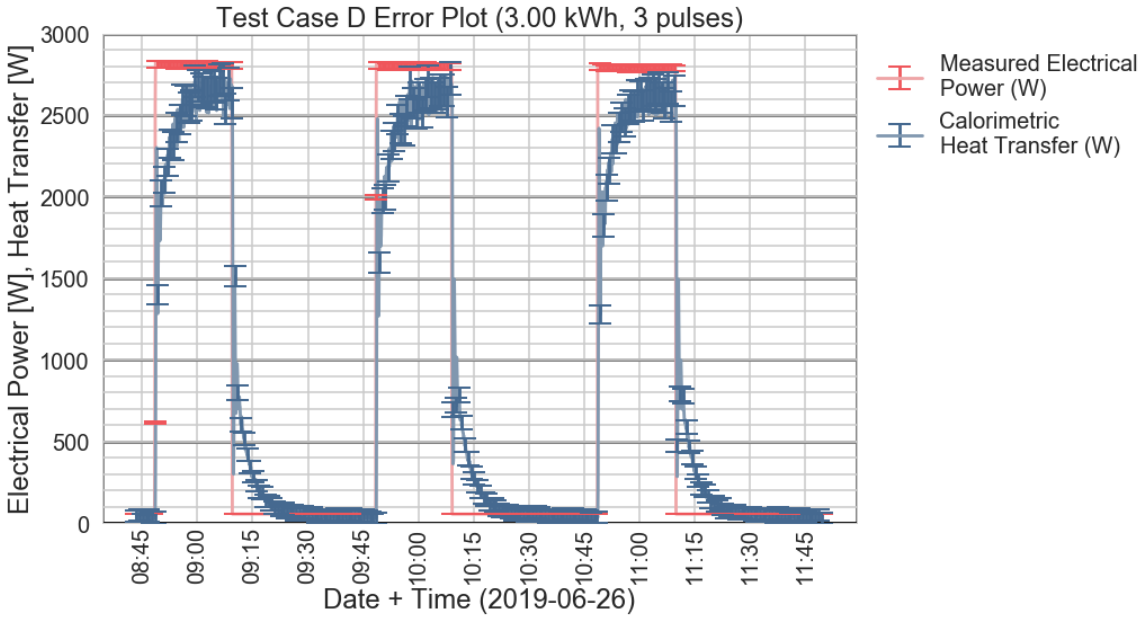

Figure 6.17: Measured power consumption and calorimetric heat transfer over time, during continuous pump Test Case D (3.00 kWh total over three 20-minute injection). Error bars indicate overall measurement uncertainty.

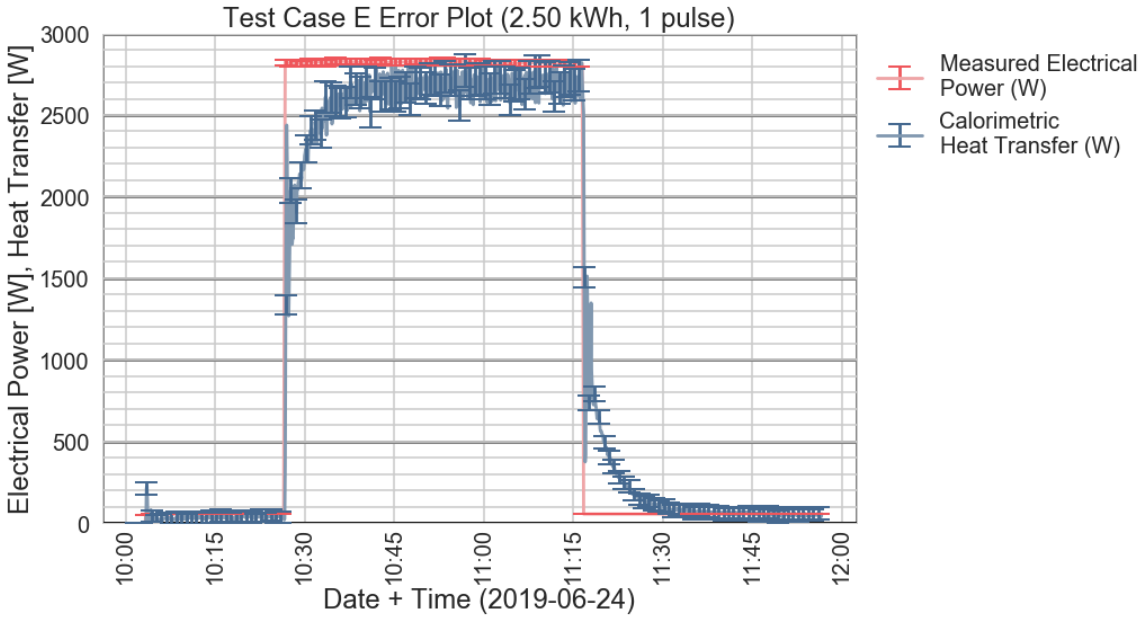

Figure 6.18: Measured power consumption and calorimetric heat transfer over time, during continuous pump Test Case E (2.50 kWh total over one 50-minute injection). Error bars indicate overall measurement uncertainty.

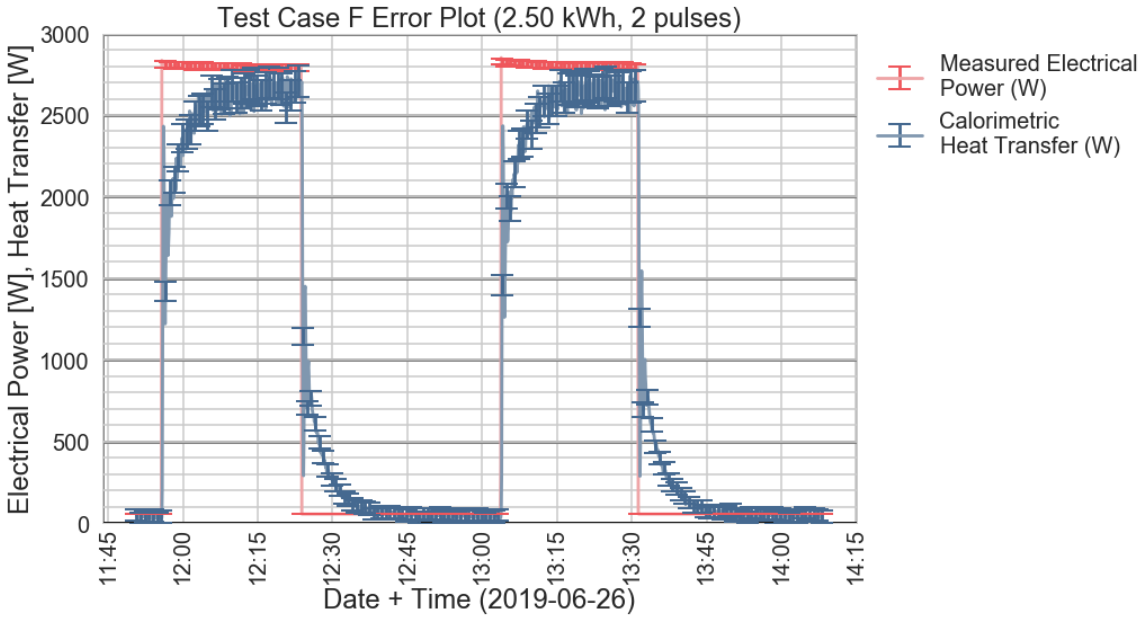

Figure 6.19: Measured power consumption and calorimetric heat transfer over time, during continuous pump Test Case F (2.50 kWh total over two 25-minute injection). Error bars indicate overall measurement uncertainty.

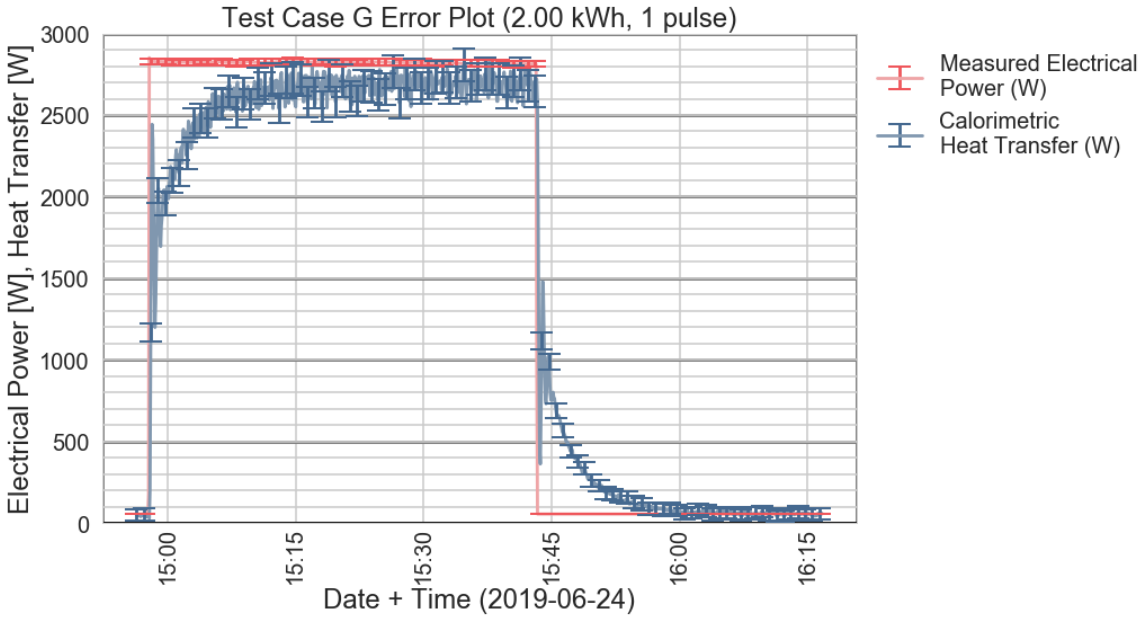

Figure 6.20: Measured power consumption and calorimetric heat transfer over time, during continuous pump Test Case G (2.00 kWh total over one 40-minute injection). Error bars indicate overall measurement uncertainty.

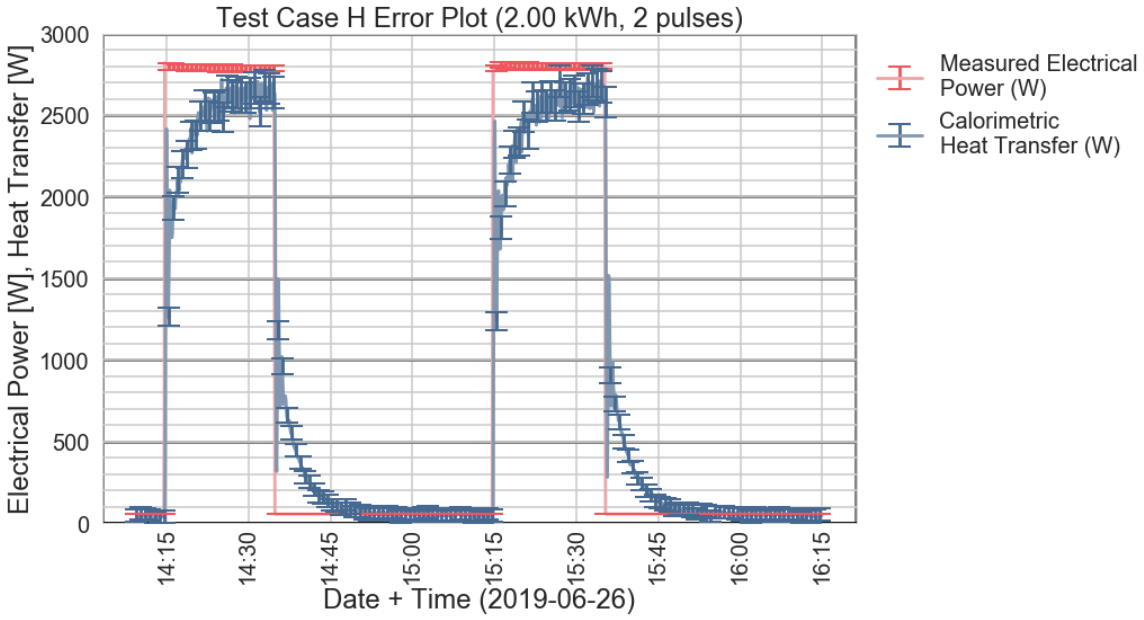

Figure 6.21: Measured power consumption and calorimetric heat transfer over time, during continuous pump Test Case H (2.00 kWh total over two 20-minute injection). Error bars indicate overall measurement uncertainty.

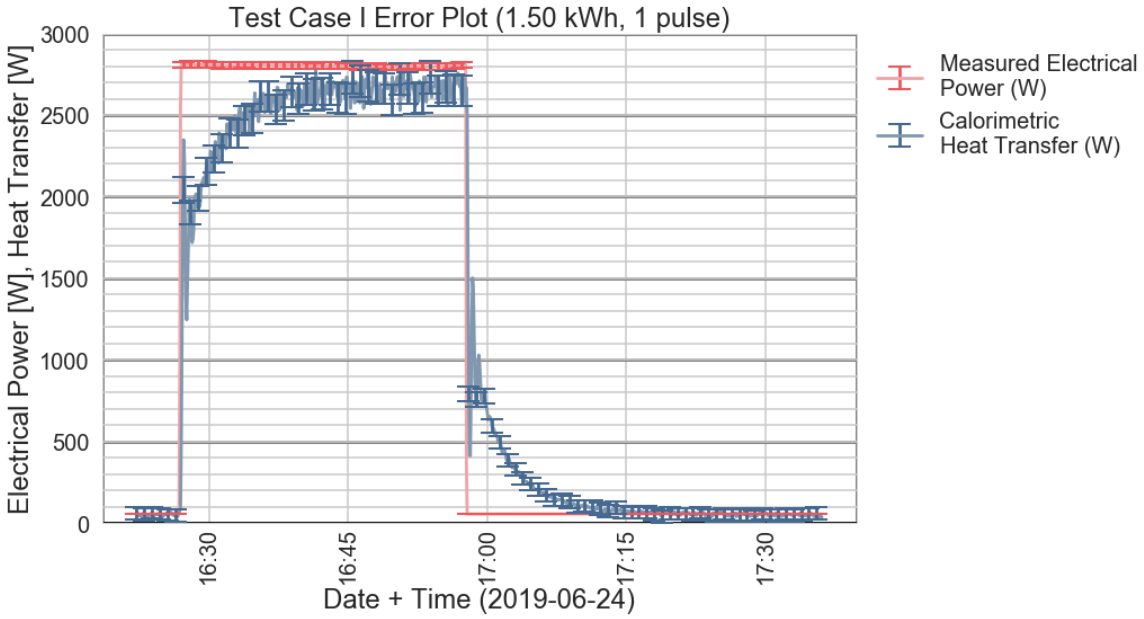

Figure 6.22: Measured power consumption and calorimetric heat transfer over time, during continuous pump Test Case I (1.50 kWh total over one 30-minute injection). Error bars indicate overall measurement uncertainty.

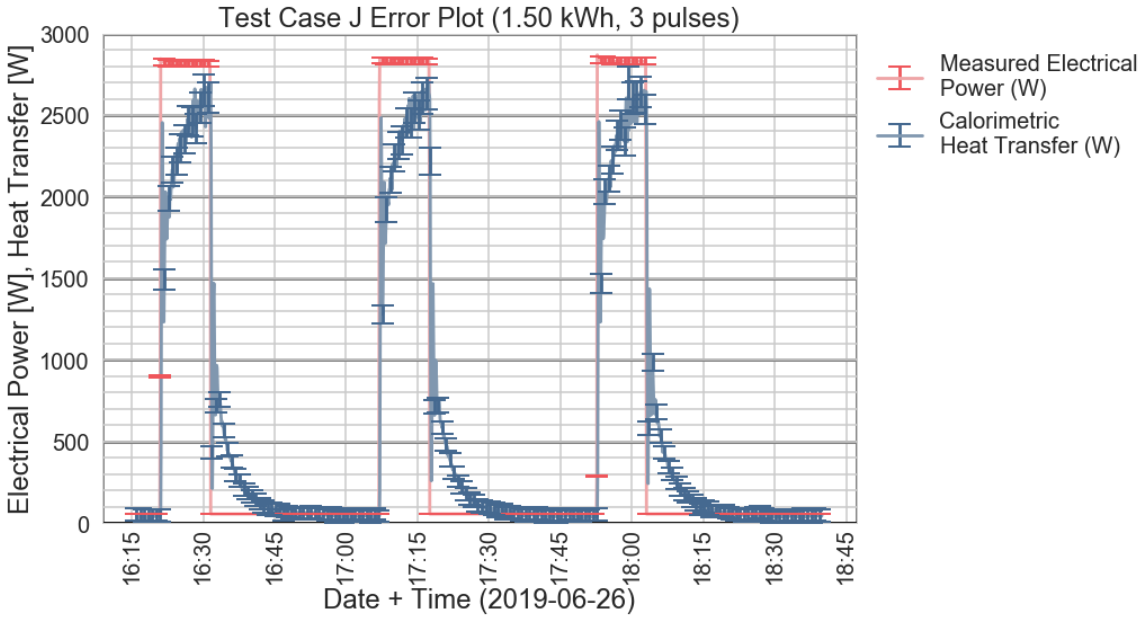

Figure 6.23: Measured power consumption and calorimetric heat transfer over time, during continuous pump Test Case J (1.50 kWh total over three 10-minute injection). Error bars indicate overall measurement uncertainty.

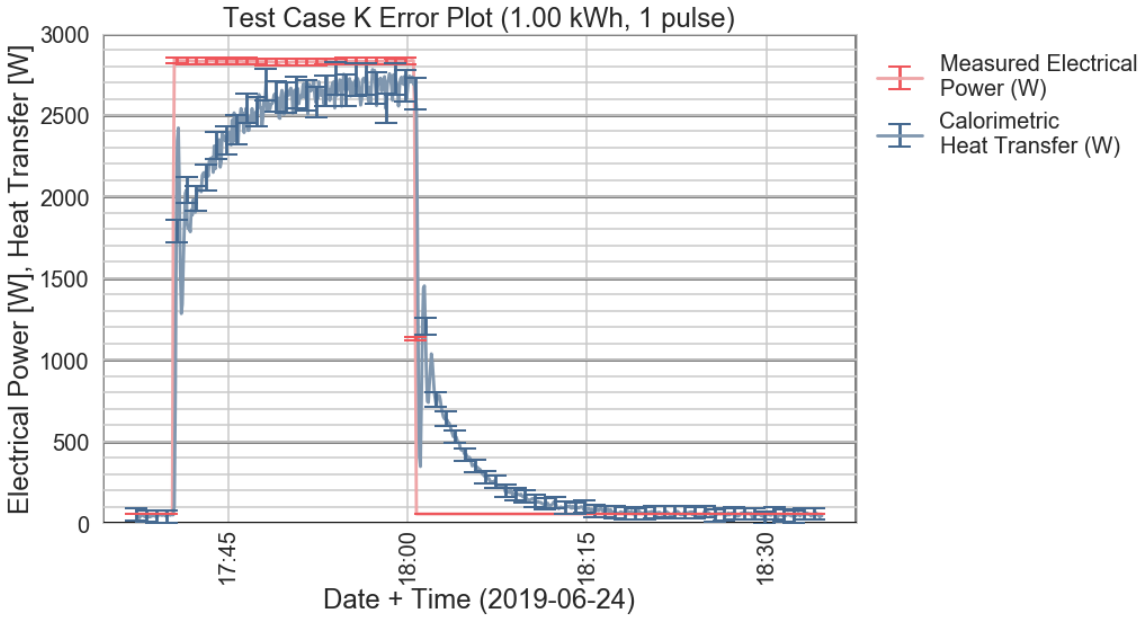

Figure 6.24: Measured power consumption and calorimetric heat transfer over time, during continuous pump Test Case K (1.00 kWh total over one 20-minute injection). Error bars indicate overall measurement uncertainty.

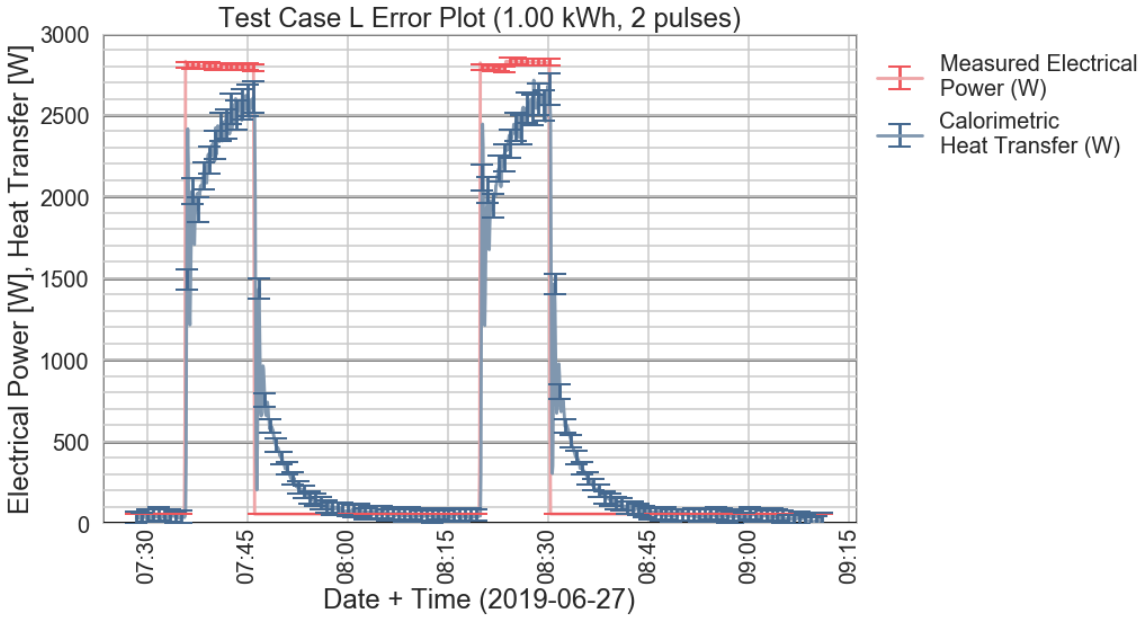

Figure 6.25: Measured power consumption and calorimetric heat transfer over time, during continuous pump Test Case L (1.00 kWh total over two 10-minute injection). Error bars indicate overall measurement uncertainty.

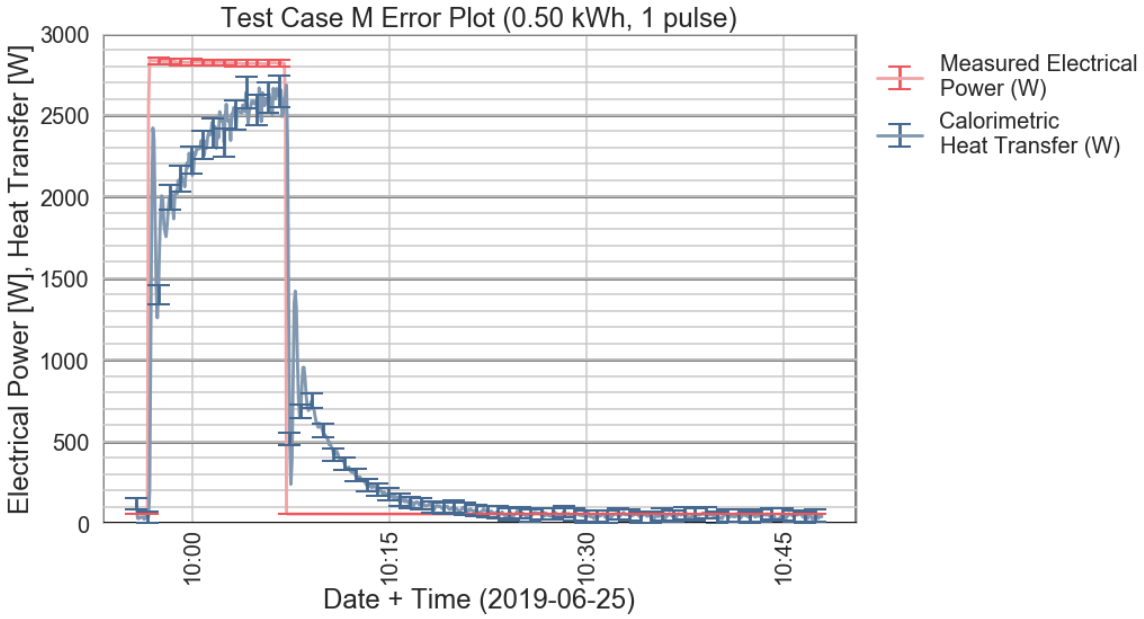

Figure 6.26: Measured power consumption and calorimetric heat transfer over time, during continuous pump Test Case M (0.50 kWh total over one 10-minute injection). Error bars indicate overall measurement uncertainty.

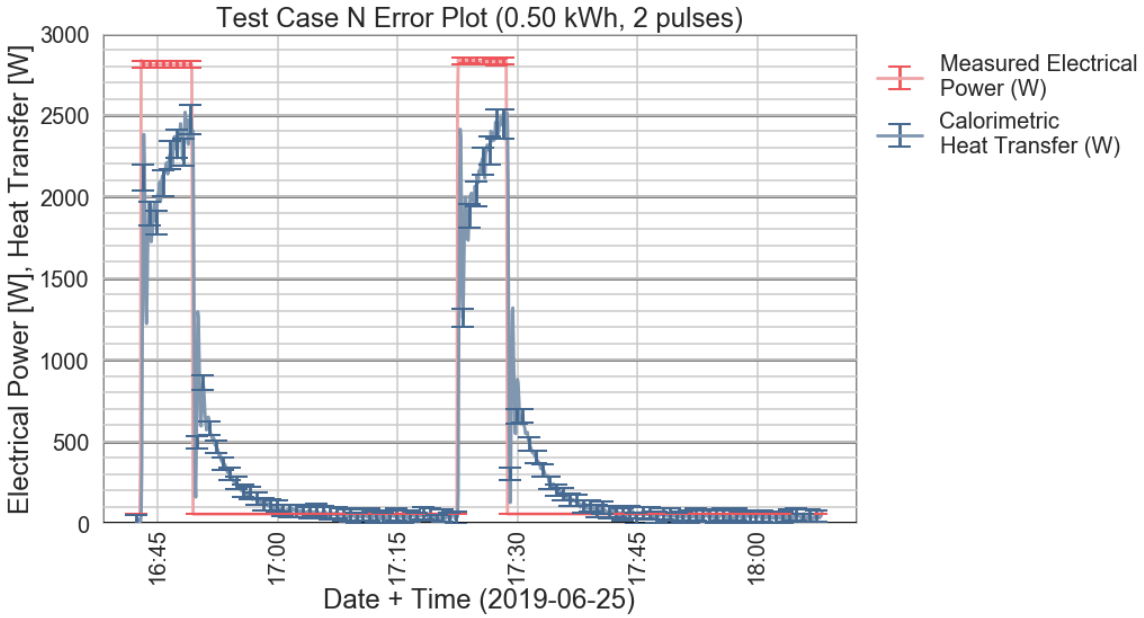

Figure 6.27: Measured power consumption and calorimetric heat transfer over time, during continuous pump Test Case N (0.50 kWh total over two 5-minute injection). Error bars indicate overall measurement uncertainty.

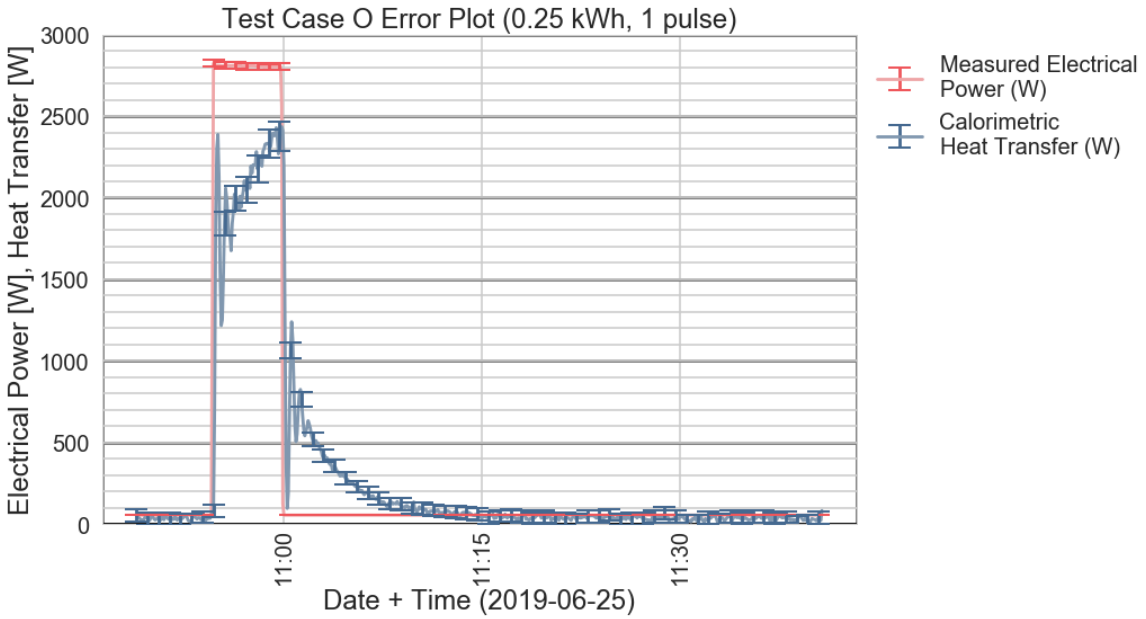

Figure 6.28: Measured power consumption and calorimetric heat transfer over time, during continuous pump Test Case O (0.25 kWh total over one 5-minute injection). Error bars indicate overall measurement uncertainty.

The next step in the analysis process was to calculate the total cumulative energy in and out of the system, along with their associated uncertainties (using Equations 6.5 and 6.6). This was easily performed when using *Pandas* data frames, as the difference between two time-series indices is easily calculable (using the `.diff()` function), as well as the sum of the columns containing the aggregated data. Graphically speaking, the measured accumulated energy of discrete time data is the area under the instantaneous heat/power curves. When the instantaneous energy measurement is multiplied by the duration of time between the next sample, this is effectively calculating the rectangular approximation of is discrete integral.

Figures 6.29 and 6.30 shows the "1-to-1" plot of the heat balance tests. The dashed line up the diagonal of the graph, represents the ideal relationship between the estimated cumulative heat injected (electrical energy consumption) and the cumulative heat actually measured. As can be seen by the linear regression line (also plotted), the cumulative calorimetric heat transfer was consistently under-measuring

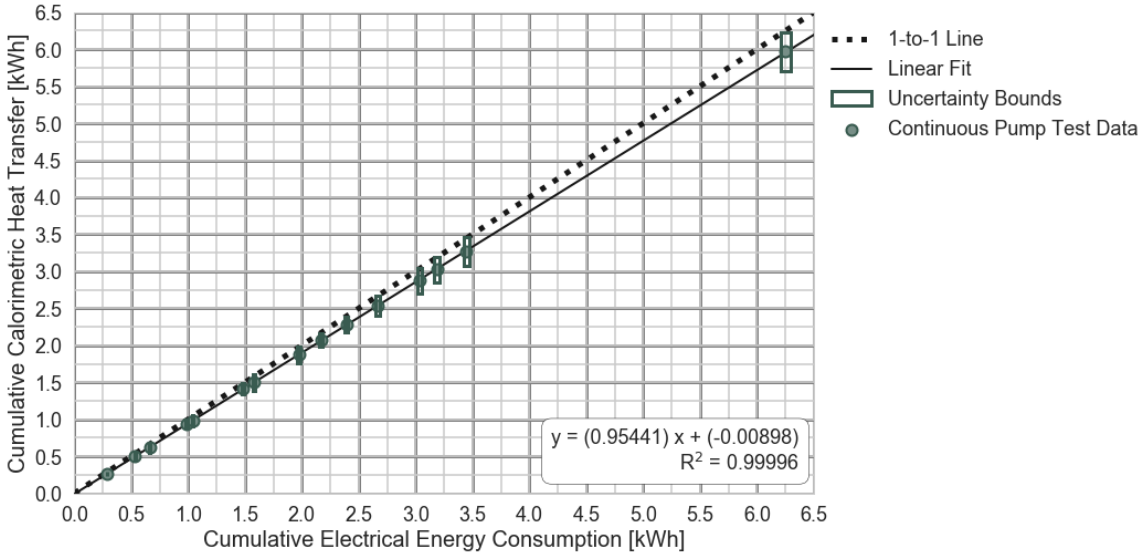

Figure 6.29: "1-to-1" plot of cumulative calorimetric heat transfer versus cumulative electrical energy consumption.

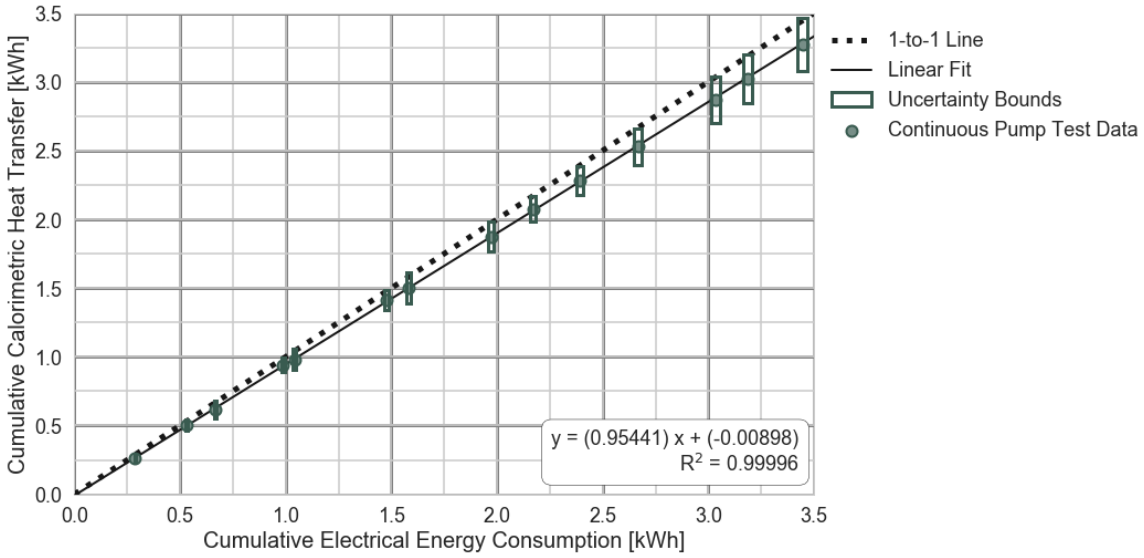

Figure 6.30: Zoomed in window of the "1-to-1" plot of cumulative calorimetric heat transfer versus cumulative electrical energy consumption.

the total electrical energy consumption measurement by about 5%. The coefficient of determination (R^2) is above 99.9% for the linear regression, suggesting that this 5% offset is a systematic/predictable error amount. Furthermore, the boxes showing the uncertainty bounds all encompass or overlap with the "1-to-1" line, confirming that the calibrated uncertainties may account for that missing 5% of cumulative heat.

However, it is more likely that this 5% error is a result of an over-estimation of the heat injected to they system due to inefficiencies in the electrical devices (e.g., heat lost through the un-insulated pump housing or electrical water heater element housings).

The same data presented in the "1-to-1" plot is shown in the following bar plots (Figures 6.31 and 6.32).

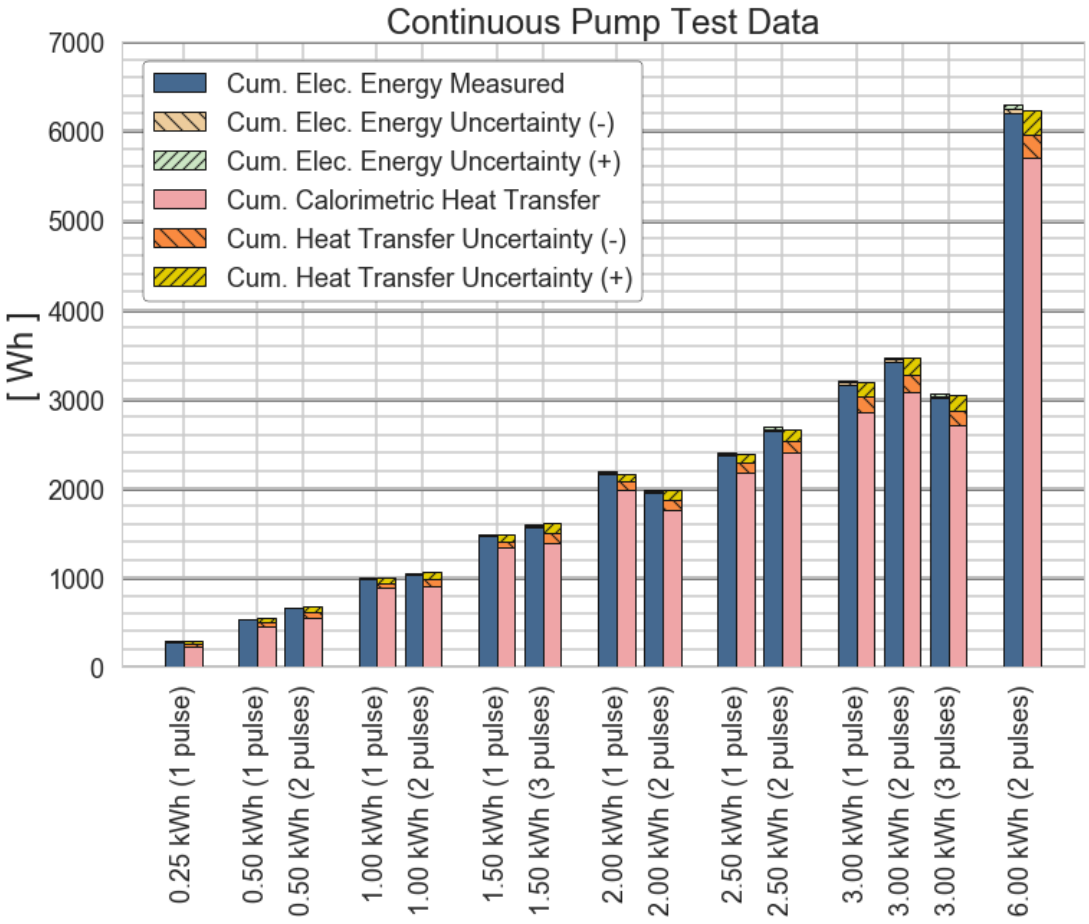

Figure 6.31: Bar plot of the continuous pump cumulative heat balance tests.

Notice that the uncertainties of both the calorimetric heat transfer measurements and electrical energy consumption measurements overlap in all but 4 of the test cases. This confirms, just like the uncertainty boxes plotted in the "1-to-1" plot suggested, that these heat balance tests were successful in identifying the in-line meter as being able to accurately measure the heat injected to the loop (specifically up to 5% of the total cumulative heat).

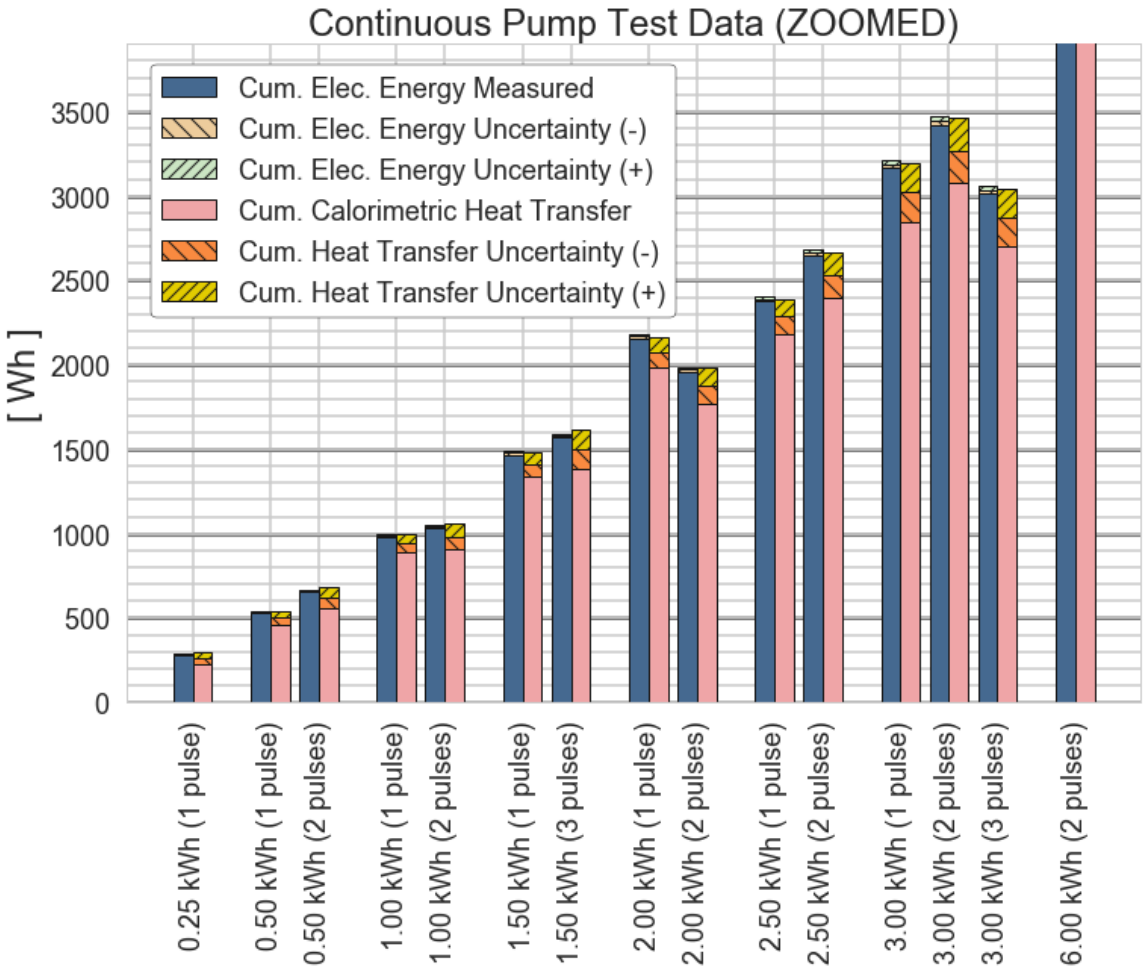

Figure 6.32: Zoomed in window of the Bar plot of the continuous pump cumulative heat balance tests.

Table 6.3 shows the data plotted for these continuous pump, cumulative heat balance tests. It also shows the measured "missing heat" and relative "missing heat" for each cumulative heat balance. The uncertainty for the absolute "missing heat" was calculated by adding the uncertainties of both the heat injected and heat measured uncertainties in quadrature (consistent with the general Equation (4.1) from the "Measurement Uncertainty" Chapter). Notice that in the cases when the uncertainty in the "missing heat" was smaller than the measured "missing heat", their respective cells in the table are colored red. These results give further evidence of our over-estimation of heat injection by not adjusting for the heat lost from the electrical devices that isn't injected into the water.

Table 6.3: Cumulative Heat Balance Results During "Continuous Circulation" Tests

Test Name	Heat Injected (W)	Heat Measured (Q)	Abs. Missing Heat ($W - Q$)	Rel. Missing Heat ($W - Q$) / W
A	6250 ± 44 Wh	5967 ± 262 W	283 ± 265 W	4.5%
B	3186 ± 22 Wh	3023 ± 174 Wh	164 ± 175 Wh	5.1%
C	3447 ± 24 Wh	3270 ± 192 Wh	177 ± 194 Wh	5.1%
D	3036 ± 21 Wh	2872 ± 168 Wh	165 ± 170 Wh	5.4%
E	2391 ± 17 Wh	2285 ± 104 Wh	107 ± 106 Wh	4.5%
F	2667 ± 19 Wh	2531 ± 134 Wh	137 ± 135 Wh	5.1%
G	2170 ± 15 Wh	2074 ± 93 Wh	96 ± 94 Wh	4.4%
H	1972 ± 14 Wh	1876 ± 111 Wh	96 ± 112 Wh	4.9%
I	1479 ± 10 Wh	1412 ± 72 Wh	67 ± 73 Wh	4.5%
J	1581 ± 11 Wh	1500 ± 113 Wh	81 ± 113 Wh	5.1%
K	988 ± 7.0 Wh	942 ± 53 Wh	45 ± 53 Wh	4.6%
L	1042 ± 7.4 Wh	982 ± 77 Wh	59 ± 77 Wh	5.7%
M	532 ± 3.8 Wh	503 ± 41 Wh	30 ± 41 Wh	5.5%
N	665 ± 4.8 Wh	617 ± 63 Wh	48 ± 63 Wh	7.3%
O	287 ± 2.1 Wh	263 ± 33 Wh	23 ± 33 Wh	8.1%

6.3.2 Cyclical Circulation

As explained in the previous chapter, the purpose of the cyclical circulation tests were to evaluate a potential methodology for better estimating the total amount of heating/cooling provided by a thermal system, after the circulation pump turns off. As seen in the previous analyses, thermal capacitance causes the true magnitude of the total heating and cooling provided to be measured with a lag based on calorimetric heat transfer measurements. That lag in the true measured magnitude of the heat transfer rate behaves similarly to a standard exponential growth/decay function. Specifically during the immediate time following a change in the amount of heat being injected, heat stored as internal energy inside the loop will cause the calorimetric heat transfer rate measurement ($\dot{Q}$) to gradually change to its new magnitude. However, should the system's flow become effectively `0`, as a result of the circulation pump turning off (or fans turning off), the calorimetric heat transfer measured will also become effectively `0`. Estimating the remaining, unmeasured amount of heating provided to the system after the circulation pump turns off (that has been stored as

internal energy in the system), will be investigated in this section.

This analysis will attempt to predict the total amount of heating provided to our test loop by creating a model of the test loop's expected response in rate of calorimetric heat transfer using a generalized exponential function. The exponential function used to model the expected response of calorimetric heat transfer rates is written below (Equation 6.7).

$$\widehat{\dot{Q}}(t) = \dot{Q}_0 + (1 - \exp -t/\tau) \cdot \left(\dot{Q}_{\mathrm{SS}} - \dot{Q}_0\right) \tag{6.7}$$

Note that the expected magnitude of instantaneous rate of heat transfer measured ($\widehat{\dot{Q}}$)is a function of 4 parameters: time (t), initial heat transfer rate ($\dot{Q}_0$), steady-state heat transfer rate ($\dot{Q}_{\mathrm{SS}}$), and a time-constant (τ). For known operating conditions (such as full compressor power or no load circulation), the steady-state heat transfer rate can be theoretically predicted. However the initial heat transfer rate must be measured and implemented based on previous system data. Additionally, the time-constant (τ) for a system, must be empirically measured based on known operating conditions in order for the model to fit correctly. Once the measured instantaneous heat transfer rate is modeled, the approximation of the discrete integral of that curve can be used to estimate the total amount of heat injected.

It it important to note that while our test loop is relatively simple, having only a single-speed circulating pump, and two constant-injection water heater elements, real GSHP systems are much more complex. Some key differences to note before proceeding include the variable rate of heat injection and cooling in a real system. The rate at which heating and cooling is provided to a real system changes as a result of changing ground temperatures, thermostat settings, environmental parameters, occupants, and electronic heat loads inside. In larger, more complex systems, the increased number of individual sub-systems make for a more complex overall system response. Each of the individual components themselves (e.g., the compressor, the

ground loop, the air distribution system, etc.) all have their own individual "thermal capacitances" that make up the overall system's thermal capacitance. Additionally, in more complex systems, there are a multitude of possible operating conditions, all of which have their own respective responses to heat-injection, based on how they change and direct the flow of building air and ventilation.

While future work could be done to better characterize and predict the amount of heating provided for more complex, real-world systems, this analysis will attempt to implement a model on our simplified verification test loop system. The main assumption that characterizes our simplified model is that the heat injection rate is considered to be relatively constant, such that our model (the response of a first-order system to a step input) will be considered reasonable.

The seven test cases (Test Cases P - V) recorded originally for this test took about two days to record. They required constant attention in order to keep track of time and turn the circulation pump and water heaters on and off as specified. In hind-sight, it was realized that the "Continuous Circulation" data previously collected could be used to artificially simulate the circulation pump turning off. This was done for a few of the "Continuous Circulation" test cases in the following analysis, in conjunction with Test Cases P - V, by manually setting the flow rate to 0 at exactly 1.5 minutes after the heaters turned off.

After recording and backing up the raw data, corresponding *Pandas* data frames were made for all the test cases considered. After the instantaneous heat transfer rate measurements ($\dot{Q}$) were made and plotted for the entire data set, the implementation of our heat transfer model began. The specific function `curve_fit` (from the `scipy.optimize` *Python* library) was used to estimate the unknown parameters in the following investigation.

The exponential model (Equation 6.7) was fit to the first rising response in each of the instantaneous calorimetric heat transfer data sets obtained. Specifically, two

methods of curve fitting were investigated. The first approach fit the model using test cases where both the initial heat transfer rate ($\dot{Q}_0$) *and* steady-state heat transfer rate ($\dot{Q}_{SS}$) were known. In other words, just the time-constant (τ) needed to be fitted for the data sets in the first curve fitting method implemented. The second method of implementation attempted to estimate not only the system's time-constant (τ) using the first heat pulse, but also the steady-state heat transfer rate it was approaching ($\dot{Q}_{SS}$).

Table 6.4 lists all the test cases and the respective curve fitting method implemented during their analysis.

Table 6.4: Curve Fitting Method Implemented

Test Name	Curve Fitting Method 1 (just τ estimated)	Curve Fitting Method 2 ($\dot{Q}_{SS}$ & τ estimated)
B	✓	
C	✓	
D		✓
E	✓	
F	✓	
G	✓	
H		✓
I	✓	
J		✓
P	✓	
Q	✓	
R	✓	
S	✓	
T	✓	
U	✓	
V	✓	

Figure 6.33 shows an example of the model's curve fitted to the first heat pulse's response, using the first investigated method (known initial and steady-state heat transfer rates, $\dot{Q}_0$ and $\dot{Q}_{SS}$). Figure 6.34 shows an example of the model's curve fitted using the second method investigated (estimating both the time-constant (τ) and the steady-state heat transfer rate ($\dot{Q}_{SS}$) it was thought to be approaching).

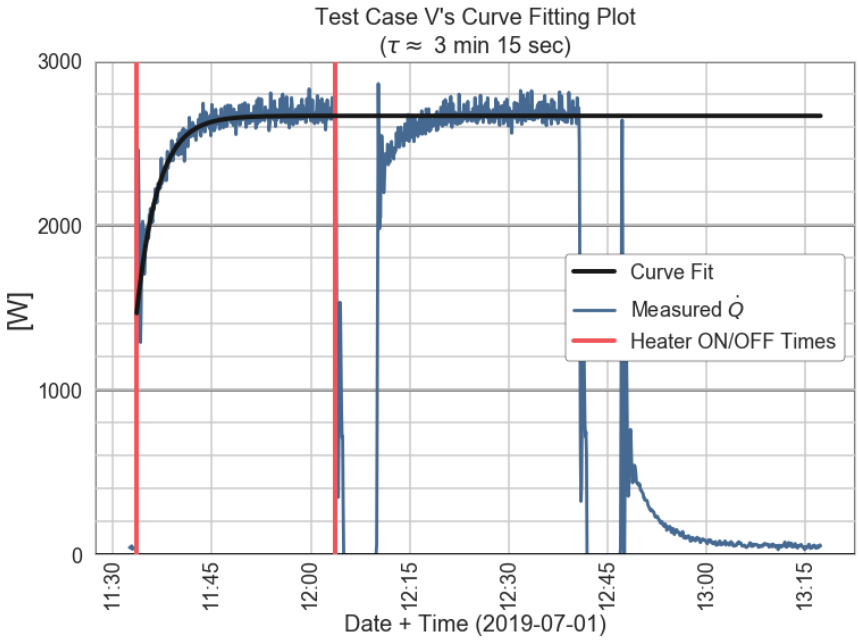

Figure 6.33: Example of curve fitted using method 1 (estimating time-constant only).

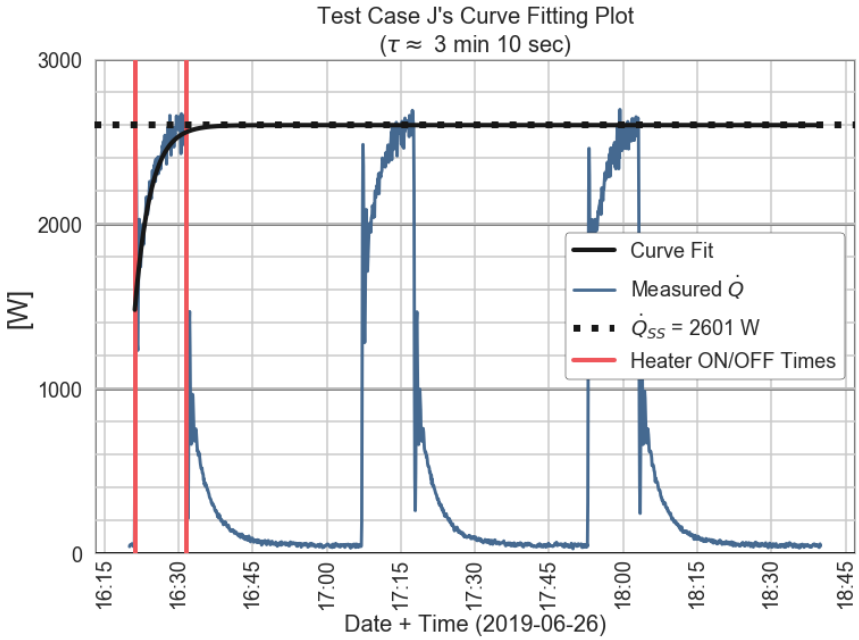

Figure 6.34: Example of curve fitted using method 2 (estimating time-constant and steady-state heat transfer rate).

With models now made for each of the respective test cases, the time-constants were then used to estimate the anticipated rate of heat transfer at times after the circulation pumps turned off. These estimated models for the time after the circulation pump turned off were then used to estimate the total cumulative heat injected into the loop.

As explained earlier, this is numerically accomplished by calculating the integral of the instantaneous calorimetric heat transfer curve. For every test case, we have complete calorimetric heat transfer data to compare the estimated models too. Additionally each test case includes the measured electrical energy consumption, which will serve as the measurement of the true heating provided (again, this is recognized to be an over-estimation of the true heating injected as a result of an uncertainty associated with heat losses from inefficiencies). In our analyses the estimated total cumulative heating provided was calculated using a rectangular approximation of the integral of the modeled curves. Figures 6.35 and 6.36 shows a visualization of the integrals calculated based on their estimated models. Note how the estimated curves were projected out 5 time-constants after the circulation pump turned off, so that they would simulate reaching steady-state heat transfer rates.

The results of the estimated cumulative heating provided tests are presented in the bar plot in Figure 6.37. Note that the electrical energy consumption (representing the total amount of heat injected) is also shown, along with the cumulative heat transfer measurement that would have been measured without additional model estimation after the circulation pump turned off. These results confirm that significant improvement (8.75% error reduction) can be made on the estimation of the cumulative amount of heating provided to the system, even after the circulation pump turns off. It is important to remember that this was successfully performed on this relatively simple thermal system. Further investigation should be done to develop models for more complex systems.

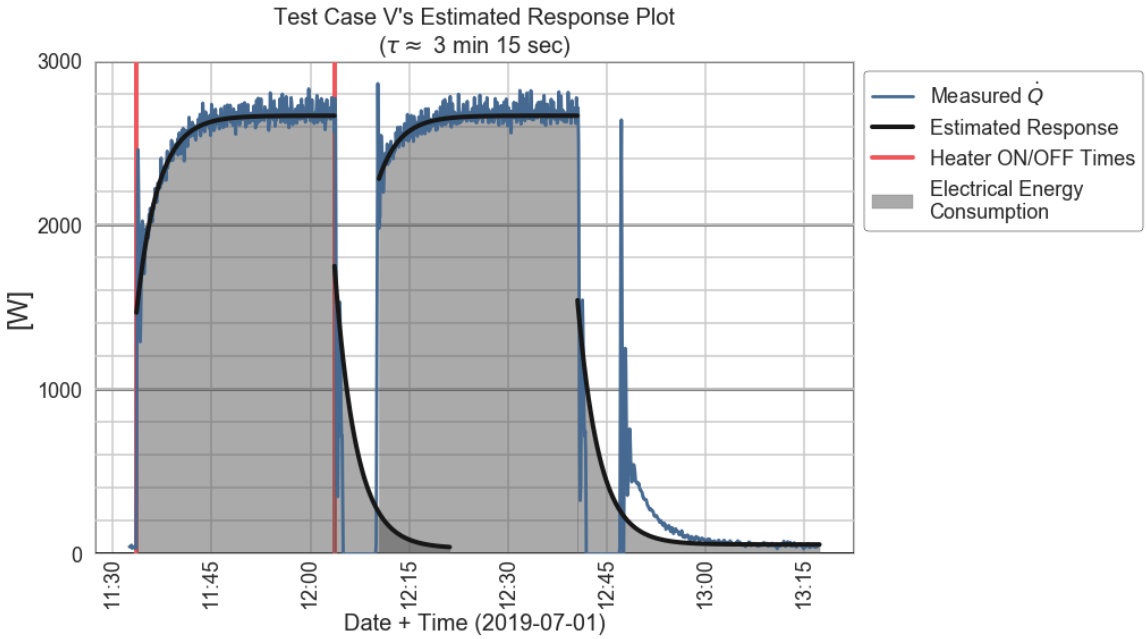

Figure 6.35: Example of estimated plot used to calculate the cumulative heat transfer after the circulation pump turns off.

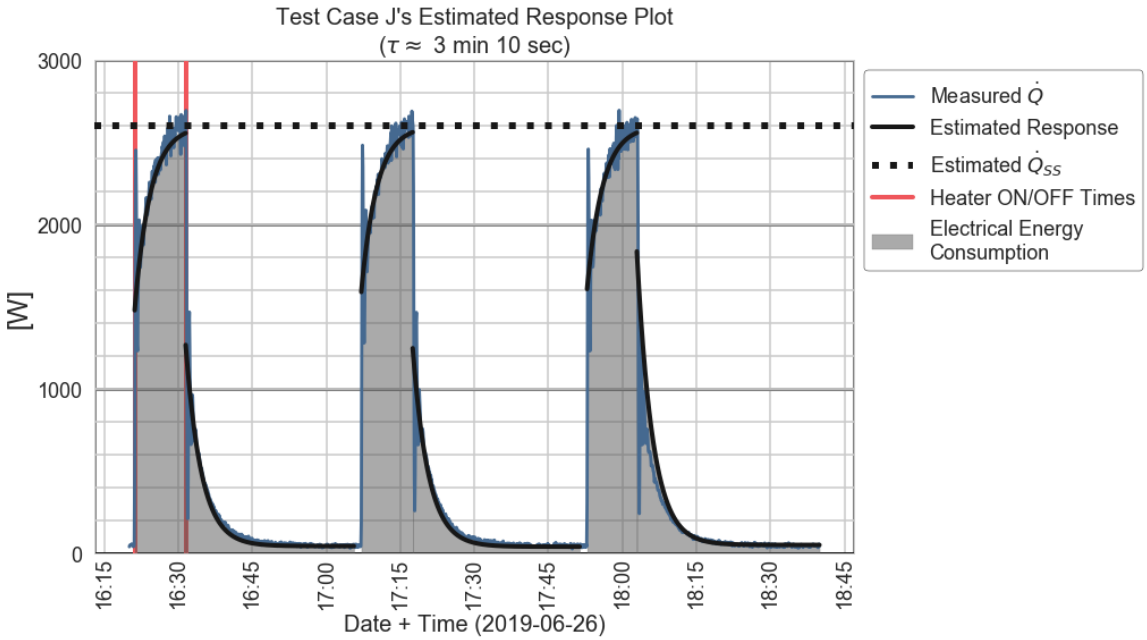

Figure 6.36: Example of estimated plot used to calculate the cumulative heat transfer after the circulation pump was artificially turned off in the continuous pump data set.

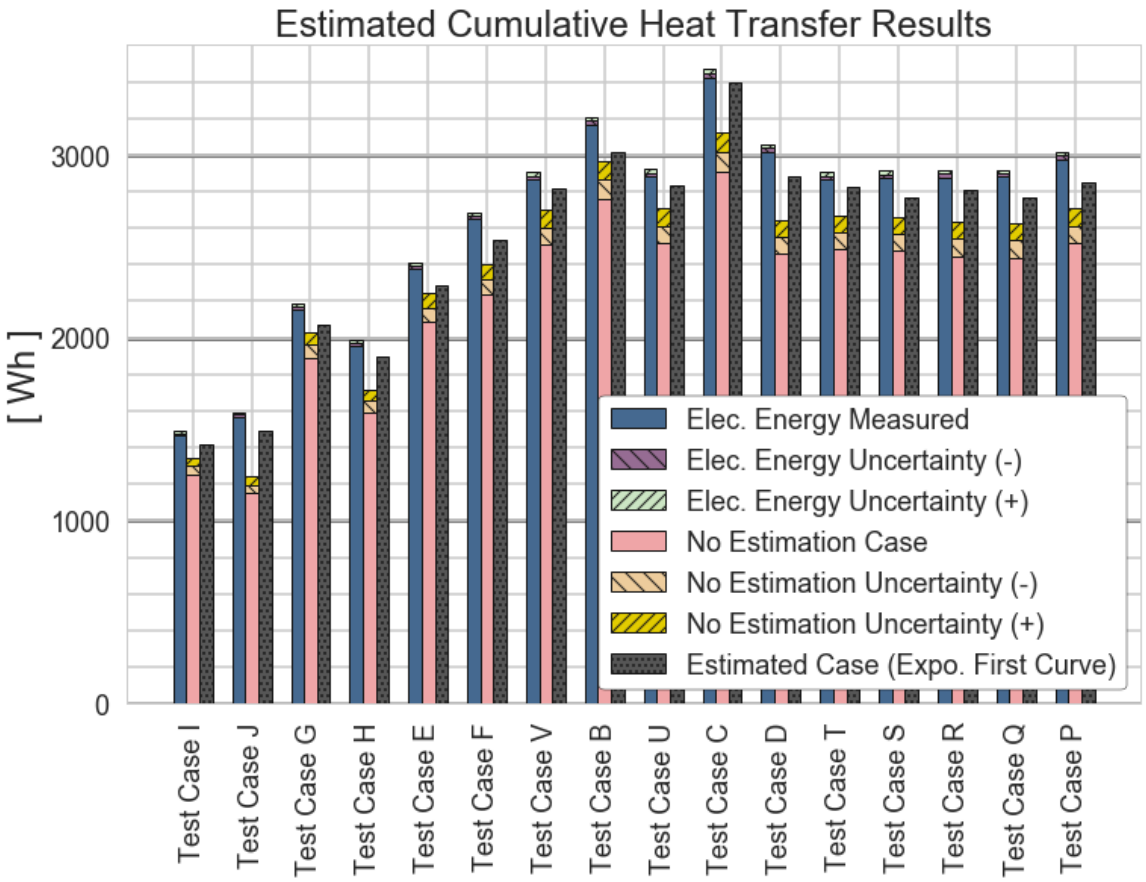

Figure 6.37: Bar plot showing the results of the estimated cumulative heat transfer tests.

Table 6.5 contains the summary of the analyses performed during the cyclical circulation, cumulative heat balance tests.

Table 6.5: Cumulative Heat Balance Results During "Cyclical Circulation" Analyses

Test Name	**As Measured**	**No Estimation**		**Modeled Estimation**	
	Cum. Heat Injected (W)	Cum. Heat Measured (Q)	Missing Heat ($W - Q$)	Cum. Heat Measured ($\widehat{Q}$)	Missing Heat ($W - \widehat{Q}$)
Units:	Wh	Wh	Wh	Wh	Wh
B	3187 ± 22	2865 ± 104	322 ± 106	3015	172
C	3447 ± 24	3017 ± 110	430 ± 112	3396	51
D	3036 ± 21	2553 ± 93	483 ± 96	2886	150
E	2391 ± 17	2165 ± 78	227 ± 80	2285	107
F	2667 ± 19	2320 ± 84	347 ± 86	2532	135
G	2169 ± 15	1963 ± 71	207 ± 76	2070	100
H	1972 ± 14	1654 ± 60	318 ± 62	1897	75
I	1479 ± 10	1298 ± 47	180 ± 48	1420	58
J	1581 ± 11	1197 ± 44	384 ± 46	1496	85
P	2997 ± 21	2612 ± 95	385 ± 97	2853	143
Q	2900 ± 20	2532 ± 92	368 ± 94	2770	130
R	2899 ± 20	2541 ± 92	358 ± 95	2807	92
S	2893 ± 20	2567 ± 93	326 ± 96	2765	129
T	2886 ± 20	2577 ± 94	309 ± 96	2829	57
U	2901 ± 20	2614 ± 95	288 ± 97	2834	67
V	2884 ± 20	2604 ± 94	281 ± 97	2816	68

CHAPTER VII

Preliminary Field Results

The following chapter provides a brief discussion on the prototype clamp-on energy meter installed in a residential ground source heat pump (GSHP) system located in Stillwater, Oklahoma. The system consists of two GSHPs that are connected in parallel with the system's ground loops. One of the GSHPs is dedicated to the up-stairs air and the other dedicated to the down-stairs air.

An early version of our clamp-on energy meter is currently installed on the down-stairs GHSP unit. It is set up to measure the down-stairs system's entering air temperature (EAT), leaving air temperature (LAT), entering water temperature (EWT), leaving water temperature (LWT), wall voltage, and the current consumed by the incoming electrical power cable inside the heat pump. The pictures on the subsequent pages show the exact location of the sensors.

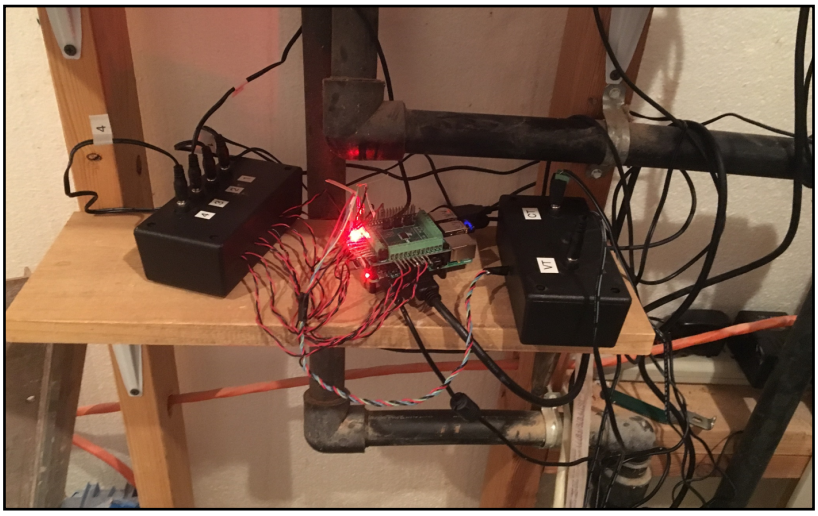

Figure 7.1: Picture of the make-shift desk used to place the raspberry pi and circuit board (loacted below the installed monitor).

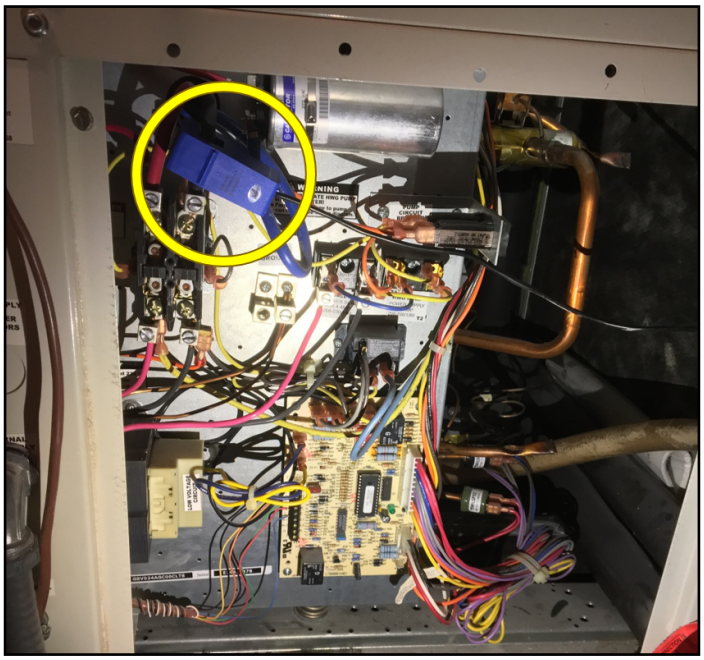

Figure 7.2: Picture of the current transducer clamped around the incoming electrical power cables inside the GSHP.

Figure 7.3: Picture of one of the thermistors measuring the on-pipe water temperature (with insulation removed).

Note that the clamp-on thermistors measuring the water temperatures (Figure 7.3) were installed using toothpaste as the thermal paste and then covered with insulation via a foam "pool noodle" (not pictured).

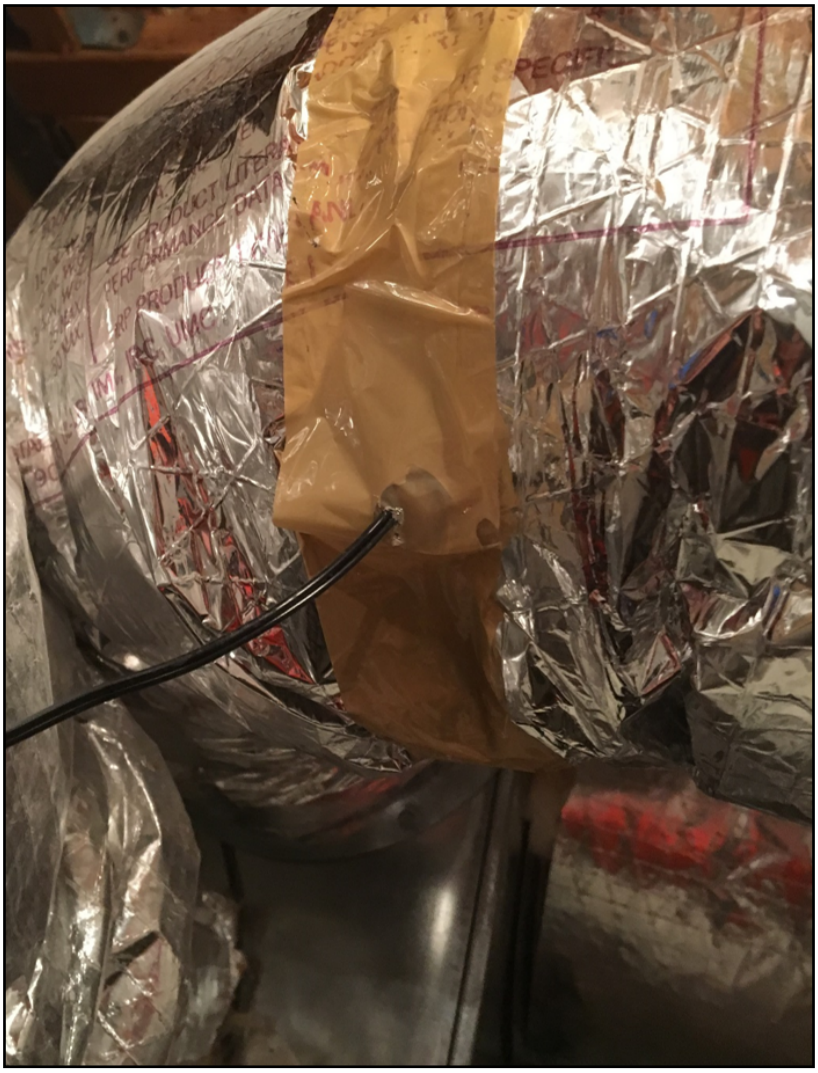

Figure 7.4: Picture of the leaving air temperature sensor sealed inside of the flexible duct coming out of the heat pump.

The thermistor measuring the leaving air temperature (Figure 7.4) was inserted inside of the flexible duct leading to the room and then the insertion cut was sealed with epoxy and tape.

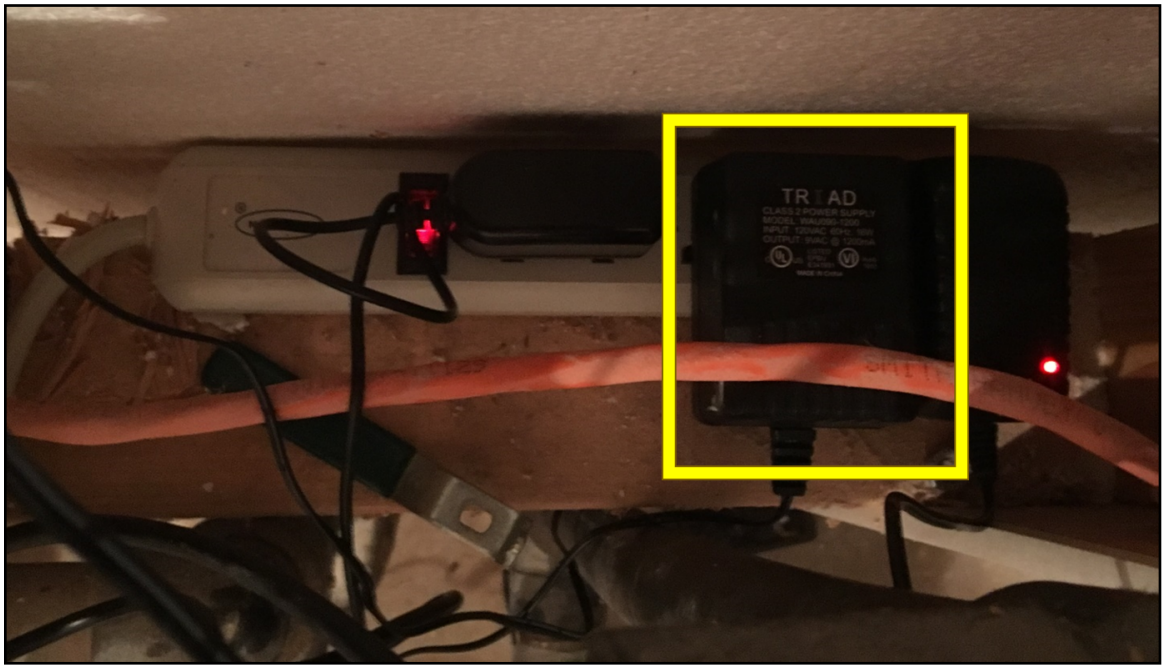

Figure 7.5: Picture of the voltage transformer plugged into the 120 V power strip, in order to measure the wall voltage.

The voltage transformer (Figure 7.5) was plugged into a power strip that was plugged into a 120 V outlet. Its voltage measurement should be doubled during analysis to estimate the 240 V voltage being supplied to the heat pump. This is a justifiable approximation, as most U.S. residential electrical systems are "split-phase" systems. Specifically a single-phase 240 V signal is supplied to the breaker from the distribution transformer across two 120 V "legs", with phases 180° apart. A center tap, or "Neutral" wire, provides an effective ground, where each leg becomes either +120 VAC or -120 VAC.

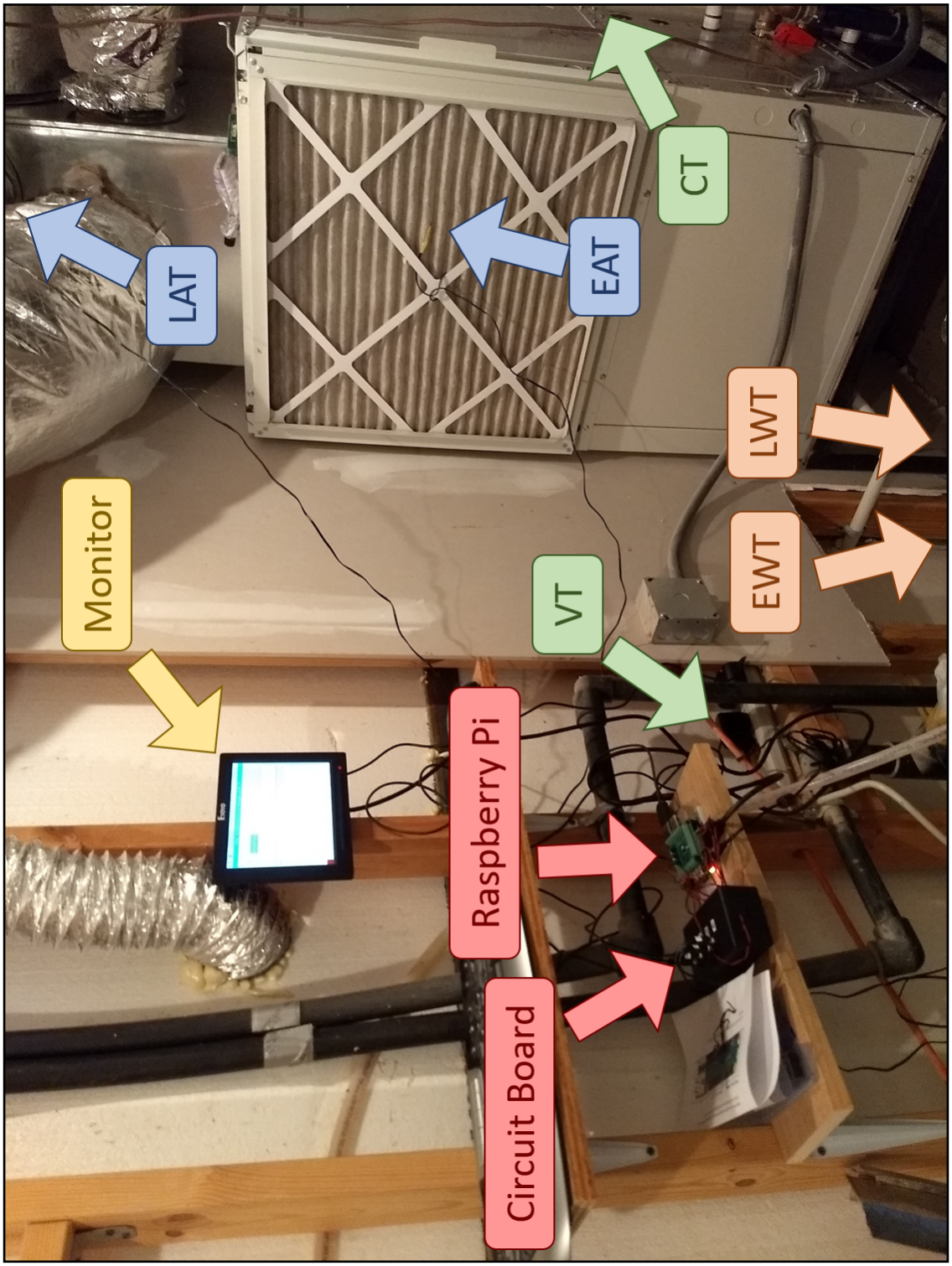

Figure 7.6: Labeled picture of the mechanical closet for a local residential GSHP system where an early version of our clamp-on energy meter is installed.

7.1 Preliminary Analysis of Field Data

The following analysis described serves to show the functionality of the *Python* `pandas` library, namely the ease in which time-series data analysis can be performed. The *Jupyter Notebook* created to run the following analyses can be found in the *Dropbox* folder referenced in Appendix C.

While the current clamp-on energy meter installed is only measuring temperatures and apparent power, a few performance metrics are still able to be calculated for the system. By visually examining the performance metrics, such as heat pump run-time, system COP (eventually), and fluid & air temperatures, a portion of the system's basic performance can be evaluated relatively quickly. Specifically, once the data is visualized, the operator can determine the time when the system performance began to change much more easily than staring at a print out of numbers. The ability to quickly visualize data should not be understated. The *Pandas* library allows for very convenient time-series data analysis and built in plotting functions to visualize the results. The following figures show a few of the performance metrics calculated using the most recently installed energy-meter, specifically containing field data from June 2019 - August 2019.

Figure 7.7 shows a set of raw temperature data measured by the clamp-on energy meter one summer day. As illustrated in the plot, as a result of having two independently controlled heat pumps, occasionally the up-stairs unit was found to turn on and circulate the water in the ground loop, while the down-stairs heat pump remained off. This caused the temperatures measured by the meter down-stairs to detect changes in fluid temperatures that weren't actually produced by the heat pump it was measuring. This made it near impossible to make sense of the original temperature measurements being recorded by the first prototype energy meter (since it

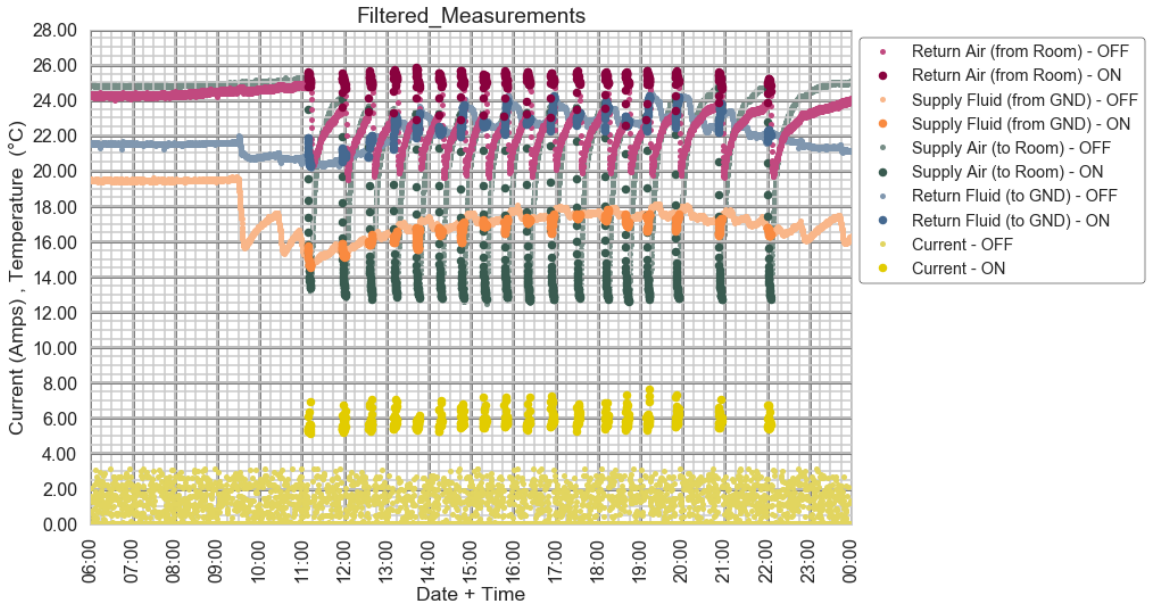

Figure 7.7: Plot of raw measurements filtered to distinguish between which samples occur while the down-stairs heat pump is on or off.

lacked meaningful power or flow data to make sense of the temperature changes). However, once a version of the meter was installed that included functioning power measurements, it was much easier to detect when the down-stairs heat pump was on or off. Furthermore, thanks to the implementation of a simple filter on top of the raw data using *Pandas*, parsing through to analyze just the data when the heat pump was "ON" was simple. Specifically the data when the heat pump was considered "ON" were easily filtered (as seen by the darker shaded lines in Figure 7.7) by selecting all data that were above 5 Amps.

In the plot seen in Figure 7.8, note how the heat pump can easily be seen to cycle on for varying durations of time. One easily calculable statistic using *Pandas* is the system run time. Figure 7.9 shows a histogram developed showing the frequency of binned run-times. This could easily be translated in to the average system run time fraction by averaging the amount of time the heat pump was on, during a given time period. Over the course of the data currently collected, the average run time for the down-stairs heat pump has been 4 minutes and 50 seconds.

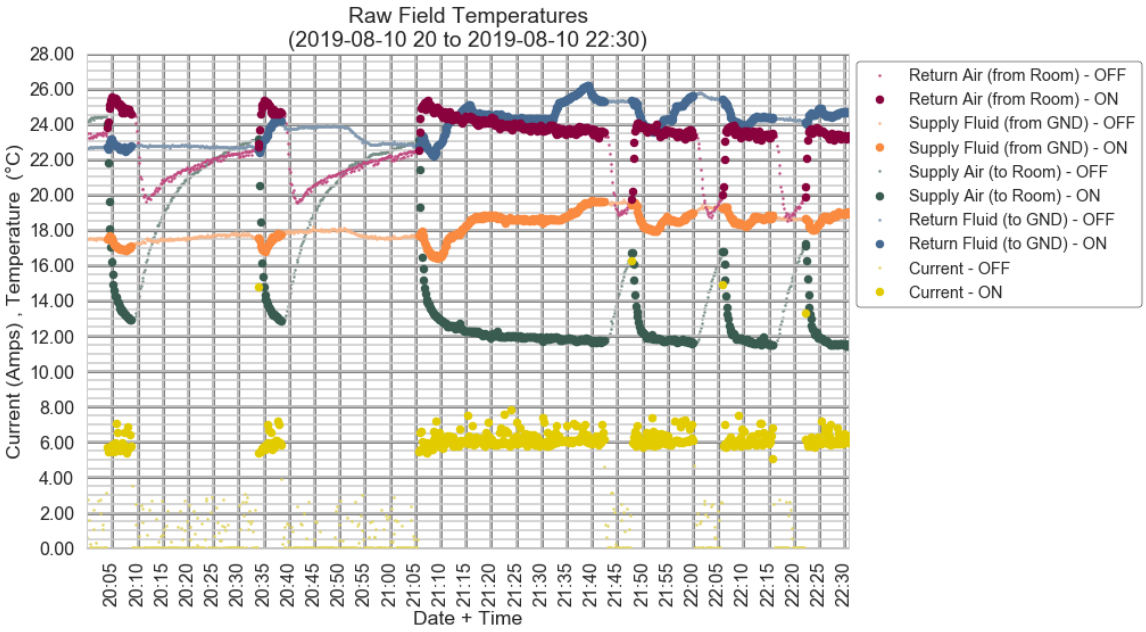

Figure 7.8: Plot of raw measurements showing the varying run times of the heat pump.

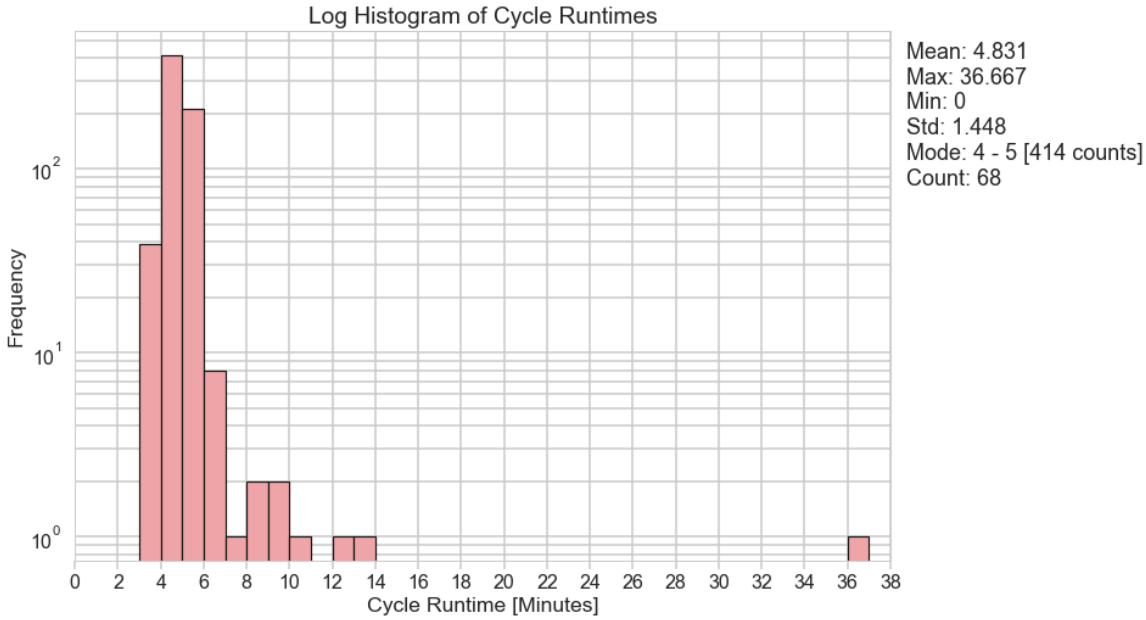

Figure 7.9: Histogram of heat pump run times.

The most notable *Pandas* function worth discussing, is the "re-sampling" function (`pd.DataFrame.resample()`). This allows for extremely large data sets (over 1 million+ lines of data) to be aggregated together based on their time stamps. The following plots show the air and on-pipe temperature measurements aggregated hourly,

daily, and weekly for when the heat pump was "ON." Note in the figure for daily-aggregated temperatures (Figure 7.11) how the minimum, maximum, and average values for each aggregated bin of data were plotted as well. The specific function applied to each column of the aggregated time-series data is customizable in *Pandas* (using the `.agg()` function) and has the potential for further complex time-series analysis in future work. The `.agg()` function has been most conveniently applied during data analysis when certain columns needed to be averaged, while others summed (such as when averaging raw measurements, but needing to sum their associated instantaneous uncertainties). As longer amounts of data are recorded, seasonal trends in the ground loop water temperatures and seasonal heating/cooling provided can be investigated in a similar manner.

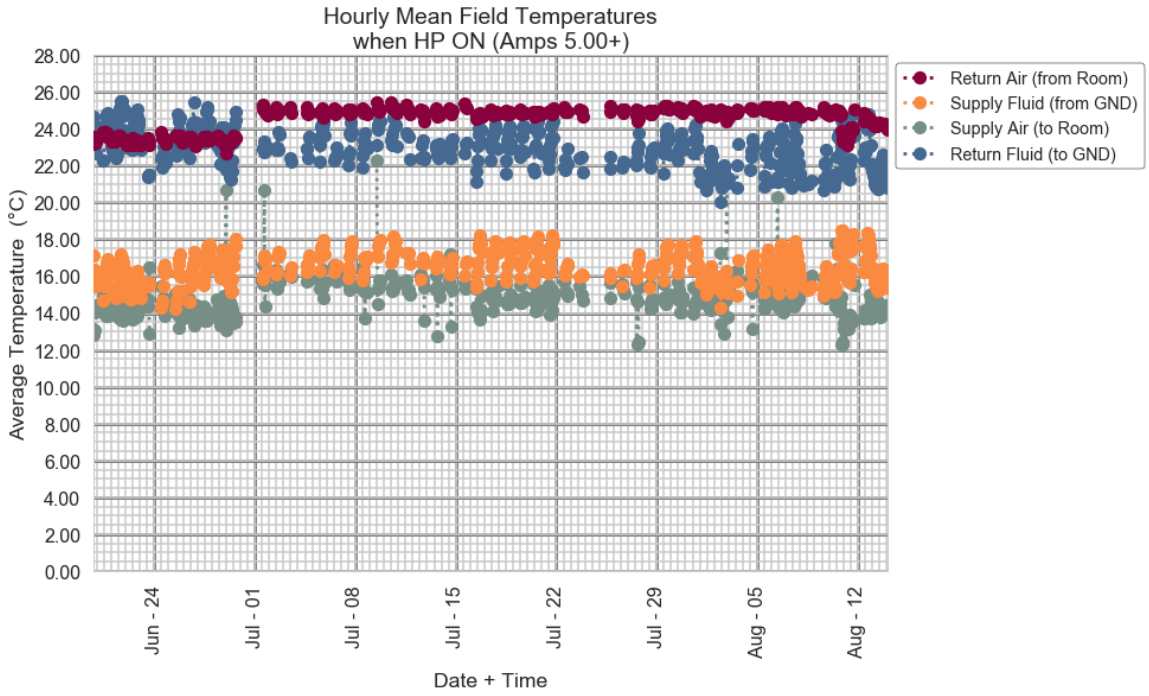

Figure 7.10: Plot of mean hourly temperatures during heat pump operation.

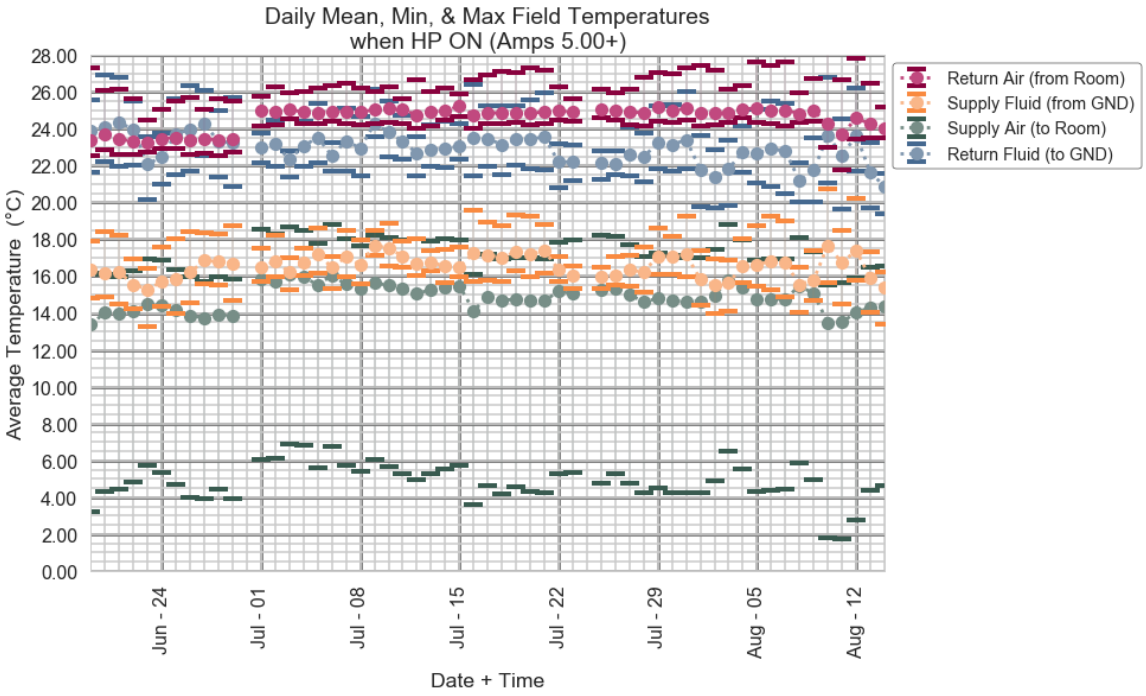

Figure 7.11: Plot of average, minimum, and maximum daily temperatures while the heat pump is "on."

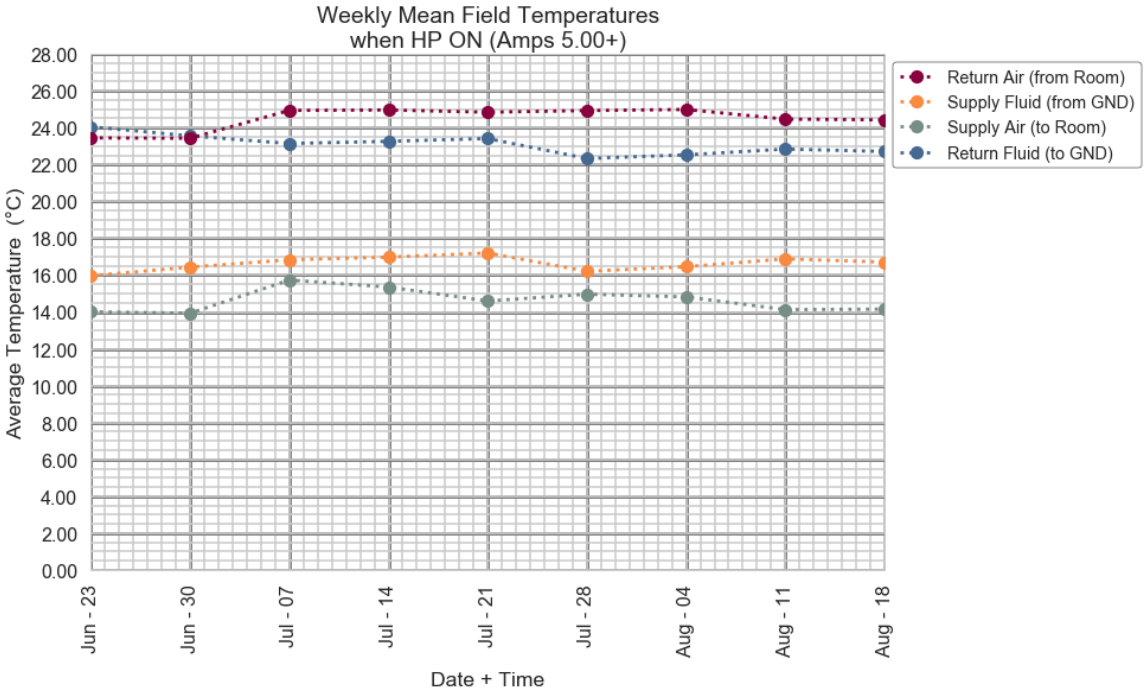

Figure 7.12: Plot of average weekly temperatures while the heat pump is "on."

While mentioned previously, it is important to note that the filter used to determine when the heat pump was considered "ON" was not selected arbitrarily. It was selected based on the heat pump's "rated load amperage" and the current measured on site during installation. A histogram of all the current measurements made while the heat pump has been considered "ON" can be found in Figure 7.13. A similar histogram was developed for when the heat pump was off (Figure 7.14). Being able to filter data easily like this will come in handy in the future in order to better quantify and allocate the contribution of parasitic loads measured with multiple current transducers in our energy meter.

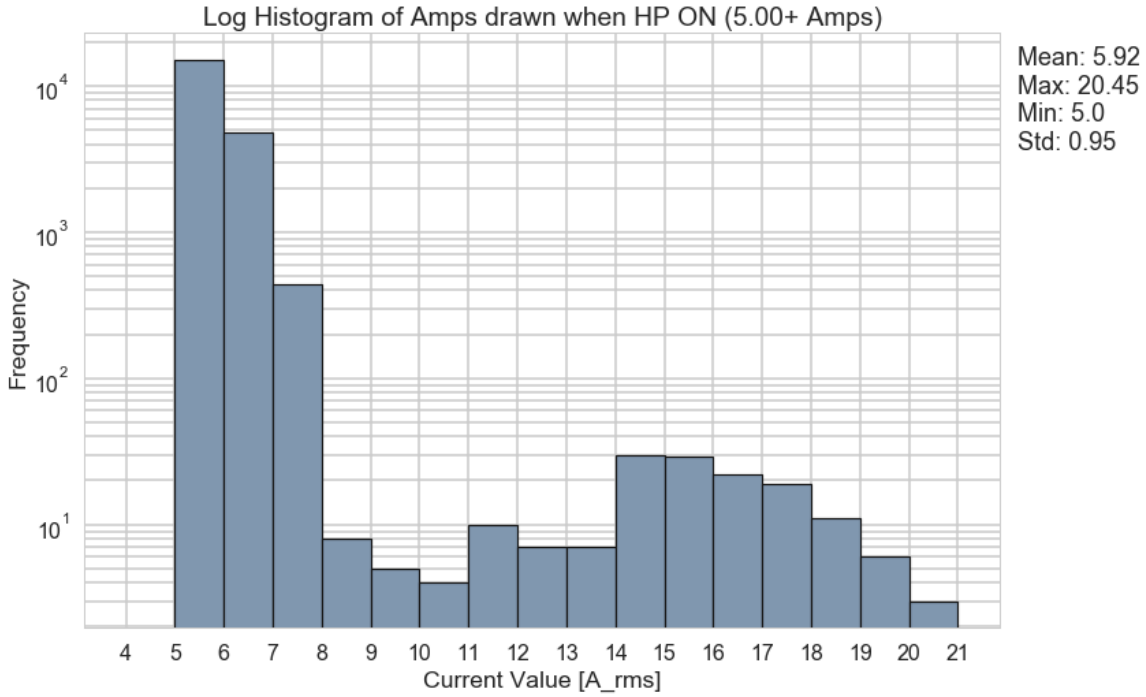

Figure 7.13: Histogram of current measurements while the Heat pump is on.

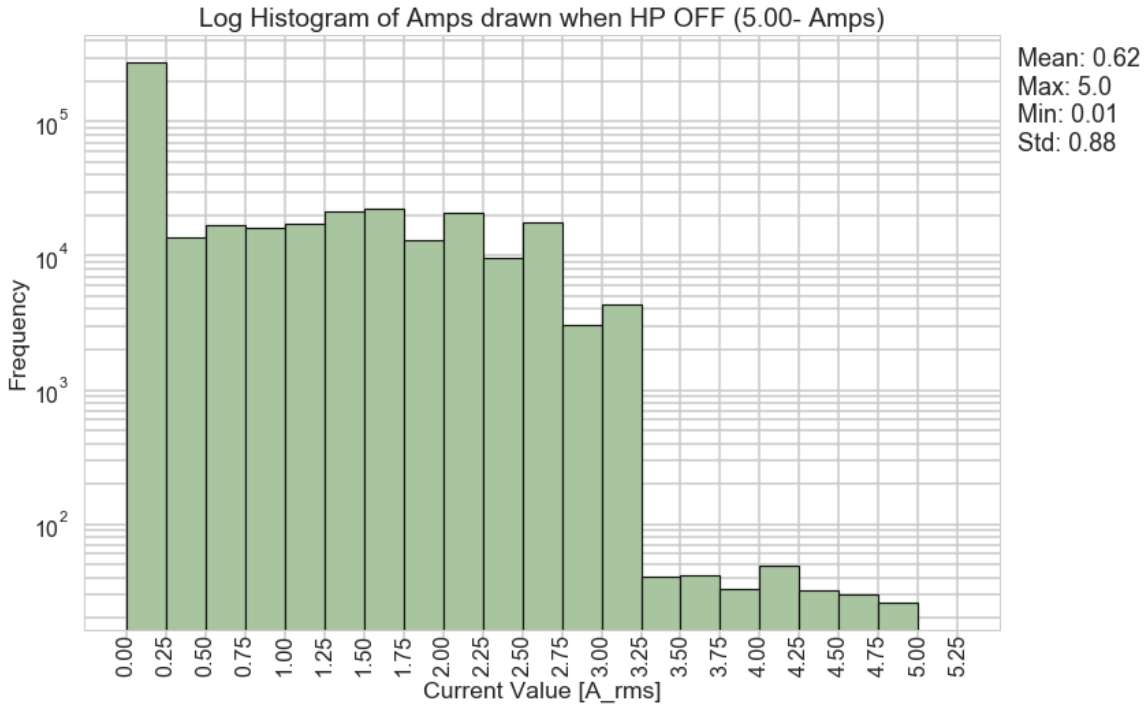

Figure 7.14: Histogram of current measurements while the heat pump is off.

Using the second curve fitting method described in the previous chapter (estimating both τ and $\dot{Q}_{SS}$ in Equation (6.7) over known transient response data sets), the system air-side time-constant was calculated. A histogram of the estimated time-constants is found in Figure 7.15. Note that the average run-time of the system (calculated earlier to be approximately 4 minutes and 50 seconds) is equivalent to approximately 6.5 time-constants. That implies that on average, by the time the heat pump turns off, the calorimetric response has likely reached steady-state conditions (99.8% of the change in operating temperature had occurred). As mentioned in the previous chapter, further investigation of models for the expected responses in the instantaneous heat transfer rate of more complex systems is necessary in order to further estimate the total cumulative heating/cooling provided after the circulation pump turns off.

In order for more meaningful performance data to be calculated, our clamp-on energy meter must incorporate some measure of flow rate. While fluid flow rate

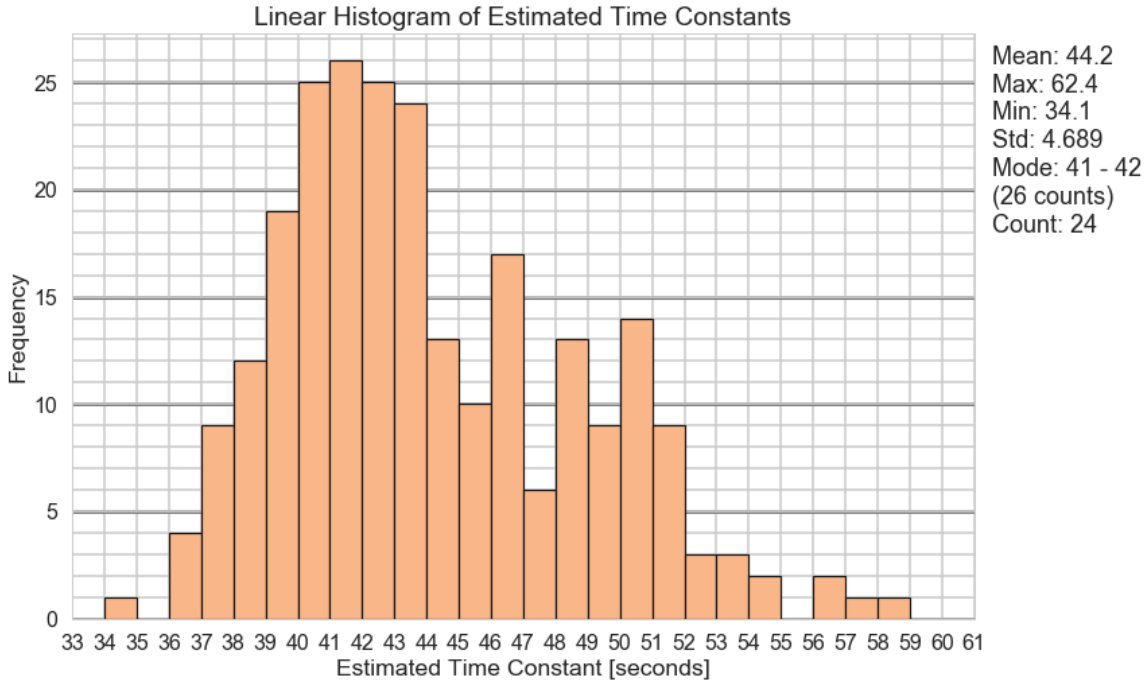

Figure 7.15: Histogram of the estimated time constants for the air-side response of the system, using the methodology described previously.

would be ideal, it is possible to back-calculate that flow rate based on performing a heat balance with the air side calorimetric heat transfer. This would require some sort of flow hood or anemometer to measure the air velocity (and secondarily the air volume flow rate). Future work should prioritize getting accurate flow measures from the clamp-on energy meter in the field, if more meaningful performance characteristics are to be measured by our clamp-on energy meter.

7.2 Lessons Learned

It can not be understated, the amount learned by actually implementing prototypes of our meter in the field throughout the design process. Many lessons were learned much faster, than if we had just stayed in the laboratory and theorized and calibrated forever. One of major contributions to the energy meter's design that can be attributed to a lessons learned in the field, was the importance of running the *Python* script on an IDE that would not store the data printed out after each measurement

on a scrolling window.

Another key design component learned from the field was the importance of sizing the burden resistor of the current transducer circuit relative to the "Locked Rotor Amperage", rather than the normal operating load. The first version of the clamp-on energy meter to implement power measurements had its ADC-board quickly "fried" in the field after it was installed (the induced voltage across the burden resistor was well above the maximum recommend input voltage). As a result, the power data being recorded was non-sensical until we could get the over-sized burden resistor replaced.

Additionally, the main motivator to automating the process of retrieving data from the *Raspberry Pi* remotely was the hassle it was to uninstall and retrieve the entire clamp-on meter each week after the first prototype was initially installed. This led to the development of the automated daily email early on in the design process.

The last key lesson learned from implementation in the field (that will be mentioned here) was the importance of configuring the *Raspberry Pi* to automatically run the `data_logger.py` script on start up. It only took after the first power outage at the field site to realize the importance of automating that process and making sure to save back-ups of the data on a regular basis. Without automatic recording on start-up the home-owner would need to go manually start the meter anytime there was a power outage.

Practical lessons such as these provided invaluable insight that affected the end design that otherwise would not have been learned (at least learned as quickly) in the lab setting.

CHAPTER VIII

Conclusions & Future Work

The following sections serve as a concluding summary of the work done to date on the prototype clamp-on energy meter developed at Oklahoma State University and recommendations for future work.

8.1 Overall Conclusions

The original goal of this entire endeavor was to begin documenting and understanding what it would take to develop a research-grade, low-cost energy meter for a residential ground source heat pump (GSHP) system. The key design theory and calibration procedures for such an energy meter were successfully documented in this work. A few key deliverables developed during the design, fabrication, and calibration of the energy meters (Ch. III) include: developing detailed circuit diagrams for each sensor required to measure calorimetric heat transfer and electrical power consumption, documented sizing methodologies for the individual circuit components, calibration procedures for each type of sensor implemented, and documented calibration uncertainties for each sensor. Table 8.1 (below) shows the updated summary of the key measurement uncertainties for each energy meter developed. Note that the clamp-on energy meter's on-pipe temperature sensors have a significantly larger amount of error resulting from their physical location on the outside of the pipe, compared to the in-line meter's temperature measurements.

Table 8.1: Summary of Energy Meter Measurement Uncertainties

Measurement	Energy Meter	Specific Steady-State Value	Experimentally Validated Uncertainty	
			Absolute (E)	Fractional (e)
ΔT	*Clamp-On*	4.36 K (7.85 R)	± 0.444 K† (± 0.800 R)	± 10.2 % (± 10.2 %)
	In-Line	4.81 K (8.66 R)	± 0.066 K (± 0.119 R)	± 1.4 % (± 1.4 %)
$\dot{V}$	(*BOTH*)	2.12 GPM (1.34×10^{-3} $\frac{m^3}{s}$)	± 0.071 GPM (± 4.46×10^{-6} $\frac{m^3}{s}$)	± 3.3% ± 3.3%
$\dot{Q}$	*Clamp-On*	2424 W (8271 Btu/hr)	± 381 W† (± 1300 Btu/hr)	± 16 % (± 16 %)
	In-Line	2670 W (9110 Btu/hr)	± 135 W (± 461 Btu/hr)	± 5 % (± 5 %)
$\dot{W}$	*Clamp-On*	2816 W (9609 Btu/hr)	± 70 W (± 239 Btu/hr)	± 2.5 % (± 2.5 %)
	In-Line	2805 W (9571 Btu/hr)	± 28 W (± 96 Btu/hr)	± 1.0 % (± 1.0 %)

† This uncertainty was updated in order to account for the sensors being located on outside of the pipe. The updated uncertainty is based on the results of the heat balance performed during Test Case B.

Additionally the design, fabrication, and implementation of a validation test loop was thoroughly documented in this thesis as well. The first set of capacity tests performed in Chapter 5.1 served to quantify the achievable range of temperature differences across the developed test loop. It was found that the fabricated test loop could achieve a temperature difference in the water of 4 - 10 K (7 - 18 R).

Next, a series of heat balances were performed to better quantify the accuracies of the in-line and clamp-on energy meters. The injected heat to the test loop was measured as the total amount of electrical energy measured from the circulation pump, and the two electric water heater elements. The calorimetric heat transfer was measured and compared to the estimation of heat injected at both a common instantaneous operating condition, as well as over time during both continuous and cyclical flow operation. The first key conclusion from these tests was quantifying the

unknown error in the clamp-on energy meter's thermistors, as a result of them being measuring from the outside of the pipes. Specifically, the on-pipe thermistors were proven to measure fluid temperature with as much as ± 0.4°C (± 0.7°F) error, if no additional correction/estimation was made accounting for their location. For the test loop's operating conditions, that particular on-pipe error manifests itself in an overall error in calorimetric heat transfer measurement of as much as 381 W (16% of the total heat transfer rate measured).

To investigate this further, an initial thermal resistance network was modeled (Figure 6.10) to attempt to ultimately estimate the true water temperature, based on the room air temperature and the intermediate on-pipe temperature. An estimated ratio of UA-values was found for the thermal resistance network model using a `scipy.optimize` solver. The initial correction implemented, based on the ratio of estimated UA-values, only proved successful during operating conditions when the heaters were turned on. This behavior of only increasing the accuracy of the clamp-on fluid temperature measurements when the heaters were turned on was consistent throughout all 22 test cases it was implemented in. Specific recommendations for future work involving estimating the fluid temperatures based on room air temperatures and on-pipe measurements will be provided in the following section.

Additional cumulative heat balance tests were performed with the in-line energy meter. The results concluded that the in-line energy meter could accurately measure the amount of heat provided to the loop with up to 5% accuracy. That remaining 5% was explained through heat being lost via radiation/convection from either the circulation pump housing and/or electrical water heater housings. Specifically, the circulation pump housing was measured to have a surface temperature of as high as 69 °C (156 °F) at certain points during the tests. This was sufficient evidence to deduce that its total measured electrical power consumption was not truly being completely transferred into the test loop's water as heat.

Furthermore, an initial model was evaluated for better estimating the total amount of heat injected to a system, despite its cyclical circulation pump operation. When standard heat pumps turn their circulation pumps off shortly after their compressor turns off (in order to save electrical energy), the ability to measure the total heating provided calorimetrically ceases (as the flow rate becomes approximately `0`). The exponential model of the expected heat transfer rate that we implemented was able to improve the estimation of the total amount of heat injected by about 8.75% of the true cumulative amount on average (compared to if no further estimate was made after the pump turned off). It is important to note that this particular implementation worked on our significantly simpler system. Actual residential GSHP systems can have much more complicated thermal responses, due to the number of sub-systems and components they contain, and their varying heating/cooling loads throughout the day.

Finally, several key lessons learned through the implementation of our clamp-on energy meter in an actual GSHP system operating in the field was discussed. Additionally, the analysis of its preliminary field data demonstrated the potential for effective time-series data analysis using the *Python* library *Pandas*. The ability to calculate meaningful performance characteristics of the residential GSHP system in the field was limited, as a result of still needing to find a way to non-invasively measure accurate volumetric flow rates.

8.2 Recommendations for Future Work

8.2.1 Clamp-On Energy Meter Recommendations

With regard to the design and implementation of the clamp-on energy meter, several recommendations can be made. While a thorough attempt was made to calibrate and implement a non-invasive ultrasonic flow meter, unfortunately it was not able to be implemented in the current version, due to its variability and inconsistency in

measuring fluid flow in the validation test loop setup. Further work should be done to attempt to implement such a non-invasive flow meter, if any sort of meaningful SPF or COP performance measurements are to be attainable by a non-invasive clamp-on energy meter.

Additionally, the estimation of the true center-of-pipe fluid temperature needs to be investigated further, if it is to be accurately estimated by the clamp-on energy meter's on-pipe temperature measurements. Specifically, more accurate characterization of the thermal resistance network and the direction of heat flow at varying operating conditions on the test loop is key. External heat sources, such as the circulation pump over-heating and conducting heat through the aluminum frame or the copper pipe itself, must be accounted for in the model. *Ground Energy Support* has done some tests calibrating on-pipe temperature measurements relative to their surrounding air temperatures that appears to be worth replicating in the future [Ground Energy Support LLC (2013)].

A potential alternative to estimating the fluid temperature via on-pipe surface temperatures, is to implement a "saddle port" on HDPE pipe for tapping. Specifically, a process could be developed to essentially "tap" the HDPE pipe without completely "opening" the closed-loop. If such a process of attaining an in-line temperature measurement post-facto was optimized, this would significantly simplify the estimation of the true center-of-pipe fluid temperature measurement needed in residential GSHP system monitoring.

Furthermore, developing and standardizing a calibration procedure that optimizes the temperature difference between a pair of thermistors, rather than just their independent absolute temperatures, would be beneficial. Automating the calibration process would improve the speed with which each batch of sensors could be calibrated as well. From a financial stand-point, finding a cheap means of calibrating sensors is imperative, even if the sensors themselves are cheap. This may be difficult in

the short-term, since the initial cost of purchasing high-accuracy reference sensors is relatively high.

Another recommendation for the future implementation of the developed clamp-on energy meter is to develop a more robust and timely way of visualizing the "live" measured data. While printing the measured values on the screen and emailing a "master" csv-file daily was sufficient for our research, it would be beneficial to create a website that downloads and visualizes the emailed data automatically. This would allow others interested in accessing the data collected to simply go to the provided `url`, rather then requiring their email be added to the list in the `data_logger.py` script manually.

Furthermore, with the individual sensor measurement uncertainties known, it would be helpful to record and display their associated uncertainty analyses with the energy meter as well. Recording, summing, and displaying the "live" cumulative uncertainty measurements, in addition to the raw measurement values, would provide a statistic that no current energy meter provides (at least of all the other meters we researched).

With regards to the electronics and measurement aspect of the energy meter, further work could be done to better characterize and understand the effect of unstable power supplies when using Analog-to-Digital conversion (ADC) boards with internal reference voltages. As discussed in Appendix H, significant error in the high precision analog voltage measurements was experienced when our ADC boards were powered by the *Raspberry Pi*'s 3.3 V and 5 V pins. Additionally, the effect of sampling speed on the accuracy of the measured voltage by the ADC board could be further investigated.

A useful next design iteration in the energy meter's sensors would be to have all burden and shunt resistors somehow soldered in with the sensors themselves. This would allow for entire sensor to be calibrated independently of the energy meter that it would later be implemented in. If the PCB board no longer contained key

sensor components needed for their calibration, the sensors could be manufactured and calibrated in the lab and then sent to any field locations that needed additional sensors. Further developing the sensors to be truly "plug-and-play" would help enable the production and implementation of residential energy meters in the future.

A final suggestion for future iterations of the energy meter would be to implement air-side calorimetric heat transfer measurements. Specifically, for research involving air-to-air systems (or "air-source heat pumps"), measuring the amount of heat transfer achieved on the air-side is vital. This would require creating some sort of flow hood, in order to estimate the volumetric flow rate of the air coming out of the heat pump. Measurements of the entering and exiting overall mean air temperature would also need to be more robustly and accurately implemented.

8.2.2 Validation Test Loop Recommendations

There are several key suggestions for the improvement and future implementation of the validation test loop as well. The first key improvement that could be made is the location of the circulation pump. In order to more easily know the expected temperature difference across the two temperature sensors when both of the water heater elements are off, it would be advantageous to place the circulation pump outside of that section of the test loop. Otherwise, achieving an operating condition with the expected temperature difference of 0 K, while the circulation pump is on, is impossible.

In addition to moving the circulation pump's location, using insulating washers and Nylon screws to secure the pipe to the *8020* aluminum frame, would also better prevent the conduction of heat across the test loop as a whole. It was found that a significant amount of heat was conducted from the circulation pump over-heating through the frame, as well as the heat from the hot water inside the pipes conducting out through the pipe clamps. Finding a way to better isolate the test loop's frame

and prevent it from becoming a heat sink for the test loop's excess heat would be beneficial.

Further work that ought to be pursued involves the automation of the test loop. Specifically one initial addition could be adding automatic thermostats/switches to turn off the heaters and verify that the pump and fans are turned on, if the fluid temperatures rise too high. Adding controls to the electrical devices, such that future heat balance tests could be operated automatically would also be ideal. This would ideally give future researchers the ability to perform tests more remotely, rather than having to manually turn heaters on and off, for several days at a time.

Another potential route for future work could involve implementing a real GSHP into the test loop for laboratory measurements. This would require controlled access to a real GSHP system in the lab. If a GSHP was accessible, connecting it in series with the validation test loop would allow for controlled testing that more closely resembles the characteristics this project initially aimed to resemble. Separately implementing an energy meter, like the ones described in this thesis, on a real GSHP in the laboratory would also provide valuable experience and insight.

Lastly, having developed an in-line energy meter capable of calculating the amount of heat injected into the test loop with up to 5% accuracy, it would be interesting to use the validation test loop setup to compare and validate the accuracy claims of other professionally developed energy meters designed specifically for HVAC applications.

References

ASHRAE (2009). *Handbook of Fundamentals - Chapter 22: Pipe Sizing*. ASHRAE.

ASHRAE (2013). *Standard 41.1 - Standard Method for Temperature Measurement*, volume 41. ASHRAE.

ASHRAE (2016). *Standard 41.8 - Standard Methods for Liquid Flow Measurement*, volume 41. ASHRAE.

ASME International (2013). ASME PTC 19.1 - Test Uncertainty.

Austin III, W. A. (1998). Development of an in situ system for measuring ground thermal properties. Master's thesis, Oklahoma State University.

Ball, D. A., Fisher, R., and Hodgett, D. (1983). Design methods for ground-source heat pumps. ASHRAE Transactions 89(2):416-440.

Boyd, T. L., Sifford, A., and Lund, J. W. (2015). The united states of america country update 2015. In *World Geothermal Congress*, page 3.

Carmo, C., Elmegaard, B., Nielsen, M., and Detlefsen, N. (2015). Empirical platform data analysis to investigate how heat pumps operate in real-life conditions. In *Proceedings of the 24th International Congress of Refrigeration*. International Institute of Refrigeration IIF/IIR.

ClimateMaster (2009). Genesis (GS) series product catalog. https://files.climatemaster.com/Genesis-GS-Series-Product-Catalog.pdf. Accessed on 8 Mar 2018.

Gleeson, C. P. and Lowe, R. (2013). Meta-analysis of european heat pump field trial efficiencies. *Energy and Buildings*, 66:637 – 647.

Ground Energy Support LLC (2013). Gxtracker on-pipe measurement of deltat error and bias correction: Sources. Accessed on 12 Nov 2018. http://groundenergy.com/wp/docs/GxTracker_DataSheet_OnPipeTemp_rev1.1.pdf.

Horwitz-Bennet, B. (2014). Geothermal: Ready for prime time. www.greenbuildermedia.com/greenproducts/geothermal-ready-for-prime-time. Accessed on 15 July 2019.

Jameco (2011). Jameco Part Number 207441 Data Sheet. Accessed on 22 August 2017.

Li, C., Hong, T., and Yan, D. (2014). An insight into actual energy use and its drivers in high-performance buildings. *Applied Energy*, 131:394 – 410.

Liu, X., McCabe, K., Hughes, P., Spitler, J., Southard, L., and Warner, J. (2019). GeoVision analysis supporting task force report: Thermal applications—geothermal heat pumps. Technical report.

Lund, J. W. and Boyd, T. L. (2016). Direct utilization of geothermal energy 2015 worldwide review. *Geothermics*, 60:66 – 93.

Nordman, R. (2016). Demonstration of field measurements of heat pump systems in buildings - good examples with modern technology: Final report.

Nordman, R. and Zottl, A. (2011). Sepemo-build-a european project on seasonal performance factor and monitoring for heat pump systems in the building sector. *REHVA Journal*, 48(4):56–61.

Open Energy Monitor (2018). Learn: An in-depth look at the basic principles of electricity monitoring, sustainable energy and more. Accessed on

9 Apr 2018. www.learn.openenergymonitor.org/electricity-monitoring/ac-power-theory/introduction.

Scofield, J. H. (2009). Do leed-certified buildings save energy? *Energy and Buildings*, 41(12):1386 – 1390.

Shannon, C. E. (1949). Communication in the presence of noise. *Proceedings of the IRE*, 37(1):10–21.

Spitler, J. D. and Gehlin, S. (2019). Measured performance of a mixed-use commercial-building ground source heat pump system in sweden. *Energies*, 12(10):2020.

Spitler, J. D. and Gehlin, S. E. (2015). Thermal response testing for ground source heat pump systemsan historical review. *Renewable and Sustainable Energy Reviews*, 50:1125 – 1137.

Steinhart, J. S. and Hart, S. R. (1968). Calibration curves for thermistors. *Deep Sea Research and Oceanographic Abstracts*, 15(4):497 – 503.

Szreder, M. (2014). A field study of the performance of a heat pump installed in a low energy house. *Applied Thermal Engineering*, 71(1):596 – 606.

Taco (2018). Taco 003/003 IFC Cartridge Circulator Performance Curves. Accessed on 30 August 2018.

Taylor, J. (1997). *An Introduction to Error Analysis : The Study of Uncertainties in Physical Measurements*. University Science Books, Sausalito, CA, 2nd ed. edition.

Tiljander, P., Alsbjer, M., and Haglund Stignor, C. (2014). Field measurement of ground source heat pump systems installed in existing buildings. In *11th IEA Heat Pump Conference 2014, Montreal*.

Uhlmann, M. and Bertsch, S. S. (2012). Theoretical and experimental investigation of startup and shutdown behavior of residential heat pumps. *International Journal of Refrigeration*, 35(8):2138 – 2149.

United States Department of Energy (2014). Buildings performance database overview. www.energy.gov/sites/prod/files/2014/06/f17/bpd_overview_2014.pdf. Accessed on 15 July 2019.

United States Department of Energy (2019). Geovision: Harnessing the heat beneath our feet. www.energy.gov/sites/prod/files/2019/06/f63/GeoVision-full-report-opt.pdf. Accessed 15 July 2019.

United States Department of Energy's Office of Energy Efficiency & Renewable Energy. Renewable energies (homepage). www.energy.gov/eere/renewables. Accessed on 15 July 2019.

United States Energy Information Administration (2015). Residential energy consumption survey (recs), 2015 recs survey data.

United States Energy Information Administration (2019a). How much energy is consumed in u.s. residential and commercial buildings? www.eia.gov/tools/faqs/faq.php?id=86&t=1. Accessed on 15 July 2019.

United States Energy Information Administration (2019b). Monthly energy review. www.eia.gov/totalenergy/data/monthly/pdf/mer.pdf. Accessed on 15 July 2019.

Zhou, B., Li, W., Chan, K. W., Cao, Y., Kuang, Y., Liu, X., and Wang, X. (2016). Smart home energy management systems: Concept, configurations, and scheduling strategies. *Renewable and Sustainable Energy Reviews*, 61:30 – 40.

Zottl, A., Nordman, R., Coevoet, M., Rivière, P., Miara, M., Benou, A., Riederer, P., Andersson, K., and Lindahl, M. (2011). Guideline for heat pump field measurements for hydronic heating systems.

sepemo.ehpa.org/uploads/media/D4_1_D2_3HYDRONIC_Version_1_0_FINAL.pdf. Accessed on 12 July 2019.

APPENDIX A

How an ADC Comparator Achieves Quantization of an Analog Signal

Section 3.3 describes the selection of an Analog-to-Digital conversion (ADC) board for our sensor system. A basic method for how ADC boards perform quantization of analog voltage signals is described in this Appendix.

As discretization of the continuous signal occurs (via sampling), quantization must take place to determine the approximate values used in that discrete time signal. This is determined using a collection of comparators inside the ADC. A comparator is essentially a tiny circuit that accepts two voltages and either outputs a `1` or a `0` based on which voltage is higher. By strategically comparing the "input voltage" (V_{in}) being measured to a known "reference voltage" (V_{ref}) the encoded, binary output from a collection of comparators can be interpreted to approximate what the input voltage's real-value is. Figure A.1, depicts an example circuit utilizing multiple comparators and an encoder inside a "3-bit flash ADC board." Note how fractions of the "reference voltage" are compared by measuring across multiples of an identical resistor in series.

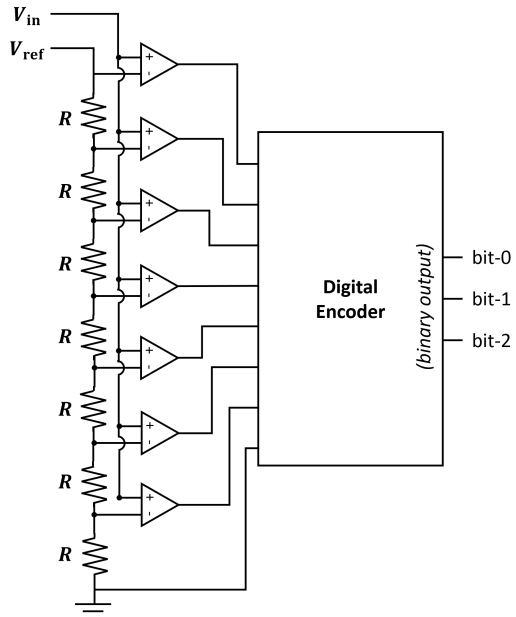

Figure A.1: Example circuit of several comparators and an encoder inside a 3-bit flash ADC. (after `www.allaboutcircuits.com/textbook/digital/chpt-13/flash-adc`)

The ADC board implemented on our energy meter, utilizes *Texas Instruments*' *ADS1115* 16-bit ADC (http://www.ti.com/lit/ds/symlink/ads1115.pdf).

APPENDIX B

Review of Ultrasonic Flow Sensor

The low-cost ultrasonic transducer we purchased and attempted to implement in our clamp-on energy meter was the `TUF-2000M-TS-2`. The manual claims that is capable of achieving "better than 1% accuracy, better than 0.2% repeatability." After stripping and appropriately connecting the provided cables to its two transducers, a 12 VDC power supply was wired in to the keypad module. "Dwyer Silicone RTV Acoustant Couplant (A-197)" was purchased as acoustic couplant for the transducers and the 1-inch copper pipe was polished and cleaned. Next the exact dimensions of the pipe were measured with a digital dial caliper and entered in to their appropriate menus, using the keypad. Table B.1 below shows the exact dimensions & parameters entered.

Menu	**Parameter**	**Value**
M11	Pipe Outer Diameter	*1.12204 in*
M12	Pipe Wall Thickness	*0.05118 in*
M14	Material	*Copper*
M16	Liner	*None, No Liner*
M20	Fluid Type	*Water (General)*
M23	Transducer Type	*Clamp-on TS-2*
M24	Transducer Mounting	*W (small pipe)*

Table B.1: Parameters input to the ultrasonic flow meter's module.

The resulting transducer spacing it calculated (Menu 25) was 1.16094 inches. A 3D-printed alignment tool was then designed and printed to ensure proper spacing and alignment of the "Up" and "Down" transducers. The following figures show a few of the pictures taken during the process of installing the ultrasonic transducers on the side of the straight pipe section. Note that the section of pipe where the transducers were installed had at least 10 inches of straight pipe upstream and 5 inches of straight pipe down stream from the nearest bend in pipe (as recommended on page 24 of the manual). This section of pipe was cleaned and polished as recommended, before applying the acoustic couplant. Also note that the first 3D-printed alignment tool (seen in the background of Figure B.1) was originally designed with the exact spacing required. However the transducers ended up having a "Quality" reading of 0 at that spacing. So later iterations of the tool allowed for spacing adjustment/correction in the horizontal direction.

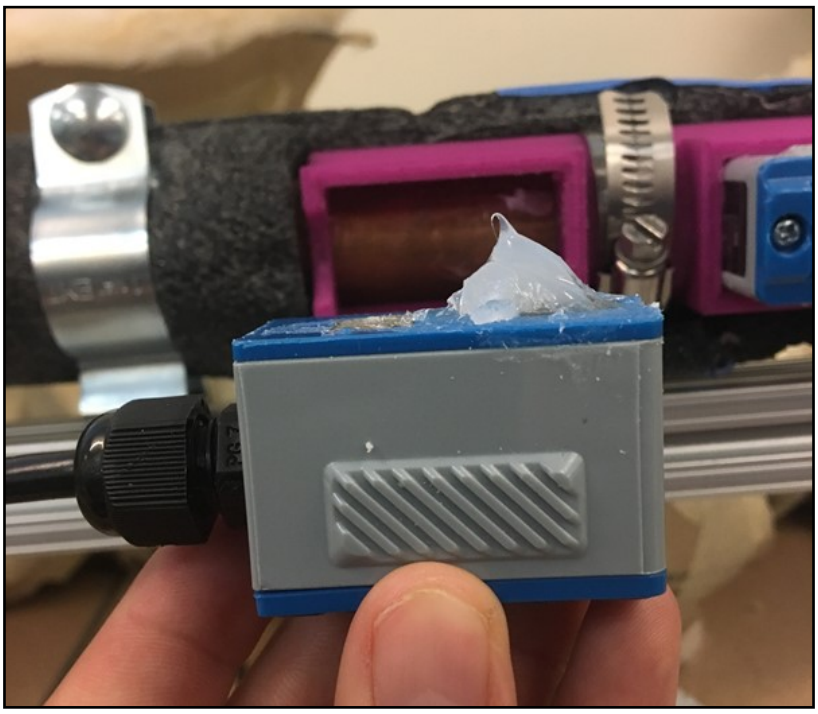

Figure B.1: Acoustic couplant added to bottom of transducer.

Figure B.2: Acoustic couplant added on the polished pipe.

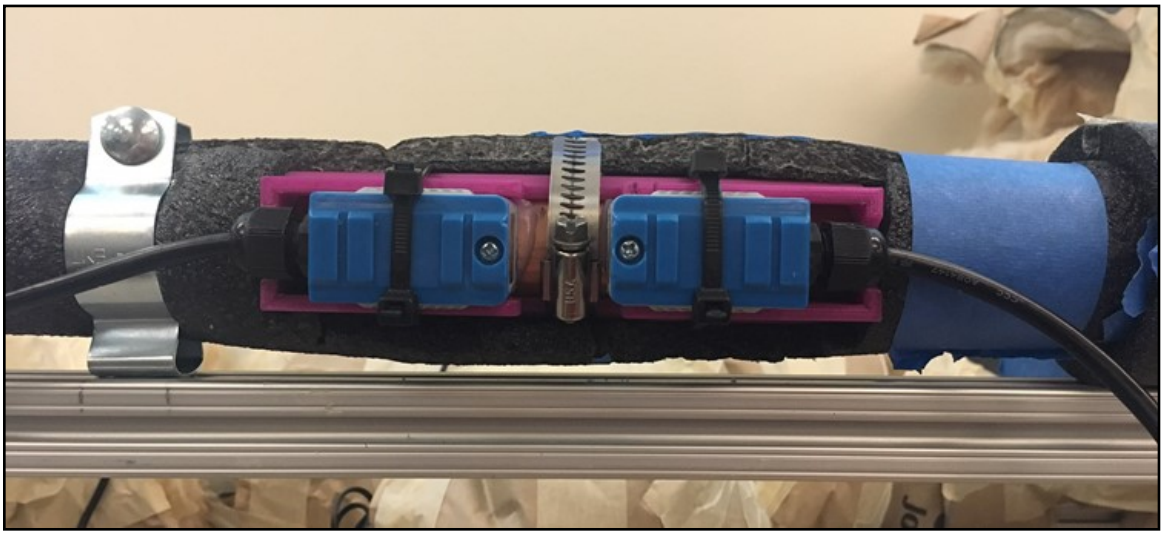

Figure B.3: Mounted transducers, using custom 3D-printed alignment tool (front view).

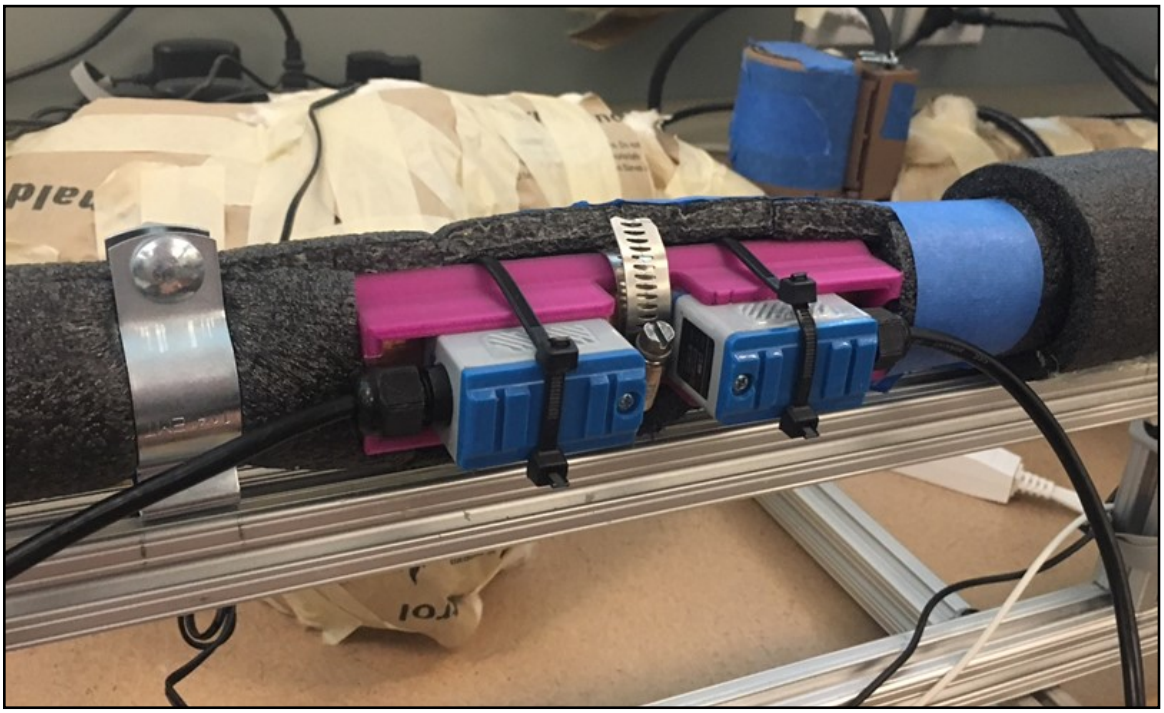

Figure B.4: Mounted transducers, using custom 3D-printed alignment tool (isometric view).

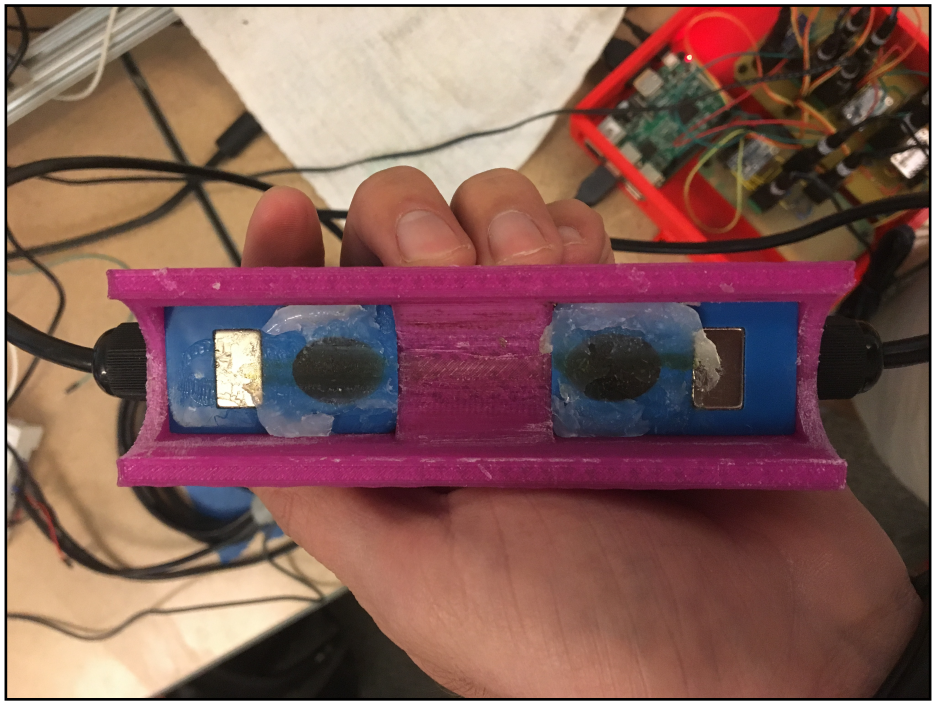

Figure B.5: Evidence of couplant leaving "no gap between the pipe surface and the transducers" (after removed from the pipe between failed attempts).

After the transducers were mounted, the couplant was visually confirmed to "leave no gap between the pipe surface and the transducers." Next, Menu 90 was pulled up to examine the "Signal Strength" and "Signal Quality" measurements. "Signal Strength" indicates the strength of the received ultrasonic signals by each transducer. "Signal Quality" refers to the "Signal-and-Noise Ratio" (SNR). The higher the SNR, the higher the accuracy. Both the `UP` and `DN` "Signal Strength" measurements read between 75.0 and 80.0 with little to no fluctuations over time. After their initial placement, the transducers were carefully tapped forwards and backwards along the horizontal direction of the alignment tool, until the "Quality" signal read between 60.0-90.0 (as required for accurate readings). With both the signal "Strengths" and "Quality" parameters within their ranges for optimal operation, the set up was left over-night to allow the acoustic couplant to cure.

The next day the "Strength" measurements were still within optimal range, but after the couplant had cured, the "Quality" dropped to an unstable range (or sometimes even 0 in a few attempts). We then would push on or move the ultrasonic transducers slightly until the quality reading would get better and back to within range (60.0-90.0). Once back in range (after the couplant had cured), we set the zero point using Menu 42 (i.e., calibrated the sensor at 0 flow). We turned on the circulation pump and adjusted the flow so that it was running at a constant 2.0 GPM. Next, we started recording the 4-20mA signal and confirmed we were reading what the keypad module was displaying. Unfortunately, the measured values from the ultrasonic flow meter were not accurate or stable, despite being within the necessary

strength and quality ranges. As seen in the data recorded (Figure B.6), the values were consistently erroneous. After about 15 minutes of erroneous, fluctuating flow readings, the true flow rate was increased to about 2.5 GPM. The quality reading immediately decreased to 0, when the flow rate increased and the ultrasonic meter appropriately held its last value (coincidentally about 2.5 GPM).

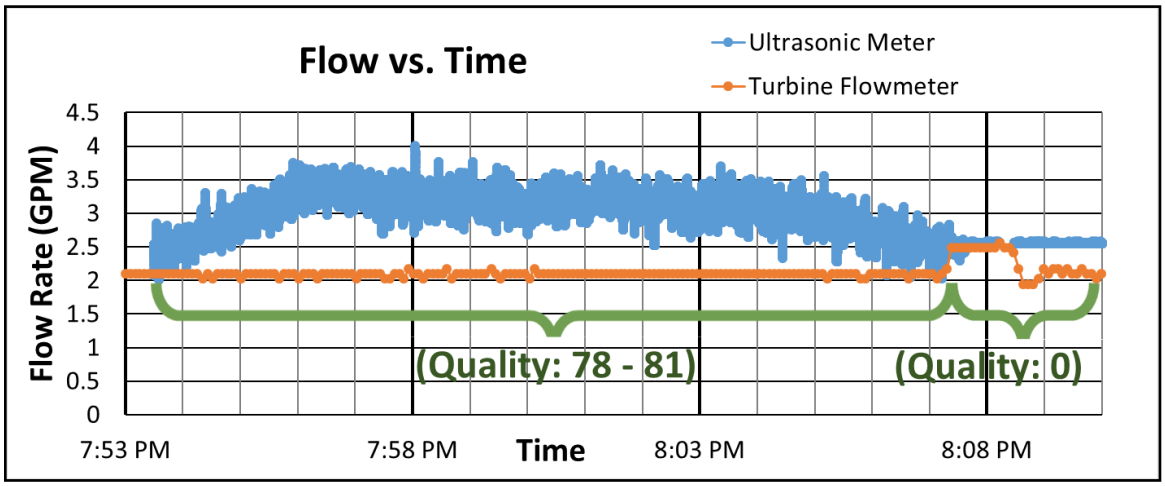

Figure B.6: Plot of data collected from ultrasonic meter (blue) and turbine flow meter (orange) for reference during testing.

Customer support from *ValueStoreUS* (the supplier) was emailed inquiring about suggestions for improving the unstable "Quality" value and inaccurate readings when it was within range and they suggested adding more coupling agent, changing coupling agent, or relocating the transducers as far away as possible from a pipe corner. We proceeded to double check that our mounting was the appropriate distance away from any reducers, expanders, or elbows in the pipe, and repeated the mounting process with additional coupling agent. Unfortunately, similar results occurred each time: the "Quality" readings would go bad after the couplant cured overnight. Then when the transducers were pushed/adjusted until they were back within the appropriate "Quality" range the next day, the measured flow rates would be off and continuously fluctuating (by about $\pm$ 0.75 $-$ 1.5 GPM). Furthermore, after adjusting the transducers, about 15 minutes later when we adjusted the flow rate, the "Quality" would drop back down to 0.

Our hypothesis is that this is a defective unit, since the manual claims such high accuracy and repeatability. We highly recommend the manufacturer provide more detailed instructions, specifically with regard to how to ensure proper alignment and spacing after the couplant has cured and what changes to expect in the "Signal Strength" and "Quality" readings before and after the couplant has cured. Specific recommendations for which coupling agent to use would also be beneficial for those seeking to use this sensor in the future.

An official Amazon review was left for the device and can found at this link:

https://www.amazon.com/gp/customer-reviews/RCCVLEYWEO7UT
/ref=cm_cr_arp_d_rvw_ttl?ie=UTF8&ASIN=B07732MYP9

APPENDIX C

Code

The codes developed for this project can be found in the following public *Dropbox* link:

https://www.dropbox.com/sh/lupuvh6avdg6cnd
/AAAIxJHt_b-KeL4CupqR7zQFa?dl=0

APPENDIX D

Parts Lists

Due to the size of the tables, the complete parts lists (including part numbers, suppliers, and online prices as of Aug. 2019) are included at the public *Dropbox* for this thesis:

https://www.dropbox.com/s/tzehlgcmeiryrkp/Parts_Lists.xlsx?dl=0

Table D.1: Test Loop

Part Name	**Quantity**
Heat Exchanger Section	
Fin-and-Tube Heat Exchanger	1
Lasko 20" 3-Speed Box Fan (White)	1
Lasko 20" High Velocity 3-Speed Fan	1
Heat Injection Section	
1" MNPT Utilitech Hot Water Heater Element (1500 W, 120 V)	2
Single-Pole Toggle Switch (15A, 125V)	2
Electrical Box Extension (Metal)	4
Toggle Switch Electrical Box Cover (Metal)	2
Blank Electrical Box Cover (Metal)	2
#18 Rubber O-Rings (10-pack)	1
12AWG/3-Wire Power Cord (Black, per foot)	12
Industrial Straight Blade Plug (15A, 125V)	2
3/8" BX/MC Wire Connector (for 1/2" KO)	2
Other Components	
1/40 HP Taco Circulation Pump (3/4" sweat)	1
Dwyer Variable Area Flowmeter	1
1/8" MNPT Watts Air Vent	1
1/2" MNPT Winters Analog Thermometer	2
1/8" MNPT Omega *ON-410-PP* Temperature Probe	2
3/4" MNPT Omega *FTB-4607* Turbine Flowmeter	1
2 Gallon Expansion Tank (Utilitech)	1
1/4" MNPT General Purpose Pressure Gauge (0-200psi)	1
1/4" MNPT Threaded Cap Plug Fitting	1
Tees	
1-1/4" (FNPTxFNPTxFNPT) Galvanized Steel Tee	2
1"x1"x1/2" (CxCxFNPT) Case Brass Tee	2
1" x 1" x 1/2" (CxCxC) Copper Tee	2

Continued on next page...

Table D.1 – continued from previous page

Part Name	Quantity
Tees (continued)	
1" x 1" x 3/4" (CxCxC) Copper Tee	1
1/4" (FNPTxFNPTxMNPT) Kobalt Brass T Fitting	1
1" x 1/2" x 1" (CxCxC) Copper Tee	2
1/8" (FNPTxFNPTxFNPT) LASCO Brass Tee	1
Elbows	
90 Copper Elbow	4
Bushings	
1/2" FTG x 1/8" FNPT Copper Bushing	3
1/2" FTG x 1/4" FNPT Copper Bushing	1
1" C x 1" C Copper Couplings	1
1-1/4"MNPT x 1"FNPT Galvanized Steel Bushing	2
Threaded Adapters	
1-1/4" MNPT x 1-1/4" C Copper Adapter	4
1" MNPT x 1" C Copper Adapter	3
1" C x 3/4" MNPT Copper Adapter	1
1" C x 3/4" FNPT Copper Adapter	2
1/8" MNPT x 1/4" Barb Brass Hose Fitting	1
1/2" FNPT x 1" C Copper Adapter	2
3/4" FTG x 3/4" FNPT Copper Adapter	1
1/2" MNPT x 1/2" MNPT Brass Nipple Fitting	2
1/8" MNPT x 1/8" MNPT Brass Nipple Fitting	1
Unions	
1" C x 1" C Copper Unions	12
Reducers / Expanders	
1-1/4" C x 1" C Copper Reducer/Expander	2
1" FTG x 3/4" C Copper Reducer/Expander	2
Valves	
1" FNPT x 1" FNPT x 1" FNPT Brass 3-Way Valve	1
3/4" FNPT x GHT Aluminum Hose Bibb (No Kink)	1
1/8" MNPT x 1/8" FNPT LASCO Brass Ball Valve	1
Straight Pipe	
1-1/4" Straight Copper Pipe (Type L, 10')	1
3/4" Straight Copper Pipe (5')	1
1" Straight Copper Pipe (10')	2

FTG – *"fitting"* (fits just inside of straight copper pipe of same diameter)
C – *"cup"* (fits around outside of straight copper pipe of same diameter)
FNPT – *"female national pipe threading"*
MNPT – *"male national pipe threading"*
GHT – *"garden hose threading"*

Table D.2: Clamp-On Energy Meter

Part Name	**Quantity**
Temperature Sensors	
5k Thermistor	4
2.1x5.5mm (Male) Plug to Wire Leads (6')	4
Heat Shrink Tubing (580 pcs)	1
3.01 k Resistor (1% tolerance, 1/4 W)	4
Flow Sensors	
Ultrasonic Flow Transducer	1
2A, 12VDC External Power Supply (2.1x5.5mm (Male) Plug, 120 V)	1
249 Resistor (1% tolerance, 1/4 W)	1
Voltage Sensors	
120VAC-to-9VAC *Triad Magnetics* Voltage Adapter (1.2A, 60 Hz)	2
120VAC-to-9VAC *HQRP* Voltage Adapter (1.3 A, 60 Hz)	1
1.4 k Resistor (1% tolerance, 1/4 W)	3
1.5 k Resistor (1% tolerance, 1/4 W)	3
10 k Resistor (1% tolerance, 1/4 W)	3
Current Sensors	
YHDC SCT-013-000	3
56.2 Resistor (1% tolerance, 1/4 W)	3
Micro-Controller	
Raspberry Pi 3B+	1
32 GB MicroSD Card	1
2.5A, 9VDC External Power Supply (MicroUSB, 120 V)	1
Analog-to-Digital Conversion Board	
Adafruit ADS1115	4
Additional Circuit Board Components	
3.1" x 5.5" PCB Board (0.1" Hole Spacing)	2
2.1x5.5mm (Female AND Male) Plug to Screw Terminal (10 pairs)	2
4A, 5VDC External Power Supply (2.1x5.5mm (Male) Plug, 120V)	1
Male Header Pins (0.1" Spacing, 50 pack of 40 pins each)	1
Assorted Female Header Pins (0.1" Spacing, 120 pcs)	1
Female-to-Female Jumper Wire Kit (6", 20 pcs)	2
Male-to-Male Jumper Wire Kit (22 AWG, 140 pack)	1
Assorted Standoff Spacers Screws & Nuts (210 pcs)	1
475 k Resistors (1% tolerance, 1/4 W)	4

Table D.3: In-line Energy Meter

Part Name	**Quantity**
Temperature Sensors	
2.25k Thermistor (*Omega ON-410-PP*)	2
1.5 k Resistor (1% tolerance, 1/4 W)	2
Flow Sensors	
Pulse Output Turbine Flow Meter (*Omega FTB-4607*)	1
2A, 12VDC External Power Supply (2.1x5.5mm (Male) Plug, 120 V)	1
10 k Resistor (1% tolerance, 1/4 W)	1
Power Sensors	
HOBO Plug Load Data Logger	3
Micro-Controller	
Raspberry Pi 3B+	2
32 GB MicroSD Card	2
2.5A, 9VDC External Power Supply (MicroUSB, 120 V)	2
Analog-to-Digital Conversion Board	
Adafruit ADS1115	1
Additional Circuit Board Components	
3.1" x 5.5" PCB Board (0.1" Hole Spacing)	1
2.1x5.5mm (Female AND Male) Plug to Screw Terminal (10 pairs)	1
Male Header Pins (0.1" Spacing, 50 pack of 40 pins each)	1
Assorted Female Header Pins (0.1" Spacing, 120 pcs)	1
Female-to-Female Jumper Wire Kit (6", 20 pcs)	1
Male-to-Male Jumper Wire Kit (22 AWG, 140 pack)	1
Assorted Standoff Spacers Screws & Nuts (210 pcs)	1

APPENDIX E

3D Printed Parts

The following 3D-printed parts' `.SLDPRT` files can be found in the public *Dropbox* for this thesis:

https://www.dropbox.com/sh/8tdcg8kfav3r3v9
/AAAb2gPeiR9sKaqKXT9N4NZIa?dl=0

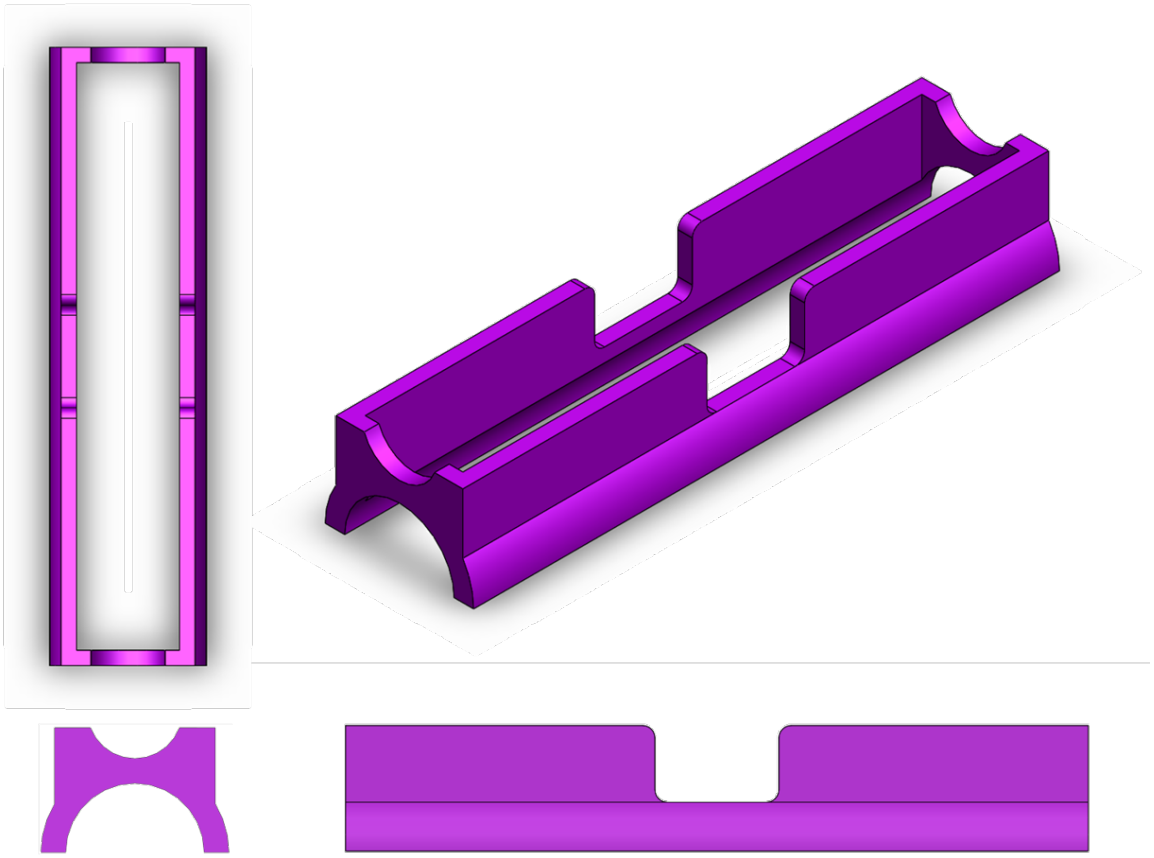

Figure E.1: Ultrasonic Flow Transducer Alignment Tool designed by Sheldon Hair (undergraduate assistant).

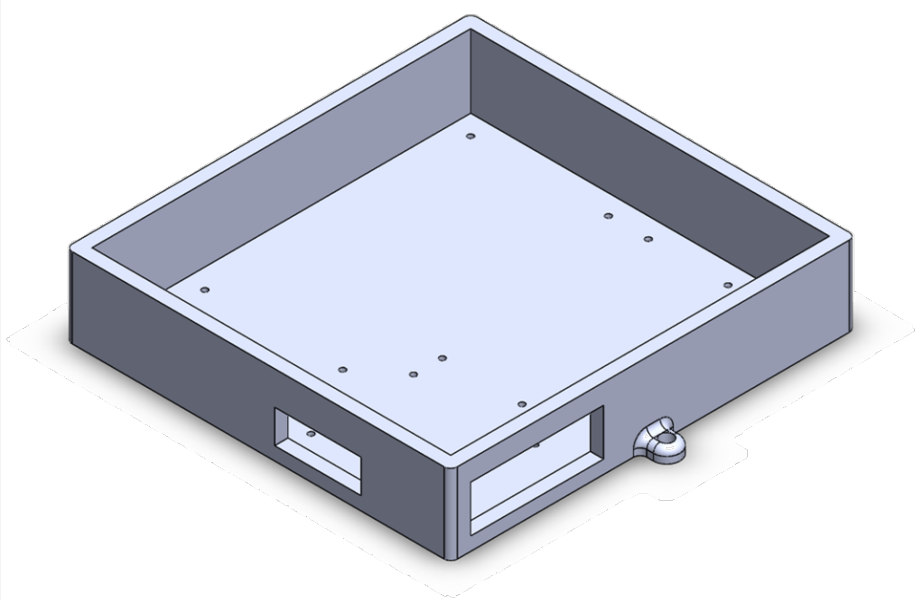

Figure E.2: Clamp-on Energy Meter Case - Bottom (Isometric View).

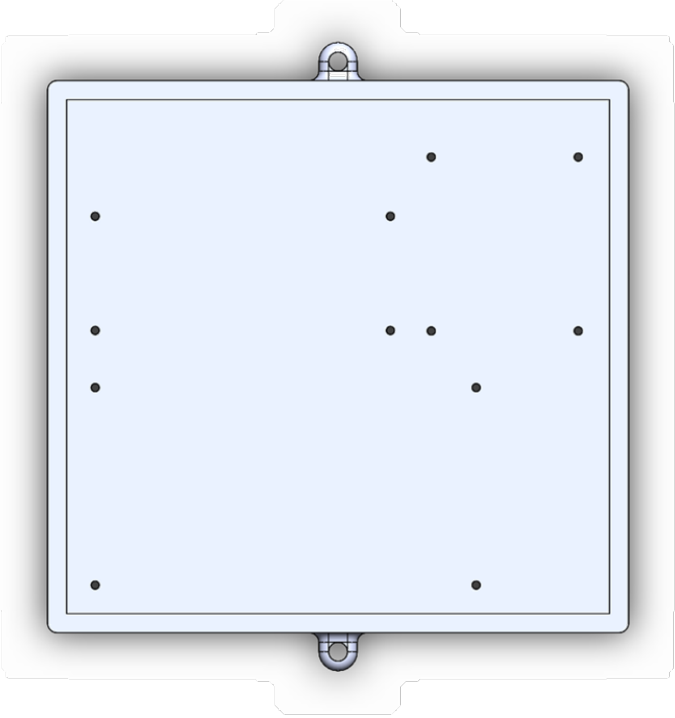

Figure E.3: Clamp-on Energy Meter Case - Bottom (Top View).

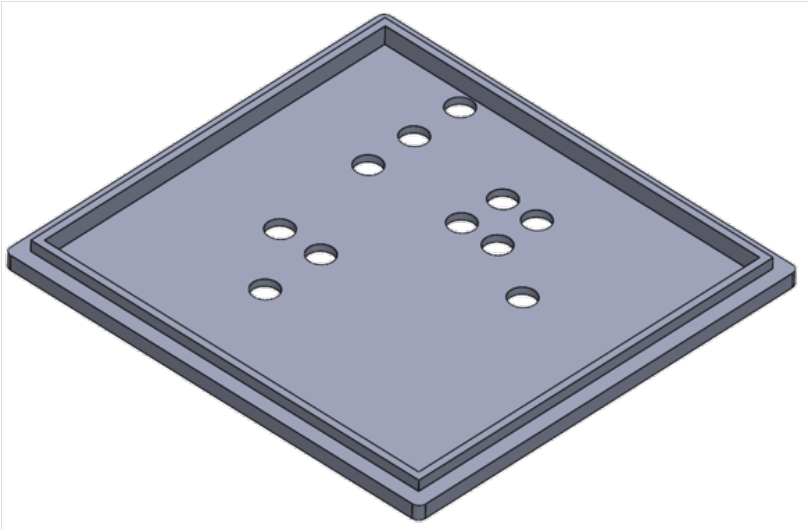

Figure E.4: Clamp-on Energy Meter Case - Top (Isometric View).

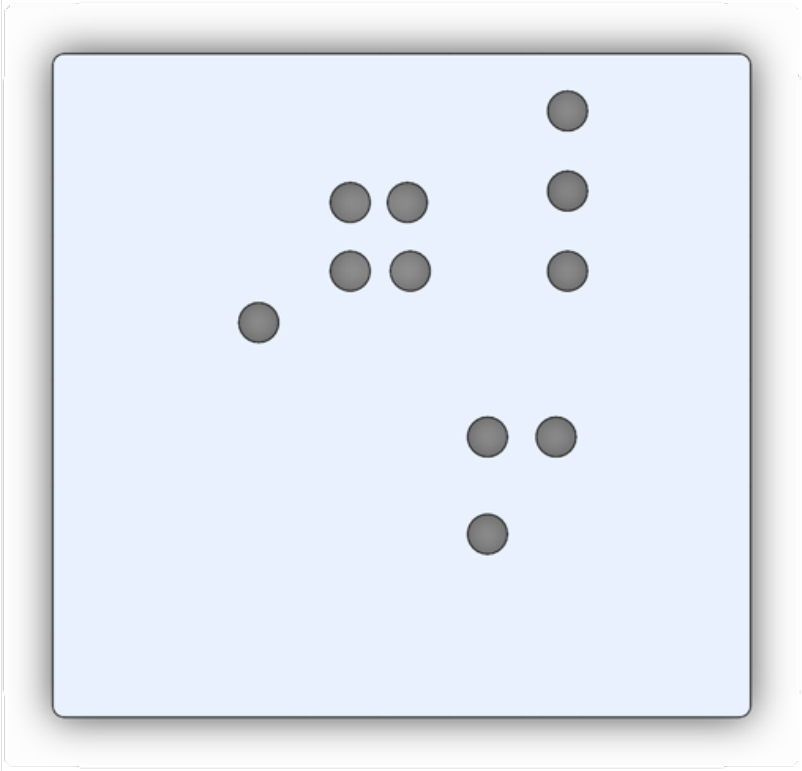

Figure E.5: Clamp-on Energy Meter Case - Top (Top View).

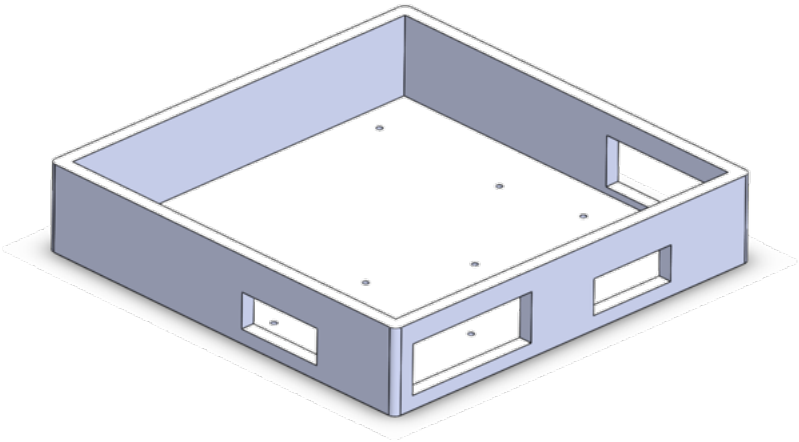

Figure E.6: In-Line Energy Meter Case - Bottom (Isometric View).

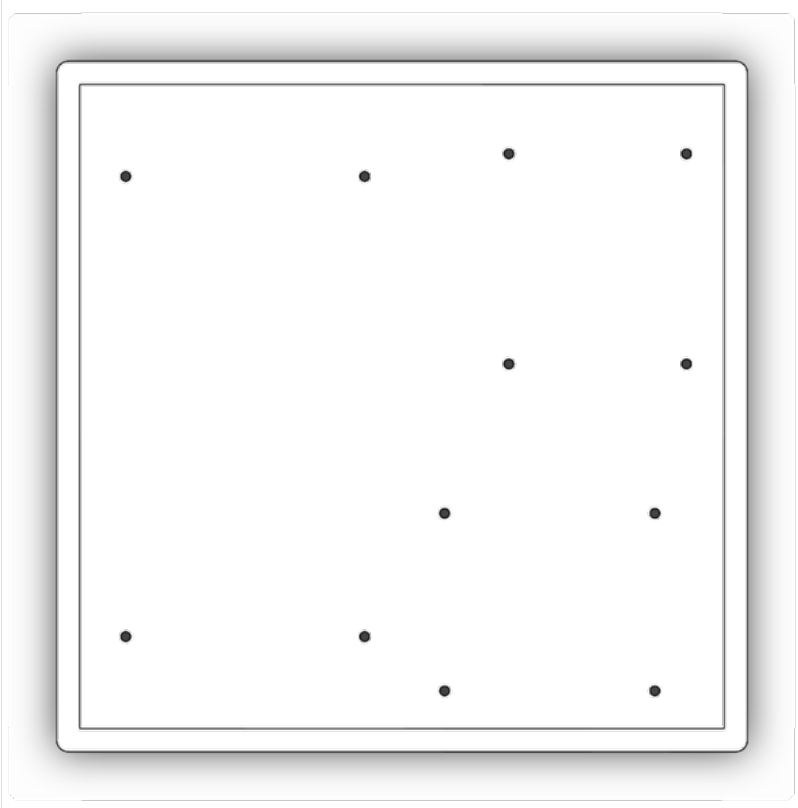

Figure E.7: In-Line Energy Meter Case - Bottom (Top View).

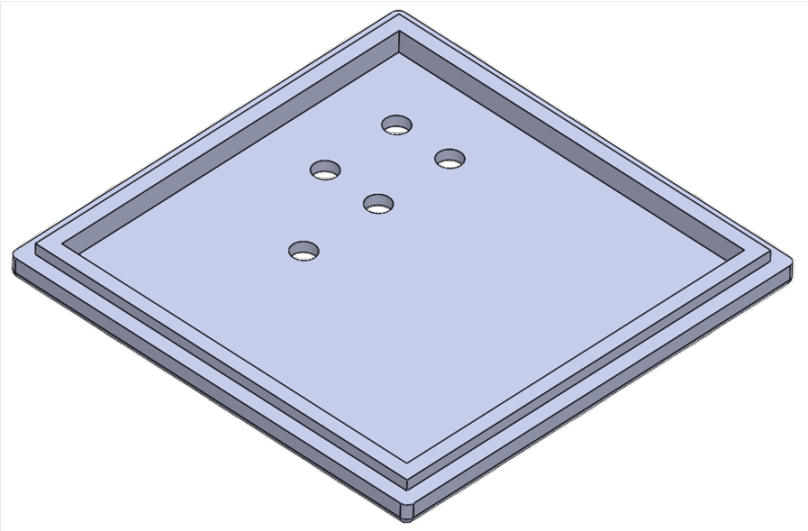

Figure E.8: In-Line Energy Meter Case - Top (Isometric View).

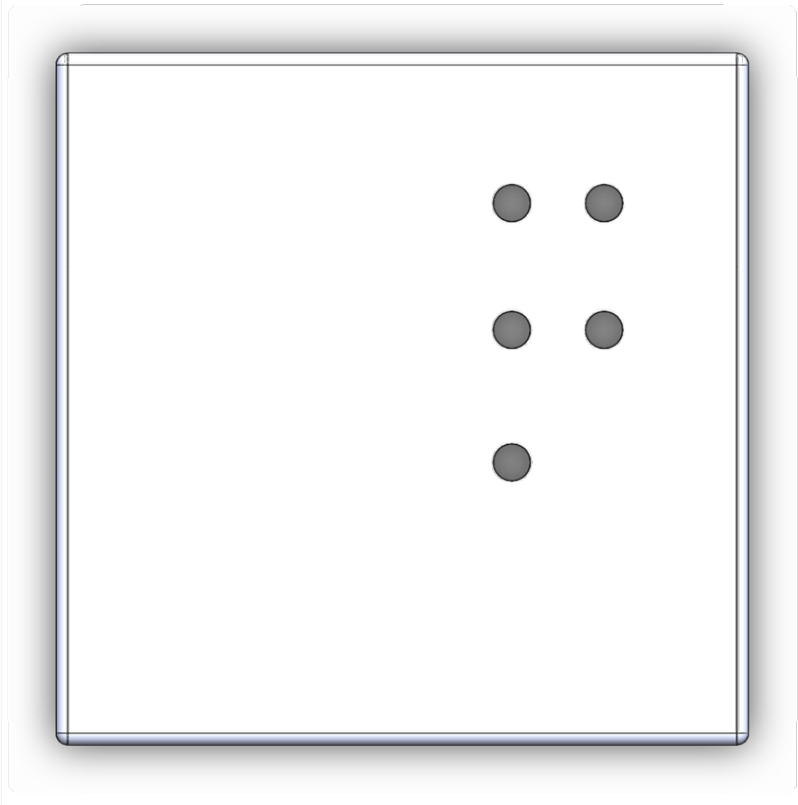

Figure E.9: In-Line Energy Meter Case - Top (Top View).

APPENDIX F

Example Excel Sheet for Shunt Resistor Sizing

The excel sheet used to size the shunt resistor can be found in this public *Dropbox* for this thesis:

https://www.dropbox.com/sh/esnnn3mf2oyvyua
/AAAJhHHHyVsx3b3YaBTTLgzya?dl=0

(Screen-shot on the next page)

(Developed from Initial Data)											
Stienhart-Hart Coefficients											
A	0.001284093										
B	0.000236383										
C	9.20014E-08										
							sum of ΔV/ΔT				
							(5°C - 55 °C)	Max ΔV/ΔT	Min ΔV/ΔT		
V_Source	5	[V]		5			33.07849018	0.052129121	0.028674487		
R_Shunt	3000	[Ω]		3000							
V_Shunt	0.62086	[V]		3.34076			Possible R_Shunt	Sum ΔV/ΔT	Max ΔV/ΔT	Min ΔV/ΔT	
i	0.000206954	[A]		0.001113586	R_shunt to MAX(Sum of ΔV/ΔT)		10762.90696	33.09858818	0.052129121	0.028687321	
R_Therm_MAX	21160		R_Therm_MIN	1490			10000	33.10529119	0.052129121	0.028691601	
V_Therm_MAX	4.379139073		V_Therm_MIN	1.659242762	R_shunt to MAX(Min of ΔV/ΔT)		4133.068964	33.11199603	0.052129121	0.028695883	
							3000	33.11870271	0.052129121	0.028700166	
R_Therm [Ω]	T_Therm [°F]	T_Therm [°C]	R_shunt [Ω]	I [A]	V_shunt [V]	V_Therm [V]	ΔT	ΔV_Therm	ΔV_Shunt	ΔV/ΔT_Therm	ΔV/ΔT_Shunt
22000	21.66	-5.74	3000	0.0002	0.6	4.4					
21995	21.67	-5.74	3000	0.00020004	0.600120024	4.399879976	0.004290581	0.000120024	0.000120024	0.027973833	0.027973833
21990	21.68	-5.73	3000	0.00020008	0.600240096	4.399759904	0.004291674	0.000120072	0.000120072	0.027977901	0.027977901
21985	21.69	-5.73	3000	0.00020012	0.600360216	4.399639784	0.004292767	0.00012012	0.00012012	0.02798197	0.02798197
21980	21.69	-5.73	3000	0.00020016	0.600480384	4.399519616	0.004293861	0.000120168	0.000120168	0.027986041	0.027986041
21975	21.70	-5.72	3000	0.0002002	0.600600601	4.399399399	0.004294956	0.000120216	0.000120216	0.027990112	0.027990112
21970	21.71	-5.72	3000	0.00020024	0.600720865	4.399279135	0.004296051	0.000120264	0.000120264	0.027994185	0.027994185
21965	21.72	-5.71	3000	0.00020028	0.600841178	4.399158822	0.004297146	0.000120313	0.000120313	0.027998259	0.027998259
21960	21.73	-5.71	3000	0.000200321	0.600961538	4.399038462	0.004298242	0.000120361	0.000120361	0.028002335	0.028002335
21955	21.73	-5.70	3000	0.000200361	0.601081948	4.398918052	0.004299339	0.000120409	0.000120409	0.028006411	0.028006411
21950	21.74	-5.70	3000	0.000200401	0.601202405	4.398797595	0.004300436	0.000120457	0.000120457	0.028010489	0.028010489
21945	21.75	-5.70	3000	0.000200441	0.60132291	4.39867709	0.004301533	0.000120506	0.000120506	0.028014568	0.028014568
21940	21.76	-5.69	3000	0.000200481	0.601443464	4.398556536	0.004302631	0.000120554	0.000120554	0.028018648	0.028018648
21935	21.76	-5.69	3000	0.000200521	0.601564067	4.398435933	0.00430373	0.000120602	0.000120602	0.028022729	0.028022729
21930	21.77	-5.68	3000	0.000200562	0.601684717	4.398315283	0.004304829	0.000120651	0.000120651	0.028026812	0.028026812

APPENDIX G

Mathematical Derivations

Derivation of overall calorimetric heat transfer absolute uncertainty:

$$\text{In general} \quad E_F = \sqrt{\left(\frac{\partial F}{\partial x_1}E_{x_1}\right)^2 + \left(\frac{\partial F}{\partial x_2}E_{x_2}\right)^2 + \ldots + \left(\frac{\partial F}{\partial x_n}E_{x_n}\right)^2} \tag{4.1}$$

$$\text{Let } F \text{ be} \quad \dot{Q} = \dot{V} \cdot \rho \cdot c_p \cdot (T_{\text{LWT}} - T_{\text{EWT}}) \tag{3.1}$$

$$\text{Such that} \quad \frac{\partial \dot{Q}}{\partial \dot{V}} = \rho c_p \left(T_{\text{LWT}} - T_{\text{EWT}}\right)$$

$$\text{and} \quad \frac{\partial \dot{Q}}{\partial \Delta T} = \rho c_p \dot{V}$$

$$\text{and} \quad E_{\dot{Q}} = \sqrt{\left(\frac{\partial \dot{Q}}{\partial \dot{V}}E_{\dot{V}}\right)^2 + \left(\frac{\partial \dot{Q}}{\partial \Delta T}E_{\Delta T}\right)^2}$$

$$\text{Therefore} \quad E_{\dot{Q}} = \sqrt{\left(\rho c_p (T_{\text{LWT}} - T_{\text{EWT}}) \cdot E_{\dot{V}}\right)^2 + \left(\rho c_p \dot{V} \cdot E_{\Delta T}\right)^2} \tag{4.4}$$

Derivation of overall calorimetric heat transfer relative uncertainty:

$$\text{In general} \quad e_F = \frac{E_F}{F} \tag{4.2}$$

$$\text{Let } F \text{ be} \quad \dot{Q} = \dot{V} \cdot \rho \cdot c_p \cdot (T_{\text{LWT}} - T_{\text{EWT}}) \tag{3.1}$$

$$\text{Such that} \quad E_{\dot{Q}} = \sqrt{\left(\rho c_p (T_{\text{LWT}} - T_{\text{EWT}}) \cdot E_{\dot{V}}\right)^2 + \left(\rho c_p \dot{V} \cdot E_{\Delta T}\right)^2} \tag{4.4}$$

$$\text{and} \quad e_{\dot{Q}} = \frac{E_{\dot{Q}}}{\dot{Q}}$$

$$\text{Therefore} \quad e_{\dot{Q}} = \frac{\sqrt{\left(\rho c_p (T_{\text{LWT}} - T_{\text{EWT}}) \cdot E_{\dot{V}}\right)^2 + \left(\rho c_p \dot{V} \cdot E_{\Delta T}\right)^2}}{\dot{V} \cdot \rho \cdot c_p \cdot (T_{\text{LWT}} - T_{\text{EWT}})}$$

$$e_{\dot{Q}} = \sqrt{\frac{\left(\rho c_p (T_{\text{LWT}} - T_{\text{EWT}}) \cdot E_{\dot{V}}\right)^2 + \left(\rho c_p \dot{V} \cdot E_{\Delta T}\right)^2}{\left(\dot{V} \rho c_p \cdot (T_{\text{LWT}} - T_{\text{EWT}})\right)^2}}$$

$$e_{\dot{Q}} = \sqrt{\frac{\left(\rho c_p (T_{\text{LWT}} - T_{\text{EWT}}) \cdot E_{\dot{V}}\right)^2}{\left(\rho c_p (T_{\text{LWT}} - T_{\text{EWT}}) \cdot \dot{V}\right)^2} + \frac{\left(\rho c_p \dot{V} \cdot E_{\Delta T}\right)^2}{\left(\dot{V} \rho c_p \cdot (T_{\text{LWT}} - T_{\text{EWT}})\right)^2}}$$

$$e_{\dot{Q}} = \sqrt{\left(\frac{E_{\dot{V}}}{\dot{V}}\right)^2 + \left(\frac{E_{\Delta T}}{\Delta T}\right)^2} \tag{4.5}$$

Derivation of individual device's
electrical power consumption absolute uncertainty:

$$\text{In general} \quad E_F = \sqrt{\left(\frac{\partial F}{\partial x_1}E_{x_1}\right)^2 + \left(\frac{\partial F}{\partial x_2}E_{x_2}\right)^2 + \ldots + \left(\frac{\partial F}{\partial x_n}E_{x_n}\right)^2} \tag{4.1}$$

$$\text{Let } F \text{ be} \quad \dot{W}_{\mathrm{x}} = V_{\mathrm{X}} I_{\mathrm{X}} \quad \text{(assuming Power Factor = 1)}$$

$$\text{Such that} \quad \frac{\partial \dot{W}_{\mathrm{X}}}{\partial V_{\mathrm{X}}} = I_{\mathrm{X}}$$

$$\frac{\partial \dot{W}_{\mathrm{X}}}{\partial I_{\mathrm{X}}} = V_{\mathrm{X}}$$

$$\text{and} \quad E_{\dot{W}_{\mathrm{X}}} = \sqrt{\left(\frac{\partial \dot{W}_{\mathrm{X}}}{\partial V_{\mathrm{X}}}E_{\mathrm{V_X}}\right)^2 + \left(\frac{\partial \dot{W}_{\mathrm{X}}}{\partial I_{\mathrm{X}}}E_{\mathrm{I_X}}\right)^2}$$

$$\text{Therefore} \quad E_{\dot{W}_{\mathrm{X}}} = \sqrt{\left(I_{\mathrm{X}} \cdot E_{\mathrm{V_X}}\right)^2 + \left(V_{\mathrm{X}} \cdot E_{\mathrm{I_X}}\right)^2}$$

Derivation of individual device's electrical power consumption relative uncertainty:

$$\text{In general} \quad e_F = \frac{E_F}{F} \tag{4.2}$$

$$\text{Let } F \text{ be} \quad \dot{W}_{\mathrm{X}} = V_{\mathrm{X}} I_{\mathrm{X}} \quad \text{(assuming Power Factor = 1)}$$

$$\text{Such that} \quad E_{\dot{W}_{\mathrm{X}}} = \sqrt{\left(I_{\mathrm{X}} \cdot E_{\mathrm{V_X}}\right)^2 + \left(V_{\mathrm{X}} \cdot E_{\mathrm{I_X}}\right)^2}$$

$$\text{and} \quad e_{\dot{W}_{\mathrm{X}}} = \frac{E_{\dot{W}_{\mathrm{X}}}}{\dot{W}_{\mathrm{X}}}$$

$$\text{Therefore} \quad e_{\dot{W}_{\mathrm{X}}} = \frac{\sqrt{\left(I_{\mathrm{X}} \cdot E_{\mathrm{V_X}}\right)^2 + \left(V_{\mathrm{X}} \cdot E_{\mathrm{I_X}}\right)^2}}{V_{\mathrm{X}} I_{\mathrm{X}}}$$

$$e_{\dot{W}_{\mathrm{X}}} = \sqrt{\frac{\left(I_{\mathrm{X}} \cdot E_{\mathrm{V_X}}\right)^2 + \left(V_{\mathrm{X}} \cdot E_{\mathrm{I_X}}\right)^2}{\left(V_{\mathrm{X}} I_{\mathrm{X}}\right)^2}}$$

$$e_{\dot{W}_{\mathrm{X}}} = \sqrt{\frac{\left(I_{\mathrm{X}} \cdot E_{\mathrm{V_X}}\right)^2}{\left(V_{\mathrm{X}} I_{\mathrm{X}}\right)^2} + \frac{\left(V_{\mathrm{X}} \cdot E_{\mathrm{I_X}}\right)^2}{\left(V_{\mathrm{X}} I_{\mathrm{X}}\right)^2}}$$

$$e_{\dot{W}_{\mathrm{X}}} = \sqrt{\left(\frac{E_{V_{\mathrm{X}}}}{V_{\mathrm{X}}}\right)^2 + \left(\frac{E_{I_{\mathrm{X}}}}{I_{\mathrm{X}}}\right)^2}$$

Derivation of overall electrical power consumption absolute uncertainty:

$$\text{In general} \quad E_F = \sqrt{\left(\frac{\partial F}{\partial x_1}E_{x_1}\right)^2 + \left(\frac{\partial F}{\partial x_2}E_{x_2}\right)^2 + \ldots + \left(\frac{\partial F}{\partial x_n}E_{x_n}\right)^2} \tag{4.1}$$

$$\text{Let } F \text{ be} \quad \dot{W}_{\text{TOT}} = \left(\dot{W}_{\text{H1}} + \dot{W}_{\text{H2}} + \dot{W}_{\text{CP}}\right)$$

$$\begin{aligned}
\text{Where} \quad \dot{W}_{\text{H1}} &= V_{\text{H1}} I_{\text{H1}} \quad \text{(assuming Power Factor = 1)} \\
\dot{W}_{\text{H2}} &= V_{\text{H2}} I_{\text{H2}} \quad \text{(assuming Power Factor = 1)} \\
\dot{W}_{\text{CP}} &= V_{\text{CP}} I_{\text{CP}} \quad \text{(assuming Power Factor = 1)}
\end{aligned}$$

$$\begin{aligned}
\text{and} \quad E_{\dot{W}_{\text{H1}}} &= \sqrt{\left(I_{\text{H1}} \cdot E_{\text{V}_{\text{H1}}}\right)^2 + \left(V_{\text{H1}} \cdot E_{\text{I}_{\text{H1}}}\right)^2} \\
E_{\dot{W}_{\text{H2}}} &= \sqrt{\left(I_{\text{H2}} \cdot E_{\text{V}_{\text{H2}}}\right)^2 + \left(V_{\text{H2}} \cdot E_{\text{I}_{\text{H2}}}\right)^2} \\
E_{\dot{W}_{\text{CP}}} &= \sqrt{\left(I_{\text{CP}} \cdot E_{\text{V}_{\text{CP}}}\right)^2 + \left(V_{\text{CP}} \cdot E_{\text{I}_{\text{CP}}}\right)^2}
\end{aligned}$$

$$\text{Such that} \quad \frac{\partial \dot{W}_{\text{TOT}}}{\partial \dot{W}_{\text{H1}}} = 1 \quad , \quad \frac{\partial \dot{W}_{\text{TOT}}}{\partial \dot{W}_{\text{H2}}} = 1 \quad , \quad \frac{\partial \dot{W}_{\text{TOT}}}{\partial \dot{W}_{\text{CP}}} = 1$$

$$\text{and} \quad E_{\dot{W}_{\text{TOT}}} = \sqrt{\left(\frac{\partial \dot{W}_{\text{TOT}}}{\partial \dot{W}_{\text{H1}}}E_{\text{H1}}\right)^2 + \left(\frac{\partial \dot{W}_{\text{TOT}}}{\partial \dot{W}_{\text{H2}}}E_{\text{H2}}\right)^2 + \left(\frac{\partial \dot{W}_{\text{TOT}}}{\partial \dot{W}_{\text{CP}}}E_{\text{CP}}\right)^2}$$

$$\text{Therefore} \quad E_{\dot{W}_{\text{TOT}}} = \sqrt{\left(1 \cdot E_{\dot{W}_{\text{H1}}}\right)^2 + \left(1 \cdot E_{\dot{W}_{\text{H2}}}\right)^2 + \left(1 \cdot E_{\dot{W}_{\text{CP}}}\right)^2} \tag{4.10}$$

Derivation of thermal resistance network model equations

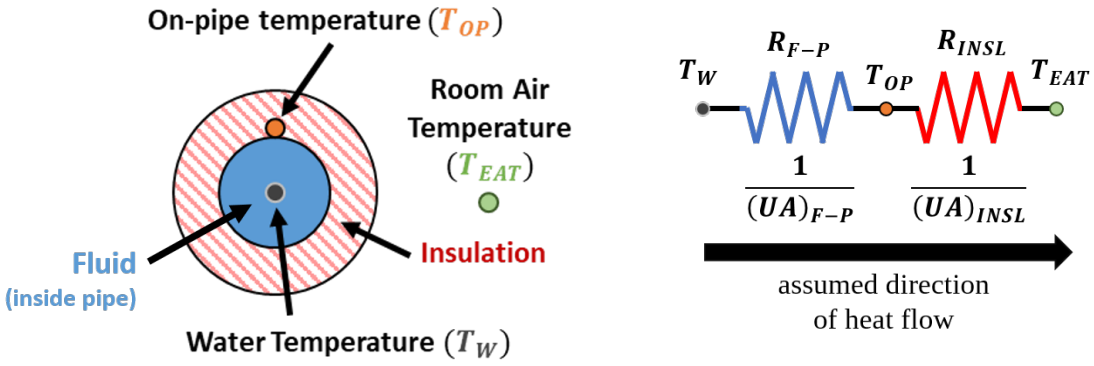

Assuming the rate of heat transfer across the network is constant.
(only the thermal resistance changes)

$$\dot{Q}_{\text{F-P}} = \dot{Q}_{\text{INSL}}$$

Solve for intermediate on-pipe temperature:

$$(UA)_{\text{F-P}}\,(T_{\text{OP}} - T_{\text{W}}) = (UA)_{\text{INSL}}\,(T_{\text{EAT}} - T_{\text{OP}})$$

$$(UA)_{\text{F-P}}T_{\text{OP}} - (UA)_{\text{F-P}}T_{\text{W}} = (UA)_{\text{INSL}}T_{\text{EAT}} - (UA)_{\text{INSL}}T_{\text{OP}}$$

$$(UA)_{\text{F-P}}T_{\text{OP}} + (UA)_{\text{INSL}}T_{\text{OP}} = (UA)_{\text{INSL}}T_{\text{EAT}} + (UA)_{\text{F-P}}T_{\text{W}}$$

$$\Big((UA)_{\text{F-P}} + (UA)_{\text{INSL}}\Big)T_{\text{OP}} = (UA)_{\text{INSL}}T_{\text{EAT}} + (UA)_{\text{F-P}}T_{\text{W}}$$

$$\widehat{T}_{\text{OP}} = \frac{(UA)_{\text{INSL}}T_{\text{EAT}} + (UA)_{\text{F-P}}T_{\text{W}}}{(UA)_{\text{F-P}} + (UA)_{\text{INSL}}} \tag{6.3}$$

Solve for estimated water temperature:

$$(UA)_{\text{F-P}}\,(T_{\text{OP}} - T_{\text{W}}) = (UA)_{\text{INSL}}\,(T_{\text{EAT}} - T_{\text{OP}})$$

$$(T_{\text{OP}} - T_{\text{W}}) = \frac{(UA)_{\text{INSL}}}{(UA)_{\text{F-P}}} \cdot (T_{\text{EAT}} - T_{\text{OP}})$$

$$\widehat{T}_{\text{W}} = T_{\text{OP}} - \frac{(UA)_{\text{INSL}}}{(UA)_{\text{F-P}}} \cdot (T_{\text{EAT}} - T_{OP}) \tag{6.2}$$

APPENDIX H

Detailed Lessons Learned about ADC Boards

Several lessons were learned throughout the development of our energy meters that came as a result of implementing and trouble-shooting Analog-to-Digital Conversion (ADC) boards. This appendix discusses in greater detail the phenomena stumbled upon and our subsequent modifications/solutions.

The initial ADC board that we purchased was the *Alchemy Power Pi-16ADC*. It was purchased because of its advertised 16-bit resolution. It was relatively inexpensive and was a sufficient board to begin learning how to measure voltages from a DC-power supply. This board came with its own *Python* library, however its supplier was contacted a few times for clarification.

To initially investigate the accuracy of the ADC board, we started out by measuring various constant analog voltages from a DC-power supply (specifically a *MASTECH HY3005F-3*). Our reference was a *Fluke 8808A Digital Multimeter* (accurate up to ±0.0002 VDC). A simple voltage divider circuit was measured, in order to drop the voltage down to within the *Pi-16ADC*'s range (0 - 2.5 V). A few interesting observation were found during this test and are explained below.

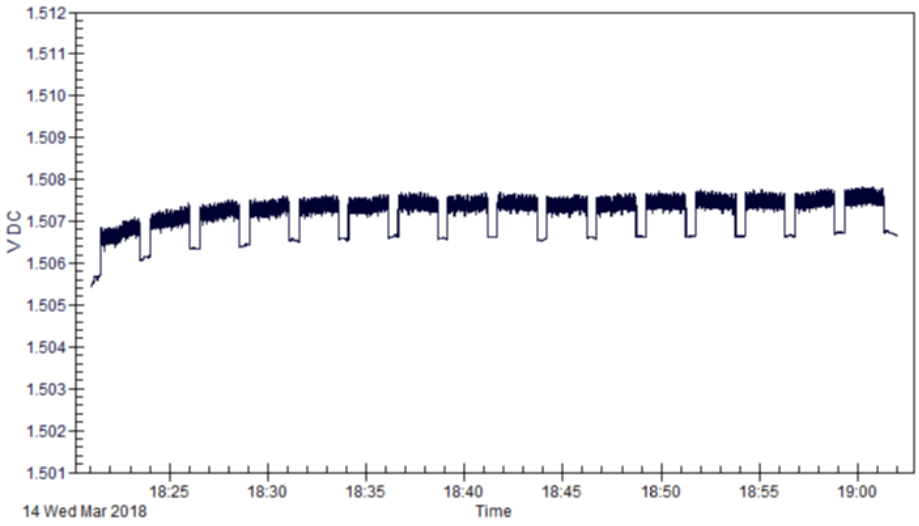

Figure H.1: Transient response discovered in the DC supply voltage during ADC calibration.

As seen in Figure H.1, the DC-power supply was found to drift up to a steady-state voltage over the course of the initial tests. As a result, we had been finding that the accuracy of the first few channels we recorded on were less accurate than the latter. In order to compensate for this, each of the 16-channels on the *Pi-16ADC*

board were sampled for a longer amount of time, and then the later values averaged together to get their average voltage reading.

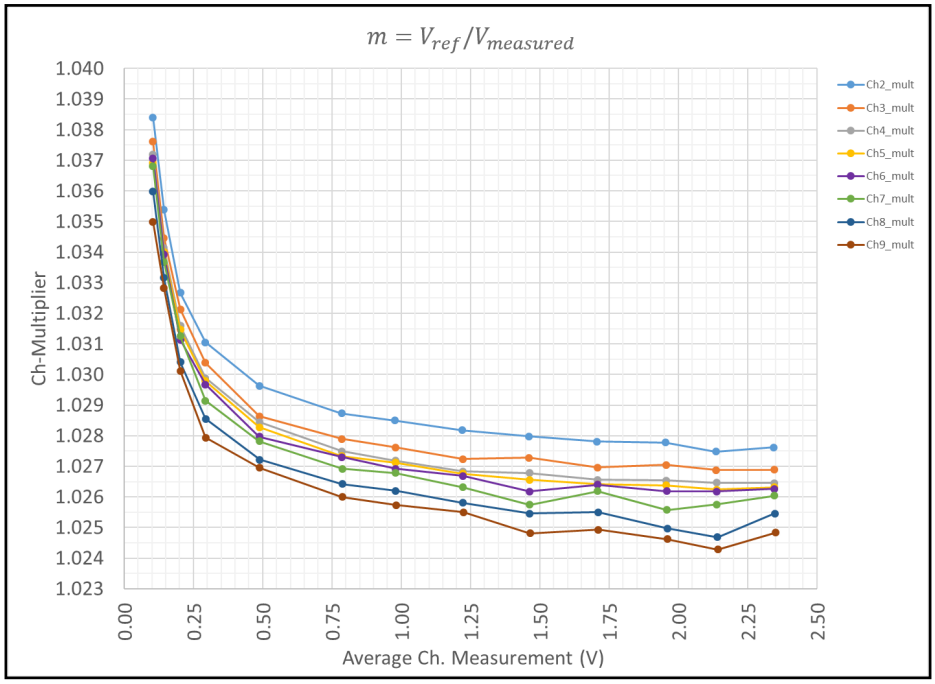

Figure H.2: Example plot of estimated conversion constants to correct measured voltage to actual voltage.

After gathering data from the reference multimeter and the *Pi-16ADC*, the error between the two was calculated. Unfortunately the average error was greater than ± 0.01 V, which was not going to allow us to very accurately measure the recommended $\pm$ 350 μV necessary to see the $\pm$ 0.01 °C temperature difference like we had hoped. In order to try to correct for this, a correction-constant was calculated at each measured voltage. As seen in Figure H.2, the calculated constant had an exponential-like form as the voltage measured increased. Equation (8.1) was then formulated to fit to the curves to calculate an appropriate "channel multiplier" for that range of voltages.

$$\text{multiplier} = C1 + C2 \cdot \exp(-C3 \cdot V_{\text{measured}}) + C4 \cdot V_{\text{measured}} \tag{8.1}$$

As can be seen by the example shown in Figure H.3, all 16 channels of the Pi-16ADC board were then fit with their own curve and their error plots produced.

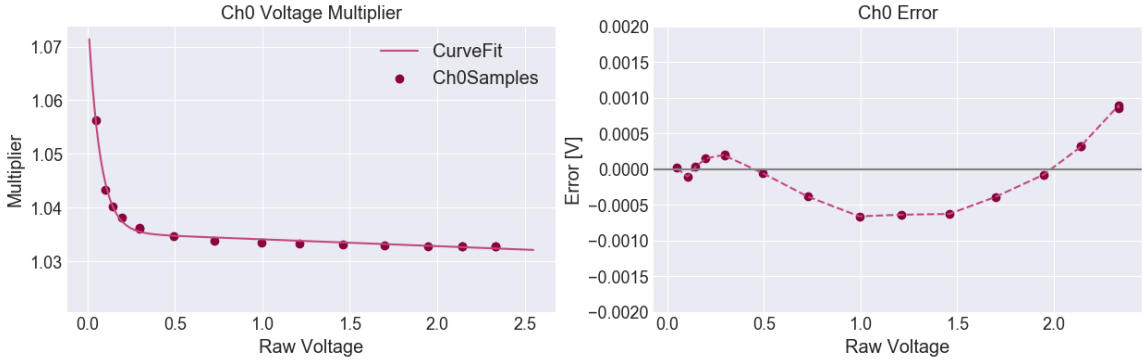

Figure H.3: Example plot of Channel 0's voltage calibration and resulting "Channel Multipliers."

The calibrated ADC boards were then let record over long periods of time in order to verify their accuracy and stability. The following plots show the strange results that were encountered.

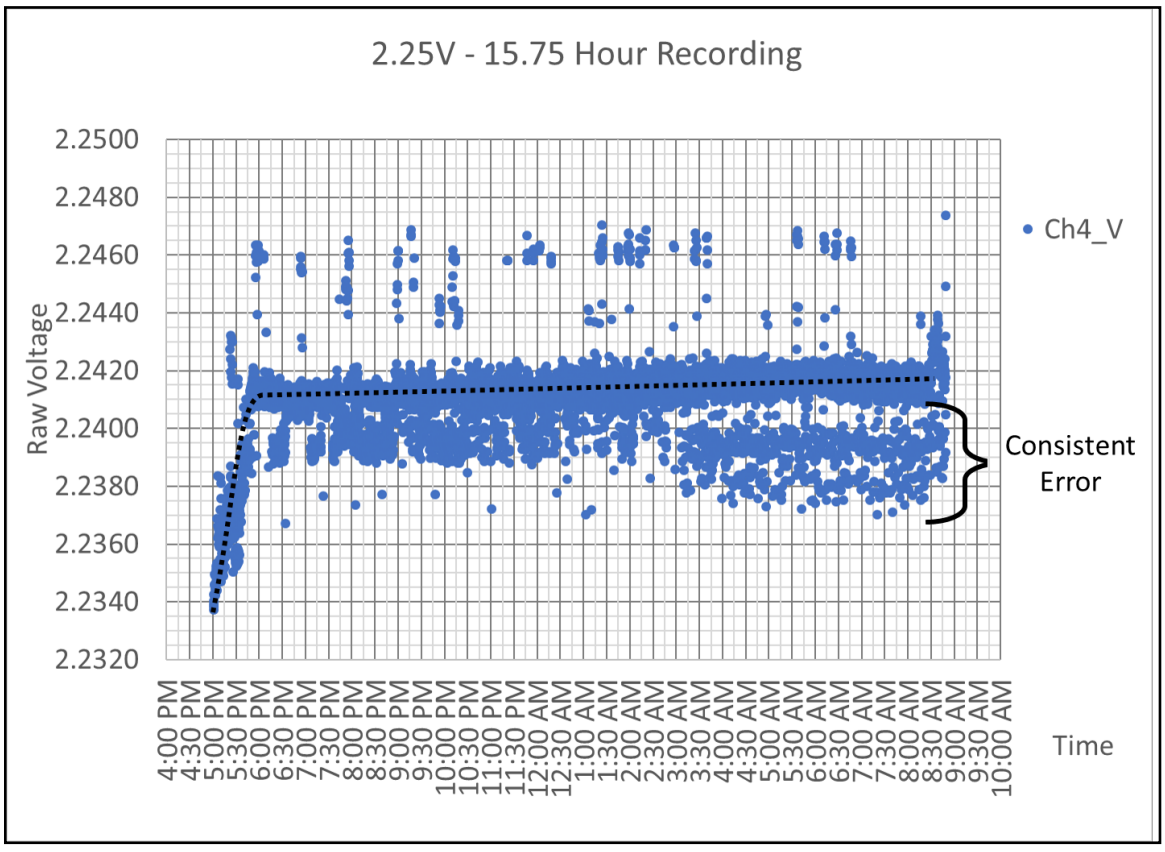

Figure H.4: Example plot showing the initial lag in raw voltage readings, as well as the sporadic errors that were seen after it did level out.

Figure H.4 shows how there was discovered to still be an initial lag in the the voltage readings after the ADC board initially started recording from a particular channel. After doing some research online, a few helpful blogs and white pa-

pers helped to explain that this lag was likely a result of cross-channel interference when sampling quickly from one channel to the next. Specifically, this article (www.embeddedrelated.com/showarticle/287/analog-to-digital-confusion -pitfalls-of-driving-an-adc) was helpful in explaining how cross-coupling between channels occurs as a result of sampling too quickly and not allowing for the internal capacitors to discharge fully between measurements.

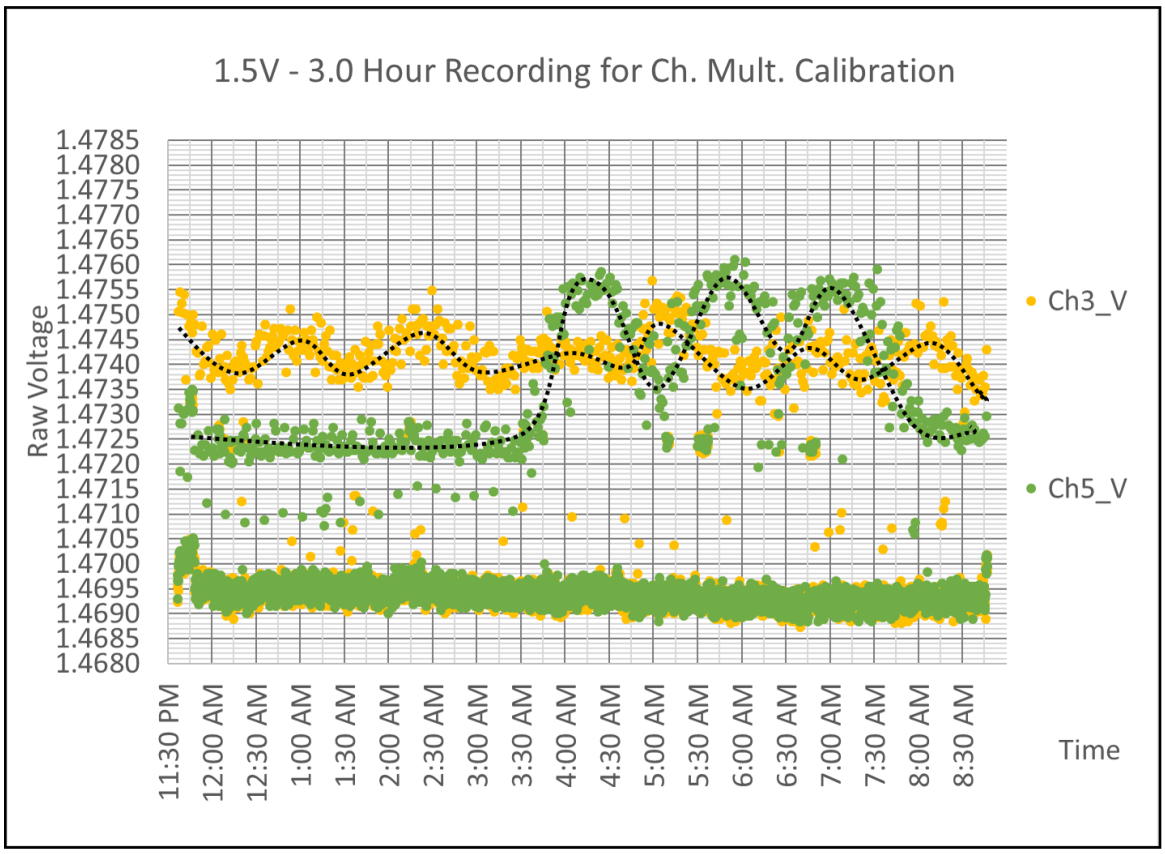

Figure H.5: Example plot showing the unexplained varying error throughout one night.

Another endurance test we ran through the night (seen in Figure H.5), found some unexpected results with the *Pi-16ADC* as well. Specifically, it appears that for no particular reason, two of the channels measured steadily around 1.4695 V throughout the night, but there was also a distinguishable trend of error interspersed as well. The dashed lines were added to show the trend that did not seem to be random. Unfortunately no explanation or solution was found for this particular "wandering-error" phenomenon we found on multiple occasions with this particular ADC board.

Eventually, after spending a significant amount of time trying to troubleshoot and accurately measure analog voltages with the *Alchemy Power Pi-16ADC*, its sampling rate was what ultimately caused us to switch ADC boards. Since it could only sample up to 17 samples-per-second (sps or Hz), we realized the only way we would be able to measure the induced current and voltage signals from the voltage and current transducers was to use an op-amp and rectifier. While this was explored, it was

discarded as we did more research and eventually landed on the *Adafruit ADS1115* ADC board.

The *Adafruit ADS1115* ADC board was the final ADC board we selected for our clamp-on energy meter and it did not pose many issues throughout its use. It was significantly more reliable than the *Pi-16ADC*, and the random floating errors (Figure H.5) were never seen again when measuring with it. As mentioned briefly in Chapter 3.3, there was a phenomena observed with the ADC board, that was later identified as a limitation of the *Raspberry Pi*.

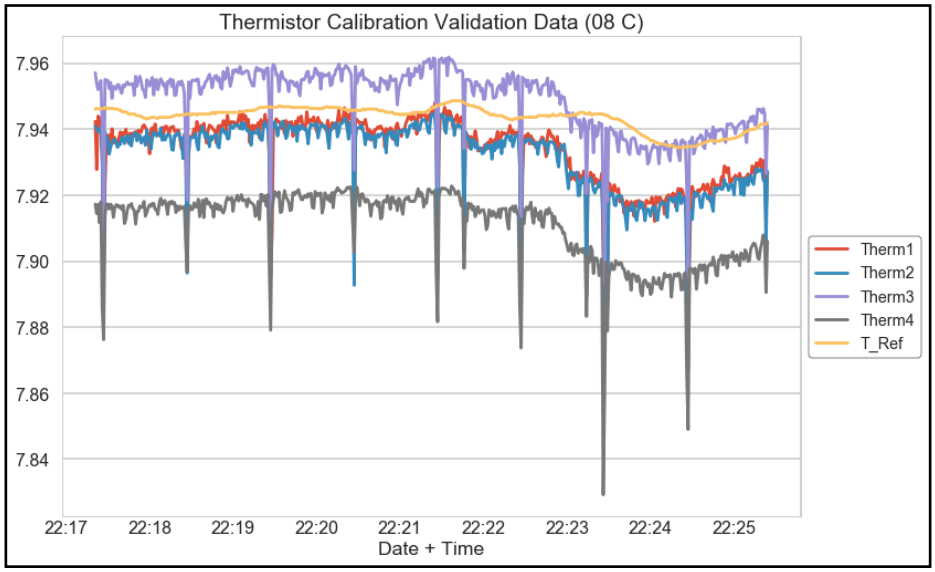

Figure H.6: Plot showing the random spikes in reading that correspond to mouse movement and and other *Raspberry Pi* processes.

During an initial thermistor calibration test, we found that the *Raspberry Pi*'s 5V-pin would spike randomly whenever the mouse was moved or it ran a task in the background. These events lined up perfectly with strange readings from the ADC board (depicted in Figure H.6). Ultimately it was determined that the sudden drops or "blips" in the *Raspberry Pi*'s 5V-pin was effecting the *Adafruit ADS1115*'s ability to regulate its internal reference voltage. Thus, as mentioned in Chapter 3.3, a separate external power supply was implemented that would more steadily power the ADC board.

The main take-away from this final lesson was that ADC boards with "internal reference voltages" must have steady power supplies, otherwise their ability to measure analog voltages to the accuracy claimed (16-bits) is hindered. While the *Raspberry Pi* can supply 5 V, the variance in amps supplied to the ADC board is too significant when other processes are taking place. Furthermore, since you can not directly set the analog reference voltage in such ADC boards, voltage divider circuits such as the one described here (https://www.jameco.com/Jameco/workshop/TechTip/temperature-measurement-ntc-thermistors.html) can not be implemented. Instead, you must measure the supply voltage directly and the intermediate voltage (as was implemented in our final design).

APPENDIX I

Design Process Diagrams

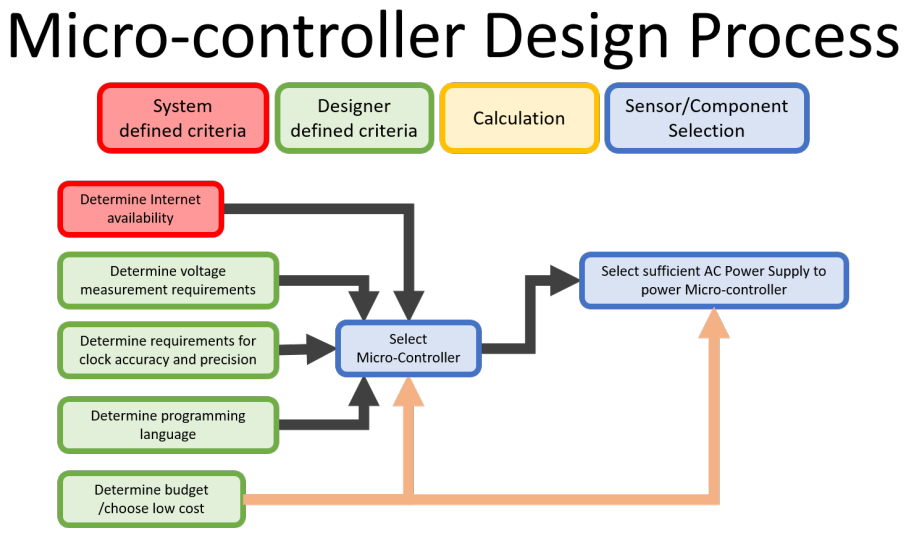

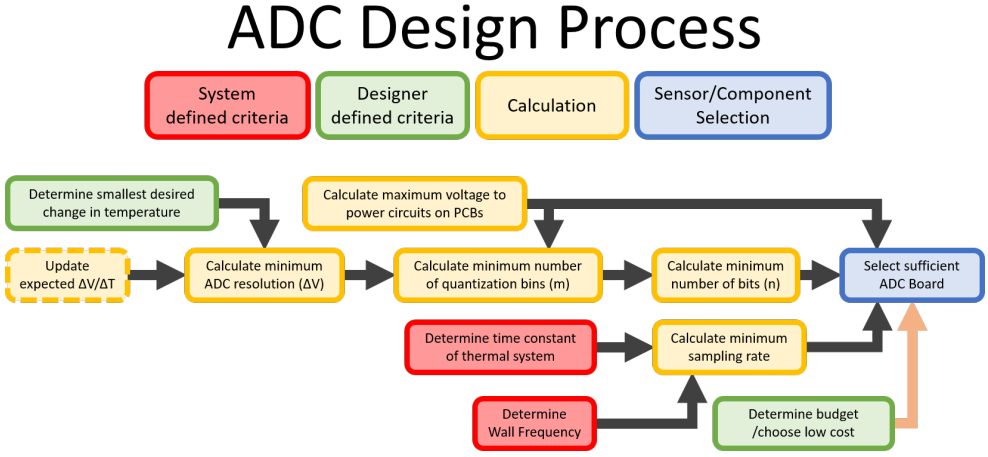

Temperature Sensor Design Process

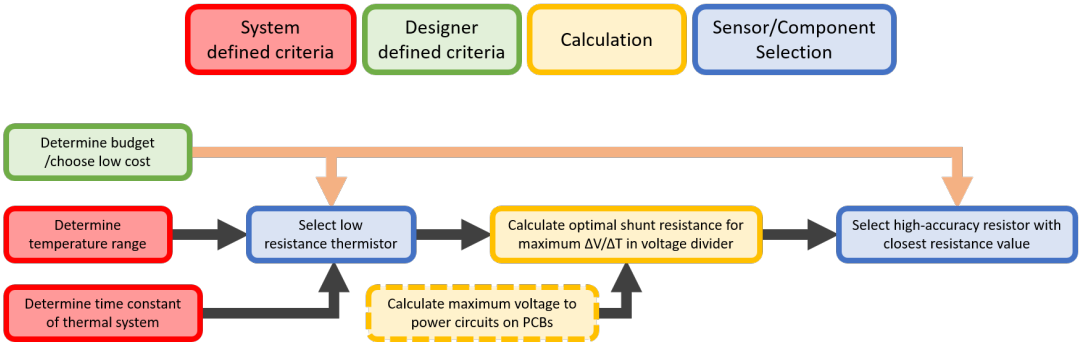

Flow Sensor Design Process

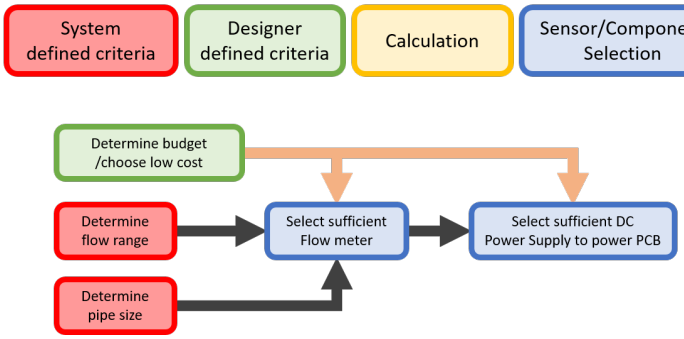

Power Sensor Design Process

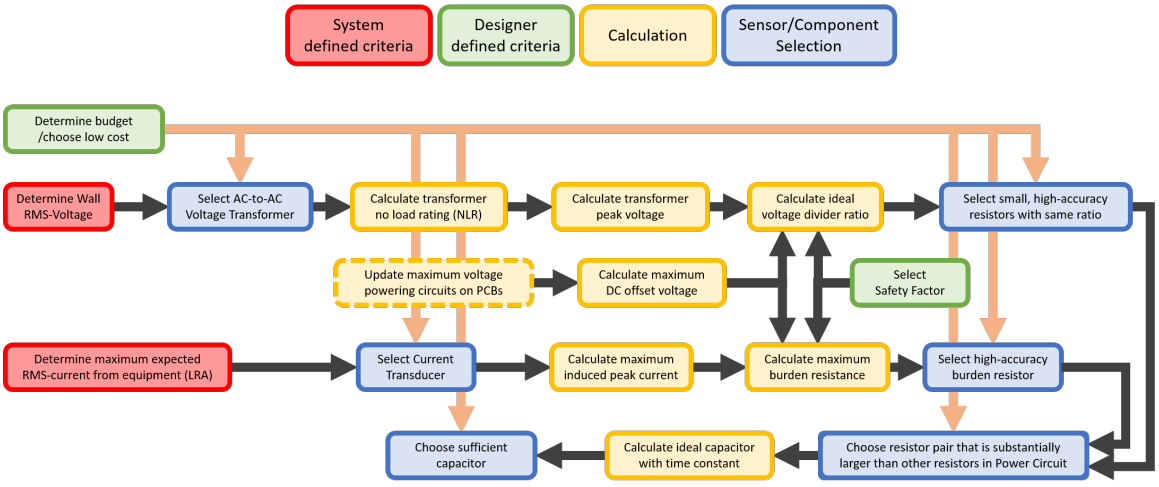

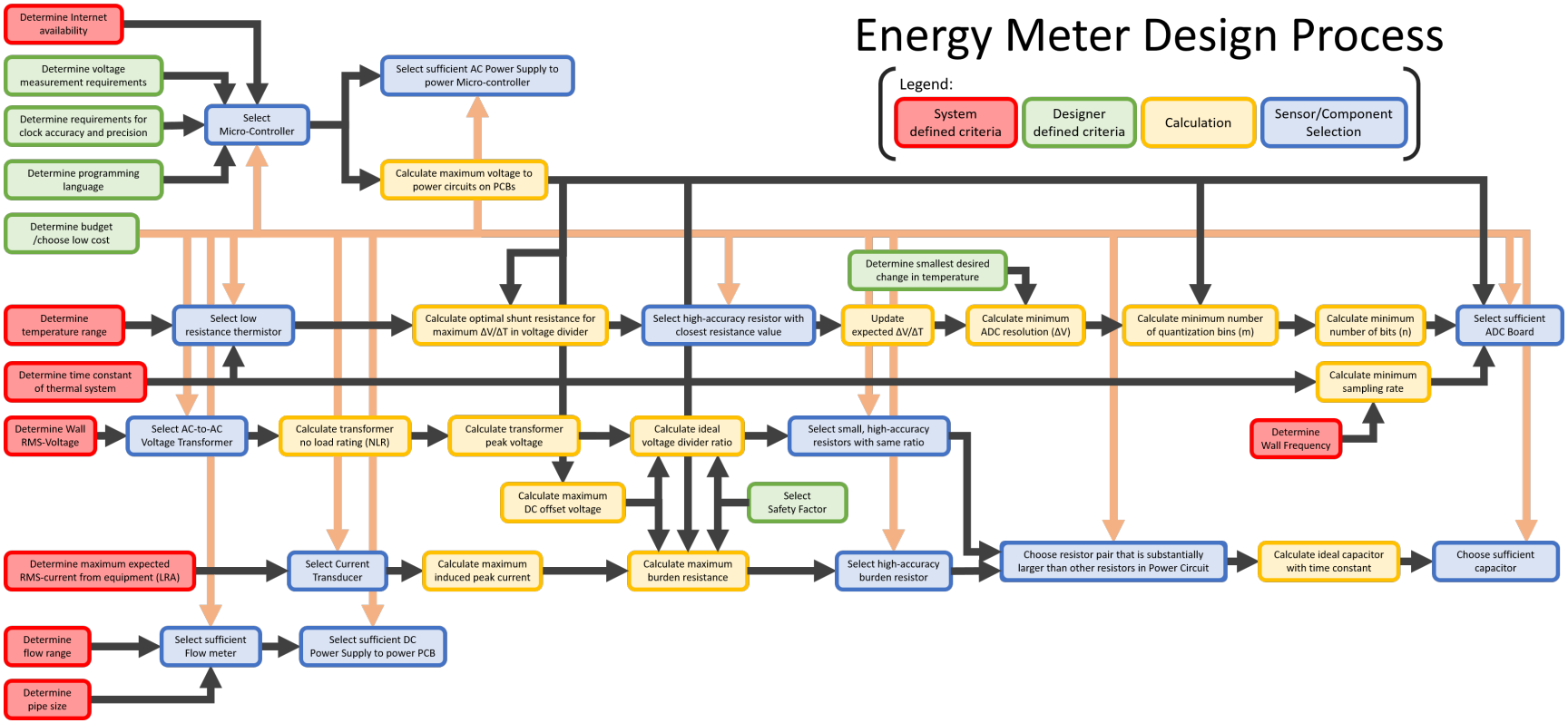
Energy Meter Design Process
Legend:
System defined criteria
Designer defined criteria
Calculation
Sensor/Component Selection
Determine Internet availability
Determine voltage measurement requirements
Determine requirements for clock accuracy and precision
Determine programming language
Determine budget /choose low cost
Select Micro-Controller
Select sufficient AC Power Supply to power Micro-controller
Calculate maximum voltage to power circuits on PCBs
Determine temperature range
Select low resistance thermistor
Calculate optimal shunt resistance for maximum ΔV/ΔT in voltage divider
Select high-accuracy resistor with closest resistance value
Determine smallest desired change in temperature
Update expected ΔV/ΔT
Calculate minimum ADC resolution (ΔV)
Calculate minimum number of quantization bins (m)
Calculate minimum number of bits (n)
Select sufficient ADC Board
Determine time constant of thermal system
Calculate minimum sampling rate
Determine Wall RMS-Voltage
Select AC-to-AC Voltage Transformer
Calculate transformer no load rating (NLR)
Calculate transformer peak voltage
Calculate ideal voltage divider ratio
Select small, high-accuracy resistors with same ratio
Determine Wall Frequency
Calculate maximum DC offset voltage
Select Safety Factor
Determine maximum expected RMS-current from equipment (LRA)
Select Current Transducer
Calculate maximum induced peak current
Calculate maximum burden resistance
Select high-accuracy burden resistor
Choose resistor pair that is substantially larger than other resistors in Power Circuit
Calculate ideal capacitor with time constant
Choose sufficient capacitor
Determine flow range
Determine pipe size
Select sufficient Flow meter
Select sufficient DC Power Supply to power PCB

VITA

Eric M. Brinkman

Candidate for the Degree of

Masters of Science

Thesis: DESIGN, DEVELOPMENT, AND VALIDATION OF A LOW-COST MEASUREMENT SYSTEM FOR RESIDENTIAL GROUND SOURCE HEAT PUMP SYSTEMS

Major Field: Mechanical and Aerospace Engineering

Biographical:

Education:

Received a Bachelors of Science in Mechanical Engineering at Oklahoma State University in May 2017.

Completed the requirements for the degree of Masters of Science with a major in Mechanical and Aerospace Engineering at Oklahoma State University in December 2019.

Experience:

Facilities Controls Engineering Intern at Texas Instruments in Dallas, TX during the summer of 2018.

Engineering Intern at Seat King, LLC and Electrex Inc. in Hutchinson, KS during the summer of 2017.

Engineering Intern for Global Partners International in Tajikistan during the summer of 2016.

Teaching Assistant at Oklahoma State University: *Systems Analysis* (MAE 3723), *Mechatronics Design* (MAE 4733), *Design of Indoor Environmental Systems* (MAE 4703), and *Engineering Analysis & Methods I* (MAE 3013)

Professional Affiliations:

ASHRAE Student Member